

UNIVERSITÉ DE GENÈVE
Département d'astronomie

FACULTÉ DES SCIENCES
Professeur T. J.-L. Courvoisier

The INTEGRAL view of galaxy clusters

THÈSE

présentée à la Faculté des sciences de l'Université de Genève
pour obtenir le grade de Docteur ès sciences,
mention astronomie et astrophysique

par

Dominique André ECKERT

de

Genève (GE)

Thèse N° 4023

GENÈVE

Atelier d'impression ReproMail

2008

ii

.

**CETTE THÈSE A FAIT L'OBJET DES PUBLICATIONS SUIVANTES:
voir Appendice B.**

Résumé En Français

Cette thèse porte sur le travail effectué à l'ISDC Data Centre for Astrophysics attaché à l'Observatoire de Genève pendant la période de 2004 à 2008. La mission principale de l'ISDC consiste à récolter, analyser et archiver les données provenant du satellite *INTEGRAL* de l'Agence Spatiale Européenne (ESA), en orbite depuis le 17 octobre 2002. La mission *INTEGRAL* a pour but l'étude des sources astrophysiques de rayonnement à haute énergie (rayons X et γ). Lors des 5 premières années de la mission, les instruments à bord du satellite ont permis la détection de plus de 500 sources de rayons à haute énergie, parmi lesquels plus de 40% étaient inconnus auparavant. Pour la plupart de ces sources, le mécanisme d'émission du rayonnement à haute énergie est l'accrétion de matière sur un objet compact (étoile à neutrons, trou noir ou naine blanche), que ce soit pour les sources galactiques (binaires X) ou extra-galactiques (noyaux actifs de galaxies, AGN). Si les binaires X et les AGN constituent la grande majorité des sources détectées par *INTEGRAL*, quelques sources d'autres types ont également été observées par le satellite. Parmi celles-ci, on trouve des rémanents de supernova, des pulsars isolés, et des amas de galaxies. Le but principal de cette thèse est l'étude des amas de galaxies dans le domaine des rayons X à haute énergie à l'aide du satellite *INTEGRAL*.

Les amas de galaxies sont les plus grandes structures gravitationnellement liées de l'Univers. Leur puits de potentiel profond comprime le gaz présent dans l'espace inter-galactique, ce qui a pour conséquence de chauffer substantiellement le gaz jusqu'à de très hautes températures ($\sim 10^7 - 10^8$ K). La densité du milieu est faible ($n_e \sim 10^{-4} - 10^{-2}$ cm $^{-3}$), et donc le milieu est optiquement mince. Par conséquent, les électrons du milieu rayonnent dans le domaine des rayons X par le processus de bremsstrahlung thermique, transformant les amas de galaxies en de puissantes sources de rayons X. Dans les amas les plus massifs, la masse baryonique du gaz dépasse très largement la masse des galaxies, et donc l'étude des amas de galaxies dans le domaine des rayons X est cruciale pour la compréhension de l'état des baryons dans l'Univers.

En plus de la grande quantité de gaz chaud révélée par les observations d'amas de galaxies dans les rayons X, il existe dans certains amas une population de particules relativistes, qui émettent du rayonnement de type synchrotron dans le domaine des ondes radio. Etant donné que les amas de galaxies sont traversés en permanence par les photons du rayonnement fossile micro-onde (Cosmic Microwave Background, CMB), l'interaction des électrons relativistes avec les photons du CMB devrait également produire une composante additionnelle d'émission dans les rayons X, qui deviendrait prépondérante dans le domaine des rayons X "durs" (hard X-rays, $E_\gamma \gtrsim 20$ keV). La détection de cette composante non-thermique est de première importance pour mesurer la valeur moyenne du champ magnétique et pour contraindre les modèles qui tentent d'expliquer la présence de particules relativistes dans certains amas (chocs engendrés par la fusion de deux amas ou désintégration de rayons cosmiques, voir le Chap. 2). En raison du manque de télescopes puissants disponibles dans cette bande d'énergie, il n'a pour l'heure pas été possible de détecter clairement la présence de cette composante. Précédant le lancement

d'*INTEGRAL*, l'observation la plus convaincante d'une telle composante dans le spectre X d'un amas de galaxies a été obtenue par le satellite italo-néerlandais *BeppoSAX* (Fusco-Femiano et al. 1999) en analysant le spectre de l'amas de Coma Berenices. Toutefois, il faut noter que cette observation est à l'heure actuelle sujette à controverse, étant donné qu'une analyse indépendante des données du satellite *BeppoSAX* par un autre groupe n'a pas permis de confirmer ce résultat (Rossetti & Molendi 2004). Dans ces conditions, les instruments à rayons X durs disponibles à bord d'*INTEGRAL* ont un rôle important à jouer dans le but de confirmer ou infirmer le résultat obtenu par *BeppoSAX*. En conséquence, le but principal de cette thèse est d'analyser les données prises par les instruments à bord d'*INTEGRAL* (en particulier l'imageur à rayons γ , IBIS) dans le but d'obtenir les meilleures images et spectres d'amas de galaxies au-delà de 20 keV et de tenter d'isoler la composante à haute-énergie.

Dans ce but, mon travail de thèse s'est concentré autour de l'analyse des amas de Coma, Ophiuchus et Perseus, qui sont les amas de galaxies les plus brillants dans les rayons X, avec l'imageur IBIS et le moniteur JEM-X à bord d'*INTEGRAL*. Dans le cas particulier de l'amas de Coma, le rayon de coeur de l'amas ($R_c \sim 10$ arcmin, Briel et al. (1992)) est supérieur à la résolution angulaire de l'instrument IBIS (6 arcmin demi-largeur à mi-hauteur, HWHM). Or, les outils standards pour l'analyse des données prises par *INTEGRAL* sont optimisés pour l'analyse des sources ponctuelles, et ne permettent pas un traitement correct des sources étendues. Par conséquent, une partie importante de ma thèse a été consacrée au développement et à la calibration d'outils permettant l'analyse de sources étendues avec IBIS, ces outils pouvant être facilement adaptés à n'importe quel instrument similaire (voir le Chap. 3 pour les détails de la méthode). Par la suite, cette méthode a été appliquée à l'analyse de l'émission X de l'amas de Coma.

Les résultats principaux de cette thèse sont présentés dans les Chap. 4 (Coma), 5 (Ophiuchus) et 6 (Perseus). En ce qui concerne Coma, l'observation de l'amas par *INTEGRAL* a permis de mettre en évidence plusieurs points inconnus jusqu'alors. Grâce à la bonne résolution angulaire d'*INTEGRAL*, nous avons pu pour la première fois résoudre la source spatialement, et nous avons pu comparer la morphologie de l'amas en rayons X durs avec sa morphologie bien connue en rayons X. Cette analyse nous a permis de mettre en évidence une région située au Sud-Ouest du coeur de l'amas dont l'émission au-delà de 20 keV excède l'extrapolation de l'émission en rayons X. Toutefois, la faible statistique ne nous a pas permis de déterminer sans ambiguïté l'origine de cette émission. En effet, deux explications plausibles peuvent être avancées: soit le gaz dans cette région est significativement plus chaud que celui du reste de l'amas, soit une composante additionnelle non-thermique, comme proposé par Fusco-Femiano et al. (1999), est présente. De nouvelles observations de l'amas par *INTEGRAL*, qui seront effectuées lors du prochain cycle d'observation, nous permettront de déterminer lequel de ces deux scénarios est correct.

L'amas d'Ophiuchus, bien que peu étudié par le passé, constitue la meilleure cible potentielle pour *INTEGRAL*. Il est situé dans la région du bulbe galactique à 10° seulement du centre de notre Galaxie. En raison de la stratégie d'observation d'*INTEGRAL*, qui consacre une fraction importante du temps d'exposition à cette région, la quantité de données accumulées par *INTEGRAL* sur cet objet est très importante, ce qui nous a permis de

détecter la source avec une haute significativité et donc d'extraire un spectre de bonne qualité. Grâce à l'addition des données du moniteur à rayons X JEM-X, nous avons pu extraire le spectre de l'objet sur une large bande (3-120 keV). L'analyse du spectre a démontré qu'un modèle purement thermique ne peut pas expliquer les données de manière satisfaisante, et qu'une composante additionnelle est requise pour obtenir un fit acceptable des données. La composante additionnelle est détectée de manière significative (6.4σ), ce qui constitue donc la meilleure observation d'une composante non-thermique dans un amas de galaxies au jour d'aujourd'hui. En comparant la composante X non-thermique avec des données existantes dans les ondes radio, nous mesurons un champ magnétique $B \sim 0.2\mu$ G. Afin de déterminer l'origine des particules relativistes, une campagne d'observation de l'amas dans les ondes radio et dans les rayons γ à haute énergie est en cours, qui devrait nous permettre de mesurer précisément le champ magnétique dans l'amas.

L'amas de Perseus est l'amas de galaxies le plus brillant du ciel X, ce qui en fait un objet extrêmement étudié depuis les années 1970. Un puissant noyau actif est présent au coeur de la galaxie centrale, NGC 1275. Le noyau actif injecte constamment une quantité importante de rayons cosmiques dans l'amas, qui contient donc une population importante de particules relativistes observées dans les ondes radio. Dans les rayons X, une longue exposition du satellite *Chandra* (Sanders et al. 2005) a révélé la présence d'une composante non-thermique dont l'extrapolation dans les rayons X durs serait clairement détectable par *INTEGRAL*. Toutefois, l'analyse des données *INTEGRAL* n'a pas confirmé ce résultat. En effet, si une composante non-thermique a bien été détectée dans le spectre *INTEGRAL*, cette composante s'est révélée ~ 3 fois plus faible que le niveau prédit par Sanders et al. (2005), et elle peut être entièrement expliquée par l'émission du noyau actif. Nous concluons donc que la détection d'une composante non-thermique par Sanders et al. (2005) était probablement due à une calibration incertaine de *Chandra* dans sa bande la plus élevée.

En conclusion, *INTEGRAL* a pu apporter d'importantes informations pour la compréhension des phénomènes dûs aux particules relativistes dans les amas de galaxies, notamment grâce à la détection significative d'émission non-thermique dans le spectre de l'amas d'Ophiuchus. Ces résultats sont importants notamment dans l'optique de la prochaine génération de télescopes à rayons X (*Simbol-X*, *NeXT*, *NuSTAR*), qui permettra de détecter la composante non-thermique dans un nombre croissant d'amas, et d'analyser en détails la structure du champ magnétique. Le lancement récent de la mission *GLAST/Fermi*, dédiée à l'étude des objets célestes dans les rayons γ à haute énergie ($E_\gamma \sim$ GeV), ouvre également de nouvelles portes pour la compréhension des mécanismes d'accélération de particules dans les amas de galaxies.

Table of contents

1	General introduction	1
2	Particle acceleration in clusters of galaxies and observational properties	3
2.1	Introduction: the Intra-Cluster Medium (ICM)	3
2.2	Evolution of the electron spectrum	5
2.3	Primary electrons	6
2.3.1	Diffusive shock acceleration	7
2.3.2	The “re-acceleration” model	9
2.4	Secondary electrons	10
2.5	Alternative models	12
2.5.1	Non-thermal bremsstrahlung from non-relativistic electrons	13
2.5.2	Production of very high energy electrons	13
2.6	Observational properties	14
2.6.1	Radio emission	14
2.6.2	Hard X-ray and Extreme UV emission	16
2.6.3	High-energy γ -ray emission	17
2.7	Methods of magnetic field measurement	18
2.7.1	Faraday rotation measure	18
2.7.2	Equipartition magnetic field	19
2.7.3	Synchrotron/inverse-Compton flux ratio	20
2.7.4	Reconciling the values obtained with different methods	20
2.8	Conclusion	21
3	Analysis of extended sources with <i>INTEGRAL</i>	23
3.1	The <i>INTEGRAL</i> mission	23
3.1.1	The coded-mask technique	24
3.1.2	The Imager on-Board <i>INTEGRAL</i> Satellite (IBIS)	25
3.1.3	The JEM-X X-ray monitor	26
3.1.4	The SPectrometer on <i>INTEGRAL</i> (SPI)	27
3.1.5	The Optical Monitoring Camera (OMC)	27
3.2	Difficulties due to the coded-mask technique	27
3.3	A method to analyze extended sources with a coded-mask instrument	29

3.3.1	The shadow pattern cast by an extended source	29
3.3.2	Shadowgram fitting	30
3.3.3	Using the standard OSA spectral extraction tool	31
3.3.4	Analysis of extended sources with JEM-X	33
3.4	Conclusion	33
4	Hard X-ray observations of the Coma cluster	35
4.1	Introduction	35
4.2	<i>INTEGRAL</i> observations of the Coma cluster	37
4.3	Analysis of <i>INTEGRAL</i> data with OSA 6.0	38
4.3.1	Hard X-ray morphology of the cluster	38
4.3.2	<i>XMM-Newton/INTEGRAL</i> spectrum of the cluster	41
4.3.3	Discussion	42
4.4	New results based on OSA 7.0	45
4.4.1	Analysis of the morphology	46
4.4.2	Determining the temperature of the South-West region	47
4.4.3	ISGRI spectra of the cluster	48
4.4.4	Discussion	49
4.5	Conclusion	49
4.6	Scientific article on the Coma cluster	52
4.7	Proceeding of the 30 th ICRC conference	59
5	Hard X-ray observations of the Ophiuchus cluster	63
5.1	Introduction	63
5.2	<i>INTEGRAL</i> observations of the Ophiuchus cluster	65
5.2.1	ISGRI data analysis	66
5.2.2	JEM-X data analysis	67
5.3	Morphological analysis	68
5.4	Broad-band spectrum of the cluster	70
5.4.1	Modeling the non-thermal component	72
5.5	Discussion	74
5.5.1	Reliability of the result	74
5.5.2	Origin of the non-thermal component	75
5.5.3	Origin of the high-energy electrons	77
5.6	Conclusion	78
5.7	Scientific article on the Ophiuchus cluster	80
6	Hard X-ray observations of the Perseus cluster	89
6.1	Introduction	89

6.2	<i>INTEGRAL</i> observations of Perseus	92
6.3	Morphology of the cluster	92
6.4	Broad-band <i>INTEGRAL</i> spectrum	93
6.4.1	Full-resolution JEM-X spectrum	93
6.4.2	Total spectrum	94
6.5	Discussion	95
6.6	Conclusion	97
7	Other scientific activities	99
7.1	The ISDC shift team	99
7.2	IGR J00291+5934	100
7.2.1	Introduction on pulsars	100
7.2.2	The discovery of IGR J00291+5934	101
7.2.3	Analysis of IGR J00291+5934	102
7.2.4	New analysis of the <i>INTEGRAL</i> data with OSA 7.0	103
7.2.5	Conclusion	105
7.3	Astronomer's Telegram (ATel) on the discovery of IGR J00291+5934 . . .	107
7.4	Scientific article on IGR J00291+5934	108
8	Conclusion and future prospects	113
9	Acknowledgements/Remerciements	115
A	Calibration work related to extended source analysis	117
A.1	IBIS PIFs and misalignment	117
A.2	ISGRI mosaicking method	119
B	List of publications	121

Chapter 1

General introduction

This thesis is based on work performed at the ISDC Data Center for Astrophysics attached to the University of Geneva between October 2004 and September 2008. The ISDC is the ground segment for the *INTEGRAL* mission of the European Space Agency, which observes the sky in the X-ray and γ -ray band since its launch on Oct. 17, 2002. The principal aim of this thesis is the study of galaxy clusters in the hard X-ray band with *INTEGRAL*.

Since the discovery of the first X-ray source, Scorpius X-1, in the 1960s, a large effort has been put in order to study X- and γ -ray emitting sources. For technical reasons, building instruments to detect high-energy sources is a difficult task. Indeed, the Earth's atmosphere is opaque to high-energy photons, and therefore it is necessary to design space missions to detect astrophysical sources. This makes the cost of the telescopes higher. Furthermore, the penetration power of high-energy photons is so large that classical mirrors cannot deflect them, and hence standard focusing techniques cannot be applied for high-energy astronomy. In the X-ray band (0.5-10 keV), this problem has been overcome thanks to the grazing-incidence technique. This method uses low incidence angles to deflect incoming photons and focus them in the detector plane. Thanks to this technique, modern X-ray missions, such as the X-ray Multi-Mirror (*XMM-Newton*) mission of the European Space Agency and the *Chandra* mission of the NASA, are capable of fine imaging (angular resolution $< 10''$) and high sensitivity. However, this technique still cannot be used in the hard X-ray (10-50 keV) and soft γ -ray bands (up to a few MeV). The study of high-energy sources in this energy range is very important, because it is the range where non-thermal phenomena induced by relativistic particles start to dominate over thermal ones. Several γ -ray emission lines (such as the $e^+ - e^-$ annihilation line at 511 keV and the ^{26}Al decay line at 1.8 MeV) can also be observed in this energy range, which allows for direct measurements of the annihilation and decay rates.

The *INTEGRAL* mission was designed for fine imaging and high-resolution spectroscopy in the hard X-ray/soft γ -ray band. In order to determine the position of high-energy sources, it uses the *coded-mask* technique, in which sky images are reconstructed from the shadow pattern of a *mask* made of opaque and transparent elements on a detector. In the first 5 years of the mission, more than 500 astrophysical sources have been detected above 20 keV thanks to this technique, among which 40% are newly-discovered sources. The characteristics of the sources detected by *INTEGRAL* have been described

by Bodaghee et al. (2007). A large majority of *INTEGRAL* sources are powered by accretion of material on compact objects. Galactic sources are mainly X-ray binary systems in which a compact object (neutron star, black hole or white dwarf) is accreting material from a stellar-type companion, while extragalactic sources are mostly active galactic nuclei (AGN), i.e. super-massive black holes ($10^6 - 10^9 M_{\odot}$) accreting material in the center of galaxies. While X-ray binaries and AGN represent a large fraction of the sources detected by *INTEGRAL*, several objects of other types have also been detected. They include supernova remnants, isolated pulsars, pulsar-wind nebulae and galaxy clusters.

Since the detection of the Coma cluster in the X-ray band in 1971, it is well known that clusters of galaxies are filled with a hot, low-density plasma, the intra-cluster medium (ICM), which produces powerful X-ray emission through thermal bremsstrahlung and line emission. In rich clusters, the total baryonic mass in the ICM largely exceeds the total mass of the member galaxies, and therefore the study of the X-ray emitting plasma is of prime importance to understand the state of baryons in the Universe. With the modern generation of X-ray telescopes like *XMM-Newton* and *Chandra*, the properties of the gas (density, temperature, pressure, entropy) can be accurately measured in a large number of clusters.

Thanks to the detection of large-scale diffuse radio emission, it is also well known that some clusters contain a large population of relativistic particles which produce synchrotron radiation in the radio domain. This implies that photons of the Cosmic Microwave Background (CMB) should interact with the relativistic electrons and gain energy. The resulting photons should therefore create a non-thermal component in the X-ray band. Because of the very strong thermal X-ray emission, detecting this component below 10 keV is difficult. On the other hand, in the hard X-ray band the non-thermal component should become observable again. Up to the present day, because of the lack of sensitive instruments in this energy range no firm detection of this component could be made. As a consequence, the aim of this thesis is to analyze *INTEGRAL* data on several clusters of galaxies and possibly detect the non-thermal component. This is important in particular to determine the magnetic-field strength in clusters and constrain the particle acceleration models which try to explain the presence of relativistic particles in galaxy clusters.

Chapter 2

Particle acceleration in clusters of galaxies and observational properties

2.1 Introduction: the Intra-Cluster Medium (ICM)

According to the standard hierarchical structure formation model, small gravitational structures (e.g., CMB anisotropies) form first, and then, under the influence of gravity, merge to form bigger and bigger structures. Since they are the biggest bound structures observed in the Universe, we hence expect that clusters of galaxies are the latest structures to form. Therefore, we expect that some clusters could still be forming, and merging with other clusters to form even larger structures (“super-clusters”, “great attractors”). Hence, the study of galaxy clusters, and in particular of clusters experiencing major merging events, is important to probe structure formation scenarios. In this framework, observations of clusters of galaxies in the X-ray band play an important role. Indeed, only about a tenth of the universe’s baryons reside in stars and galaxies, while the vast majority is left in intergalactic space. Within massive clusters, the gas falls into the deep potential wells of the forming objects. The large potential energy is converted into kinetic energy by compression, shocks and turbulent energy diffusion, which results in substantial heating of the falling gas. The compressed gas then forms an extended gaseous halo which fills a large fraction of the cluster volume and can only remain in a state close to hydrostatic equilibrium if its speed is similar to the typical velocity of a cluster galaxy. This is generally in the range 300 to 1,200 km/s, which corresponds to temperatures of $\sim 1 - 10$ keV ($10^7 - 10^8$ K). The typical density of the medium is low ($n_e \sim 10^{-4} - 10^{-2}$ cm $^{-3}$), so the medium is optically thin. The heated electrons of the intracluster medium (ICM) will therefore radiate in the X-ray range through thermal bremsstrahlung, transforming clusters of galaxies into bright X-ray sources. The gas also contains large amounts of heavy elements, probably injected in the ICM through supernova explosions and galactic winds. Because of the high plasma temperatures, the ionization level of the heavy elements is high, which produces ionization and recombination emission lines in the X-ray spectrum, such as Fe XXV and Fe XXVI emission lines at 6.5 and 6.8 keV. For all these reasons, the study of galaxy clusters at X-ray wavelengths is crucial to understand the evolution of the gas which has not condensed into stars and galaxies, and cannot be observed in visible

light (see Voit (2005) for a review).

Based on X-ray spectra and morphologies, one can outline three categories of clusters: merging, post-merger and cooling core clusters. If a cluster remains in a relaxed state on long timescales, the gas of the ICM is expected to start cooling because of radiative losses. The gas should therefore slowly fall inwards and condensate into galaxies. This is called the “cooling flow” model (Fabian 1994). The Perseus cluster ($z = 0.0176$) is the prototype of such clusters. Cooling-core clusters are characterized by a low temperature in the core, increasing with radius. The left panel of Fig. 2.1 shows a temperature map of the Perseus cluster from *Chandra* observations (Sanders et al. 2005). The temperature ranges from ~ 2.5 keV in the center up to ~ 8 keV in the peripheral regions. In addition, the central cD galaxy of several well-known cooling core clusters (e.g. Perseus, Virgo and Centaurus) exhibits some AGN activity, which probably has an influence on the state of the intracluster gas. In several cases such as Perseus, it is believed that AGN activity injects a large amount of energy in the ICM and could be responsible for stopping the cooling flow.

On the other hand, some clusters exhibit signs of merging activity at the present time. The “Bullet cluster” 1ES 0657-55.8 (Tucker et al. 1998) is the most striking example of a merging cluster (see the right panel of Fig. 2.1). From *ASCA* data, its temperature was found to be $kT = 17.4 \pm 2.5$ keV, making it the hottest known X-ray cluster. The X-ray image clearly shows the interaction between the major cluster (on the left) and a smaller cluster, whose morphology has been strongly modified by the merging event. Evidence for prominent bow shocks give an estimate for the shock velocity of $\approx 4,500$ km/s, which corresponds to a shock Mach number way above unity (Markevitch et al. 2004). Finally, post-merger clusters are characterized by irregular morphologies and hot temperatures, but do not show evidence of merging activity. For these reasons, they are believed to have experienced a major merger in the past. In some cases, a weak cooling-flow is observed in the central regions. The bright, nearby Ophiuchus cluster ($z = 0.028$, Johnston et al. (1981)) is an example of such clusters.

During cluster merging events, we expect that the hot ICM gas of the two clusters will interact, which will possibly create giant shock waves that will propagate through the ICM of the merging clusters. In this framework, models predict that a fraction of the particles will be accelerated, and will produce a population of relativistic electrons within the clusters (the “primary electrons” or “re-acceleration” scenario). Alternatively, interaction of cosmic-ray protons with the thermal ICM ions could produce a cascade of particles that could lead to the presence of relativistic particles (the “secondary electrons” model). In this chapter, I will present the different particle acceleration scenarios that could be responsible for the presence of relativistic electrons in clusters of galaxies. I will present the observational properties of the different scenarios, and compare them with existing observations.

2.2 Evolution of the electron spectrum

In this section, I will present the basic formulae describing the evolution of the population of relativistic particles. I will also present the different energy loss processes which

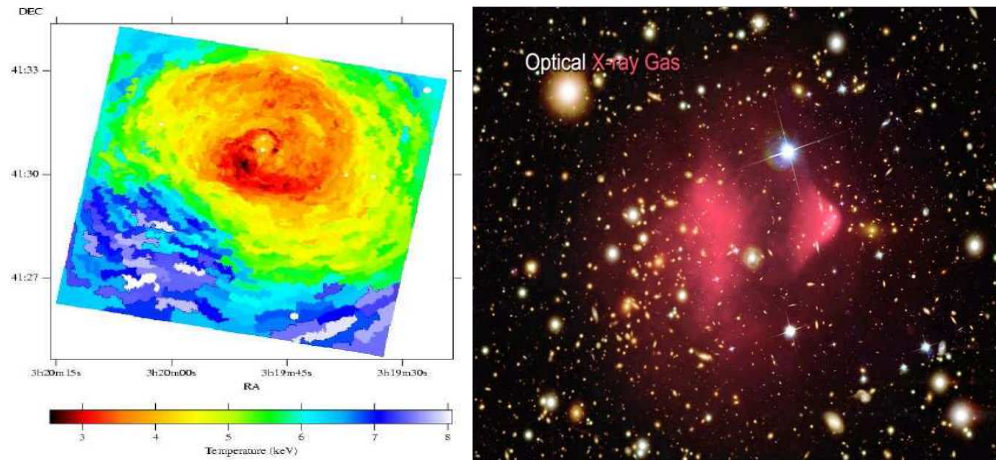


Figure 2.1: Left: Chandra temperature map of the Perseus cluster (Sanders et al. 2005). The uncertainties range from 0.1 keV in the coolest regions to 0.5 keV in the hottest regions. The white spots are subtracted point sources. Right: Chandra X-ray image of the “Bullet cluster” 1ES 0657-55.8 super-imposed on an optical image of the region (Markevitch et al. 2004).

modify the electron spectrum, and show a few results of simulations of electron spectra for different initial populations and acceleration efficiencies. This follows Sarazin (1999).

The evolution of the cosmic-ray electron population in clusters is given by the difference between gains and losses:

$$\frac{\partial N(E)}{\partial t} = \frac{\partial}{\partial E} [b(E)N(E)] + Q(E), \quad (2.1)$$

where $N(E)dE$ and $Q(E)dE$ give respectively the number of electrons and the total rate of production of new electrons in the energy range $[E, E + dE]$, and $b(E) \equiv -\left(\frac{dE}{dt}\right)$ gives the total energy-loss rate for particles with an energy of E . The energy-loss processes involved are Coulomb interactions with the thermal ICM electrons and radiation through synchrotron (low-frequency radio), inverse-Compton (hard X-ray) and non-thermal bremsstrahlung (high-energy γ -ray) processes. It is usually more convenient to write equation 2.1 as a function of the Lorentz factor γ instead of the kinetic energy $E = (\gamma - 1)m_e c^2$:

$$\frac{\partial N(\gamma)}{\partial t} = \frac{\partial}{\partial \gamma} [b(\gamma)N(\gamma)] + Q(\gamma). \quad (2.2)$$

Coulomb losses due to elastic collisions with thermal electrons give a loss rate that is approximately (Rephaeli 1979):

$$b_{Coul}(\gamma) \approx 1.2 \times 10^{-12} n_e \left[1.0 + \frac{\ln(\gamma/n_e)}{75} \right] s^{-1}, \quad (2.3)$$

where n_e is the thermal electron density in the cluster, which is typically of the order of 10^{-3} cm^{-3} . The collisions between cosmic-ray electrons and thermal ions will also induce

energy losses through non-thermal bremsstrahlung. In the very-low density limit, the loss rate due to bremsstrahlung is given by (Blumenthal & Gould 1970):

$$b_{brems} \approx 1.51 \times 10^{-16} n_e \gamma [\ln(\gamma) + 0.36] s^{-1}. \quad (2.4)$$

Clusters of galaxies are also filled by a large-scale magnetic field $B \sim 1 \mu G$. Relativistic electrons will therefore spiral along the magnetic field lines and radiate through synchrotron processes. In the ultra-relativistic limit ($\gamma \gg 1$), the expression for the loss rate due to synchrotron radiation is given by

$$b_{syn}(\gamma) = \frac{4}{3} \frac{\sigma_T}{m_e c^2} \gamma^2 U_B = 1.3 \times 10^{-21} \gamma^2 \left(\frac{B}{1 \mu G} \right)^2 s^{-1}, \quad (2.5)$$

where σ_T is the Thompson cross-section and $U_B = \frac{B^2}{8\pi}$ is the energy density of the magnetic field (see Rybicki & Lightman (1985) for details). Finally, the electrons will also up-scatter photons of the Cosmic Microwave Background (CMB) to higher energies. The loss function for inverse-Compton (IC) scattering is the same as the synchrotron case with the magnetic energy density replaced by the energy density of the incoming radiation field,

$$b_{IC}(\gamma) = \frac{4}{3} \frac{\sigma_T}{m_e c^2} \gamma^2 U_{CMB} = 1.37 \times 10^{-20} \gamma^2 (1+z)^4 s^{-1}, \quad (2.6)$$

where U_{CMB} is the energy density of the radiation field of the CMB and z is the redshift of the cluster. At very high energies ($\gamma > 10^9$), the Thompson cross-section is replaced by the smaller Klein-Nishina cross-section, and therefore the inverse-Compton losses are smaller. In the Thompson regime, the ratio between IC and synchrotron losses is given by

$$\frac{b_{syn}}{b_{IC}} = \frac{U_B}{U_{CMB}} \approx 0.095 (1+z)^{-4} \left(\frac{B}{1 \mu G} \right)^2. \quad (2.7)$$

We can see here that as long as the magnetic field is not too strong, IC losses will dominate over synchrotron losses. The left panel of Fig. 2.2 shows the behaviour of the different loss functions as a function of γ for a generic cluster with $n_e = 10^{-3} \text{ cm}^{-3}$, $B = 1 \mu G$ and $z = 0$. At low energies, Coulomb losses dominate, whereas at higher energies ($\gamma > 10^3$), the electrons cool mostly through IC and synchrotron radiation. One can define an instantaneous timescale for particle losses by

$$t_{loss} \equiv \frac{\gamma}{b(\gamma)}. \quad (2.8)$$

The right panel of Fig. 2.2 shows the behaviour of t_{loss} as a function of γ for different values of n_e and B . The characteristic features of t_{loss} for parameters relevant to clusters are a maximum at $\gamma \sim 100 - 500$, for which the loss timescale is quite long ($\sim 3 - 10 \text{ Gyr}$). Thus, particles with energy in this range can accumulate for long periods in clusters.

2.3 Primary electrons

The ‘‘primary electrons’’ or ‘‘re-acceleration’’ model predicts that the interactions in the ICM will create giant shock waves, where particles would be accelerated through first-

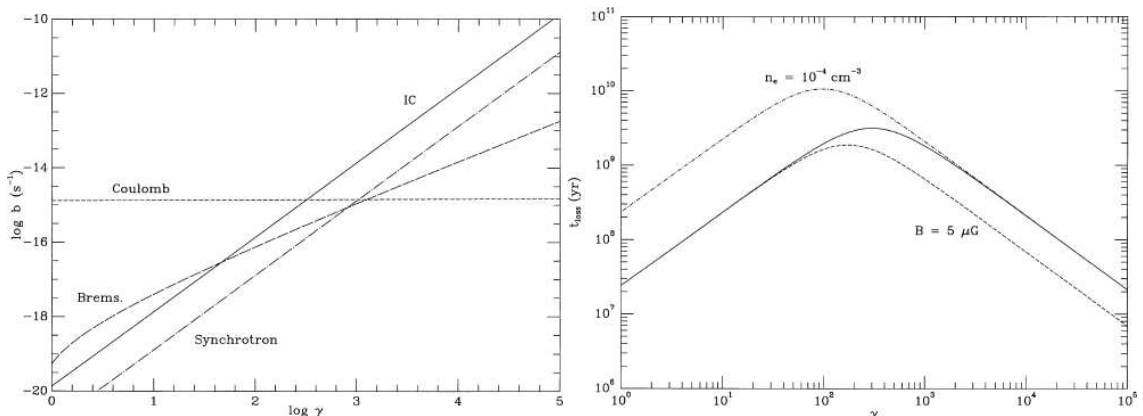


Figure 2.2: Left: Loss function $b(\gamma)$ for the different electron cooling processes: Coulomb losses, non-thermal bremsstrahlung emission, synchrotron and inverse-Compton radiation. The curves assume $n_e = 10^{-3} \text{ cm}^{-3}$, $B = 1 \mu\text{G}$ and $z = 0$. Right: Cooling timescale t_{loss} as a function of γ in a cluster with $n_e = 10^{-3} \text{ cm}^{-3}$ and $B = 1 \mu\text{G}$ (solid curve). The dashed curve assumes a magnetic field of $5 \mu\text{G}$, and the dot-dashed curve uses a density $n_e = 10^{-4} \text{ cm}^{-3}$. The figures are from Sarazin (1999).

order Fermi processes, i.e. diffusive shock acceleration (DSA). In this section, I will start by presenting the standard diffusive shock acceleration theory (Blandford & Ostriker 1978), and then apply it to the specific case of cluster merging events.

2.3.1 Diffusive shock acceleration

Shock acceleration occurs during multiple interactions of particles in which a small amount of energy is gained at each interaction. The ingredients of this theory are collisionless shocks in a plasma, i.e. shocks of width less than the mean free path of the particles. This part follows Courvoisier (2007). An illustration of the geometry of the interaction is shown in Fig. 2.3.

Let us now consider a particle of mass m moving with a relative velocity Δv parallel to the x axis in the reference frame of an isotropised plasma. On both sides of the shock region, two zones of plasma are moving with velocities u_1 and u_2 with respect to the reference frame (zones 1 and 2 of Fig. 2.3). In these zones, we assume that there exists a source of wave turbulence with wave velocity $w \ll \Delta v$, tending to make the particle distribution isotropic in the frame of the background medium. In the collisionless shock zone, the particle doesn't change its momentum or incidence angle. But since the plasma itself changes speed in the shock front, from the point of view of the plasma the relative velocity of the particle changes. The y and z component of the relative momentum do not change, since the particle moves parallel to the x axis, but the x component changes by a factor $m(u_1 - u_2)$, which is the difference of momentum due to the velocity change of the plasma:

$$P_{z_1} = P_{z_2}; \quad P_{y_1} = P_{y_2}; \quad P_{x_1} = P_{x_2} - m(u_1 - u_2). \quad (2.9)$$

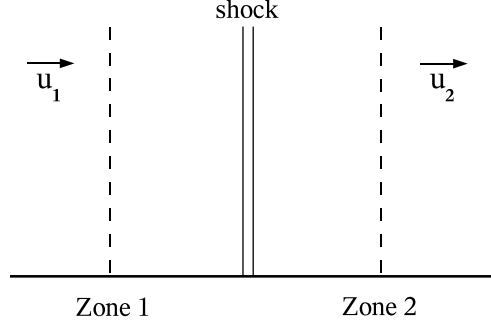


Figure 2.3: Interaction geometry for the diffusive shock acceleration process. Particle distributions are isotropised upstream and downstream of the shock in zones 1 and 2 (Credit: T. Courvoisier).

Using the conservation of the square of the momentum one finds

$$|\mathbf{p}_1|^2 = p_{x_1}^2 + p_{y_1}^2 + p_{z_1}^2 \quad (2.10)$$

$$= |\mathbf{p}_2|^2 - 2m\mathbf{p}_2 \cdot (\mathbf{u}_1 - \mathbf{u}_2) \quad (2.11)$$

$$= |\mathbf{p}_2|^2 - 2\mu_1 |\mathbf{p}_2| m \Delta u \quad (2.12)$$

where we have neglected the term in $(\mathbf{u}_1 - \mathbf{u}_2)^2$ and μ_1 is the cosine of the angle between \mathbf{p}_2 and $(\mathbf{u}_1 - \mathbf{u}_2)$. In order for the particle to cross the shock front we must have $\mu_1 v_1 > -u_1$, and so μ_1 has to satisfy the condition $1 > \mu_1 > -\frac{u_1}{v_1}$. Using $|\mathbf{p}_2| \simeq |\mathbf{p}_1|$ one finds

$$|\mathbf{p}_1|^2 = |\mathbf{p}_2|^2 \left(1 - \frac{2\mu_1}{|\mathbf{p}_2|} m \Delta u \right) \quad (2.13)$$

$$\simeq |\mathbf{p}_2|^2 \left(1 - \frac{2\mu_1}{|\mathbf{p}_1|} m \Delta u \right) \quad (2.14)$$

And hence,

$$|\mathbf{p}_2| \simeq |\mathbf{p}_1| \left(1 + \frac{\mu}{|\mathbf{p}_1|} m \Delta u \right) \quad (2.15)$$

Behind the collisionless shock zone the particles are re-isotropised, so if the particle comes back to the zone it will have a momentum

$$\bar{p}_1 = p_2 \left(1 - \frac{\mu_2 \Delta u}{v_2} \right) \quad (2.16)$$

where μ_2 must satisfy the condition $-1 < \mu_2 < -\frac{u_2}{v_2}$. The difference of momentum of the

particle is therefore

$$\Delta p = \bar{p}_1 - p_1 \quad (2.17)$$

$$= p_2 \left(1 - \frac{\mu_2 \Delta u}{v_2} \right) - p_1 \quad (2.18)$$

$$= p_1 \left(1 + \frac{\mu_1 \Delta u}{v_1} \right) \left(1 - \frac{\mu_2 \Delta u}{v_2} \right) - p_1 \quad (2.19)$$

$$\simeq \left(\frac{\mu_1}{v_1} - \frac{\mu_2}{v_2} \right) p_1 \Delta u \quad (2.20)$$

The gain of momentum per particle is therefore

$$\frac{\Delta p}{p_1} \simeq \frac{\Delta u}{v} (\mu_1 - \mu_2). \quad (2.21)$$

To calculate the mean energy gain one considers a population of isotropised particles. The probability of crossing the shock region is therefore proportional to $|\mu v + u|$. Hence,

$$\left\langle \frac{\Delta p}{p_1} \right\rangle = \frac{\int_{-u/v_1}^1 d\mu_1 |\mu_1 v_1 + u_1| \int_{-1}^{-u_2/v_2} d\mu_2 |\mu_2 v_2 + u_2| \frac{\Delta p}{p}}{\int_{-u/v_1}^1 d\mu_1 |\mu_1 v_1 + u_1| \int_{-1}^{-u_2/v_2} d\mu_2 |\mu_2 v_2 + u_2|} \quad (2.22)$$

Performing the integration using eq. 2.21, we find at first order in $\frac{\Delta u}{v}$

$$\left\langle \frac{\Delta p}{p_1} \right\rangle = \frac{4\Delta u}{3v}, \quad \text{with } v \simeq v_1 \simeq v_2. \quad (2.23)$$

This is a first order process in $\frac{\Delta u}{v}$, so at each scattering, in average particles gain a momentum proportional to their original momentum.

The spectrum of accelerated particles can be computed under the assumption that the escape probability of a particle at each scattering does not depend on energy. It is then found that the power law index α depends only on the shock properties, which means that strong shocks will systematically lead to similar particle distributions. Indeed, the power-law slope α is determined uniquely by the shock Mach number $\mathcal{M} = \frac{v}{v_s}$ of the colliding plasmas (where $v_s = \sqrt{\frac{\partial p}{\partial \rho}}$ is the sound speed in the plasma), $\alpha = 2\frac{\mathcal{M}^2+1}{\mathcal{M}^2-1}$ (Gabici & Blasi 2003). For Mach numbers $\mathcal{M} \approx 1$, α is large, and the spectrum of accelerated particles is very steep. For high Mach numbers $\mathcal{M} \gg 1$, $\alpha \approx 2$, and particles can be efficiently accelerated up to high energies.

2.3.2 The “re-acceleration” model

In the specific case of cluster merging events, it has been shown (e.g. Berrington & Dermer (2003)) that large merger shocks are unlikely to accelerate particles up to high energies, the very large amount of energy released during the merging event ($\sim 10^{63} - 10^{64}$ ergs) participating mostly to heating of the thermal gas. Indeed, in such a case the shock Mach number $\mathcal{M} \sim 1.4$, and the spectrum of the particles accelerated through DSA is very steep. Such weak shocks can only play a role as heaters of the ICM, while being irrelevant

for particle acceleration.

On the other hand, cluster “accretion shocks”, i.e. infall of small, cool groups of galaxies on major clusters, can have shock Mach numbers $\mathcal{M} \sim 2 - 4$, which results in a much flatter spectrum. Accretion shocks are therefore potential sites of particle acceleration up to high energies (e.g. Ryu et al. (2003)). Accretion shocks occur around the virial radius, $R_v \approx 3$ Mpc for a cluster of mass $M = 10^{15} M_\odot$, with typical velocities of a few thousand km/s. Petrosian (2001) showed that the acceleration of the background thermal particles in accretion shocks is not a viable mechanism to produce the observed spectra of high-energy electrons (see Sect. 2.6), because the enormous energy input required cannot be supplied by merger shocks. To account for this difficulty, Brunetti et al. (2001) noted that electrons with $\gamma \sim 100 - 500$ can have a lifetime comparable to the Hubble time (see the right panel of Fig. 2.2), and proposed a two-phase scenario, where electrons injected in the ICM via different processes (supernovae, AGN, accretion shocks) would accumulate at Lorentz factors $\sim 100 - 500$ for cosmological timescales, and would be re-accelerated by a merger shock through diffusive shock acceleration in a second phase, on rather short timescales (~ 0.5 Gyr). This is called the “re-acceleration” model.

For relatively weak magnetic fields ($B < B_{eq} = 3 \mu G$), the radiative lifetime of $\gamma \sim 10^4$ electrons is given by $t_{loss} \sim 5 \times 10^{15} (B_{\mu G})^{1/2}$ s. In order to generate the observed electron spectra, the re-acceleration process must compensate completely the radiative losses, and the re-acceleration efficiency should be $\chi \sim 1/t_{loss} \sim 2 \times 10^{-16} (B_{\mu G})^{-1/2} \text{ s}^{-1}$. In this framework, the re-acceleration time needed to accelerate $\gamma \sim 100$ electrons up to $\gamma \sim 10^4$ is $\sim 0.6 - 0.7$ Gyr. Figure 2.4 shows the predicted electron spectra as a function of the magnetic field for a re-acceleration timescale of 0.8 Gyr. We can see that as long as the magnetic field is not too high ($B \lesssim 1 \mu G$) and under reasonable assumptions, it is possible to re-accelerate electrons up to $\gamma \sim 10^4$.

If the magnetic field intensity decreases with the radius r from the cluster centre, it follows that a constant electron spectrum can only be produced if the re-acceleration efficiency increases with radius, $\chi(r) \propto 1/\sqrt{B(r)}$. Therefore, if the re-acceleration efficiency is taken to be constant, it follows that the peripheral regions with lower magnetic fields will show steeper electron spectra.

In conclusion, re-acceleration models can produce electron spectra in agreement with the observations of giant radio halos (see Sect. 2.6.1), as long as the mean central magnetic field value is not too high. Since the radiative lifetime of the electrons is rather short, they predict a tight connection between the presence of $\gamma \sim 10^4$ electrons and re-acceleration processes, such as cluster accretion shocks. Another interesting feature of the model is the spectral steepening which is expected in the outer regions of the cluster, due to the decrease of the mean magnetic field. However, these models do not predict the presence of high-energy electrons in cooling core clusters, where there is no evidence for a re-acceleration phase.

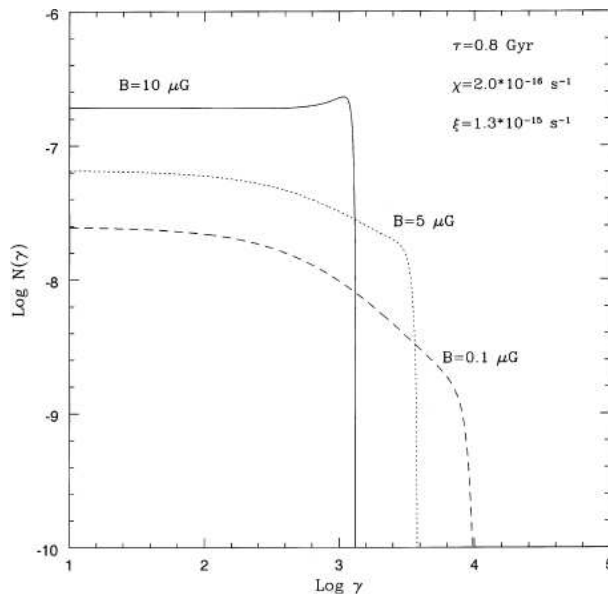


Figure 2.4: Electron spectra predicted by a primary re-acceleration model where $\gamma \sim 100$ electrons are re-accelerated to higher energies through diffusive shock acceleration (Brunetti et al. 2001), for different magnetic field values. The models assume a re-acceleration time-scale $\tau = 0.8$ Gyr and a re-acceleration efficiency $\chi = 2 \times 10^{-16} \text{ s}^{-1}$.

2.4 Secondary electrons

It has been known since the beginning of the 20th century that a large number of energetic charged particles of extrasolar origin (“cosmic-rays”) are detected in the Earth neighbourhood. The spectrum of cosmic-ray protons has been extensively studied for a long time (see Fig. 2.5 for the spectrum of cosmic-ray protons from 10^8 up to 10^{21} eV). The spectrum is well-represented by a broken power-law with a break energy $E \sim 10^{15}$ eV. The spectral index of the low-energy part is flatter ($\alpha \sim 2.5$) than the high-energy part ($\alpha \sim 3.0$). The protons with an energy lower than the break energy are expected to be of galactic origin (supernova remnants, pulsars), while the higher energy part is expected to be extra-galactic (probably active galactic nuclei). The fact that very similar spectra are found over many decades of relativistic energy and in quite different physical environments suggests that a general mechanism for cosmic-ray acceleration is at work. At the highest energies ($E \sim 10^{19} - 10^{20}$ eV), the spectrum shows a possible hardening (“the ankle”). Above 10^{20} eV, the energy of the protons is sufficient to produce pions through interactions with the photons of the CMB. This implies that protons with $E > 10^{20}$ eV should lose energy through pion production and pile-up at energies just below the threshold energy. The spectrum should show a cut-off above 10^{20} eV (the Greisen-Zatsepin-Kuzmin (GZK) cut-off).

In the “secondary electrons” model, the relativistic electrons are not produced directly from merger shocks, but are produced by interactions of the large population of cosmic-ray protons with the thermal ions of the ICM. If the momentum of the cosmic-ray exceeds the threshold $p \approx 0.8 \text{ GeV } c^{-1}$, these interactions will produce pions, and a cascade of

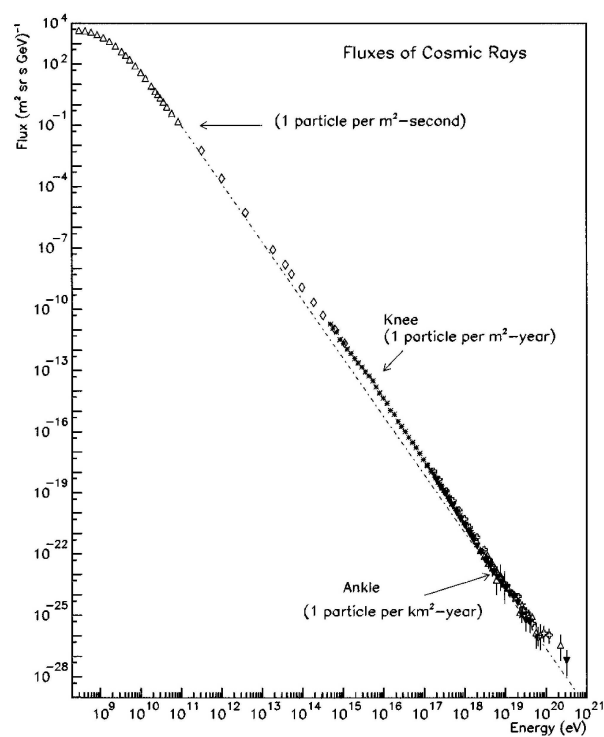


Figure 2.5: Spectrum of cosmic-ray protons entering the Earth’s atmosphere (data compiled by J. Swordy). The spectrum is well-represented by a broken power-law with a break energy $E_b \sim 10^{15}$ eV (“the knee”). A possible hardening at the highest energies, the so-called “ankle”, can be seen.

particles (or “fireball”) will start, resulting in a population of relativistic electrons. The detailed scenario is the following:

$$p + p \rightarrow p + p + n\pi \quad (2.24)$$

The charged pions decay into

$$\pi^\pm \rightarrow \mu^\pm + \nu_\mu/\bar{\nu}_\mu \rightarrow e^\pm + \nu_e/\bar{\nu}_e + \nu_\mu + \bar{\nu}_\mu. \quad (2.25)$$

They hence produce a population of relativistic electrons, which will radiate in the low-frequency radio domain through synchrotron radiation and in the hard X-ray range through inverse-Compton scattering with the Cosmic Microwave Background. On the other hand, the neutral pions will decay directly into two photons,

$$\pi^0 \rightarrow 2\gamma. \quad (2.26)$$

The energy of the photons will be $E > \frac{m_\pi}{2} \sim 70$ MeV. The radiation will therefore occur in the high-energy γ -ray domain.

To compute the electron spectrum induced by this phenomenon, following Pfrommer et al. (2007) we assume that the differential proton momentum distribution per volume element can be approximated by a power-law, which is the case for the observed cosmic-ray spectrum on Earth:

$$f_p(p_p) = \frac{dN}{dp_p dV} = C_p p_p^{-\alpha_p} \theta(p_p - q_p), \quad (2.27)$$

where C_p is the normalization, $\theta(x)$ is the Heaviside step function, q_p is the low-energy cut-off of the proton distribution and α_p is the cosmic-ray spectral index, which is assumed to be constant. The pion production spectrum, which describes the produced number of pions per unit time, volume and momentum, can be approximately described as

$$s_\pi(p_\pi, p_p) = \frac{dN}{dt dV dp_\pi dp_p} = c n_N \xi(p_p) \sigma_{pp}(p_p) \theta(p_p - p_{th}) \delta(p_\pi), \quad (2.28)$$

where n_N is the density of target nucleons, σ_{pp} is the inelastic proton-proton cross-section, $\xi(p_p)$ is the pion multiplicity, i.e. the number of pions produced in one reaction, and $p_{th} = 0.78$ GeV c^{-1} denotes the threshold cosmic-ray proton momentum for pion production. Averaging over the proton momentum, one gets the pion source function, i.e.

$$s_{\pi^\pm}(p_\pi) = \int_{-\infty}^{\infty} dp_p f_p(p) s_\pi(p_\pi, p_p), \quad (2.29)$$

where $f_p(p)$ is taken from Eq. 2.27. In the high-energy limit, generally the pion multiplicity can be described as a constant factor $\xi(p_p) \approx 2$, and the mean pion momentum is hence given by

$$\langle p_\pi \rangle \approx \frac{m_p p_p}{2m_\pi \xi}. \quad (2.30)$$

In the $\pi^\pm \rightarrow e^\pm$ chain, 3 neutrinos are produced, which take away a large fraction of the energy. The mean energy of the produced secondary electrons is therefore

$$\langle E_e \rangle \approx \frac{1}{4} \langle E_{\pi^\pm} \rangle. \quad (2.31)$$

The electron source function can thus be approximated by

$$s_e(p)dp = s_\pi(p_\pi(p)) \frac{dp_\pi}{dp} dp = \frac{4m_e}{m_{\pi^\pm}} s_{\pi^\pm} \left(\frac{4m_e}{m_{\pi^\pm}} p \right) dp \quad (2.32)$$

$$= \frac{4}{3} 16^{1-\alpha_p} c \sigma_{pp} n_N \left(\frac{m_e}{m_p} \right)^{1-\alpha_p} dp \quad (2.33)$$

Finally, we can write down the injection spectrum of cosmic-ray electrons resulting from hadronic reactions of cosmic-ray protons with ambient gas protons,

$$f_{inj,pp} dp = C_{inj,pp} p^{-\alpha_p} dp, \quad (2.34)$$

where

$$C_{inj,pp} = \frac{4}{3} 16^{2-\alpha_e} c \tau_{pp} \sigma_{pp} n_N C_p \left(\frac{m_e}{m_p} \right)^{2-\alpha_e}. \quad (2.35)$$

The electron spectral index α_e is given by $\alpha_e = \alpha_p + 1$, and $\tau_{pp} = \min[(c\sigma_{pp}n_N)^{-1}, \tau_{Hubble}]$. Not surprisingly, the electron spectrum is proportional to the cosmic-ray proton normalization C_p , the target nucleon density n_N and the interaction timescale τ_{pp} .

This model predicts the presence of a large population of relativistic electrons in all massive clusters, independently of their current state. Indeed, since protons do not radiate, their typical lifetime is very long. Therefore, relativistic protons injected in the ICM through different mechanisms (merger shocks, supernovae, jets of active galactic nuclei) will remain in the cluster for cosmological timescales, and produce secondary electrons continuously throughout the cluster. The resulting spectral index is quite flat, and the model does not predict a high-energy cut-off for cosmic-ray protons with energies $E < 10^{15}$ eV. Another important feature of the model is the prediction of high-energy γ -ray emission from π^0 decay (Eq. 2.26).

2.5 Alternative models

Motivated by the discrepancy between the magnetic field values obtained from Faraday rotation measure and synchrotron/IC ratio (see Sect. 2.7), alternative models have been proposed to explain the observational properties of galaxy clusters. In this section, I will make a brief overview of two of these alternative models. The first one involves a non-Maxwellian energy distribution of the thermal ICM electrons (e.g. Blasi (2000), Dogiel et al. (2007)), while the second one investigates the possibility of very high energy ($E \gtrsim 100$ TeV) electrons that would be continuously produced throughout the cluster (Timokhin et al. (2004), Inoue et al. (2005)).

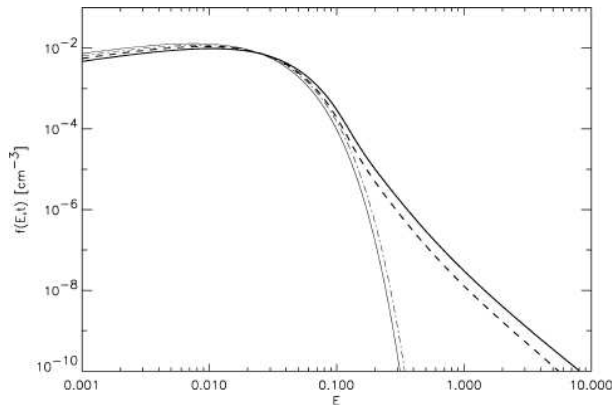


Figure 2.6: Spectra of thermal electrons accelerated because of turbulence in the ICM at different time periods (from Blasi (2000)). At $t = 0$ (thin solid line), the distribution is assumed to be Maxwellian with $kT = 8.21$ keV, typical of the Coma cluster. The dashed line and the thick solid line show the evolution of the spectrum after an acceleration time $t = 5 \times 10^8$, respectively 10^9 yr.

2.5.1 Non-thermal bremsstrahlung from non-relativistic electrons

In a completely thermalized non-relativistic plasma, the velocity distribution of the particles is given by the Maxwell-Boltzmann distribution, i.e., the probability that an electron has a velocity v in a plasma at a temperature T is given by

$$dP \sim e^{-E/kT} d^3v \sim v^2 e^{-\frac{mv^2}{2kT}} dv. \quad (2.36)$$

If the medium is optically thin, all the radiation produced by the interaction between the electrons and the ions will escape, and the electrons will radiate through “thermal bremsstrahlung”. The shape of the corresponding spectrum is given by

$$\frac{dE}{dV dt dv} \sim n_e n_i T^{-1/2} e^{-hv/kT}. \quad (2.37)$$

On the other hand, if the plasma is not completely thermalized, the observed spectrum will differ from Eq. 2.37. To explain the observed high-energy tail in the X-ray spectrum of some clusters (see Sect. 2.6.2), Blasi (2000) suggested that the electron energy distribution might significantly differ from a Maxwellian distribution because of turbulence in the ICM, resulting in stochastic particle acceleration. Figure 2.6 shows the evolution of the thermal electron spectrum for a Coma-like cluster at $kT = 8.21$ keV for different acceleration periods.

Under reasonable assumptions, Blasi (2000) find that after an acceleration time of 1 Gyr, a high-energy tail sufficient to explain the observed hard X-ray flux has formed. However, Petrosian (2001) analyzed the model, and found that it faces several theoretical problems. For acceleration rates smaller than the Coulomb loss rate, the effect of energising the plasma is to primarily heat the plasma, with very few particles being accelerated to higher energies. For acceleration rate similar to the Coulomb loss rates, a high-energy tail can form, but only for a short time ($< 10^6$ yr), and will be thermalized rapidly. A longer

period of acceleration will result in a runaway situation, where most of the particles will be accelerated to high energies, dislocating the thermal plasma.

In conclusion, although very elegant, this model faces several difficulties to reproduce the observed hard X-ray spectra.

2.5.2 Production of very high energy electrons

Some models have investigated the production of very high energy electrons ($E \sim 100$ TeV) throughout the volumes of clusters and their observational properties. Assuming magnetic fields of several μG , such electrons would then produce synchrotron radiation in hard X-rays and interact with CMB photons to produce TeV emission through IC processes. For electrons with such high energies, the energy-loss timescale is very short, and therefore, such electrons would need to be constantly injected throughout the cluster volumes.

At least two different mechanisms have been proposed to inject high-energy electrons steadily in clusters. Timokhin et al. (2004) invoked the existence of very high energy γ -rays ($E \sim 10^{16}$ eV), whose energy would be sufficient to produce $e^+ - e^-$ pairs via interactions with the diffuse extragalactic photon background:

$$e^+ + e^- \rightleftharpoons \gamma + \gamma. \quad (2.38)$$

On the other hand, Inoue et al. (2005) suggested that very high energy cosmic-rays accelerated up to $\sim 10^{18}$ eV in cluster accretion shocks with high Mach numbers could interact with CMB photons and also create very high energy $e^+ - e^-$ pairs.

However, it must be noted that these models both face important problems. While the existence of a large population of 10^{16} eV photons in clusters is hypothetical, the amount of energy required to accelerate efficiently high-energy protons up to very high energies is enormous and cannot be easily supplied by merger shocks.

2.6 Observational properties

Observational evidence for the presence of high-energy particles in several clusters of galaxies is found in low-frequency radio, hard X-ray and high-energy γ -ray energy ranges. Since it is the energy range where the best observational information on the non-thermal emission has been obtained so far, I will emphasize on the observations of clusters in the radio domain. I will also present the state of the observations of non-thermal emission in the hard X-ray and extreme UV domain before the launch of *INTEGRAL*. Finally, I will briefly summarize the attempts of detecting high-energy γ -rays so far with the EGRET instrument on board the *Compton Gamma-Ray Observatory* (CGRO), and present the expectations for the *GLAST* mission.

2.6.1 Radio emission

Since the detection of radio radiation from the Coma cluster in the 1970s, there has been growing evidence for the existence of large-scale diffuse radio sources associated to clusters of galaxies, which cannot be obviously associated with any individual galaxy (see the review by Feretti & Giovannini (2007) for details). These diffuse radio sources have been associated with synchrotron radiation from a population of relativistic electrons with $E_e \gtrsim 1$ GeV in addition to the thermal ICM. The synchrotron emission is produced by the spiralling motion of relativistic particles in a magnetic field. An electron with energy $E = \gamma m_e c^2$ in a magnetic field \vec{B} experiences a $\vec{v} \times \vec{B}$ force which makes it follow a helical path along the field lines, emitting radiation into a cone of half-angle $1/\gamma$ (see Rybicki & Lightman (1985) for details). For electrons with a given Lorentz factor γ , the radiation is a continuum concentrated around the typical frequency, which can be expressed as

$$\nu_{sync} = \frac{3eB}{2\pi m_e c} \gamma^2 \approx 1 \text{ GHz} \frac{B}{1\mu\text{G}} \left(\frac{\gamma}{10^4} \right)^2. \quad (2.39)$$

In the more realistic case of an electron population with a power-law distribution, the total observed spectrum is a superposition of synchrotron spectra, resulting in a power-law photon spectrum.

Cluster diffuse radio sources are characterized by steep ($\alpha = 1 - 2$) power-law spectra, and are classified into three categories: halos, relics and mini-halos. Giant halos are large-scale (> 1 Mpc) diffuse sources with low surface brightness ($\sim 1 \mu\text{Jy arcsec}^{-2}$), which are generally unpolarized. Their morphology resembles the thermal X-ray emission. The radio source Coma C associated with the Coma cluster (see the left panel of Fig. 2.7), which was the first diffuse radio source associated with a cluster of galaxies (Willson 1970), is the prototype of a giant halo. Unlike the presence of thermal X-ray emission, the presence of diffuse radio emission is not a common feature in clusters of galaxies. Indeed, the detection rate of radio halos in a complete cluster sample is $\sim 5\%$ (Giovannini et al. 1999). In general, the clusters which show radio halo are characterized by recent merger processes and no cooling core. From the spectra of radio halos, one can compute the radiative lifetime of the relativistic electrons (see Fig. 2.2). The corresponding electron lifetime is $\sim 10^8$ yr, which implies that the acceleration phase is recent or still on-going. In several cases (e.g. the Coma cluster, Giovannini et al. (1993)), it has been found that the spectral index rapidly steepens with increasing radius. This feature is explained naturally by the re-acceleration scenario (see Sect. 2.3), and can hardly be explained by secondary models, which suggests that the electrons that produce giant radio halos are mostly primary (Brunetti et al. 2001). This result has been confirmed thanks to cosmological simulations considering both the primary and the secondary components by Pfrommer (2007).

On the other hand, relics are irregularly shaped and occur in the peripheral regions of clusters. They also show a high level of polarization. The relic source 1253+275, which can be seen on Fig. 2.7 South-West of the giant halo, was the first discovered relic source. Spectacular examples of two giant almost symmetric relics are found in Abell 3376 (see Fig. 2.8) and Abell 3667 (Rottgering et al. 1997). In most cases, powerful relics are detected in clusters with giant radio halos, but in some cases, weak radio relics can be found in cooling core clusters. Theoretical models propose that they are induced by shock waves

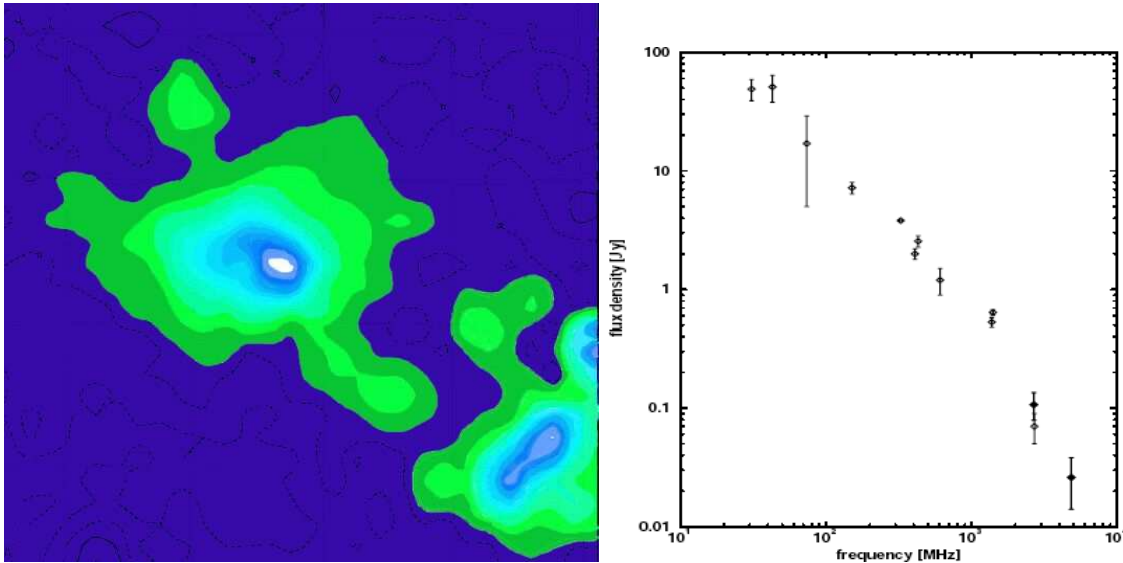


Figure 2.7: Left: 1.4 GHz image of the Coma C radio halo from the 100-m Effelsberg telescope (Deiss et al. 1997). Compared to the thermal X-ray emission from the ICM, the centroid of the source is displaced by ~ 5 arcmin. Right: Radio spectrum of Coma C compiled by Thierbach et al. (2003). The spectrum shows a break at high frequencies.

from merging events or interaction between a radio galaxy and the intracluster gas.

Mini-halos are diffuse radio sources at the center of cooling core clusters, usually surrounding a powerful radio galaxy. They are similar to giant halos, but on a smaller scale ($\lesssim 500$ kpc). The diffusive radio emission from the Perseus cluster is the prototype of such sources. Since there is an anti-correlation between the presence of a cooling core and that of a major merging event, mini-halos are the only diffuse cluster radio sources not associated with cluster mergers. Because of the absence of merging events correlated with these sources, the electron population at the origin of mini-halos could be secondary (Pfrommer & Enßlin 2004). In the cases where AGN activity is observed in the central galaxy (e.g. Perseus), turbulence induced by the central AGN has also been proposed as the origin of the mini-halo (Fabian et al. 2006). Alternatively, re-acceleration through magneto-hydrodynamical (MHD) turbulence has also been proposed as the origin of the relativistic electrons (Gitti et al. 2002).

2.6.2 Hard X-ray and Extreme UV emission

Observations at radio wavelengths clearly establish the presence of a population of relativistic electrons with Lorentz factor $\gamma \sim 10^4$ in some clusters of galaxies. One therefore expects that the relativistic electrons will interact with the radiation field (mostly the CMB) through inverse-Compton processes. The typical energy for IC scattering of $\gamma \sim 10^4$ electrons on the CMB is

$$h\nu_{IC} = \frac{4}{3}h\nu_{init}\gamma^2 \approx 90\text{keV} \frac{\nu_{init}}{\nu_{CMB}} \left(\frac{\gamma}{10^4}\right)^2, \quad (2.40)$$

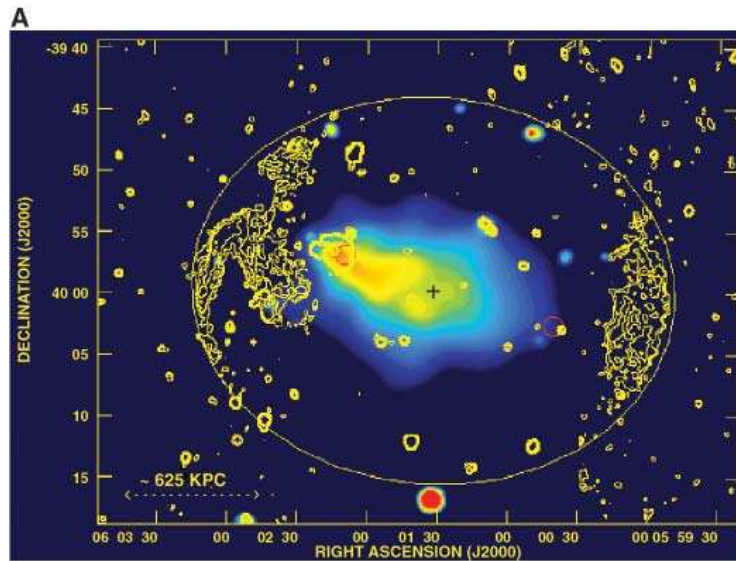


Figure 2.8: 0.2-2 keV X-ray image of the Abell 3376 cluster from the ROSAT PSPC instrument with 1.4 GHz radio contours from the Very Large Array overlaid (Bagchi et al. 2006). The relics unveil one of the most powerful merging events detected so far.

where ν_{init} is the energy of the photon before scattering and $h\nu_{CMB} = 0.66$ meV is the typical energy of the CMB. Therefore, we can see that CMB photons will be up-scattered in the hard X-ray/soft γ -ray domain. The detection of the hard X-ray IC radiation is made difficult because of the very strong thermal X-ray emission of the ICM, which peaks in the 1 – 10 keV range. Above 20 keV, the thermal bremsstrahlung emission, which decreases exponentially with energy, should become negligible, and the non-thermal emission should become observable again.

The first attempts of detecting a non-thermal tail in the X-ray spectrum were made by the OSSE detector on board CGRO in the beginning of the 1990s (Rephaeli et al. 1994). However, the authors were only able to put upper limits on the non-thermal flux. The first claim of a non-thermal hard X-ray excess was made by Fusco-Femiano et al. (1999) using the Phoswich Detection System (PDS) instrument on board *BeppoSAX*. The authors report on a 100 ksec observation of the Coma cluster, which leads to a 4.5σ excess above 20 keV compared to the extrapolation of the thermal emission (see Fig. 2.9). Fusco-Femiano et al. (2004) confirmed the result using a second 150 ksec observation, and the same result was also found by Rephaeli & Gruber (2002) using *RXTE* data, although with a lower confidence level. However, Rossetti & Molendi (2004) analyzed the same data with another software package, and could not detect the non-thermal component. The controversy between the two groups is still on-going, which still casts doubts on the existence or not of the non-thermal component in the Coma cluster.

Possible signatures of non-thermal emission were also found in other clusters, in particular Abell 2256 (Fusco-Femiano et al. 2005) with *BeppoSAX* and Perseus (Sanders et al. 2005) with *Chandra*. Coma and Abell 2256 are well-known merging clusters with powerful radio

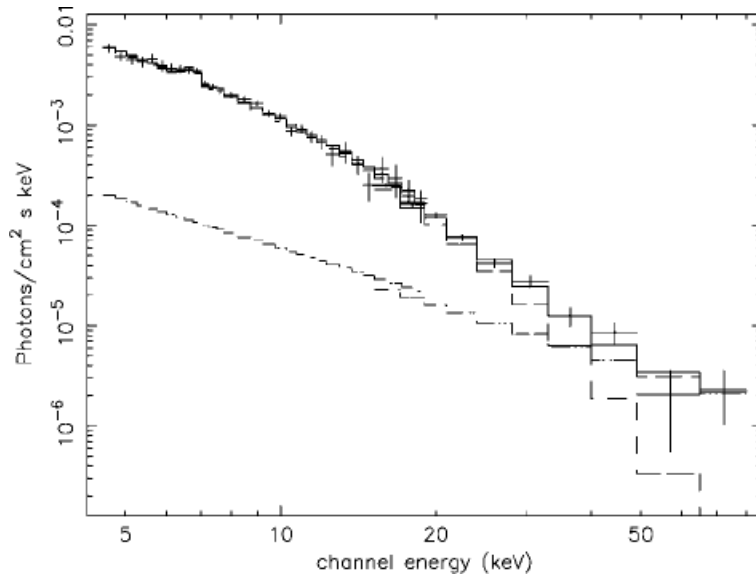


Figure 2.9: Hard X-ray spectrum of the Coma cluster obtained with the PDS (15-80 keV) and HPGSPC (4.5-20 keV) instruments on board BeppoSAX (Fusco-Femiano et al. 1999). The dashed line represents the thermal component ($kT = 8.5 \pm 0.5$ keV), while the dashed straight line is the non-thermal component with a photon index $\Gamma = 1.6$.

halos, while Perseus is the text-book example of a cluster with a strong cooling core and a radio mini-halo, which makes it very different from the two others.

Apart from the HXR band, IC scattering of $\gamma \sim 100$ electrons on the CMB could also be observable in the Extreme Ultra Violet (EUV) band, where the thermal X-ray emission becomes weaker. Bowyer et al. (2004) presented observations of the Coma cluster with the *EUVE* instrument, showing that the detected emission exceeded the extrapolation of the thermal X-ray emission. The authors interpret this result as IC emission from secondary electrons. This excess emission could also be due to the presence of cooler gas ($kT \sim 0.2$ keV, Kaastra et al. (2003)), but the non-observation of emission lines expected from a gas at this temperature (e.g. O_{VI}) casts doubts on this interpretation.

2.6.3 High-energy γ -ray emission

The initial motivation for the interest in high-energy γ -ray emission ($E > 100$ MeV) from clusters of galaxies arose from the possibility that cosmic rays might be confined in the potential well of clusters for cosmological timescales, and could interact with the thermal ICM protons to produce cascades of pions (see Sect. 2.4). In this case, the neutral pions produced in the reaction will decay into 2 γ -ray photons at energies $E > \frac{m_{\pi^0}}{2} = 70$ MeV.

Apart from secondary mechanisms, several other models predict the existence of high-energy γ -rays from clusters (see Blasi et al. (2007) for a review). In particular, it has been found that the lifetime of $\gamma \sim 100 - 500$ electrons is comparable to the Hubble time (see Fig. 2.2). If massive clusters contain a large population of such electrons, as

predicted by the re-acceleration models (see Sect. 2.4), some clusters of galaxies should become observable in this energy range because of non-thermal bremsstrahlung from the $\gamma \sim 100 - 500$ electrons, which should be present in all massive clusters. Alternatively, some models predict the existence of a population of very high energy electrons ($E \gtrsim 100$ TeV), which should up-scatter the photons of the CMB up to the TeV range (see Sect. 2.5.2).

The first attempts of detecting high-energy γ -ray emission from clusters of galaxies were made by the EGRET instrument on board *CGRO*. Reimer et al. (2003) presented the results of EGRET observations of 58 clusters. Although they failed to detect any of them, they computed upper limits for the γ -ray flux of these clusters which have been used to constrain the models. In the best studied cases, such as Coma, the upper limit reported by EGRET allows to show that the relativistic electrons responsible for the radio halo cannot be completely secondary. The EGRET upper limit on the γ -ray flux of the Coma cluster also implies that no more than 10 – 30% of the thermal energy is under the form of relativistic particles. The Large Array Telescope (LAT) on board the *GLAST* satellite, which was successfully launched on June 10, 2008, should reach a sensitivity better than EGRET by a factor of 10. It will therefore put strong constraints on the secondary models.

Using cosmological simulations with both primary and secondary electron components, Pfrommer (2007) estimated the γ -ray luminosity through π^0 decay of a number of nearby clusters. Figure 2.10 shows the γ -ray ($E > 100$ MeV) flux function of the cluster sample. Based on these results, the author predicts that *GLAST* will detect ~ 10 nearby clusters.

In conclusion, although there has been no detection yet of high-energy γ -ray emission from a galaxy cluster, observations with *GLAST* will put strong constraints (even in the case of a non-detection) on the particle acceleration models, especially secondary, and will probe the energy content of relativistic particles in clusters.

2.7 Methods of magnetic field measurement

Observations of diffuse radio sources associated with clusters of galaxies imply the existence of large-scale magnetic fields in the range $B \sim 0.1 - 10 \mu G$ throughout the volume of clusters. This value exceeds the magnetic field expected from adiabatic amplification of seed fields. Because the radiative lifetime of high-energy electrons is proportional to $1/B$, a good knowledge of the magnetic field is important to constrain the properties of the population of relativistic electrons in clusters. The existence of these relatively strong magnetic fields also raises the question of the origin of the field. In this section, I will present the three different methods which have been used to derive magnetic field values in clusters: Faraday rotation measure, equipartition and synchrotron/IC ratio. This section follows Feretti & Giovannini (2007).

2.7.1 Faraday rotation measure

The synchrotron radiation from cosmic radio sources (e.g. radio galaxies) is well known to be linearly polarized. A linearly polarized electromagnetic wave at a wavelength λ travelling

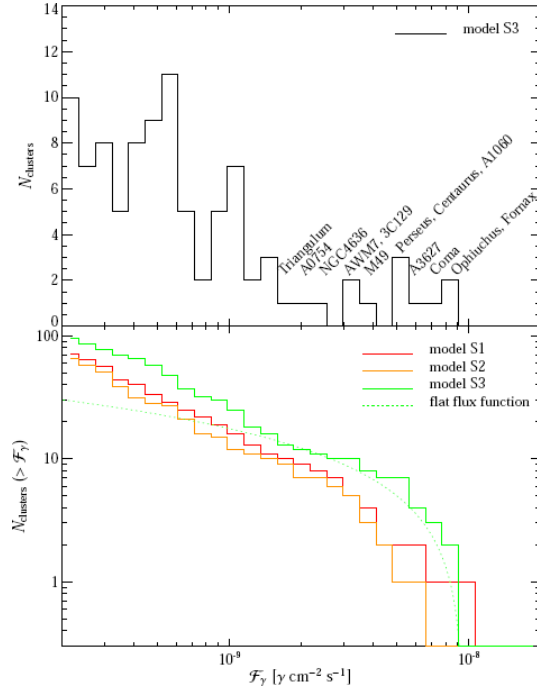


Figure 2.10: Predictions for the γ -ray flux from π^0 decay from a model considering both primary and secondary electron populations (Pfrommer 2007).

through a magnetized medium of diameter L will see its polarization angle rotate by an angle $\Delta\chi = \text{RM}\lambda^2$, where RM, the “Faraday rotation measure”, is defined as

$$\text{RM} = \frac{e^2}{2\pi m_e^2 c^4} \int_0^L n_e \vec{B} \cdot d\vec{l}. \quad (2.41)$$

Numerically,

$$\text{RM} = 812 \int_0^L n_e B_{\parallel} dl \quad \text{rad m}^{-2}, \quad (2.42)$$

where n_e is in units of cm^{-3} , B in units of μG and the path length l is in kpc. By convention, RM is positive (negative) for a magnetic field directed towards (away from) the observer. The values of RM can be obtained by measuring the polarization of a linearly polarized radio source located in the background or within the cluster, at three or more wavelengths. Once the contribution of our Galaxy is subtracted, the dominant contribution should come from the ICM. Assuming a density profile $n_e(r)$, the mean magnetic field B_{\parallel} can be determined from Eq. 2.42.

Kim et al. (1991) presented magnetic field estimates through Faraday rotation measure in a sample of 53 clusters. Their analysis revealed that relatively high values of magnetic field, $B \sim 1\text{--}5 \mu\text{G}$, are widespread in the ICM. More recently, Clarke et al. (2001) analyzed data of a sample of 16 clusters, with the same conclusion. They also noted that the RM decreased when the position of the background source was slightly away from the center

of the cluster, which indicates that the magnetic field strength could be decreasing with radius.

2.7.2 Equipartition magnetic field

In a synchrotron source, the total energy is given by the energy of the relativistic particle (U_e for electrons and U_p for protons) plus the energy in the magnetic field (U_B),

$$U_{tot} = U_e + U_p + U_B. \quad (2.43)$$

The total magnetic energy U_B is

$$U_B = \int_V u_B dV \equiv \frac{B^2}{8\pi} \Phi V, \quad (2.44)$$

where the “filling factor” Φ is the fraction of the source volume occupied by the magnetic field. Estimating the amount of energy in the relativistic particles, one can derive the condition of minimal energy. Assuming that the total energy in protons is proportional to that in electrons, $U_p = kU_e$, the condition of minimal energy is obtained when

$$U_B = \frac{3}{4}(1+k)U_e. \quad (2.45)$$

The total energy content is therefore minimal when U_B and U_e are approximately equal. For this reason, the magnetic field value which minimizes the total energy is known as the equipartition magnetic field. The total minimum energy density $U_{\min} = U_{\min}/V\Phi$ (in erg cm⁻³) can be expressed in terms of observables as

$$u_{\min} = 1.23 \times 10^{-12} (1+k)^{4/7} \nu_0^{4\alpha/7} (1+z)^{(12+4\alpha)/7} I_0^{4/7} d^{4/7}, \quad (2.46)$$

where ν_0 is the characteristic synchrotron frequency (see Eq. 2.39) in MHz, I_0 is the source brightness which is directly observed at the frequency ν_0 in mJy arcsec⁻², d is the source depth along the line of sight in kpc, and α is the source spectral index. The magnetic field for which the minimum energy assumption is achieved is derived as

$$B_{eq} = \left(\frac{24\pi}{7} u_{\min} \right)^{1/2}. \quad (2.47)$$

One must be aware that the magnetic field values derived with this method rely on several assumptions. Indeed, since the population of relativistic electrons might not be in equilibrium, the assumption of minimal energy might not be valid. Furthermore, the value of the ratio between the relativistic electron and proton energy, k , is uncertain, as well as the volume filling factor Φ .

The magnetic field estimates through equipartition assumption typically find values for the magnetic field which are slightly lower than those derived through Faraday rotation measure ($B \sim 0.5 - 1 \mu G$, Thierbach et al. (2003), Feretti et al. (1995), Beck et al. (2003)).

2.7.3 Synchrotron/inverse-Compton flux ratio

In the case of the population of relativistic electrons found in clusters of galaxies, the incoming radiation field is dominated by the CMB radiation, whose properties are very well known. In this case, the ratio between radio synchrotron and hard X-ray IC emission is given by (see Sect. 2.2)

$$\frac{b_{syn}}{b_{IC}} = \frac{U_B}{U_{CMB}} \approx 0.095(1+z)^4 \left(\frac{B}{1 \mu G} \right)^2. \quad (2.48)$$

Assuming that the non-thermal HXR emission which is observed in several clusters (see Sect. 2.6.2) is due to IC emission from the same electrons that produce radio halos, one can use Eq.2.48 to determine the mean magnetic field value. This method is the most unbiased for the determination of cluster magnetic fields, but it requires a good knowledge of the hard X-ray emission, which is not yet the case.

Using their estimate of the excess flux from the Coma cluster, Fusco-Femiano et al. (1999) estimate a magnetic field $B \sim 0.15 \mu G$, which is an order of magnitude less than the value derived from Faraday rotation measure. For comparison, equipartition between the energy emitted through synchrotron and IC is achieved for a magnetic field $B_{eq} = 3 \mu G$. The low values $B \ll B_{eq}$ obtained with this method indicate that IC energy losses dominate over synchrotron losses.

2.7.4 Reconciling the values obtained with different methods

As shown above, magnetic field estimations obtained with different methods lead to very different results. In the specific case of the Coma cluster, the tentative detection of hard X-ray emission leads to a low magnetic field $B \sim 0.15 \mu G$, while measurements of Faraday rotation measure in the central regions of the cluster lead to magnetic field values as high as $6 \mu G$. In order to reconcile the values derived using different methods, several mechanisms were proposed.

The method of magnetic field measurement through Faraday rotation measure relies on several assumptions. In particular, in order to derive the mean magnetic field value along the line of sight, magnetic field and density profiles must be assumed. Beck et al. (2003) showed that if the magnetic field and density profiles are correlated, which is the case in a turbulent medium, the magnetic field values obtained through Faraday rotation measure can be strongly over-estimated. If this explanation is correct, the low magnetic field values derived through synchrotron/IC flux ratio would be correct, and turbulence in the ICM would induce an over-estimation of the magnetic field. Alternatively, Goldshmidt & Rephaeli (1993) suggested a radial decrease of the magnetic-field profile, as indicated by Farady rotation measure in some clusters. Given that the measurement of hard X-ray emission was integrated over a wide area because of the large field-of-view of the PDS instrument on board *BeppoSAX*, it would mean that the hard X-ray emission would come predominantly from the outer regions of the cluster where the magnetic field is low, while the radio synchrotron emission would be peaked towards the centre.

On the other hand, if the magnetic field values inferred from Faraday rotation measure are correct and do not show a steep radial decrease, the hard X-ray emission cannot come from IC scattering from the same electron population which produce the radio emission. In this case, several models have been proposed in order to explain the high level of HXR emission. Bremsstrahlung from a non-Maxwellian energy distribution of the thermal electrons (see Sect. 2.5.1) appears as the most elegant alternative model for the hard X-ray emission, even though it faces important energetic problems. Scenarios invoking the existence of very high energy electrons which would radiate at hard X-rays through synchrotron processes have also been proposed (see Sect. 2.5.2), but this scenario appears to be rather extreme because of the very small energy-loss timescales of such electrons.

2.8 Conclusion

In this chapter, I have presented the observational properties of the population of relativistic electrons which is observed in a number of clusters of galaxies, and discussed the theoretical models which could explain the existence of the high-energy electrons. Figure 2.11 from Petrosian et al. (2008) summarizes our current knowledge of the electron spectrum in the ICM. At low energies, the thermal Maxwellian distribution is shown, while at higher energies, the non-thermal power-law distribution which produces the radio synchrotron emission is displayed. A possible non-thermal tail in the thermal spectrum, which was discussed in Sect. 2.5.1, is also shown.

In Sect. 2.3 and 2.4, I have discussed the two main models for the origin of the population of relativistic electrons, “primary” and “secondary”, and compared some of their features with existing observations. We find that both scenarios face important problems. Namely, primary electrons scenarios can reproduce the main features of the observed radio halos and relics, but only for a short period. On the other hand, secondary electrons rely on the presence of a large population of relativistic protons, which should be present in all clusters because of their very long lifetime, and therefore, they cannot reproduce the observed correlation between mergers and radio halos. In a cosmological simulation treating both primary and secondary electrons, Pfrommer (2007) found that the primary component is dominating in merging and post-merger clusters, i.e. is the origin of giant halos, while the secondary component, which is independent on the state of the cluster, should dominate in cooling core clusters, and produce radio mini-halos. Such models can also reproduce the radial dependence of the spectral index detected in several cases.

One of the most challenging aspects for the models is the discrepancy between magnetic field values derived from Faraday rotation measure and from synchrotron/IC flux ratio (Sect. 2.7). Indeed, all models agree that if the relatively high magnetic field values obtained through Faraday rotation measure are correct, the HXR flux cannot be due to IC scattering of the same electrons with the CMB. To solve this problem, a few models have been developed which do not interpret the HXR radiation in terms of IC scattering (Sect. 2.5). Although there is now more and more evidence of the existence of non-thermal HXR radiation from several clusters, the existence of the component at this level is still debated (Sect. 2.6.2). Observations of clusters in the HXR band with better angular resolution and sensitivity are therefore required to constrain the particle acceleration models.

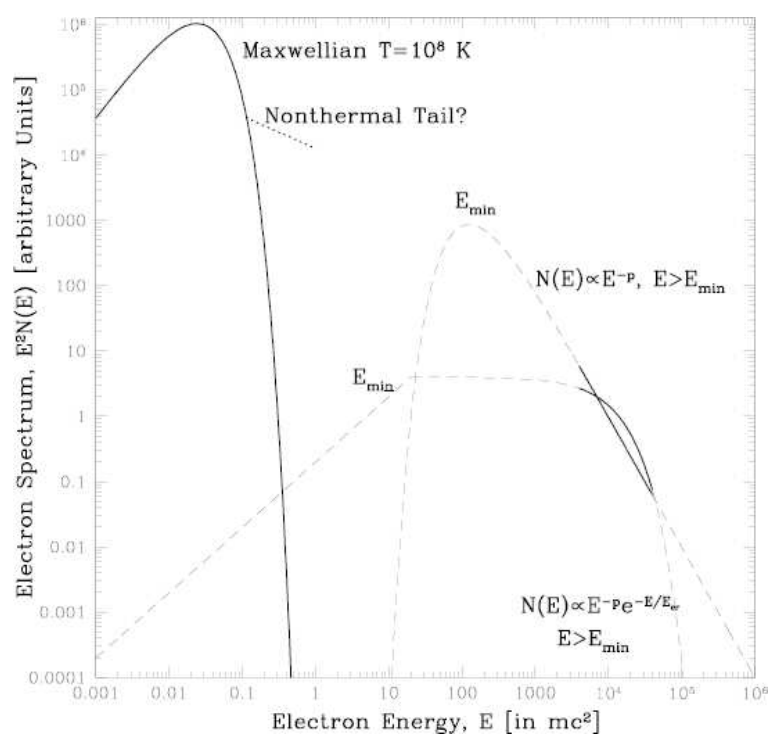


Figure 2.11: Energy spectrum of electrons required in a Coma-like cluster to explain the thermal X-ray emission (Maxwellian at $T \approx 10^8$ K), the radio synchrotron and HXR inverse-Compton emission (non-thermal power-law). A possible non-thermal tail in the Maxwellian distribution, discussed in Sect. 2.5.1, is also displayed. The figure is from Petrosian et al. (2008).

Observations of clusters at high-energy γ -rays ($E > 100$ MeV) with the LAT instrument on board the *GLAST* satellite, which has been successfully launched on June 10, 2008, could open a new window on the high-energy processes in clusters, and will in any case constrain the different particle acceleration scenarios. Indeed, secondary models predict a γ -ray flux which will be firmly detectable with *GLAST*, and therefore, even a non-detection will put stringent constraints on the models.

Chapter 3

Analysis of extended sources with *INTEGRAL*

In this chapter, I will describe my activities related to the *INTEGRAL* mission. After a brief description of the *INTEGRAL* satellite and its instruments, I will explain why the standard data analysis tools are not well suited for extended sources, and I will present the methods that I have developed in the purpose of analyzing extended sources, and in particular clusters of galaxies, with coded-mask instruments.

3.1 The *INTEGRAL* mission

The INTernational Gamma-RAY Laboratory (*INTEGRAL*) mission (Winkler et al. 2003) is an X- and γ -ray space mission of the European Space Agency (ESA). The satellite was successfully launched on October 17, 2002 from Baïkonour, Kazakhstan, after almost 20 years of planning and building. The instruments on board the spacecraft are designed for the imaging and spectroscopic study of high-energy sources, from the optical band to the γ -rays. In more details, the spacecraft carries 2 main scientific instruments which operate in the hard X-ray/soft γ -ray domain, the IBIS imager (Ubertini et al. 2003) and the SPI spectrometer (Vedrenne et al. 2003), and 2 monitors, the X-ray monitor JEM-X (Lund et al. 2003) and the optical camera OMC (Mas-Hesse et al. 2003). Figure 3.1 shows a schematic view of the *INTEGRAL* spacecraft with the location of the different instruments. The characteristics of the instruments will be described later in this chapter, with a larger emphasis on IBIS and JEM-X, which are the more relevant instruments for this work.

A revolution of *INTEGRAL* around the Earth lasts 72 hours on a highly eccentric orbit, with an apogee of 154,000 km and a perigee of 10,000 km. The orbit of the satellite was chosen such that *INTEGRAL* spends most of its time ($\sim 90\%$) outside the electron radiation belts. This reduces the rate of background particles significantly, and therefore the satellite can observe the sky continuously for ~ 200 ksec. The spacecraft performs 3 different observation strategies: staring, hexagonal and 5×5 dithering pattern. The staring strategy is used mainly for calibration purposes, while the hexagonal and dithering patterns are optimised for observations dedicated to IBIS and SPI respectively.

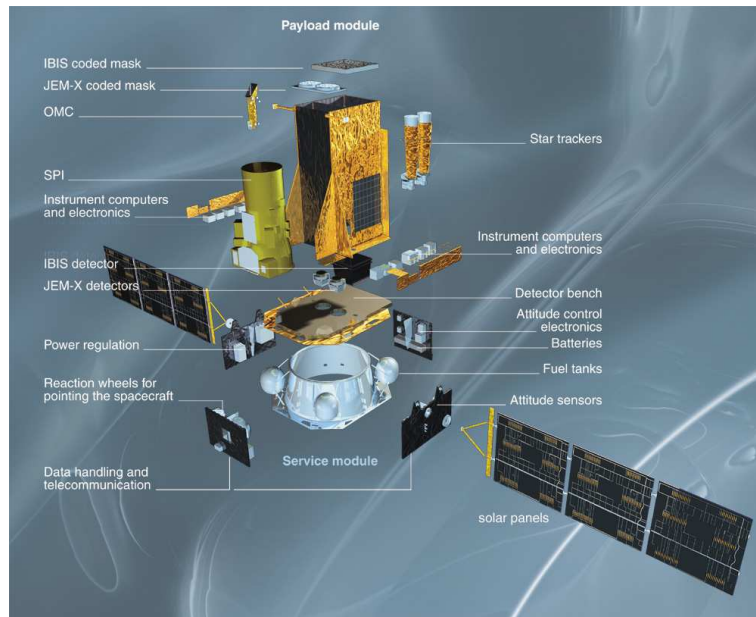


Figure 3.1: An exploded view of the *INTEGRAL* spacecraft (Credits: ESA 2002). The 4 scientific instruments are loaded on the “payload module”, on top of the “service module”, which contains the operational systems.

The ISDC (Courvoisier et al. 2003) is the data centre for *INTEGRAL*. It is funded by a consortium of European institutes, with two main goals: organize the data flow from the satellite, and provide an easy-to-use data analysis software to the scientific community. *INTEGRAL* data are transmitted from the satellite to the ISDC in 6 seconds. The data are then processed and stored, and an automatic analysis of the data is generated. The results of the quick-look analysis are then checked by the ISDC scientist on duty. If anything new is found in the data (e.g. new source discovered, gamma-ray burst, outburst of a transient source), the ISDC sends an alert to the scientific community to describe the discovery and request follow-up observations by other instruments.

Apart from the data-flow related activities, the ISDC also has the responsibility to distribute the standard *INTEGRAL* data analysis software. The instrument-specific software are prepared by the instrument teams and distributed by the ISDC under the form of a complete package, the Offline Scientific Analysis (OSA) software.

3.1.1 The coded-mask technique

Because of the strong penetration power of γ -rays, it is not possible to focus high-energy photons on a given point using mirrors. Therefore, the standard mirror optics, as well as the grazing incidence optics used by X-ray telescopes, cannot be used for γ -ray observations. For this reason, it has always been difficult to observe the sky in the hard X-ray/soft γ -ray band with sufficient angular resolution and sensitivity. In this section, I will present the technique used by all the high-energy instruments on board *INTEGRAL* in the purpose of observing hard X-rays and soft γ -rays with sufficient angular resolution

and sensitivity.

To make images of the sky in the hard X-ray band, the high-energy instruments use the coded-mask technique. In this method, a piece of absorbing material with several holes (the “mask”) is placed ahead of the detector (see the top of Fig. 3.1). The shadow of the mask cast by a γ -ray source on the detector allows to determine the position of the source, and reconstruct the sky images, provided that the orientation of the mask-detector system is known in celestial coordinates. More precisely, the detector output D is given by the convolution of the sky image by the mask pattern plus a background array,

$$D = I \star M + B, \quad (3.1)$$

where I is the original sky image, M is the mask pattern and B is the background. If there exists a decoding array G such that $M \star G = \mathbb{I}$, where \mathbb{I} is the identity matrix, then the sky images can be easily reconstructed using the equation

$$I' = D \star G = I + B \star G. \quad (3.2)$$

I' differs from the real sky image only by the background term $B \star G$, which can be measured and removed. The variance of the reconstructed sky image can also be computed using the relation

$$V = G^2 \star D. \quad (3.3)$$

In this framework, the signal-to-noise of a source is given by

$$\frac{S}{N} = \frac{C_S}{\sqrt{C_S + C_B}}, \quad (3.4)$$

where C_S and C_B are respectively the source and the background count rates. For further details on image deconvolution with a coded-mask instrument, see Goldwurm et al. (2001).

The angular resolution of a coded-mask instrument is given by the angle subtended by the smallest mask holes as seen from the detector. For example, in the case of the IBIS instrument, the ISGRI detector is located 3.2 m from the mask, and the smallest mask holes have a size of 11.2×11.2 mm. The angular resolution of the instrument is therefore $\arctan(11.2/3200) = 12.6$ arcmin.

In a coded-mask instrument, the field of view (FOV) is separated between the Fully Coded Field Of View (FCFOV), where sources cast a whole mask pattern on the detector, and the Partially Coded Field Of View, where only a fraction of the detector is in the shadow of the mask. For a source in the FCFOV, the angular resolution and sensitivity are optimal, while the effective area and the angular resolution of the instrument decrease for sources in the PCFOV.

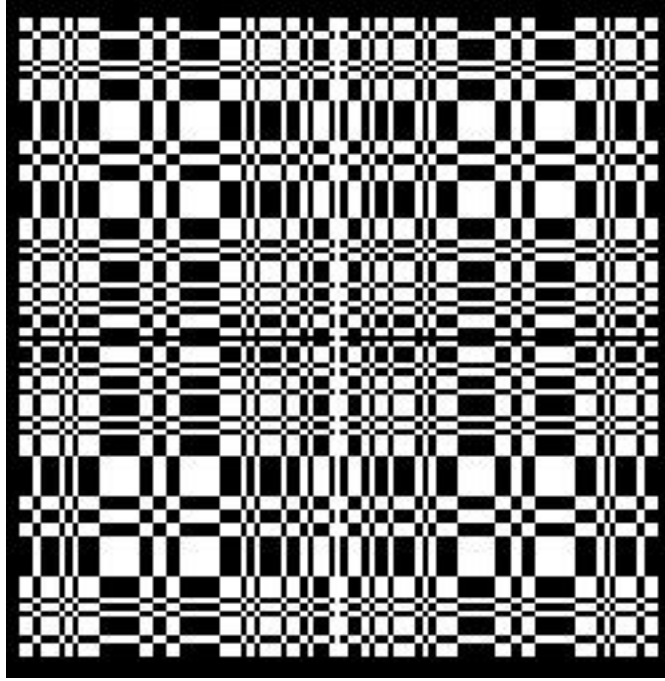


Figure 3.2: The IBIS mask pattern. The geometrical properties of the mask have been chosen such that the decoding array $G = 2M - 1$.

3.1.2 The Imager on-Board INTEGRAL Satellite (IBIS)

The Imager on-Board *INTEGRAL* Satellite (IBIS, Ubertini et al. (2003)) instrument is one of the two main instruments on board *INTEGRAL*. Because of its good angular resolution and sensitivity in the 15 keV - 2 MeV range, it is currently the best instrument available in this energy range for the study of hard X-ray sources. Like the other high-energy instruments on-board *INTEGRAL*, it uses the coded-mask technique (see Sect. 3.1.1). The IBIS mask (see Fig. 3.2) is a square array made of 95×95 individual square cells of size 11.2×11.2 mm. The geometry of the IBIS mask is a cyclic representation of a MURA (Modified Uniformly Redundant Array) of order 53 (see Gottesman & Fenimore (1989) for the detailed properties of URA patterns). The main property of MURA patterns is that their cyclic auto-correlation gives a δ function. The IBIS mask has the property that the decoding array is simply given by $G = 2M - 1$, and therefore the sky images can be reconstructed using Eq. 3.2.

The detector of the IBIS instrument is made of 2 different layers, ISGRI (INTEGRAL Soft Gamma-Ray Imager, Lebrun et al. (2003)), operating in the 15-400 keV band, and PICsIT (Pixellated Imaging CaeSium Iodide Telescope, Di Cocco et al. (2003)), located below ISGRI, observing the sky in the 180 keV - 2 MeV band. Since the energy range covered by PICsIT is not relevant to this work, I will only describe the properties of ISGRI in more details.

ISGRI is the low-energy layer of IBIS. It is designed as an array of 128×128 pixels of cadmium telluride (CdTe), organised in 8 modules of pixels. With a mask-ISGRI distance

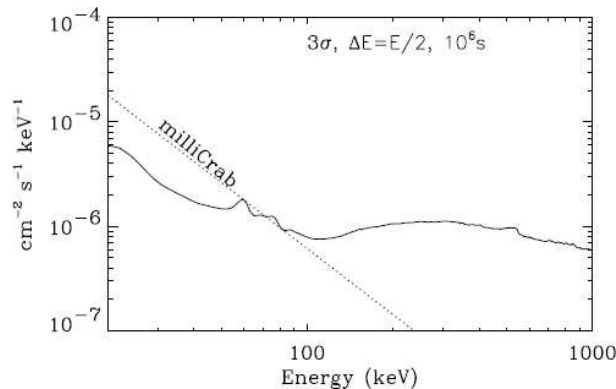


Figure 3.3: Sensitivity of the ISGRI detector as a function of energy (Lebrun et al. 2003). The solid curve shows the minimum flux level for which a 3σ detection can be achieved in a 1 Msec observation, compared to the mCrab flux level (dashed line).

of 3.2 m the angular resolution is $12'$ Full Width at Half-Maximum (FWHM) and a 10σ source can be localized with an accuracy of $1'$. The total ISGRI area is around 3600 cm^2 but dead zones between pixels and between modules restrict the sensitive area to 2621 cm^2 . The total FOV of the instrument is large, $29^\circ \times 29^\circ$, but the FCFOV, where the sensitivity and angular resolution are optimal, is restricted to a $9^\circ \times 9^\circ$ region. Figure 3.3 shows the sensitivity curve of ISGRI as a function of energy. The sensitivity peaks in the 25-55 keV range, where ISGRI can achieve a 3σ detection of an 0.3 mCrab source in an exposure time of 1 Msec. Since IBIS in general and ISGRI in particular have been designed mostly for good imaging capabilities and deep sensitivity, the energy resolution of the instrument ($\sim 6\%$ at 50 keV) is not sufficient for the detailed spectroscopic study of the sources (e.g. detection of narrow emission lines), but since the instrument offers the best signal-to-noise in the hard X-ray range, it is well suited to study the continuum emission from astrophysical objects.

3.1.3 The JEM-X X-ray monitor

The Joint European Monitor in X-rays (JEM-X, Lund et al. (2003)) is the X-ray instrument on board *INTEGRAL*, operating in the 3-35 keV band. It is designed for the spectral, imaging and timing study of the sources detected by IBIS and SPI. The instrument consists of two identical co-aligned microstrip gas chambers, JEM-X1 and JEM-X2, which are switched on alternatively during the mission. Its angular resolution ($3.35'$ FWHM) is better than IBIS, which allows for a better point source location accuracy ($15''$ for a 10σ detection).

Unlike the IBIS mask pattern, the JEM-X mask does not have a specific geometrical shape, but was chosen randomly in order to minimize the systematic effects that arise from calibration uncertainties. Since the instrument was designed as a monitor instead of a main instrument, the effective area of both JEM-X instruments (500 cm^2) is much smaller than that of ISGRI. The FOV is also much smaller than IBIS (4.8° in diameter for the FCFOV, 7.5° half-response). Most of the time, the observation strategy of *INTEGRAL*

is a 5×5 dithering pattern, and in this case, the effective JEM-X exposure time on the target is only 10% of the total observation time. Therefore, the JEM-X exposure time available for a given source is always much lower than the corresponding ISGRI exposure time, which reduces the efficiency of the instrument.

3.1.4 The SPectrometer on INTEGRAL (SPI)

The SPectrometer on *INTEGRAL* (SPI), operating in the 20 keV-8 MeV range, is designed for high-resolution spectroscopy of γ -ray emission lines, in particular the electron-positron annihilation at 511 keV or the ^{26}Al decay emission line at 1.8 MeV. It is a coded-mask telescope with a mask designed as a Hexagonal Uniformly Redundant Array (HURA) on top of a detector formed of 19 individual Germanium detectors, which provide a very fine spectral resolution of 1 keV@ 511 keV. This makes the instrument 100 times more sensitive than previous instruments in this domain.

The FoV of the instrument is hexagonal with a diameter of 31° . The angular resolution (2 degrees) is not as good as that of ISGRI, which can lead to source confusion in the central regions of our Galaxy. On the other hand, the moderate angular resolution makes SPI more sensitive to diffuse emission compared to IBIS, while for point-like sources the sensitivity of IBIS is better than that of SPI by a factor ~ 10 .

Among the most striking results from SPI, the sensitivity of the instrument to diffuse emission allowed for the study of the spatial distribution of positrons in our Galaxy through the detection of emission at 511 keV. Using an intensity map of the 511 keV line in our Galaxy, Weidenspointner et al. (2008) showed that the emission is correlated with the distribution of low-mass X-ray binary (LMXRB) systems, which could indicate that positrons are created in LMXRBs and ejected in the intergalactic medium, e.g. via jets.

3.1.5 The Optical Monitoring Camera (OMC)

The OMC is the first optical instrument operating alongside with X-ray and γ -ray instruments. It features a 1024×1024 pixels CCD chip and a $5^\circ \times 5^\circ$ FOV. The OMC was designed for optical follow-up observations of γ -ray detected sources and for the detection of optical emission (afterglow) from Gamma-Ray Bursts (GRBs).

3.2 Difficulties due to the coded-mask technique

The coded-mask technique used by the high-energy instruments on-board *INTEGRAL* has allowed astronomers to make the most sensitive imaging analysis of the sky in the hard X-ray/soft γ -ray domain to the present day. Indeed, although the same technique was already used in the late 1980s/early 1990s by the french-russian satellite *GRANAT*, the sensitivity of the hard X-ray instrument on-board *GRANAT*, SIGMA, was lower by a factor of 10 compared to the similar instruments on-board *INTEGRAL*, so the all-sky survey performed by *INTEGRAL* is much deeper than the one of *GRANAT*. On the other hand, several hard X-ray detectors with good sensitivity, such as the PDS instrument on-board *BeppoSAX*, the HEXTE instrument on-board *RXTE*, or more recently the Hard

X-ray Detector (HXD) on-board *Suzaku*, have also monitored the sky in the hard X-ray band, but all these instruments are non-imaging, so the data could always be affected by the presence of additional sources in the FOV of the instruments, and it was not possible to extract any information on the morphology of the hard X-ray sources.

For all these reasons, the high-energy instruments on-board *INTEGRAL*, in particular the IBIS/ISGRI soft γ -ray imager and the JEM-X X-ray monitor, allow us for the first time to study the morphology of several apparently extended sources (i.e. sources with an apparent size larger or comparable to the point-spread function (PSF) of the instrument), such as clusters of galaxies, supernova remnants, or the Galactic center region. However, one must be careful when dealing with extended sources with a coded-mask instrument, because of the specificities of this technique. In a coded-mask instrument, the detector image (or “shadowgram”) consists of the superposition of the shadow patterns of all individual sources in the field-of-view,

$$S(x, y) = \sum_{i=1}^n f_i \cdot PIF_i(x, y) + b \cdot BM(x, y), \quad (3.5)$$

where n is the number of sources, f_i is the flux of the i th source, and $PIF_i(x, y)$, the “Pixel Illumination Fraction”, gives the fraction of the detector pixel with coordinates (x, y) which is illuminated by the i th source. $BM(x, y)$ is a “background map”, i.e. a model of the background in each detector pixel (x, y) . Such a map can be computed by averaging shadowgrams over a long time period. The total background is therefore given by $bB(x, y)$.

When dealing with extended sources with a coded-mask instrument, the shadow pattern projected by the source on the detector significantly differs from the standard point-source case. Figure 3.4 shows the ISGRI PIF of an extended source (a uniform disk with a radius of 30 arcmin) compared to the usual point-source PIF. It is clear that in such a case, the extension of the source must be taken into account for a correct flux estimate and spectral extraction. Specific tools for the study of extended sources should therefore be developed in the purpose of analyzing extended sources.

On the other hand, the imaging software, which performs cross-correlations between the detector image and the sky positions, should be able to detect the extension of the source, as long as the source is not too large. Indeed, if the observed source becomes too large compared to the resolution of the instrument, the detector image of this source will become almost uniform, and the source will therefore be treated as background. Renaud et al. (2006b) studied the sensitivity of the ISGRI instrument for extended sources. Figure 3.5 shows the flux of a simulated extended source with the morphology of a uniform disk reconstructed by the standard OSA imaging software as a function of the radius of the disk. The results show that as long as the size of the source is smaller or comparable to the PSF of the instrument ($R < 8'$), the imaging software reproduces $> 90\%$ of the flux. However, for sources with larger radius, the sensitivity of the instrument is proportional to R^{-2} .

It is also important to note that for very extended sources, the angular resolution of the instrument significantly drops. In this case, the smallest mask holes become more and

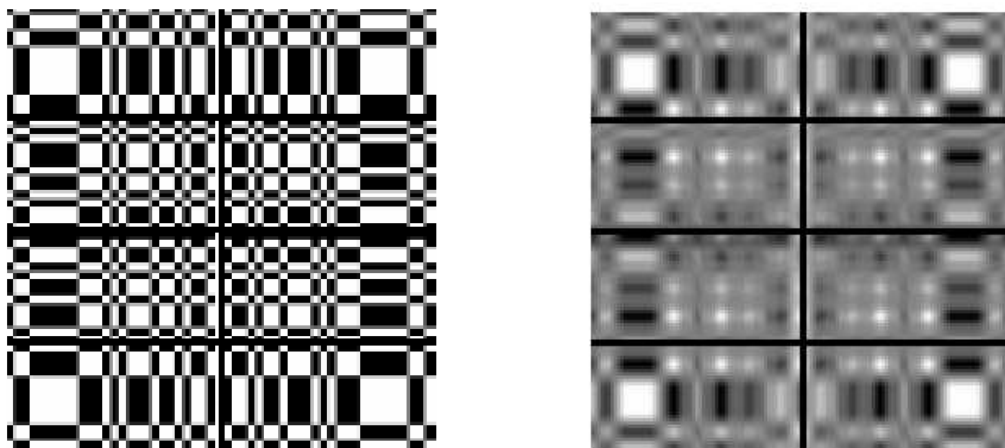


Figure 3.4: The shadow pattern (or PIF) of the mask of the IBIS telescope cast by a point source (left) and a circular source with a radius of 30 arcmin (right) located along the axis the instrument.

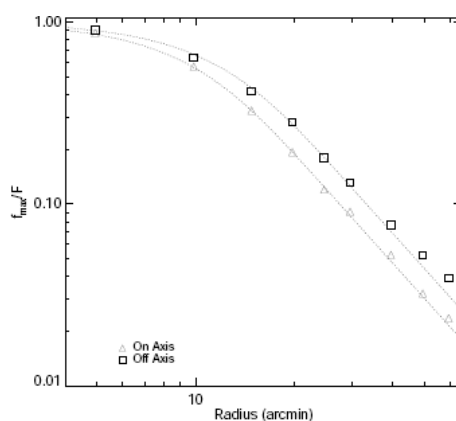


Figure 3.5: Relative reconstructed peak flux as a function of the source radius for a uniform disk observed on-axis (triangles) and 9° off-axis (squares) (Renaud et al. 2006b). Below $\sim 8'$, the flux loss is limited, whereas above this value, the peak flux decreases as R^{-2} .

more blurred by the extension of the source (see Fig. 3.4), and since the angular resolution of the instrument is given by the angle subtended by the smallest mask holes as seen from the detector, the extension of the source also affects the angular resolution of the instrument. For sources with an angular extent bigger than the largest mask holes, the angular resolution of the source is lost, and the source is treated as background by the software.

In conclusion, the standard data analysis tools, which have been developed for the study of point sources, are not well suited for the analysis of extended sources. Consequently, a significant part of my PhD work was devoted to the development of analysis tools which treat the extended nature of several sources detected by *INTEGRAL* properly into account.

3.3 A method to analyze extended sources with a coded-mask instrument

In this section, I will present a generic method which can be used to extract fluxes and spectra of extended sources in a pixelized coded-mask instrument. This method requires that the morphology of the source is known, either from the mosaic image or from instruments operating at other wavelengths. All the codes which are described in this section are available on demand.

3.3.1 The shadow pattern cast by an extended source

The Pixel Illumination Fraction gives the fraction of each pixel of the detector that is illuminated by the source. For a pixel that is completely in the shadow of the mask, the PIF will be 0, whereas in the case of a fully illuminated pixel, the PIF will be equal to 1. Obviously, the PIF of an extended source is different from that of a point source, since some pixels might be illuminated by only a fraction of the total extension of the source, which cannot happen for a point source (see Fig. 3.4). So, to describe an extended source properly, one has to create an appropriate model for it.

Our method to create such a model is the following: we create a grid of positions on the sky covering the extended source, compute the PIF for all the positions of this grid, and then average the PIFs, weighted by a model surface brightness for the source, which we assume to be known.

In more details, let \mathbf{n} be the unity vector describing the direction of the source centroid. We choose a $m \times m$ coordinate grid around \mathbf{n} with an angular distance $\Delta\alpha$ between the grid positions, such that the whole source is covered by the grid, and let $\text{PIF}_{i,j}$ be the PIF extracted for the grid position $i, j = 1 \dots m$. Assuming a surface brightness profile $I(\mathbf{r})$, the total PIF is given by the formula

$$\text{PIF}_{tot} = \frac{1}{N} \sum_{i,j=1}^m I_{i,j} \text{PIF}_{i,j}, \quad (3.6)$$

where $I_{i,j} = I(\mathbf{r} - \mathbf{n})$ (\mathbf{r} being the unity vector corresponding to the (i, j) grid position),

and N is the total normalization,

$$N = \sum_{i,j=1}^m I_{i,j}. \quad (3.7)$$

In the case of galaxy clusters, it is reasonable to assume a spherical isothermal β -profile,

$$I(\mathbf{r}) \propto \frac{1}{\left(1 + \frac{r^2}{R_c^2}\right)^{3\beta/2}}, \quad (3.8)$$

which is commonly used to describe the X-ray surface brightness of clusters. The parameters of the profile are the HWHM of the source, R_c , and the compactness of the source, β .

We created a PERL script which uses this method to create the ISGRI PIF for an extended source. The code uses the standard OSA tool for PIF creation, `ii_pif`, to create the standard point-source PIF for all grid points. The code can be used for any appropriate surface brightness profile as well as m and $\Delta\alpha$ parameters, and can be easily adapted to any pixelized coded-mask instrument.

3.3.2 Shadowgram fitting

In the standard OSA spectral extraction tool for ISGRI, `ii_spectra_extract`, provided by the ISGRI team, the source model is created using a source catalog given in input, and it is not possible to use an extended-source model to analyze the data. Therefore, in order to extract the flux of an extended source in a correct way, we created a tool that extracts the properties of a source with any kind of PIF in the shadowgram.

To extract ISGRI fluxes and spectra with any source model, we wrote a C++/ISDCROOT code which fits an input source model to the data, for an arbitrary number of sources. For the fitting procedure, we use the MINUIT library from ROOT to minimize the quantity

$$\chi^2 = \sum_{i=1}^N \frac{(S(i) - M(i))^2}{V(i)}, \quad (3.9)$$

where N is the number of properly-working detector pixels, S is the corrected shadowgram in a given energy band, V is the variance on the shadowgram, and M is a shadowgram model. For a field containing n sources, the model is simply given by

$$M(i) = \sum_{j=1}^n f_j \text{PIF}_j(i) + B(i), \quad (3.10)$$

where f_j and PIF_j are the flux, respectively the shadow pattern of the j th source and $B(i)$ is the total background counts in the i th detector pixel. If the average background in each detector pixel remains approximately constant for a sufficiently long period of time, the background will be proportional to a specific background pattern, a *background map*, which can be computed by averaging shadowgrams over a long time period. If a

sufficiently accurate background map BM is available, the background in a given detector pixel can be approximated by

$$B(i) = b \cdot BM(i), \quad (3.11)$$

where b is a constant parameter which can be fitted. This method allows us to use only 1 free parameter to describe the total background. To take the variability of the background into account, it is possible to prepare background maps for different time periods, which will be more accurate than a single background map prepared for the entire mission.

The free parameters of the fitting procedure are therefore the fluxes of the n sources, $\{f_j\}_{j=1..n}$, and the background normalization b . The off-axis correction (mainly the absorption due to the NOMEX structure which supports the IBIS mask) is then applied to compute the output fluxes, which are finally stored into a file in FITS format. The same procedure can of course be applied to any energy band in order to extract the spectrum of a source. To increase the signal-to-noise of the source, a mean flux weighted by the variance can be computed by combining all flux measurements. Indeed, in such a case the signal-to-noise of the result increases like $\frac{S}{N} \propto \sqrt{n}$, where n is the number of measurements. It must be noted that for a correct measurement of a source spectrum, the spectrum of all sources in the FOV with similar or larger flux must also be extracted. Indeed, for a coded-mask instrument, a single detector pixel can be illuminated simultaneously by several sources, and therefore the spectra cannot be extracted independently.

Since the source PIF is an input of the program, an extended source model as described in Sect. 3.3.1 can be used to extract properly the total flux of an extended source. Unfortunately, this method is model-dependent, since it requires that the surface brightness profile of the source is known, and therefore it cannot be used to study the morphology of a source.

3.3.3 Using the standard OSA spectral extraction tool

Since our spectral extraction method is model-dependent, it does not allow us to determine the properties of one particular region in an extended source. For instance, the ISGRI 18-30 keV image of the Coma cluster cannot be well represented by an extrapolation of the 1-10 keV profile because of a significant excess to the SW of the cluster core (see Sect. 4.3.1), and we have shown that the hard X-ray profile can be relatively well approximated by the superposition of two point sources. In such a case, the standard OSA spectral extraction tool, `ii_spectra_extract`, can be used to extract the spectrum of a region in a model-independent way. However, while using this tool one must be aware of the limitations due to the incorrect source model. In this paragraph, I will describe how the standard OSA spectral extraction tool deals with extended sources, and in particular how to cross-calibrate the results with data from another instrument.

To evaluate quantitatively the fraction of the total flux extracted by `ii_spectra_extract`, I simulated ISGRI data of a Coma-like source (a spherical beta-model with $\beta = 0.75$) and extracted the spectrum of the simulated source with the standard parameters. To

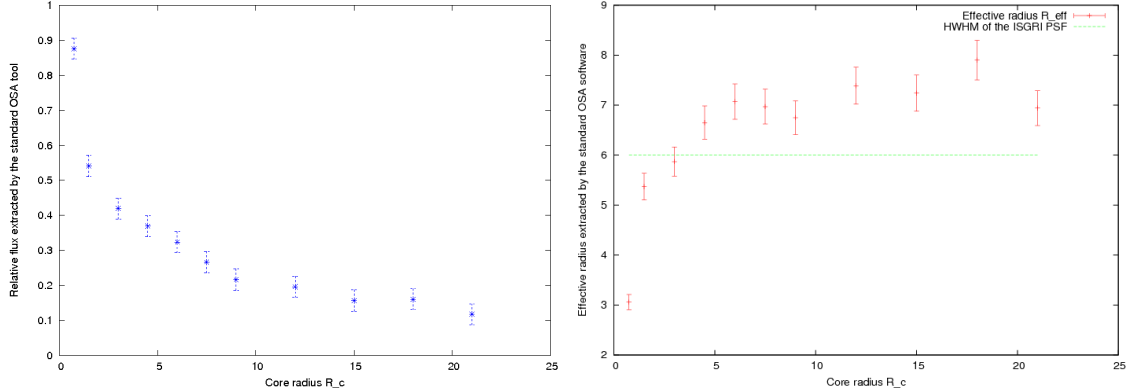


Figure 3.6: Left: Relative flux extracted by the standard OSA spectral extraction tool for an extended source with a surface brightness profile described by a beta profile with $\beta = 0.75$ and different values of R_c . Right: Effective radius R_{eff} as a function of the core radius R_c (see text).

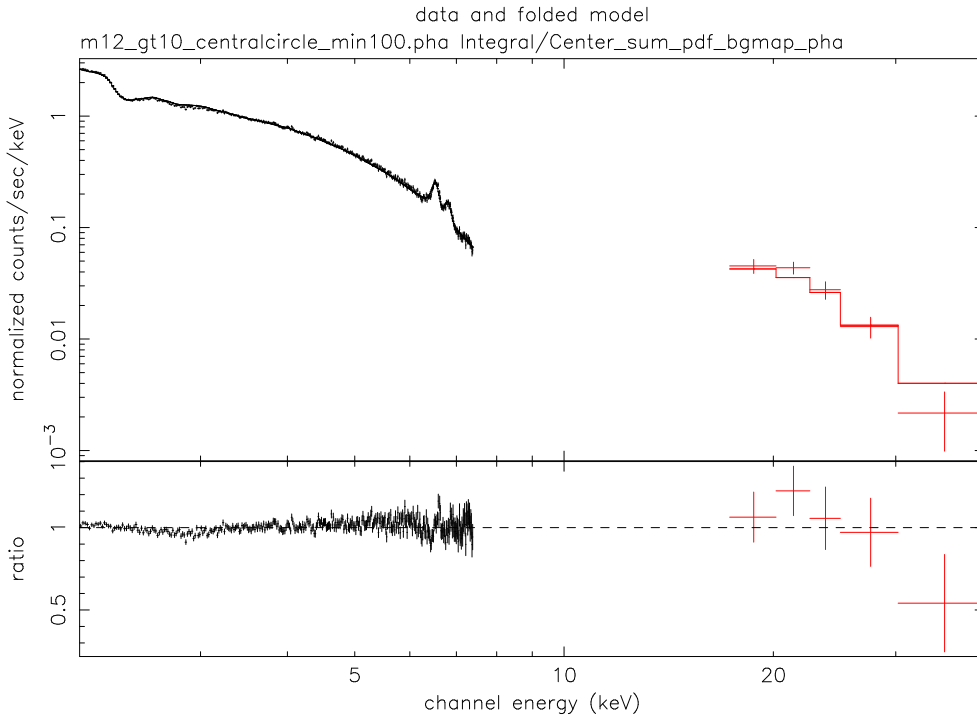
simulate source spectra, I used the fakeit function of the XSPEC package (Arnaud 1996) to simulate thermal bremsstrahlung counts spectra at a temperature of 7.9 keV (the temperature of the central part of the Coma cluster), taking into account the response matrix (RMF) and ancillary response (ARF) of ISGRI. Then I created an extended PIF using the method described in Sect. 3.3.1, for different core radii R_c . Finally, I developed a C++/ISDCROOT code which uses the extended PIF and the simulated spectra to create ISGRI shadowgrams with Poissonian background.

The left panel of Fig. 3.6 shows the relative flux of the simulated source extracted with the standard OSA spectral extraction tool `ii_spectra_extract`, for different core radii R_c . For the simulations, the beta-model is integrated up to a radius of $R_{max} = 30$ arcmin. The error bars were estimated by performing the simulations a large number of times and computing the distribution of results. We can see that the relative extracted flux decreases quickly with the core radius. For a core radius $R_c \sim 10$ arcmin, the extracted flux is less than 20% of the total flux. Hence, the effect of the extension of the source on the results cannot be neglected.

The right panel of the figure shows the effective radius R_{eff} such that

$$\frac{F_{obs}}{F_{tot}} = \frac{\int_0^{R_{eff}} I(r)r dr}{\int_0^{R_{max}} I(r)r dr}. \quad (3.12)$$

R_{eff} represents the effective integration radius in which the spectrum is extracted. This radius is especially important to ensure a correct cross-calibration between spectra extracted with ISGRI and other instruments with better spatial resolution, e.g. instruments on board *XMM-Newton* and *Chandra*. Indeed, the flux extracted with these instruments strongly depends on the integration radius, and therefore it is important for comparison with ISGRI spectra to have a good knowledge of the corresponding integration radius. We can see in Fig. 3.6 that for core radii smaller than the PSF of the instrument, the value



jnevalei 4-Mar-2008 12:23

Figure 3.7: *XMM-Newton/MOS1 and INTEGRAL/ISGRI spectrum of the Coma cluster centre. For correct cross-calibration, the MOS spectrum has been extracted in a radius of 7.2 arcmin from the centre (see text).*

of R_{eff} increases quickly, whereas for values of R_c similar or larger than the ISGRI PSF R_{eff} converges to a constant value,

$$R_{eff} = 7.2 \pm 0.3 \text{ arcmin.} \quad (3.13)$$

Figure 3.7 shows the *XMM-Newton/MOS1* and *INTEGRAL/ISGRI* spectrum of the center of the Coma cluster. The ISGRI spectrum is extracted with standard OSA 7.0, while the MOS1 spectrum is extracted in a radius of 7.2 arcmin. We can see that the cross-calibration of the instruments agrees very well. This is extremely important to make quantitative results based on the spectra.

3.3.4 Analysis of extended sources with JEM-X

Unlike ISGRI, JEM-X is a micro-strip gas chamber, and therefore it is not pixelized. In this case, an incoming photon can be recorded at any place in the detector, with an error on the position of the photon which depends on energy. This makes the situation different, because in the case of a pixelized detector, the output is only given by the total number of counts in a specific pixel. A projection of the mask on each specific pixel can therefore be computed for any given sky position, and the PIF can be directly fitted to the detector output. For JEM-X, the situation is reversed: photons are *back-projected* on the sky and correlated with a specific sky coordinate. This method allows us to produce sky images

which can be directly used to study the morphology of a source.

Therefore, for the study of extended sources with JEM-X, we perform standard imaging analysis in order to create sky images. For spectral extraction, we use the `mosaic_spec` executable available in the OSA package to fit the sky images and extract fluxes and spectra from the deconvolved images.

3.4 Conclusion

In this chapter, I have presented some of the work that I have been doing as a contribution to the *INTEGRAL* mission, and in particular the methods that I have developed in collaboration with ISDC scientists on the analysis of extended sources with *INTEGRAL*. The instruments on board *INTEGRAL* allow us for the first time to study the morphology of hard X-ray sources, such as clusters of galaxies, supernova remnants or the Galactic center region. After a brief introduction on the *INTEGRAL* mission, I have explained the reasons why one must be careful when dealing with extended sources with a coded mask instrument, and I have presented several methods to extract quantitative results on extended sources with *INTEGRAL*. In the following chapters, I will present the results obtained with this method on several extended sources, in particular the Coma, Ophiuchus and Perseus clusters.

Chapter 4

Hard X-ray observations of the Coma cluster

4.1 Introduction

The Coma galaxy cluster (Abell 1656) is, with the Perseus and Virgo clusters, one of the best studied clusters of galaxies. Historically, the interest of the astronomical community for Coma has been large for a long time (see Biviano (1998) for a historical review). Indeed, during a long period of time (~ 1950 -1980) the number of publications on Coma has been a large fraction (more than 10%) of the total number of publications on clusters of galaxies. It was discovered in 1785 by Sir William Herschel, who noticed a concentration of “fine nebulae” in the constellation of Coma Berenices. The first cartography of the cluster was made by Wolf (1901), who counted more than 100 “nebulae”. More than 30 years later, Zwicky (1937) analyzed the velocity dispersion of the galaxies in the cluster and made the first discovery of dark matter. He used the virial theorem to estimate the total mass of the cluster, which he found to be $M > 5 \times 10^{14} M_{\odot}$. The corresponding mass-to-light ratio was large, $M/L > 50 M_{\odot}/L_{\odot}$, which implied the existence of a form of invisible matter. Coma was also the first cluster for which diffuse X-ray (Meekins et al. 1971) and radio (Willson 1970) emission was detected.

Since Coma is located close to the north Galactic pole ($b = 88^{\circ}$), obscuration by dust in this direction is very small, and the cluster can be extensively studied in visible light. Although the cluster has been known for a very long time, its full extent was only understood in the 1960s. It is estimated that it contains over 3,000 galaxies within its virial radius of ~ 3 Mpc, making it the prototypical rich cluster. The core of the cluster is dominated by two giant elliptical cD galaxies, NGC 4874 and NGC 4889. As expected in very rich clusters, the galaxies in the center of the cluster are predominantly elliptical and lenticular because of the large number of interactions between the galaxies. Spirals can only be found in the outskirts of the cluster, where galaxy interactions are less frequent. Figure 4.1 from Jenkins et al. (2007) shows an optical image of the cluster from the Sloan Digital Sky Survey (blue) combined with a Spitzer IR image (red). The faint green dots are mostly dwarf galaxies within the cluster. The redshift of the cluster is $z = 0.023$, which corresponds in a Λ CDM cosmology to an angular diameter distance of 99 Mpc. Only 5% of the clusters contain as many galaxies as Coma, and none of them are as close, which

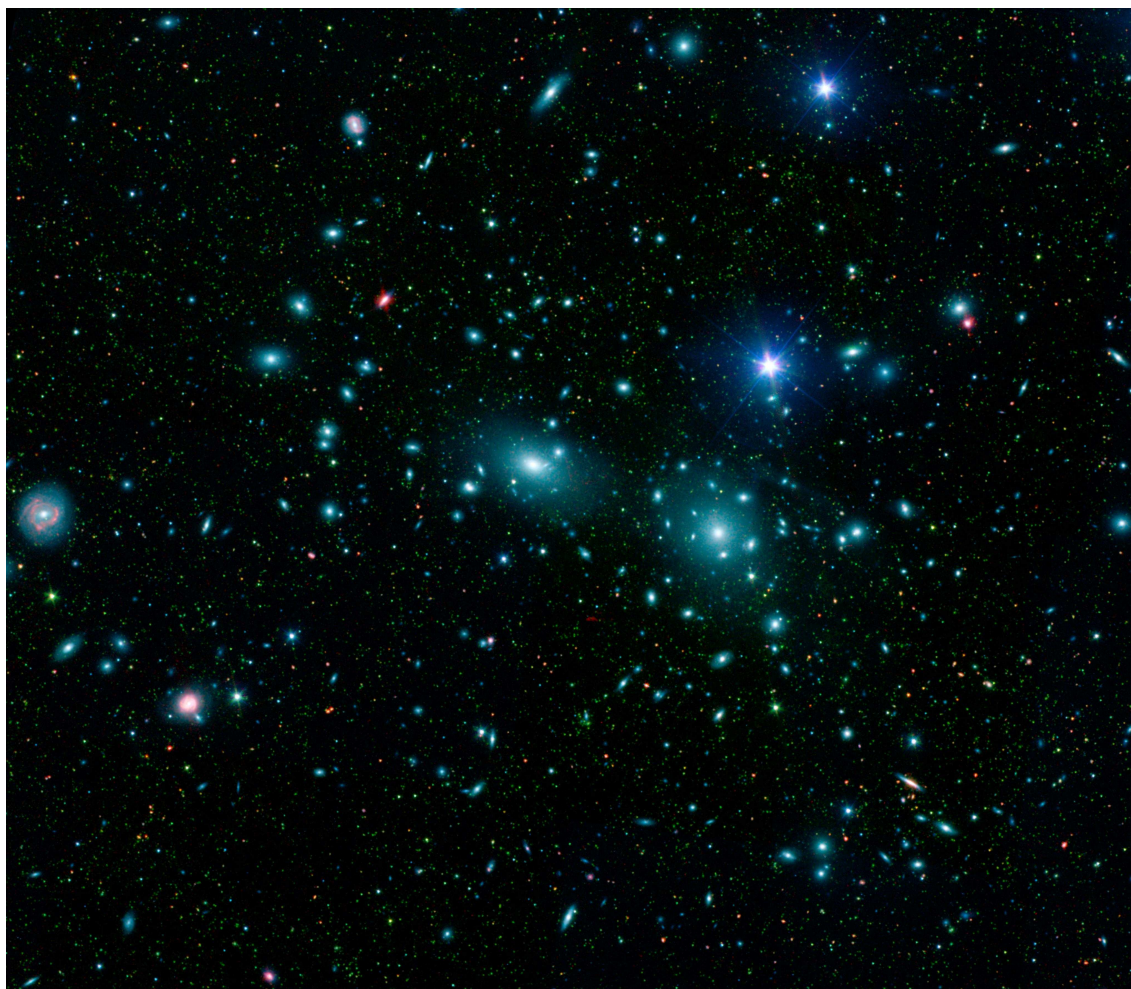


Figure 4.1: Combined optical (blue, Sloan Digital Sky Survey) and IR (red, Spitzer) image of the core of the Coma cluster (Jenkins et al. 2007). The core is dominated by the two giant ellipticals NGC 4874 (right) and NGC 4889 (left). The faint green dots are mostly dwarf galaxies inside the cluster.

makes Coma an ideal subject for the study of rich galaxy clusters.

The distribution of galaxies and velocities in the cluster is close to isotropic, and therefore, it was thought for a long time that Coma was the prototype of a relaxed cluster. However, there is now compelling evidence that Coma is formed of several substructures, which reveal an intense history of cluster merging. Indeed, Mellier et al. (1988) identified 9 independent galaxy over-densities, associated with the most massive galaxies of the cluster. In particular, a group centered on the massive galaxy NGC 4839 apparently falling towards the main cluster has been detected 30 arcmin South-West (SW) from the cluster center. The presence of two very massive cD galaxies in the core of the cluster has also been interpreted as the signature of two different groups of galaxies. It is now thought that NGC 4874 used to be the center of the original Coma cluster, while NGC 4889 was the main galaxy of a sub-cluster which has now merged with the main cluster (Colless & Dunn 1996).

The Coma cluster has also been extensively studied in the X-ray range since the first detection in 1971. The first X-ray maps of the cluster showed an almost spherical morphology, with a surface brightness profile reasonably described by an iso-thermal beta-model,

$$I(r) \propto \frac{1}{\left(1 + \left(\frac{r}{R_c}\right)^2\right)^{\frac{3\beta}{2}}}, \quad (4.1)$$

with $R_c \sim 10$ arcmin and $\beta \sim 0.75$ and a temperature in the central region of $kT \sim 8.1$ keV. Using *ROSAT* observations, Briel et al. (1992) showed that the cluster exhibits several sub-structures, in agreement with the results obtained in the optical. In particular, the NGC 4839 group at the SW of the center was clearly seen. The *ROSAT* image also revealed the presence of gas connecting the NGC 4839 group with the main cluster. The authors therefore interpreted the SW sub-structure as a small group falling onto the main cluster.

A 220 ksec mosaic observation of the cluster with *XMM-Newton* allowed to confirm the presence of significant sub-structures, which demonstrate the un-relaxed state of the cluster. Figure 4.2 shows an X-ray mosaic image of the cluster in the 0.3-2.0 keV band obtained with *XMM-Newton* (Briel et al. 2001). Using the same data, Arnaud et al. (2001) presented a temperature map of the cluster, and identified a hot ($kT \sim 10$ keV) region SW of the cluster core, located between the main cluster and the NGC 4839 group. The authors interpreted this hot structure as adiabatic compression due to the gas falling from the sub-cluster. Neumann et al. (2003) confirmed the presence of this hot region, and identified another cold ($kT \sim 1$ keV), filamentary structure South-East of the center, which could be due to another sub-group.

Apart from extensive studies in the optical and X-rays, the cluster was also the first for which diffuse radio emission not associated with the radio galaxies was detected. This observation revealed the existence of a population of relativistic (Lorentz factor $\gamma \sim 10^4$) particles along with the hot ICM (see Sect. 2.6.1 for a detailed review). The radio emission of the Coma cluster is divided into two distinct structures, the giant radio halo (usually called Coma C) roughly similar in morphology to the X-ray emission, and the radio relic 1253+275, a filamentary structure located close to the NGC 4839 group (see Fig. 2.7). The discovery of radio emission from Coma raised new questions on the history of the cluster. Indeed, it shed light on the existence of a population of relativistic electrons accelerated inside the cluster and of large-scale magnetic fields $B \sim 0.1 - 10 \mu G$, whose origin are not yet fully understood. This is the final proof that despite of its apparently relaxed state, Coma is a forming object which is still experiencing major changes.

The discovery of radio synchrotron radiation from Coma immediately implied the existence of a second component in the X-ray spectrum of the cluster due to inverse-Compton (IC) scattering of relativistic electrons on the CMB, which would dominate over the thermal emission above 20 keV (see Sect. 2.6.2 for a review). The detection of the hard X-ray (HXR) non-thermal emission is of a crucial importance to measure in an un-biased way the

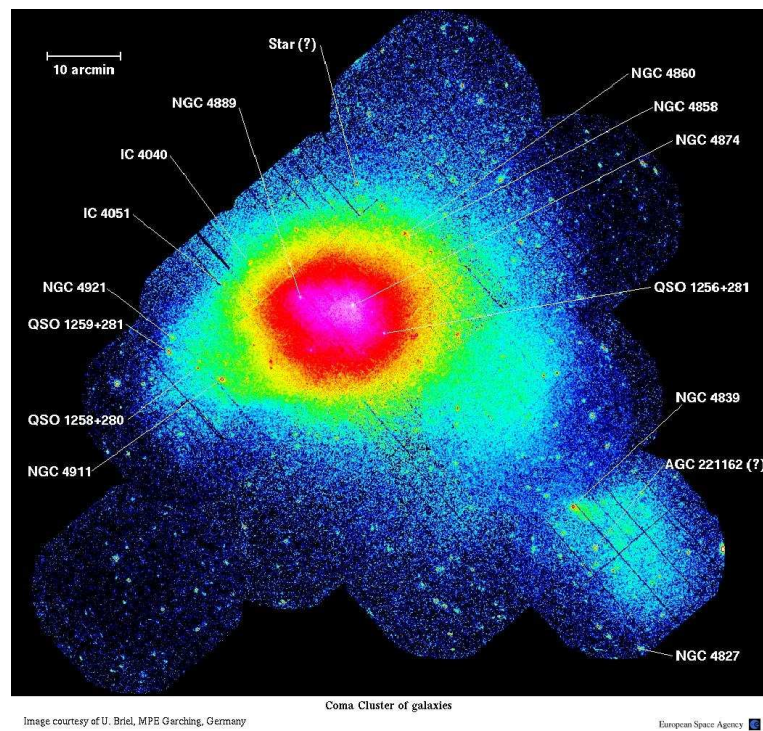


Figure 4.2: XMM-Newton image of the cluster in the 0.3-2.0 keV band (Briel et al. 2001). The falling sub-cluster around NGC 4839 SW of the cluster core is clearly seen. Several point sources detected in X-rays are highlighted as well.

INTEGRAL revolution number	Observation dates	No of pointings	Observing time [ks]
0036	Jan 29-31, 2003	63	140.1
0071-72	May 14-18, 2003	135	304.5
0274-75	Jan 10-15, 2005	57	202.4
0317-18	May 19-25, 2005	99	333.4
0324-25	Jun 9-11, 2005	47	164.5
			1,144.9

Table 4.1: INTEGRAL observation log on the Coma cluster

magnetic field strengths and to constrain the particle acceleration models. Again, Coma was the first cluster for which the detection of HXR emission was claimed (Fusco-Femiano et al. (1999), see Fig. 2.9). But an analysis of the same data by another group (Rossetti & Molendi 2004) cast doubts on this result, and the low magnetic field values measured with this method are inconsistent with the values derived using other methods (see Sect. 2.7). Therefore, confirmation of this result by another instrument is important.

4.2 *INTEGRAL* observations of the Coma cluster

The IBIS/ISGRI instrument on board *INTEGRAL* (see Sect. 3.1.2) is the first imaging instrument in the hard X-ray band with sufficient continuum sensitivity (which peaks in the 30-60 keV band). The PSF of the instrument ($6'$ HWHM) is slightly narrower than the extension of the core of Coma ($R_c = 10.5'$). Hence, ISGRI should be able to resolve the source spatially, and, if present, to locate the hard X-ray emitting region. To the present day, two *INTEGRAL* open-program proposals dedicated to the study of Coma have been performed, for a total observation time of 1.1 Msec. Table 4.1 summarizes the existing *INTEGRAL* data on Coma. Unfortunately, a significant fraction of the observation time was affected by solar flares, and therefore the data from a few revolutions (0274-0275) are barely useable.

Renaud et al. (2006a) presented a first analysis of the cluster with *INTEGRAL* using the first 500 ksec observation (revolutions 0036, 0071 and 0072). Even though they were unable to constrain the morphology or the spectrum of the source because of the low detection significance of the source (6σ), the first analysis allowed the authors to show that the source appeared as extended for ISGRI, and that it would be possible with the addition of more data to study the HXR morphology of the cluster with ISGRI. They also presented the difficulties of analyzing extended sources with a coded-mask instrument. The first results of the full 1.1 Ms observation were presented in Eckert et al. (2007a) (see the full paper in Sect. 4.6). A complementary analysis of the same data with a different software, leading to similar results, was also presented by Lutovinov et al. (2008).

The main technical difficulty resides in the fact that the shadow pattern cast by an extended source on the detector plane is very different from the case of a point source (see Sect. 3.3 for the details). While the imaging software should in principle be able to detect

an extended source, the sensitivity of the instrument to extended sources decreases due to the specifications of the coded-mask technique. On the other hand, the standard spectral extraction tool always uses point source models to extract fluxes and spectra, so the error induced by the extension of the source can be quite large.

4.3 Analysis of *INTEGRAL* data with OSA 6.0

In this section, I will present an analysis of the full set of *INTEGRAL* data based on the OSA 6.0 software. The results of this analysis were published in Eckert et al. (2007a) and Eckert et al. (2007b).

4.3.1 Hard X-ray morphology of the cluster

We processed the full set of data (see Table 4.1) with the Offline Scientific Analysis (OSA) software version 6.0, and created sky images in the 18-30, 30-50 and 50-100 keV bands. It must be noted that the status of the energy calibration in OSA 6.0 was not satisfactory enough below 22 keV, and therefore, it was difficult to extract quantitative information in this band. We chose to use the data below 22 keV anyway for the imaging analysis to ensure a sufficient signal-to-noise in this band. To increase the photon statistics, we combined the resulting sky images to create a single mosaic for each energy band. While the source was clearly detected (at the 11σ level) in the 18-30 keV band, we were not able to detect the source above 30 keV.

Figure 4.3 shows the OSA 6.0 ISGRI mosaic image of the Coma cluster in the 18-30 keV band with $3 - 10\sigma$ significance contours. The yellow crosses represent the position of the two central cD galaxies, NGC 4874 and NGC 4889, and of the quasar EXO 1256+281, a background object which is quite bright in X-rays. The centroid of the 1-10 keV emission is located close to NGC 4874. A first look at the image indicates that the source is extended for ISGRI (see the image of the point source NGC 4388 in the inset for comparison), and that the morphology of the source is elongated in the North-East/South-West direction.

To compare the hard X-ray morphology of the source with the soft X-ray profile, we analyzed existing *XMM-Newton* data. In June 2000, *XMM-Newton* (Jansen et al. 2001) performed a mosaic observation of the Coma cluster, in order to cover the largest possible area. We analyzed the corresponding data of the EPIC/PN camera on board *XMM-Newton* (Strüder et al. 2001) with the SAS software version 6.5 to extract images and spectra. The main problem when analyzing extended sources with the standard SAS software is the background determination. Indeed, in the case of point sources, the SAS software requires the input of the user to determine a source-free region in the same FOV, where the background level can be measured. However, in the case of Coma, it is not possible to use this method, since the FOV of the EPIC instrument (27×27 arcmin²) is too small compared to the extension of the source. To alleviate this problem, we used blank-sky pointings as described in Read & Ponman (2003) to estimate the background level. Finally, we created a mosaic from all the different pointings. The resulting mosaic in the 1-10 keV band can be found in the left panel of Fig. 4.4. The lines which cross the

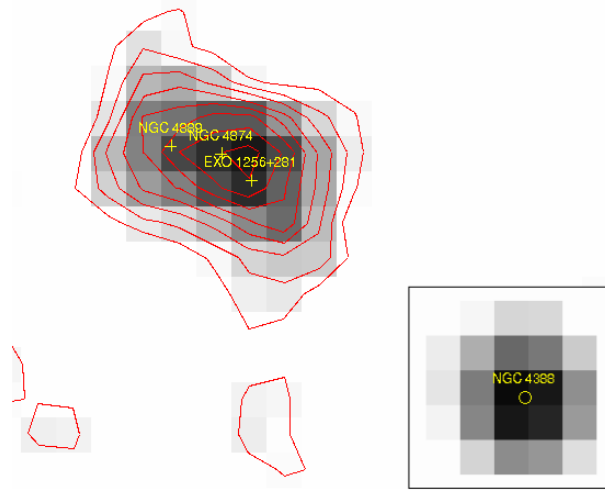


Figure 4.3: Standard OSA 6.0 significance image of the Coma cluster with ~ 1.1 Ms of data, in the 18-30 keV energy band. Significance contours from 3 to 10σ in steps of 1σ are overlaid in red. The position of the 3 brightest X-ray point sources is also displayed. For comparison, the inset in the bottom right corner shows a mosaic image of a known point source in the same field, NGC 4388.

center of the image are artifacts due to the gaps between the different modules. Similarly, the excesses which can be seen around the lines are induced by the mosaicking procedure.

The angular resolution of the EPIC instrument (6.6 arcsec FWHM) is much better than that of ISGRI, and therefore it is not possible to compare directly the images extracted with the two instruments. To compare the hard X-ray morphology of the source with the lower energy thermal profile, we smoothed the *XMM-Newton* mosaic image and convolved it with a Gaussian of half-width 6 arcmin, which corresponds to the angular resolution of ISGRI. After appropriate re-binning, the resulting image can be directly compared with the hard X-ray image obtained with ISGRI. The right panel of Fig. 4.4 shows the convolved PN image with 18-30 keV ISGRI contours overlaid. On this image, one can clearly see that the centroid of the hard X-ray emission is displaced towards the South-West (SW) direction compared to the 1-10 keV emission. To make the displacement more obvious, we rebinned the smoothed PN image to the same binning as the ISGRI mosaic, and then subtracted the rebinned PN profile from the ISGRI image. For the subtraction, the PN image was re-normalized such that the difference between the two images would cancel at the peak of the 1-10 keV emission, between NGC 4874 and NGC 4889. Figure 4.5 shows the resulting image, in units of σ . Significant residuals ($\sim 6\sigma$) are found South-West of the cluster core.

To quantify this effect, we fitted the hard X-ray profile $I(\vec{r})$ with several models for the morphology of the source, i.e.

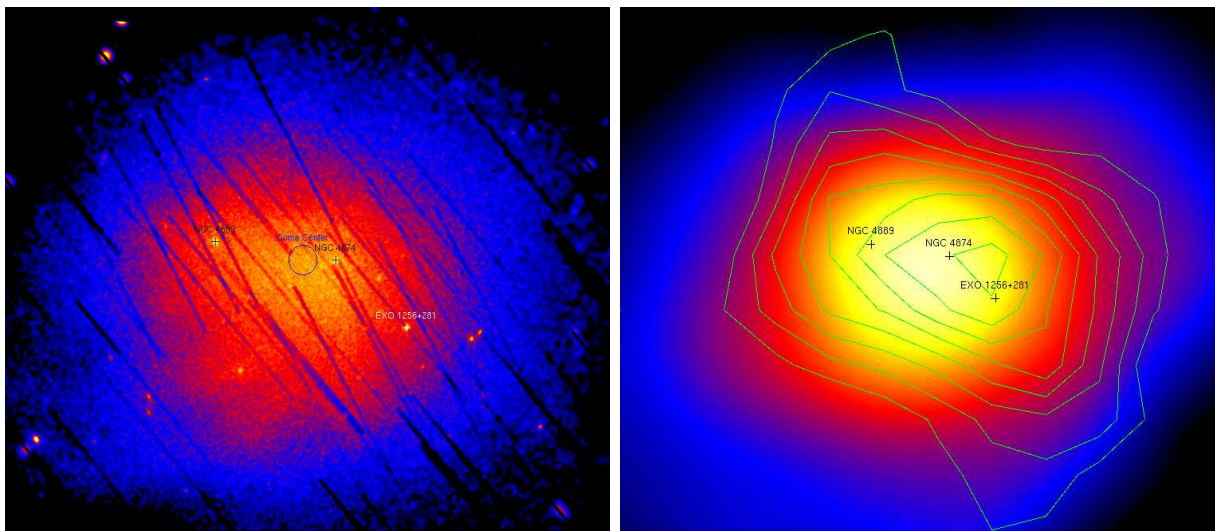


Figure 4.4: Left: XMM-Newton/EPIC mosaic image of the center of the Coma cluster extracted from the Coma mosaic observation. The lines are artifacts due to the gaps between the modules of the detector. The positions of the two central cD galaxies, NGC 4874 and NGC 4889, as well as the quasar EXO 1256+281 are displayed. Right: Same as previous, but convolved with a two-dimensional Gaussian to match the angular resolution of ISGRI. The green contours represent the ISGRI 18-30 keV brightness contours extracted with OSA version 6.0.

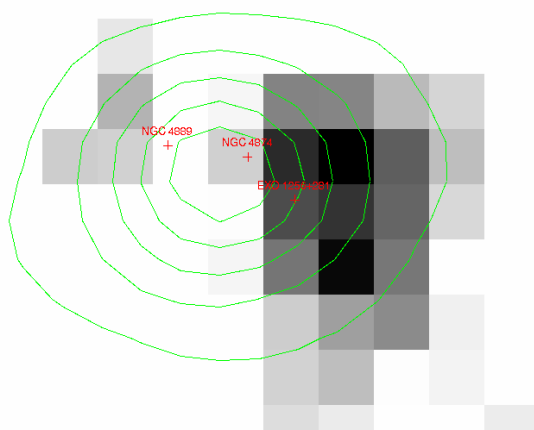


Figure 4.5: ISGRI significance image after the subtraction of the properly renormalized EPIC image (see text). Significant excess ($\sim 6\sigma$) are found SW of the cluster core. The green contours show the 1-10 keV surface brightness profile extracted from the smoothed EPIC mosaic.

1. Model 1: A single point source,

$$I(\vec{r}) = A \exp \left[-\frac{(\vec{r} - \vec{r}_0)^2}{2\sigma^2} \right], \quad (4.2)$$

i.e. a Gaussian with a standard deviation $\sigma = 4.8$ arcmin fixed to the PSF of the instrument and a central position \vec{r}_0 left free while fitting;

2. Model 2: A double point source, with the position of the two sources, \vec{r}_1 and \vec{r}_2 , left free while fitting;
3. Model 3: An ellipse-shaped extended source, given by

$$I(\vec{r}) = A \exp \left[-\frac{((\vec{r} - \vec{r}_3) \cdot \vec{n})^2}{2\sigma_1^2} - \frac{((\vec{r} - \vec{r}_3) \times \vec{n})^2}{2\sigma_2^2} \right], \quad (4.3)$$

where \vec{n} is the unit vector in the direction of the major axis of the ellipse (given by the ellipse inclination angle θ), \vec{r}_3 is the position of the centroid of the ellipse, and σ_1 , σ_2 are the standard deviations of the major, respectively minor axes of the ellipse. All these parameters are left free while fitting.

4. Model 4: A superposition of an extended source with the morphology of the core of the Coma cluster in the 1-10 keV band, plus an additional point source. The 1-10 keV surface brightness profile is described by a Gaussian convolved with the ISGRI PSF, i.e. a Gaussian with a half-width of 10 arcmin,

$$I(\vec{r}) = A \exp \left[-\frac{(\vec{r} - \vec{r}_c)^2}{2\sigma_3^2} \right] + B \exp \left[-\frac{(\vec{r} - \vec{r}_4)^2}{2\sigma^2} \right], \quad (4.4)$$

where \vec{r}_c is the position of the centroid of the soft X-ray emission and $\sigma_3 = 10'$. \vec{r}_4 is the position of the additional point source which is left free while fitting, and σ is fixed to the half-width of the PSF in the same way as in model 1.

Fitting the ISGRI profile with a single point source (Model 1), we find that the data are poorly described by this model. In this case, we find that the centroid of the source is displaced compared to the centroid of the 1-10 keV emission by 4.5 arcmin, which confirms the visual impression from the right panel of Fig. 4.4. The best fit is achieved with an ellipse-shaped extended source (Model 3), where $\sigma_1 = 16.8' \pm 0.5'$ and $\sigma_2 = 11.7' \pm 0.4'$. The ellipse inclination angle is $\theta = 61 \pm 4^\circ$. It is interesting to note that the θ angle corresponds roughly to the direction towards the falling sub-cluster around NGC 4839.

Acceptable fits are also achieved with Models 2 and 4. In the case of Model 4, the additional source is found at RA=194.71±0.01 and DEC=27.87±0.01, which is located 6.1 arcmin away from the nearest X-ray point source, the quasar EXO 1256+281. Therefore, association of the SW excess with this object can be rejected at the 90% level.

4.3.2 *XMM-Newton/INTEGRAL* spectrum of the cluster

We also attempted to extract the combined *XMM-Newton*/PN and *INTEGRAL*/ISGRI spectrum of the cluster. To extract the *INTEGRAL* spectrum, we used the method described in Sect. 3.3. In more details, we used the best fit to the hard X-ray morphology of

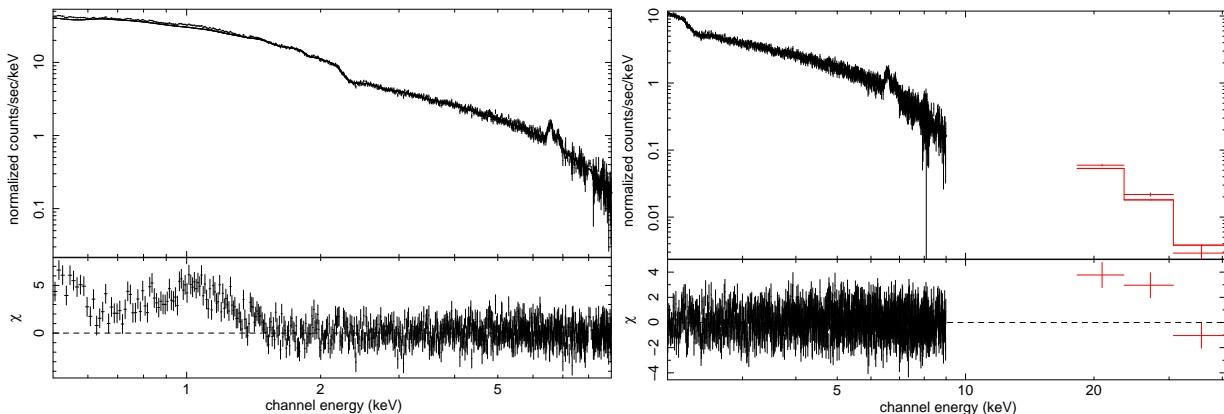


Figure 4.6: Left: *XMM-Newton*/EPN spectrum of the Coma cluster. The solid line shows a MEKAL model at $kT = 7.9$ keV fitted to the 2-10 keV part of the spectrum. Significant residuals are found below 2 keV. Right: *XMM-Newton*/EPN and *INTEGRAL*/ISGRI spectrum of the Coma cluster extracted in the region which gives the best fit to the hard X-ray morphology in order to ensure the best signal-to-noise at high energy. No obvious excess is found in the ISGRI spectrum.

the source presented above (i.e., an ellipse-shaped extended source with $\sigma_1 = 16.8' \pm 0.5'$ and $\sigma_2 = 11.7' \pm 0.4'$) to compute an extended PIF for every pointing, and we fitted the shadowgrams in several different energy bands to this model to extract the spectrum of the source. To constrain the temperature of the source and investigate a possible excess at high energies, we also extracted the 0.5-10 keV *XMM-Newton*/EPN spectrum in the same region to ensure correct cross-calibration between the two instruments.

In order to extract the properties of the thermal component, we fitted the 0.5-10 keV *XMM-Newton* spectrum with a single-temperature MEKAL model. The best fit to the data gives a temperature $kT = 7.1 \pm 0.1$ keV and an iron abundance of 0.22 ± 0.01 compared to the solar value. Even though the quality of the fit ($\chi_{red}^2 = 1.37$ for 905 d.o.f.) is acceptable, several features are seen below 2 keV. Fitting only the 2-10 keV part of the spectrum, we get an excellent fit ($\chi_{red}^2 = 1.02$) with a significantly higher temperature, $kT = 7.9 \pm 0.1$ keV. The left panel of Fig. 4.6 shows the *XMM-Newton* 0.5-10 keV spectrum with a MEKAL model fitted to the 2-10 keV part only. We can see that a significant excess is found at low-energy, even though no absorption model was used. Such a soft excess was already detected in the Coma cluster by Nevalainen et al. (2003). It could be due either to the presence of cooler gas ($kT \lesssim 1$ keV) or to a non-thermal component with a photon index $\Gamma > 1.7$. If the additional component is thermal, it could be the sign of Warm Hot Intergalactic Medium (WHIM) (a low-density medium which should be present in the filaments between clusters), which is actively searched for to the present day. On the other hand, if the emission is non-thermal, it would confirm the possible detections of Soft X-ray/Extreme UV emission which could be due to inverse-Compton scattering of relativistic electrons with the CMB. Unfortunately, the quality of the data is not yet sufficient to distinguish between the two scenarios.

In order to study the high-energy emission, we used only the 2-10 keV part of the spectrum to determine the temperature of the gas and extrapolate it to higher energies. The

right panel of Fig. 4.6 shows the resulting spectrum. Since no significant emission was detected above 30 keV, it is not surprising to see that the ISGRI spectrum does not show any high-energy excess.

Even though we have found that the nearest bright X-ray point source detected in the *XMM-Newton* image, the quasar EXO 1256+281, is not found at the correct position to explain the SW excess emission that we detect in the mosaic image, the angular distance between the centroid of the SW excess and the source (6.1') is close to the half-width of the ISGRI PSF. Therefore, to further investigate the possible association of the excess with this source, we extracted the spectrum of this source from *XMM-Newton* data and compared it with the emission of the SW region. There exists a population of highly-absorbed AGN ($n_H > 10^{23} \text{ cm}^{-2}$), which are quite bright above 20 keV, but are relatively faint below 10 keV because of the very high intrinsic absorption. If EXO 1256+281 is highly-absorbed, it could contribute significantly to the observed hard X-ray flux. However, we found that the X-ray properties of EXO 1256+281 do not show a strong intrinsic absorption. The 0.5-10 keV spectrum of the quasar is well-represented by an absorbed power-law with photon index $\Gamma = 1.9$ and 0.5-10 keV flux of $5 \times 10^{-13} \text{ ergs cm}^{-2} \text{ s}^{-1}$. The column density of the source is consistent with the galactic value. Moreover, there is no evidence for a turn-over of the spectrum. The extrapolation of the model to the ISGRI range falls short of the ISGRI detection by almost 2 orders of magnitude. This proves that the association of the excess with this source is highly unlikely.

4.3.3 Discussion

Our analysis revealed the existence of a region SW of the cluster core which shines more strongly in hard X-rays compared to the soft X-ray emission. To investigate the origin of the hard X-ray emission from this region, we considered three possibilities: a highly-absorbed point source, a hotter region, and diffuse non-thermal emission.

In the case of a highly-absorbed point source, we find that there is no obvious candidate in the high angular-resolution *XMM-Newton* image at the corresponding position. The closest relatively bright X-ray point source is the background quasar EXO 1256+281, which is located 6.1 arcmin away. However, given the ISGRI point source location accuracy of $\sim 1'$ for a source detected with a significance of 10σ , the association of the excess with this source is rejected at the 3σ level. On the other hand, we cannot exclude the possibility that the excess is due to an unknown highly-absorbed source. Indeed, many of the newly-discovered *INTEGRAL* sources have a very high intrinsic absorption, which makes them weak in soft X-rays and much brighter above 20 keV. Besides, it is expected from X-ray background measurements to find a population of highly-absorbed AGN, which would be responsible for the peak at 30 keV in the spectrum of the X-ray background. However, given that the sensitivity of *INTEGRAL* above 20 keV is much lower than the sensitivity of existing instruments in the 1-10 keV band (*XMM-Newton*, *Chandra*), most of the highly-absorbed sources detected by *INTEGRAL* have been identified as well by the lower-energy instruments. Therefore, we conclude that the association of the SW excess with a point source not detected in the 1-10 keV band with *XMM-Newton* is unlikely.

Since we exclude the possibility that the *INTEGRAL* emission in the SW region is due to a highly-absorbed point source, we conclude that the excess found in this region is of diffuse origin. From the same *XMM-Newton* data, Neumann et al. (2003) constructed a 0.5-2.0/2.0-5.0 keV hardness-ratio map of the cluster, which they interpreted as a temperature map (see Fig. 4.7). From this analysis, they report the presence of a very hot ($kT > 10$ keV) region West of the cluster core (designated as "Western Structure" on Fig. 4.7). We note that this region roughly corresponds to the excess region detected by ISGRI. Assuming that the emission comes from a very hot region located SW of the cluster core, we estimated the properties of the gas required to produce the emission detected by ISGRI. Extracting the X-ray flux of the SW region within a radius of 6 arcmin corresponding to the PSF of ISGRI and comparing it to the ISGRI flux of the region in the 18-30 keV band, we find that a plasma temperature of $kT = 12 \pm 2$ keV can produce the excess emission detected by ISGRI. To characterize the density of the gas, we used the emission measure along the line of sight (see Arnaud (2005)),

$$EM(r) = \int n_e^2 dl, \quad (4.5)$$

which can be obtained from the surface-brightness profile $S(\theta)$,

$$EM(r) = \frac{4\pi(1+z)^4 S(\theta)}{\Lambda^{ff}(T)} \text{ with } r = d_A(z)\theta, \quad (4.6)$$

where $d_A(z)$ is the angular diameter distance at the cluster redshift z and $\Lambda^{ff}(T)$ is the emissivity of the gas in a given energy band,

$$\Lambda^{ff}(T) = \int_{\nu_{\min}}^{\nu_{\max}} \epsilon_{\nu}^{ff} d\nu, \text{ where } \epsilon_{\nu}^{ff} = 6.8 \cdot 10^{-38} Z^2 n_e n_i T^{-1/2} e^{-h\nu/kT} \bar{g}_{ff} \text{ ergs s}^{-1} \text{ cm}^{-3} \text{ Hz}^{-1}. \quad (4.7)$$

For a temperature in the 10 – 14 keV range, we calculated an emission measure $0.16 \leq EM \leq 0.26 \text{ cm}^{-6} \text{ pc}$. Assuming that the hot region has an angular size of $\sim 6'$ (similar to the IBIS PSF) at the distance of Coma ($d_A \sim 100 \text{ Mpc}$), we deduce a gas density $n \sim 10^{-3} \text{ cm}^{-3}$. This result is reasonable for a rich cluster like Coma. Therefore, we conclude that the presence of a hot region at $kT = 12 \pm 2$ keV can explain the excess detected by *INTEGRAL* in the SW region.

Alternatively, the excess emission detected in the SW region could be due to non-thermal emission from relativistic particles. If a strong non-thermal component is present in this region, it could bias the temperature measurement based on the hardness ratio, since the non-thermal component would contribute more strongly in the hard band. Hence, this interpretation does not contradict the works of Neumann et al. (2003) and Arnaud et al. (2001). If we assume that the non-thermal emission comes from inverse-Compton scattering from the same electrons that produce the synchrotron radio halo, and if the strength of the magnetic field does not significantly vary within the inner regions of the cluster, then the morphology of the radio and of the hard X-ray emissions is expected to be strongly correlated.

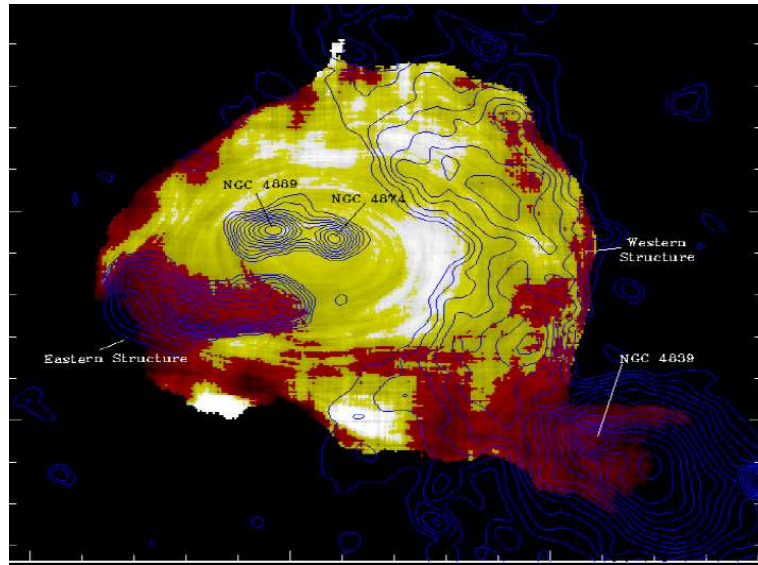


Figure 4.7: *XMM-Newton/MOS temperature map of the Coma cluster (from Neumann et al. (2003)). Red regions correspond to temperatures below 8 keV, yellow regions to $8 \text{ keV} < kT < 10 \text{ keV}$ and white regions to $kT > 10 \text{ keV}$.*

Deiss et al. (1997) presented the results of an observation of the radio halo Coma C at 1.4 GHz with the Effelsberg 100-m telescope (a large, single-dish antenna which is especially efficient to study weak extended radio sources). Interestingly, they found that the radio emission is displaced by ~ 4 arcmin compared to the maximum of the X-ray emission. To determine if the radio and hard X-ray emissions are correlated, we used the 1.4 GHz radio map of Deiss et al. (1997) and compared the radio surface brightness contours with the *INTEGRAL* SW excess (Eckert et al. 2007b). Figure 4.8 shows the resulting image. We can see that the peak of the radio emission coincides very well with the position of the *INTEGRAL* excess. Namely, the centroid of the 1.4 GHz radio emission is found at RA=194.76 and Dec=+27.93 (90% error radius of 1.2 arcmin), 2.5 arcmin away from the centroid of the *INTEGRAL* SW excess (RA=194.73, Dec=+27.89 with a 90% error radius of 3 arcmin). The position of the two peaks is compatible.

Assuming that the excess emission detected by *INTEGRAL* in the SW region is non-thermal, and that the majority of the non-thermal emission comes from this region, one can use the radio spectrum of the Coma C source together with the *INTEGRAL* flux measurement of the SW region in the 18-30 keV band to constrain the magnetic field in this region of the cluster (see Sect. 2.7.3). To construct the Spectral Energy Distribution (SED) of the non-thermal component, we used a compilation of radio measurements between 100 MHz and 5 GHz presented by Thierbach et al. (2003) together with our hard X-ray measurement. To model the non-thermal component, we assumed a relativistic electron population with a spectral index of 2.0 and an exponential high-energy cut-off, in a magnetic field B . We discretized the electron population as a superposition of monochromatic distributions, computed the synchrotron/inverse-Compton spectra for each discretized distribution according to Blumenthal & Gould (1970) and summed the resulting spectra. Figure 4.9 shows the resulting SED with models computed for different

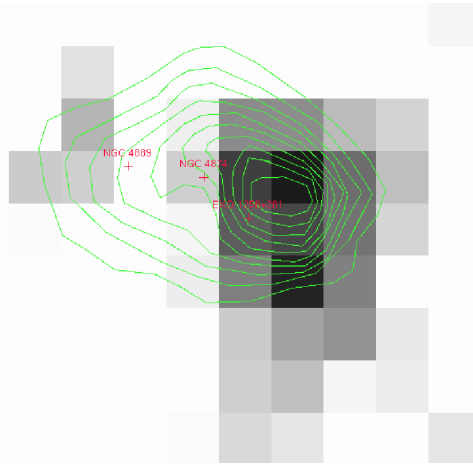


Figure 4.8: *INTEGRAL* South-West excess image compared to 1.4 GHz radio contours from Deiss et al. (1997). The position of the radio peak is remarkably well correlated with the *INTEGRAL* excess.

values of B and E_{cut} . We can see that a synchrotron/IC model with a magnetic field $B \sim 0.1 \mu G$ and an electron cut-off energy $E_{cut} \sim 1$ GeV can reproduce the observed radio and hard X-ray properties. The magnetic field value is consistent with the value $B \sim 0.16 \mu G$ derived by Fusco-Femiano et al. (1999) from the *BeppoSAX* flux of the non-thermal tail in the X-ray spectrum. However, it is an order of magnitude lower than the magnetic field values derived from Faraday rotation measure (see Sect. 2.7.1). In the specific case of Coma, this discrepancy could be explained by the fact that the radio/IC emission is displaced compared to the center of the cluster. Indeed, it is reasonable to think that the magnetic field strength is not uniform within the cluster and decreases towards lower-density regions, where the *INTEGRAL* excess is found. Therefore, the discrepancy between the magnetic field strengths derived with different methods would be resolved if the magnetic field shows a steep radial profile. In any case, this treatment relies on the assumption that the origin of the excess flux in the SW region is non-thermal, which cannot be firmly established, since the source was not detected above 30 keV, and therefore no spectral information on the region could be extracted.

4.4 New results based on OSA 7.0

The OSA software version 7.0 was released in September 2007, bringing several important improvements to the calibration of the instruments. Concerning the IBIS instrument, a better understanding of the low-energy threshold of the ISGRI detector ensures a correct energy calibration down to 17 keV for spectral extraction and 15 keV for imaging. New background maps were also computed, allowing for a better subtraction of the background, and hence better imaging results. The JEM-X software was also significantly improved. In particular, the imaging software was greatly improved, allowing for artifact-free mosaics. However, the status of the JEM-X spectral extraction software is still problematic. Indeed, in a field containing several sources, the spectra of weak sources will be strongly contaminated by the presence of stronger sources. For this reason, it is currently better

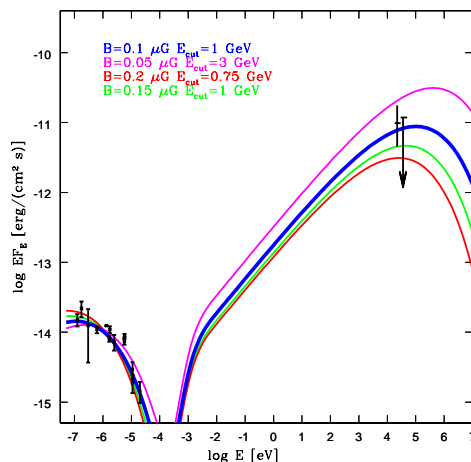


Figure 4.9: Spectral Energy Distribution of the non-thermal emission assuming that the INTEGRAL SW excess comes from inverse-Compton scattering of relativistic electrons with the CMB. The radio data are from Thierbach et al. (2003). The color curves show numerical models for the SED with different values of magnetic field B and electron cut-off energy E_{cut} .

to create JEM-X mosaics in several energy bands and extract spectra directly from the mosaics. To take advantage of the calibration improvements introduced in OSA 7.0, we performed a new analysis of ISGRI and JEM-X data on the Coma cluster.

4.4.1 Analysis of the morphology

We created ISGRI mosaics in the 15-20, 20-30, 30-60 and 60-200 keV bands, and JEM-X mosaics in the 3-10 and 10-18 keV bands, which allows us to get a broad-band coverage of the source. Since the field-of-view (FOV) of JEM-X is much smaller than that of IBIS and half of the observation was performed in standard 5×5 dithering mode, the available amount of data is much smaller (250 ksec). Figure 4.10 shows the resulting ISGRI images of the source in the 4 energy bands. The source is detected with high significance ($\sim 10\sigma$) in the first two bands. Interestingly, the source is very close to detection (4.2σ) in the 30-60 keV band. This is a real improvement compared to the OSA 6.0 analysis, where the source was not detected at all in this energy band. We can see that the excess is found very close to the position of the radio peak, which could favour the non-thermal interpretation of the SW excess. However, the detection significance is still not sufficient to make firm conclusions on the origin of the hard X-ray emission from the SW region. In the highest energy band (60-200 keV), the source is still not detected.

In addition, the new analysis of the data with OSA 7.0 allowed us to detect the source below 10 keV with JEM-X (see the left panel of Fig. 4.11). Compared to the PSF of JEM-X, the source is very extended (over 25 arcmin full extent in the JEM-X image). The morphology of the source is almost circular, and corresponds very well with the *XMM-Newton*/PN contours, which shows that JEM-X has the capabilities required to study the

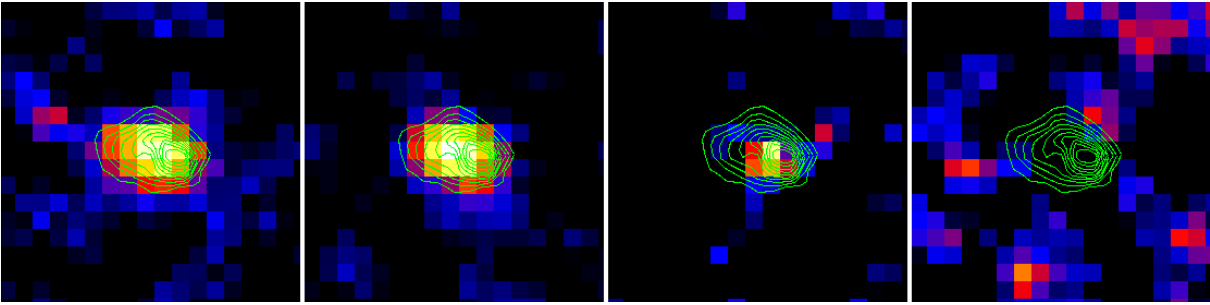


Figure 4.10: *IBIS/ISGRI OSA 7.0 significance images of the Coma cluster in the 15-20, 20-30, 30-60 and 60-200 keV bands (from left to right). The green contours show the 1.4 GHz radio emission.*

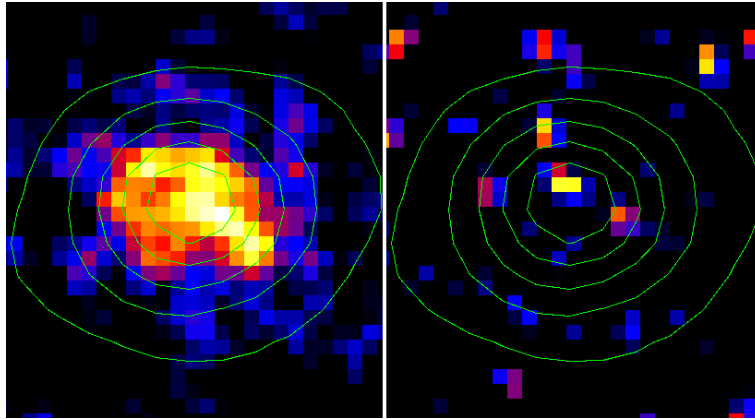


Figure 4.11: *INTEGRAL/JEM-X significance images of the Coma cluster in the 3-10 (left) and 10-18 keV bands. The green contours represent the surface brightness profile of the source extracted from XMM-Newton/PN. In the lower energy range, the full extent of the source is about 25 arcmin. In the higher energy band, the source is still not detected, but a 3σ excess is found close to the centre of the XMM-Newton emission.*

morphology of the source. On the other hand, the existing amount of data unfortunately did not allow us to detect the source in the 10-18 keV, where the input of JEM-X could be crucial (right panel of Fig. 4.11). A 3σ excess is found close to the center of the cluster, so with the addition of more data, we will be able to detect the source in this band as well.

Since the improvements in the analysis software allowed us to detect the source at higher energies, we created a mosaic image over a broad energy band (15-60 keV) to ensure the best possible signal-to-noise, and we performed again the subtraction between the hard and soft X-ray images, in order to investigate further the emission from the SW region. Figure 4.12 shows the equivalent of Fig. 4.8 with OSA 7.0. The correlation between the hard X-ray and the radio morphology is confirmed by the new analysis.

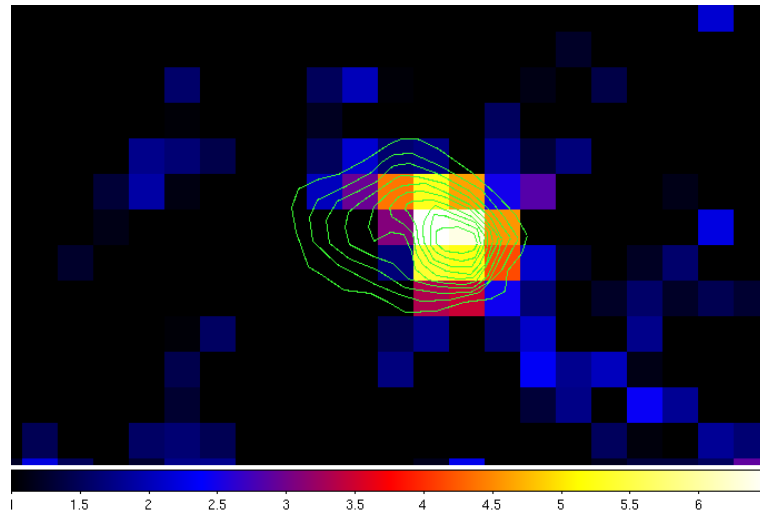


Figure 4.12: *INTEGRAL/ISGRI 15-60 keV significance OSA 7.0 image subtracted for the 1-10 keV XMM-Newton/PN profile. The contours show the radio emission at 1.4 GHz from Deiss et al. (1997).*

4.4.2 Determining the temperature of the South-West region

Obviously, to determine the nature of the hard X-ray emission from this region, it is necessary to know the temperature of the gas in this region with the best possible accuracy. However, if a strong non-thermal component is present in this region, it could bias the temperature which would be measured by fitting the *XMM-Newton* data with a single MEKAL model. Therefore, we seek a way to measure the temperature of the gas without relying on the continuum. Such a tool is provided by the temperature-dependent flux ratio of the emission lines due to Fe K α transition: iron XXV (helium-like) at 6.5 keV and XXVI (hydrogen-like) at 6.8 keV (see Nevalainen et al. (2003) for details on the method). These emission lines are well-detected in the high-statistics PN data, which allows us to measure the intensity of both lines independently. Figure 4.13 from Nevalainen et al. (2003) shows the dependence of the line ratio on the temperature of the gas. We can see that the line ratio is a very steep function of the temperature, and therefore it can be a very useful tool to measure gas temperatures.

In order to constrain the temperature of the gas in the SW region, we constructed a temperature map of the cluster based on FeXXV/FeXXVI line ratio. We extracted *XMM-Newton*/PN spectra in 5×5 arcmin² boxes corresponding to ISGRI sky pixels, and measured the relative intensity of the two emission lines in the different boxes. Unfortunately, several regions with lower surface brightness have been observed for a rather short exposure time (~ 15 ksec) with *XMM-Newton*, so in some cases the errors on the temperatures measured through FeXXV/FeXXVI line ratio are rather large. The 1σ errors on the temperature span between 0.3 keV in the center up to more than 1 keV in the low surface-brightness regions. Figure 4.14 shows the corresponding temperature map of Coma. The central temperature of ~ 8.3 keV is consistent with the measurements based on spectral fitting. The region SW of the cluster core indeed appears slightly hotter than the core

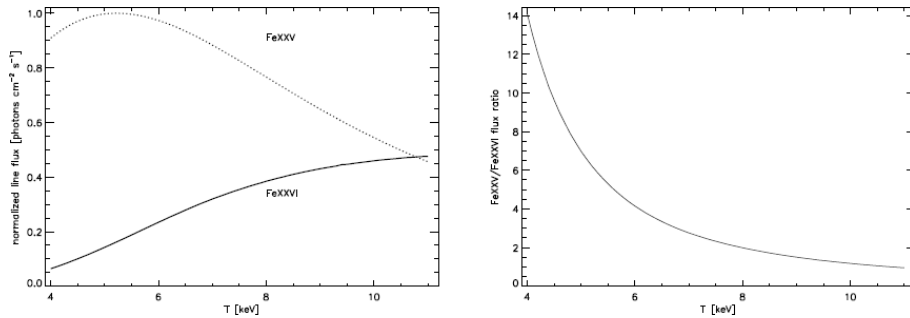


Figure 4.13: Calibration of the FeXXV/FeXXVI line ratio method (figure from Nevalainen et al. (2003)). Left: Dependence of the relative intensity of both lines on the gas temperature. Right: FeXXV/FeXXVI line ratio as a function of temperature.

($kT \sim 9$ keV). In particular, box #24 is hotter ($kT \sim 10.3$ keV), but the error on the measurement is rather large (~ 1 keV). Moreover, the *INTEGRAL* excess is centred on boxes #13,14,18 and 19, which are not significantly hotter than the mean temperature of 8.5 keV.

To summarize, it appears that the short *XMM-Newton* exposure on the SW region is not yet sufficient to determine the temperature of the gas in this region with a good enough accuracy. However, it seems that the region where the *INTEGRAL* excess is seen is indeed slightly hotter than the center of the cluster, but that this temperature (~ 9 keV) cannot explain the whole emission detected by *INTEGRAL*. A longer observation of the region with *XMM-Newton* would allow us to refine our measurement of the temperature with the FeXXV/FeXXVI line ratio and fix the thermal component to investigate a possible non-thermal component.

4.4.3 ISGRI spectra of the cluster

We also took advantage of the better energy calibration and background modeling introduced in OSA version 7.0 to extract new spectra of the cluster. In Sect. 4.3.1, we showed that although the source is clearly extended for ISGRI, it can be reasonably well described by a superposition of 2 point sources. Therefore, we used the OSA standard spectral extraction software, `ii_spectra_extract`, to extract the spectrum of the cluster represented as the superposition of 2 point sources, one at the maximum of the 1-10 keV emission, and the other at the centroid of the SW excess. The angular distance between the two positions is 14 arcmin, which is slightly more than the IBIS PSF, so normally there should be no contamination between the two spectra. In order to confirm this, we simulated ISGRI data for two point sources separated by an angular distance of 14 arcmin with very different spectral shape, and extracted the spectrum of the simulated data in the standard way. The OSA 7.0 software reproduced the normalization and spectral shape of the two simulated sources accurately, and therefore we conclude that it is possible to extract spectra with minimal contamination even for sources as close as 14 arcmin.

Fitting the two spectra with a single bremsstrahlung model, we find that the emission from the SW region is significantly harder than that of the center of the cluster. The best fit to the spectrum of the central region gives $kT = 7.1_{-0.9}^{+1.1}$, in agreement (within 1σ) with the

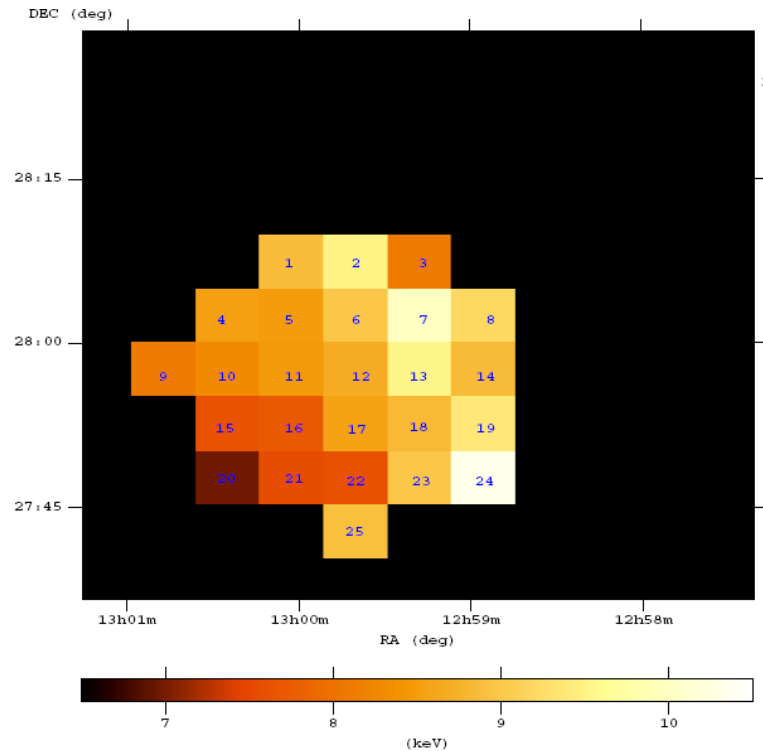


Figure 4.14: Temperature map of the Coma cluster based on $FeXXV/FeXXVI$ line ratio (figure courtesy of Jukka Nevalainen).

temperature extracted from the line ratio. In the SW region, the fit gives $kT = 10.7^{+2.5}_{-1.8}$ keV. This temperature is slightly higher, but consistent with the temperature of 9.0 keV measured through the $FeXXV/FeXXVI$ line ratio. In this case, we note that the source is possibly detected in the 40-60 keV band (at the 3σ level) and the 60-120 keV band (2σ). The quality of the fit ($\chi^2_{red} = 1.49$ for 5 d.o.f.) is acceptable, but not optimal. Fixing the temperature of the bremsstrahlung at $kT = 9.0$ keV as found from *XMM-Newton* data, we find a 2σ excess at high-energies. Such an excess is not seen in the spectrum of the central region. Figure 4.15 shows the spectrum of the SW region extracted with OSA 7.0, fitted by a bremsstrahlung model at $kT = 9.0$ keV (dashed red line) plus a power-law (dashed green) with a fixed photon index $\Gamma = 2.0$.

Although the high-energy excess in the spectrum of the SW region is not yet significant, a comparison with the spectrum of the central region clearly indicates that the spectrum of the region is harder. This is another indication in favour of the non-thermal interpretation of the excess emission from this region.

4.4.4 Discussion

With the currently available data, it is not yet possible to firmly distinguish between the thermal and non-thermal interpretations of the hard X-ray emission discovered by *INTEGRAL* South-West of the cluster core. In order to discover the origin of the emission, it is crucial to get the best possible knowledge of the gas temperature. With the help

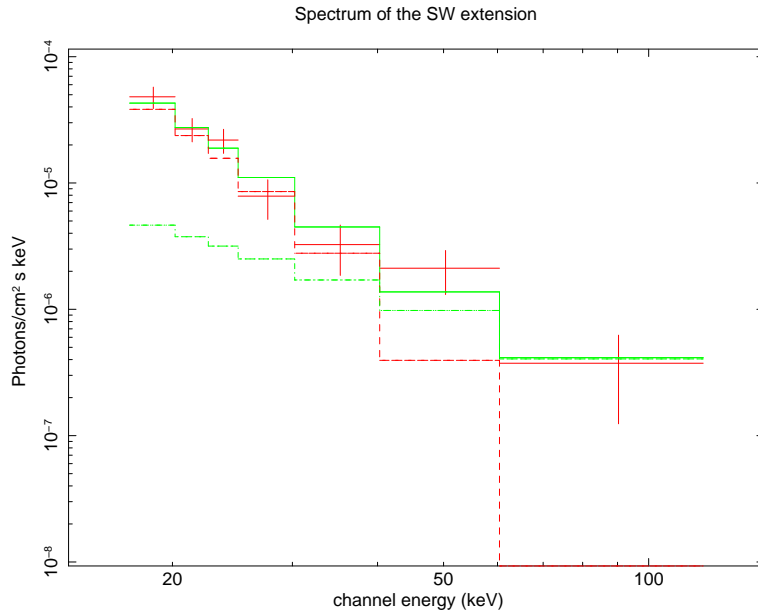


Figure 4.15: *ISGRI OSA 7.0 spectrum of the SW region, fitted by a thermal bremsstrahlung (dashed red line) plus a power-law with a fixed photon-index $\Gamma = 2.0$ (dashed green line). The temperature of the thermal component was fixed to the value $kT = 9.0$ keV measured through the *XMM-Newton*/PN FeXXV/FeXXVI line ratio.*

of the FeXXV/FeXXVI line ratio, which provides an un-biased tool to measure the temperature of the gas in the SW region, we found that this region is indeed slightly hotter (~ 9.0 keV) than the central region, and therefore, a part of the excess can be explained by the presence of hot gas. However, a temperature of 9.0 keV would not be sufficient to explain completely the hard X-ray emission detected by *INTEGRAL*. The relatively short *XMM-Newton* exposure time on the SW region does not allow us yet to determine the temperature in this region with sufficient accuracy. In order to achieve this goal, we plan to propose an additional observation of the region with *XMM-Newton* for the next Announcement of Opportunity (AO).

The new analysis of the *INTEGRAL* data with the OSA 7.0 software also brought several elements to the discussion. In particular, the detection of the source in the 30-60 keV band as well as the detection of the source with JEM-X are crucial to understand the origin of the emission. The new ISGRI image of the excess region allowed us to refine the position of the excess, and we have seen that the emission correlates extremely well with the radio emission at 1.4 GHz. If this correlation is real, it would demonstrate in a very elegant way that the excess emission is non-thermal, and that it is due to inverse-Compton scattering of GeV electrons with CMB photons. Moreover, the difference of spectral shape between the central and SW regions, which reveals a 2σ excess at high-energies in the SW region, but no excess in the central region, also points towards the non-thermal interpretation. However, the signal-to-noise above 30 keV is not yet sufficient to rule out the thermal scenario. Therefore, we proposed another 1 Ms observation of the cluster for the *INTEGRAL* AO6, which was accepted by the *INTEGRAL* Time Allocation Committee (TAC) as a grade B proposal. The new observation, which has not been scheduled yet, will definitely allow us

to discriminate between the two interpretations. If we find that the excess is non-thermal, we will be able to unambiguously measure the magnetic field in the cluster, and find a possible particle acceleration site located in the region where the gas of the NGC 4839 sub-cluster interacts with that of the main cluster.

4.5 Conclusion

Since it is the closest rich galaxy cluster and it shows obvious signs of merging activity, the Coma cluster is an excellent candidate for the detection of non-thermal hard X-ray emission. Using *BeppoSAX* observations of the cluster, Fusco-Femiano et al. (1999) claimed the detection of such emission. However, an independent analysis of the same data (Rossetti & Molendi 2004) did not confirm the result. In order to investigate this point, we analyzed a 1 Ms *INTEGRAL* observation of the cluster with *INTEGRAL*. Although it is not yet possible for us to confirm the existence of a non-thermal excess, we resolve the source spatially, and we find evidence for a region South-West (SW) of the cluster core which shows excess emission in hard X-rays compared to the extrapolation of the 1-10 keV surface brightness profile. Interestingly, this extension corresponds to the direction of the falling sub-cluster around NGC 4839. To investigate the origin of the excess, we considered three different possible origins for the emission of this region: an additional X-ray point source under the form of an obscured Active Galactic Nucleus (AGN), the presence of hotter gas in this region of the cluster, and diffuse non-thermal emission.

Although we cannot exclude the possibility that the emission comes from a Compton-thick AGN ($n_H \gtrsim 10^{24} \text{ cm}^{-2}$) which would be completely invisible in the soft X-ray range, we find that there is no obvious counterpart for such an object, and that the only possible X-ray counterpart, the quasar EXO 1256+281, cannot explain the hard X-ray emission from this region. Therefore, we conclude that a significant contamination of the spectrum by a point source is unlikely. This indicates that the emission from the SW region is probably of diffuse origin. If the emission comes from the presence of a very hot region in the cluster, we find that a gas at the temperature $kT = 12 \pm 2 \text{ keV}$ can explain the observed properties of the region. Obviously, an accurate measurement of the temperature with another instrument is necessary to check this hypothesis. In particular, the FeXXV/FeXXVI line ratio, which allows us to measure the temperature of the gas without relying on the continuum, can be an important tool to constrain the temperature of the gas. Using existing *XMM-Newton* data, we presented a temperature map of the cluster, which indeed shows that the temperature of the gas in the SW region is slightly higher than the central value. However, the rather low temperature difference ($\sim 9 \text{ keV}$ instead of 8.1 keV) is probably not sufficient to explain completely the excess emission detected by *INTEGRAL* in this region. In any case, the uncertainty on the temperature value is still too large to make final conclusions on this scenario. A further observation of the cluster with *XMM-Newton*, allowing for a much improved signal-to-noise in the iron line intensity measurements, is required to settle this issue.

Recently, Lutovinov et al. (2008) presented a complementary analysis of the same *INTEGRAL* data set with a different software package. They confirm the extension of the source towards the NGC 4839 sub-cluster and also conclude with good confidence that

the contribution of point sources to the observed emission is negligible. Assuming that the emission is completely thermal, they also combine the *INTEGRAL* image with earlier *ROSAT* observations to derive a temperature map of the cluster. The resulting temperature map nicely confirms our result on the temperature of the SW region. Finally, they also extracted the total spectrum of the cluster in order to investigate a possible non-thermal component. However, for combination with an existing *RXTE/PCA* spectrum they extract the spectrum over a full 1° circle corresponding to the PCA field-of-view. Using such a large region with ISGRI is probably not a good idea, since the sensitivity of the instrument drops quickly for very extended source. As a result, their flux measurement in the hard band (1.6σ in the 44-107 keV band?) is affected by very large uncertainties, and any possible non-thermal excess is lost.

Finally, we presented the results of a new analysis of the data with the latest OSA software, version 7.0. Interestingly, we find a 4.2σ detection in the 30-60 keV band, where according to the *BeppoSAX* measurement 60% of the flux should be non-thermal. Comparing again the hard X-ray emission with the 1-10 keV profile, we find that the excess emission in the SW correlates extremely well with the radio emission at 1.4 GHz, which is also slightly displaced compared to the thermal X-ray emission. Such a correlation is actually expected if the hard X-ray emission from this region is non-thermal. If this correlation is real, it provides an elegant confirmation of the non-thermal nature of the excess. Moreover, it proves the inverse-Compton nature of the non-thermal hard X-ray emission, which has been debated because of the low magnetic-field value deduced from the radio/HXR ratio. Unfortunately, we cannot yet confirm this result through a significant excess in the spectra. In order to confirm this result, we proposed an additional observation of the cluster with *INTEGRAL*, which has been accepted by the Time Allocation Committee as a grade B proposal. The additional observing time will allow us to definitely determine the origin of the emission.

4.6 Scientific article on the Coma cluster

A&A 470, 835–841 (2007)
 DOI: 10.1051/0004-6361:20077268
 © ESO 2007

**Astronomy
&
Astrophysics**

South-West extension of the hard X-ray emission from the Coma cluster

D. Eckert^{1,2}, A. Neronov^{1,2}, T. J.-L. Courvoisier^{1,2}, and N. Produit^{1,2}

¹ INTEGRAL Science Data Centre, 16 Ch. d'Ecogia, 1290 Versoix, Switzerland
 e-mail: Dominique.Eckert@obs.unige.ch

² Geneva Observatory, University of Geneva, 1290 Sauverny, Switzerland

Received 9 February 2007 / Accepted 14 May 2007

ABSTRACT

Aims. We explore the morphology of hard (18–30 keV) X-ray emission from the Coma cluster of galaxies.

Methods. We analyse a deep (1.1 Ms) observation of the Coma cluster with the ISGRI imager on board the *INTEGRAL* satellite.

Results. We show that the source extension in the North-East to South-West (SW) direction ($\sim 17'$) significantly exceeds the size of the point spread function of ISGRI, and that the centroid of the image of the source in the 18–30 keV band is displaced in the SW direction compared to the centroid in the 1–10 keV band. To test the nature of the SW extension we fit the data assuming different models of source morphology. The best fit is achieved with a diffuse source of elliptical shape, although an acceptable fit can be achieved assuming an additional point source SW of the cluster core. In the case of an elliptical source, the direction of extension of the source coincides with the direction toward the subcluster falling onto the Coma cluster. If the SW excess is due to the presence of a point source with a hard spectrum, we show that there is no obvious X-ray counterpart for this additional source, and that the closest X-ray source is the quasar EXO 1256+281, which is located 6.1' from the centroid of the excess.

Conclusions. The observed morphology of the hard X-ray emission clarifies the nature of the hard X-ray “excess” emission from the Coma cluster, which is due to the presence of an extended hard X-ray source SW of the cluster core.

Key words. galaxies: clusters: individual: Coma cluster – X-rays: galaxies: clusters – gamma rays: observations

1. Introduction

Clusters of galaxies are the biggest bound structures of the universe, and, according to the hierarchical scenario of structure formation, the latest to form. They are filled by a hot (10^8 – 10^9 K) plasma, called Intra Cluster Medium (ICM), and thus radiate in soft X-ray bands through thermal Bremsstrahlung.

Since clusters of galaxies are the latest and biggest structures to form, we expect some of them to be still forming, and experiencing major merging events with smaller clusters. This is the case of the Coma cluster, that is currently merging with the NGC 4839 group. In such events, the merging of the ICM of the two clusters creates shock fronts in which theory predicts that a large population of particles would be accelerated to high energies (Sarazin 1999). This phenomenon should then produce a reheating of the gas and create a higher temperature plasma that would radiate more strongly in hard X-rays. Alternatively, interaction of the population of mildly relativistic electrons that produce the halos of galaxy clusters via synchrotron radiation (Feretti & Giovannini 2007) with the Cosmic Microwave Background would then produce hard X-ray emission through inverse Compton processes, and thus add a power-law tail to the spectrum in the hard X-ray domain. Another possible model involves a population of multi-TeV electrons that would radiate in hard X-rays through synchrotron emission (Timokhin et al. 2004). Detection of this hard X-ray excess would help in learning more about the cosmic ray population detected by radio observations. Furthermore, characterization of the morphology of the hard X-ray emission would bring a possible identification of acceleration sites, and since clusters of galaxies are one of the

few possible candidates for acceleration of cosmic rays at high energies, it would bring important information on the origin of cosmic rays.

Recent reports of detection of a hard X-ray excess by *Beppo-SAX* (Fusco-Femiano et al. 2004) and *RXTE* (Rephaeli & Gruber 2002) in the Coma cluster appear to confirm the existence of a high energy tail of the spectrum of merging clusters, and thus prove the existence of particle acceleration sites in these clusters. However, these detections are quite weak and controversial (Rossetti & Molendi 2004), and since the hard X-ray instruments on both *Beppo-SAX* and *RXTE* are non-imaging, contamination by very hard point sources inside the cluster cannot be excluded (e.g. by the central galaxy NGC 4874, NGC 4889 or the QSO EXO 1256+281). In addition, no information on the morphology of the hard X-ray emission was obtained. Renaud et al. (2006a) presented an analysis of a first 500 ks set of *INTEGRAL* data and were not able to confirm the presence of a hard X-ray excess or to sensibly constrain the hard X-ray morphology of the source.

In this paper, we use the imaging capabilities of the IBIS/ISGRI instrument (Lebrun et al. 2003) to extract information on the hard X-ray emission of the Coma cluster. In Sect. 3, we present the results of our imaging analysis of the ISGRI data, and compare them with existing *XMM-Newton* data in the soft X-ray domain. In Sect. 4.1, we describe a method to analyse extended sources with a coded mask instrument to extract quantitative flux measurements, and apply it to the case of the Coma cluster. In Sect. 5, we present a combined *XMM/INTEGRAL* spectrum of the cluster. Finally, discussion of our results is presented in Sect. 6.

Table 1. INTEGRAL observation log on the Coma cluster.

INTEGRAL revolution number	Observation dates	No. of pointings	Observing time [ks]
0036	Jan. 29–31, 2003	63	140.1
0071-72	May 14–18, 2003	135	304.5
0274-75	Jan. 10–15, 2005	57	202.4
0317-18	May 19–25, 2005	99	333.4
0324-25	Jun. 9–11, 2005	47	164.5
			1144.9

2. Data

Our analysis covered 401 Science Windows (ScWs) of public data, for a total of 1.1 Ms of observation. We analysed the data with the latest release of the Offline Scientific Analysis (OSA), version 6.0, and eliminated ScWs with a high background level. We used the remaining data to create a mosaic image in the standard way. Table 1 gives the log of the observation.

The *XMM-Newton* image is produced using the data of the PN camera taken in June 2000 during the Coma mosaic observation (Briel et al. 2001). We used the SAS software version 6.5 and the background subtraction method from the Birmingham group (Read & Ponman 2003) to analyse the data.

3. Imaging analysis in the hard X-ray domain

3.1. Mosaic image of the Coma cluster

Figure 1 shows a mosaic image in the 18–30 keV band extracted with the standard OSA 6.0 tools, using the data described in Table 1, with 3–10 significance contours. For comparison, we show in the inset in the right bottom corner of the image a mosaic image of a point source (NGC 4388) produced using a comparable amount of data and normalized so that the amplitude of the brightest pixel is the same as in the case of Coma cluster.

A first look at the image indicates that the Coma cluster source is extended. It is not surprising, since the angular size of the core of the Coma cluster in 1–10 keV energy band is $D \approx 20'$ (Schuecker et al. 2004), which is larger than the size of the point spread function (PSF) of ISGRI ($2\sigma = 12'$, which is the angle subtended by a 11.2 mm mask hole at a distance of 3200 mm).

A comparison of the 18–30 keV image with the image in 1–10 keV band obtained with *XMM-Newton* is shown in Fig. 2. The left panel of this figure shows the *INTEGRAL* image with the overlaid contours obtained by smoothing the *XMM-Newton* image with the ISGRI PSF (modelled as a Gaussian of full width $12'$). The right panel of the figure shows the residuals of the *INTEGRAL* mosaic image after subtraction of the smoothed *XMM-Newton* image, renormalized in a way that the difference between *INTEGRAL* and *XMM-Newton* flux cancels at the maximum of the *XMM-Newton* emission. One can clearly see that significant residuals are left in the South-West (SW) part of the *INTEGRAL* source after the subtraction. This indicates that the hard X-ray source detected by *INTEGRAL* is more extended in the SW direction than the *XMM-Newton* source.

3.2. Source morphology from mosaic image

To clarify the nature of the SW extension of the *INTEGRAL* source we attempted to fit the ISGRI image assuming different

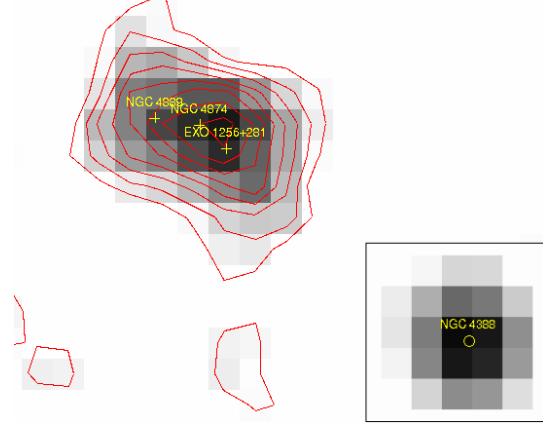


Fig. 1. Standard OSA 6.0 significance image of the Coma cluster with ~ 1.1 Ms of data in the 18–30 keV energy band. Significance contours from 3 to 10σ in steps of 1σ are overlaid in red. The position of the 3 brightest X-ray point sources is shown. For comparison, the inset in the bottom right corner shows a mosaic image of a known point source in the same field, NGC 4388.

surface brightness distributions $I(\mathbf{r})$ of the hard X-ray source. Specifically, we consider the following possibilities:

- **Model 1:** a single point source given by a Gaussian with the half-width equal to the size of the PSF of ISGRI,

$$I(\mathbf{r}) = A \exp\left[-\frac{(\mathbf{r} - \mathbf{r}_0)^2}{2\sigma^2}\right], \quad (1)$$

where \mathbf{r}_0 is the central vector position of the source which is left free while fitting;

- **Model 2:** a superposition of two point sources with overlapping PSFs,

$$I(\mathbf{r}) = A \exp\left[-\frac{(\mathbf{r} - \mathbf{r}_1)^2}{2\sigma^2}\right] + B \exp\left[-\frac{(\mathbf{r} - \mathbf{r}_2)^2}{2\sigma^2}\right], \quad (2)$$

where $\mathbf{r}_1, \mathbf{r}_2$ are the positions of the two sources which are left free;

- **Model 3:** an ellipse-shaped extended source with the surface brightness profile

$$I(\mathbf{r}) = A \exp\left[-\frac{((\mathbf{r} - \mathbf{r}_3) \cdot \mathbf{n})^2}{2\sigma_1^2} - \frac{((\mathbf{r} - \mathbf{r}_3) \times \mathbf{n})^2}{2\sigma_2^2}\right], \quad (3)$$

where \mathbf{n} is the unit vector in the direction of the major axis of the ellipse, \mathbf{r}_3 is the position of the centroid of the ellipse and σ_1, σ_2 are the sizes of the major and minor axes of the ellipse which are all left free while fitting;

- **Model 4:** a superposition of an extended source with morphology of the core of Coma cluster in the 1–10 keV energy band (the surface brightness profile described by a Gaussian convolved with the ISGRI PSF, i.e. a Gaussian with a half-width of $10'$) and of an additional point source

$$I(\mathbf{r}) = A \exp\left[-\frac{(\mathbf{r} - \mathbf{r}_c)^2}{2\sigma_3^2}\right] + B \exp\left[-\frac{(\mathbf{r} - \mathbf{r}_4)^2}{2\sigma^2}\right], \quad (4)$$

where \mathbf{r}_c is the position of the centroid of the soft X-ray emission and $\sigma_3 = 10'$. \mathbf{r}_4 is the position of the additional point source which is left free while fitting, and σ is fixed to the half-width of the PSF in the same way as in model 1.

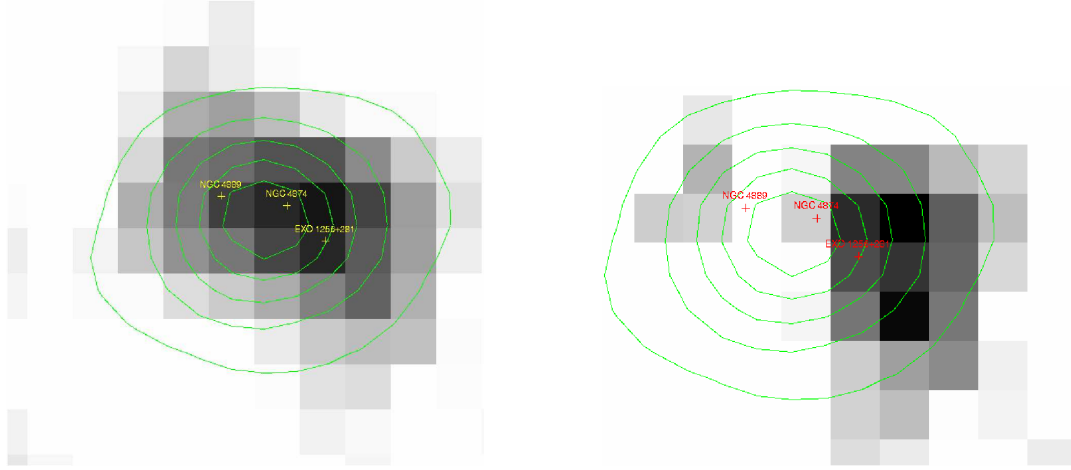


Fig. 2. *Left:* *INTEGRAL* mosaic image with contours from *XMM-Newton* overlaid. The *XMM-Newton* image is smoothed with a Gaussian of the width $12'$ to match the angular resolution of *INTEGRAL*. *Right:* the residuals after the subtraction of the *XMM-Newton* profile from the *INTEGRAL* image (see text). The South-West excess in the residual image is apparent.

We fitted the 21×21 pixels ($105' \times 105'$) part of the image around the catalog position of the Coma cluster minimizing the χ^2 of the fit, defined as

$$\chi^2 = \sum_{i,j=1}^{21} \frac{(\text{IMG}(i, j) - I(i, j))^2}{\text{VAR}(i, j)} \quad (5)$$

where $\text{IMG}(i, j)$ and $\text{VAR}(i, j)$ are the values of intensity and variance in a given image pixel (i, j) . The best fit results for the four models are shown in Fig. 3.

Fitting the intensity image with a single point source (Model 1), we find that the source position (the vector \mathbf{r}_0 in (1)) is shifted compared to the centroid of the *XMM-Newton* image in the SW direction by $\Delta\text{RA} = 3.9'$, $\Delta\text{Dec} = 0.5'$. The rather high reduced χ^2 of the fit with a point source model, $\chi_{\text{red}}^2 = 1.91$ (for 437 degrees of freedom) indicates that the single point source model does not provide a good description of the source morphology, confirming the analysis shown in Fig. 2.

Fitting the source morphology with a two point sources (Model 2), one finds a better reduced $\chi_{\text{red}}^2 = 1.33$. The two point sources model provides the possibility of finding the direction of extension of the source. Namely, the best fit is provided by the model in which the two point sources are situated at $\text{RA}_1 = 195.04 \pm 0.01$, $\text{Dec}_1 = 28.00 \pm 0.01$ and $\text{RA}_2 = 194.77 \pm 0.01$, $\text{Dec}_2 = 27.90 \pm 0.01$. The angular distance between the two point sources is $d_{12} = |\mathbf{r}_1 - \mathbf{r}_2| = 15.3' \pm 0.6'$. The ratio of intensities of the two sources is $A/B = 0.84$. The distance between the two point sources is larger than the size of the PSF of ISGRI, which confirms again that the source cannot be described by Model 1.

The best fit to the morphology of the source is found when fitting the image with the model of an elliptically-shaped source (Model 3). The fit results in a reduced $\chi_{\text{red}}^2 = 1.23$. The parameters of the best fit model are $\sigma_1 = 16.8' \pm 0.5'$, $\sigma_2 = 11.7' \pm 0.4'$ and the coordinates of the centroid of the ellipse, \mathbf{r}_3 , $\text{RA} = 194.89 \pm 0.01$, $\text{Dec} = 27.94 \pm 0.01$. The direction of the major axis of the ellipse, \mathbf{n} , is inclined at the angle $\theta = 61 \pm 4^\circ$. One can see that the fitted position of the centroid of the ellipse is shifted in the same direction as the position of the single point source

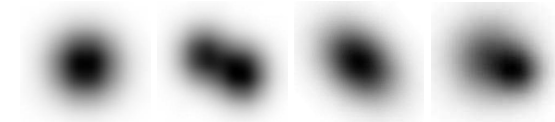


Fig. 3. Comparison between the best fits to *INTEGRAL* mosaic image (see Fig. 1) with a standard point source PSF (*left*), the PSF of 2 point sources (second from the left), the PSF of an extended source with the shape of an ellipse (third from the left) and the PSF of a source with the morphology of the Coma cluster in the 1–10 keV plus an additional point source (*right*).

fit, \mathbf{r}_0 . The size of the major axis of the ellipse, σ_1 is roughly equal to d_{12} .

The fit by an extended source of the shape of the Coma cluster in the 1–10 keV band plus an additional point source (Model 4) gives a good fit, $\chi_{\text{red}}^2 = 1.36$. The additional point source is found at $\text{RA} = 194.71 \pm 0.01$ and $\text{Dec} = 27.87 \pm 0.01$, which is located $6.1'$ away from the quasar EXO 1256+281. Figure 4 shows the position of the fitted point source on the residual image with 1σ , 2σ and 3σ error contours.

4. A method to analyse extended sources with a coded mask instrument

4.1. Description of the method

The imaging capabilities of ISGRI make it possible to obtain information on the morphology of the hard X-ray emission of the Coma cluster and other slightly extended sources for the first time. However, the standard Offline Scientific Analysis (OSA) software distributed by ISDC (Courvoisier et al. 2003) is optimized for point sources, and is not well suited for slightly extended sources. We present here a method based on Pixel Illumination Fraction (PIF) which extracts the properties of slightly extended sources with a coded mask instrument (see also Renaud et al. 2006b).

For a coded mask instrument, the sky images and, in particular the mosaic image studied in the previous section, are

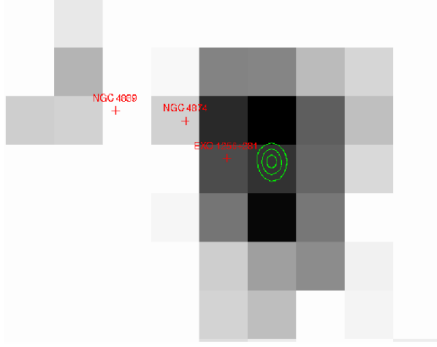


Fig. 4. Residual image after subtraction of the scaled *XMM-Newton* image from the *INTEGRAL* mosaic image. The position of the fitted point source from Model 4 is displayed with 1σ , 2σ and 3σ error contours. The positions of the brightest AGNs embedded in the cluster is also displayed.

produced by the backprojection of the shadow patterns cast by the sources in the field of view on the plane of the sky. The shadow pattern produced when observing a FOV containing n sources is a superposition of the shadow patterns of all the individual sources,

$$S(x, y) = \sum_{i=1}^n f_i \cdot \text{PIF}_i(x, y) + B(x, y), \quad (6)$$

where f_i and $\text{PIF}_i(x, y)$ are the flux, respectively the shadow pattern (called “Pixel Illumination Fraction”) of the i th source and $B(x, y)$ is the background in the pixel with coordinates (x, y) . The Pixel Illumination Fraction gives the fraction of each pixel of the detector illuminated by the source. For a pixel that is completely in the shadow of the mask, the PIF will be 0, whereas in the case of a fully illuminated pixel, the PIF will be equal to 1. It is understandable that the PIF of an extended source is different from that of a point source, since some pixels might be illuminated by only a fraction of the total extension of the source, which cannot happen for a point source. Thus to describe an extended source properly, one has to create an appropriate model for it. Our method to create such a model is the following: we create a grid of positions on the sky covering the extended source, compute the PIF for all the positions of this grid, and then average the PIFs, weighted by a model surface brightness for the source, e.g. a spherical isothermal β -profile,

$$I(r) \propto \frac{1}{\left(1 + \frac{r^2}{a^2}\right)^\beta}. \quad (7)$$

Figure 5 shows the PIF for an on-axis source, in the case of a point source and for an extended source described by the model of Eq. (7) with $a = 30'$.

Since the standard OSA tools always use the PIF for a point source, in the case of an extended source they do not extract fluxes and spectra correctly. To extract the flux of an extended source, we created a tool that fits the detector image (or *shadowgram*) with any kind of PIF, either point-like or extended with a given surface brightness model. Our tool creates a correct PIF for every source in the FOV, and then fits the shadowgram to the model described in Eq. (6), where 1 or more sources might be extended. To check the coherence of our method, we have simulated the shadowgram one can expect with 2 sources, one

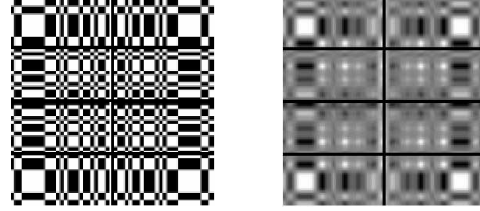


Fig. 5. The Pixel Illumination Fraction (PIF) of the IBIS/ISGRI instrument for a source in the center of the field of view (white = 1, black = 0): *left*: for a point source; *right*: for an extended source with a surface brightness described by an isothermal β -profile, with a source size $a = 30$ arcmin.

extended in the middle of the FOV with a flux $F_1 = 40$ counts per fully illuminated pixel (cpp hereafter) and one point-like in the corner of the FOV with a flux $F_2 = 80$ cpp, with a Gaussian background, and extracted the fluxes of the 2 sources with our tool. The results gave us $F_1 = 40.0 \pm 0.7$ cpp and $F_2 = 80.4 \pm 1.2$ cpp, which shows that our method is indeed extracting fluxes properly.

This method can also be used to extract spectra: we analyzed the data with the standard OSA tools to create shadowgrams in all the energy bands desired for the spectrum, and then used our fitting tool to extract a flux with the correct PIF in all the energy bands, and reconstruct a spectrum (see Sect. 5).

It is important to note that the use of a PIF-based method for weak extended sources could be complicated because of the specifics of operation of the *INTEGRAL* satellite. Namely, each *INTEGRAL* observation is split into several kilosecond-long intervals of continuous data taking, called Science Windows (ScWs). The statistics of the signal from a weak source in each ScW is below the background statistics. Moreover, the statistical properties of the low-statistic signal in the ISGRI imager are not well known. This means that the use of Gaussian statistics for the fitting of the shadowgrams is not completely correct, and can give wrong results. On the contrary, the method of analysis based on the mosaic image is better suited for the analysis of weak extended sources. In any case, the two methods should be considered complementary, and for this reason we present results based on both methods in this paper.

4.2. Hypothesis of multiple point sources

One possible explanation for the shape of the mosaic image (Fig. 1) is that one or several point sources contribute to the observed flux. We analyse this possibility here. Candidate sources are the cluster itself and bright AGNs at close angular distances. The three brightest AGNs in soft X-rays are the central radio galaxy NGC 4874, NGC 4889 and the QSO EXO 1256+281. Figure 1 shows the position of these 3 point sources on the ISGRI image.

We used the method described in Sect. 4.1 to fit the shadowgram in the 18–23 keV band by the PIF of 3 point sources at the position of the sources given above. We extracted the flux of each of these 3 sources, and created a model of the deconvolved image with the flux found.

Figure 6 shows the result of the subtraction of the fitted model from the mosaic image in the 18–23 keV. We can see on the image that the outer parts of the source are not well described by the model, specially the region at the bottom right and the left, where 5.5σ excesses are observed in the mosaic

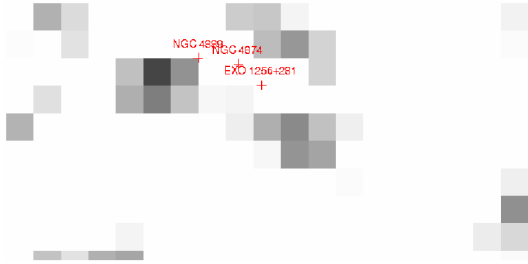


Fig. 6. Subtraction between the mosaic image in the 18–23 keV band and the model obtained with the fit of the data with the sum of NGC 4874, EXO 1256+281 and NGC 4889. While the center of the emission is well described, the outer parts of the image show a deviation of up to 5.5σ from the model.

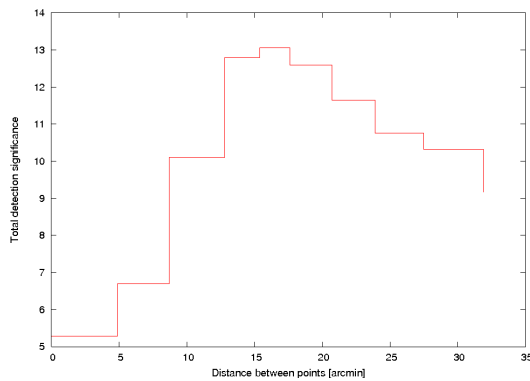


Fig. 7. Computation of the total detection significance in the 18–23 keV band as a function of the distance between 2 fake sources along the major axis of the ellipse.

compared to the model image. This analysis suggests that the emission seen by *INTEGRAL* is more extended than what can be explained by the superposition of the brightest AGNs in the cluster.

To confirm this, we fit the data with 2 fake point sources placed along the major axis of the ellipse, and computed the detection significance for different distances of the 2 fake sources. In the case of a single point source, we would expect the detection significance to drop when we increase the distance between the 2 fake sources, whereas in the case of 2 sources whose PSF overlap, we expect the detection significance to peak at the distance between those 2 sources. The position of the 2 sources for which the detection significance peaks will therefore allow us to compare this result with the position of known point sources inside the cluster. If there is a possible point source counterpart in soft X-rays, this will give an indication that contamination of the hard X-ray flux by point sources is likely. The result of this computation is shown in Fig. 7.

We can see in Fig. 7 that the detection significance peaks at a distance of 17 ± 2 [arcmin], which is fully compatible with the result obtained from the mosaic in Sect. 3.1. Since we expect the thermal emission from the cluster to dominate in this energy range, we would expect the two points to be located on the centre of the cluster (that lies $1'$ south of NGC 4874) and one of the other AGNs. However, the distance between the centre of the cluster and EXO 1256+281 ($4.6'$) or NGC 4889 ($8.9'$) is at least

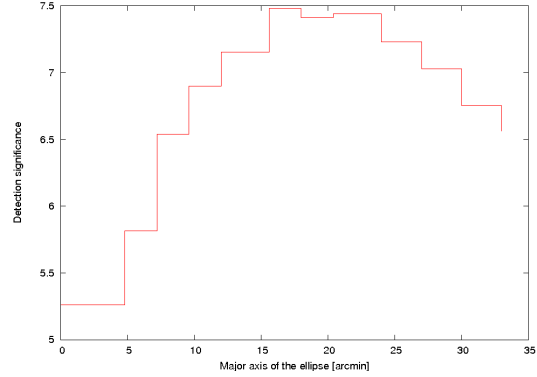


Fig. 8. Detection significance of the source computed with an ellipse-shaped PIF in the 18–23 keV band as a function of the major axis of the ellipse.

a factor of 2 smaller than the distance we found. This is a strong argument in favour of extended emission.

4.3. Extended emission analysis

We used the same method to analyse the ISGR1 data with the assumption that the emission is indeed diffuse emission. We used the angle of the ellipse found from the mosaic analysis (see Sect. 3.1) to create PIFs of an extended source with the method explained in Sect. 4.1, weighted by a surface brightness given by Model 3 (see Eq. (3)). We used our tool to fit all the data with this model for several different values of σ_1 and σ_2 with a ratio $\frac{\sigma_1}{\sigma_2} = 1.43$ fixed by the results of the image fitting, and finally computed the detection significance of the source for all the different models. The result is shown in Fig. 8.

We can see in this figure that the detection significance also peaks at a major axis size of about 17 [arcmin], which is again comparable to the results obtained from the mosaic. We can see that the maximum detection significance is lower than in the case of 2 point sources, but this does not mean that the model of 2 point sources gives a better representation of the data: indeed, the error on the fit increases with the size of the source, because the contours of the smallest holes of the mask become more and more unclear (see Fig. 5), and thus the imaging method is less accurate. It is thus irrelevant to compare directly Figs. 7 and 8, but both show independently the fact that the source is not point-like, and provide a measurement of the apparent size of the source in hard X-rays.

From this analysis, we conclude that if we use a source size smaller than the limit of $17'$, we lose a part of the total flux of the cluster, and thus the detection significance increases with the size. In the opposite case, we collect more background, so the detection significance starts to drop. The best estimate of the total flux of the cluster is therefore given at a major axis size of 17 [arcmin], which gives $F_{\text{tot}} = 0.31 \pm 0.04$ counts/s in the 18–30 keV band. From now on, we will use this model to extract fluxes and spectra.

We also performed another complementary analysis: we fitted the data with 4 sources, i.e. the extended model described above and the 3 AGNs. The fit converges to a solution that puts 80% of the flux in the extended emission. This model cannot be used to extract a flux, because the fluxes of the 4 sources become strongly anti-correlated. However, it means that the

840

D. Eckert et al.: South-West extension of the hard X-ray emission from the Coma cluster

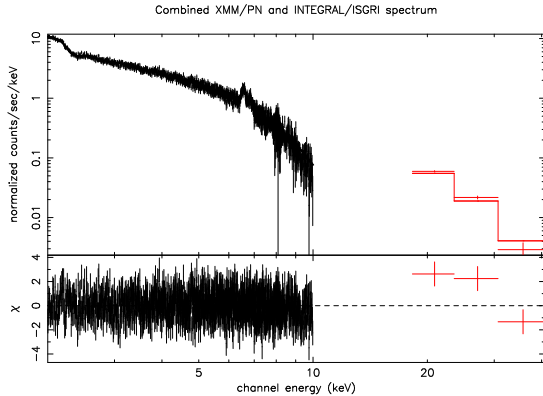


Fig. 9. Combined *XMM*/PN and *INTEGRAL*/ISGRI spectrum. The PN spectrum is fitted by a MEKAL model at a temperature $kT = 7.9 \pm 0.1$ keV. The bottom plot shows the residuals of the best fit compared to the data. There is no obvious deviation to this spectrum from the ISGRI data points up to 40 keV.

extended source model describes the data better than the sum of point sources.

5. Spectral analysis

To extract the spectrum of the source correctly, we used the method described in Sect. 4.1. We used the hard X-ray shape of the source extracted from the *INTEGRAL* image to create a PIF covering the whole size of the source, and extracted the flux from the shadowgram of each pointing in 3 different energy bands: 18–23, 23–30 and 30–40 keV (the source is not detected at higher energies). We then performed a weighted sum over the flux extracted from all pointings to get a total spectrum in these 3 energy bands. We also extracted the *XMM*/PN spectrum of the cluster with the background subtraction method from the Birmingham group, in a region chosen such that the *XMM-Newton*/*INTEGRAL* intercalibration factor is equal to 1. Finally, we fitted this spectrum in XSPEC with the MEKAL model (Kaastra & Mewe 2000). We extrapolated the fitted model to higher energies and compared it to the data points obtained with ISGRI. The result is shown in Fig. 9.

Because of the very low statistics at energies above 30 keV, we are not able to confirm or deny the presence of a non-thermal hard X-ray excess emission. Indeed, the extended nature of the source makes it difficult to extract a significant spectrum up to high energies, since the already low statistics is spread over several sky pixels. A longer exposure time is therefore required to make conclusions on the presence or not of a hard X-ray excess emission above 30 keV.

Although there is strong evidence that EXO 1256+281 cannot explain the *INTEGRAL* SW extension, the angular distance between the fitted position and EXO 1256+281 ($6.1'$) is close to the half-width of the ISGRI PSF. Hence, we further investigate this point by extracting the spectral properties of this object, assuming the identification of the additional point source with EXO 1256+281.

To this end, we fitted the excess in the ISGRI image by a point source at the position of EXO 1256+281, and extracted the flux for this source. Figure 10 shows the *XMM-Newton* spectrum of EXO 1256+281 with the ISGRI point extracted using this method. The *XMM-Newton* spectrum is well fitted by a

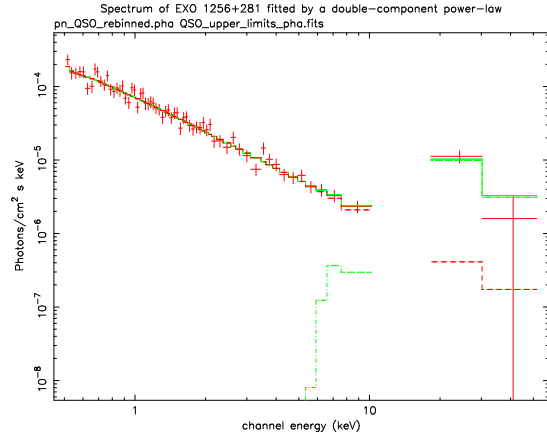


Fig. 10. *XMM-Newton* spectrum of the quasar EXO 1256+281 with one ISGRI data point obtained by fitting the south-west excess in hard X-rays by a point source at the position of EXO 1256+281. The ISGRI upper limit in the 30–50 keV band is shown. The spectrum is fitted by the sum of a power law (dashed red) and a heavily absorbed component dominating the flux at higher energies (dashed green).

simple powerlaw with the photon index $\Gamma = 1.63 \pm 0.07$ and 0.5–10 keV flux 5×10^{-13} ergs cm^{-2} s^{-1} . The flux of the source in the *INTEGRAL* energy band is much higher than the extrapolation of the powerlaw found in *XMM-Newton* data. This implies the presence of an additional spectral component which dominates the source above 10 keV. To model this component, we added a heavily absorbed power law typical of Seyfert 2 galaxies to the fit. Taking into account the upper limit in the 30–50 keV band, the fit gives $n_{\text{H}} = (4.0 \pm 1.7) \times 10^{24}$ cm^{-2} , and $\Gamma \geq 3.0$ to match the upper limit. This index is much steeper than the unified Seyfert 2 spectral index ($\Gamma = 1.79$ with a dispersion $\sigma = 0.23$, Risaliti 2002), and hence, the properties of this source would be very unusual for a Seyfert 2 galaxy. From this statement together with the imaging arguments presented in the previous sections, we conclude that the contribution of known point sources to the observed flux is very unlikely between 10 and 40 keV.

Assuming that the SW excess is due to the presence of diffuse emission, which gives the best representation of the data, one can try to constrain the properties of the gas needed to explain the emission from this region. We attempted to make a joint fit of the 1–10 keV spectrum extracted from a circle of a radius of $6'$ centered at the position of the SW excess and the 18–50 keV spectrum extracted from the SW region from the *INTEGRAL* mosaic image in the same way as in the case of an additional point source. Assuming that all the flux from the SW region comes from a higher temperature plasma, we fitted the data with the thermal bremsstrahlung model. This results in a temperature of $kT = 12 \pm 2$ keV. The corresponding estimate of the emission measure (EM) is $0.16 \leq EM \leq 0.26$ cm^{-6} pc, which is reasonable for external regions of the cluster. We can thus conclude that the presence of a hotter region ($10 \text{ keV} < kT \leq 14 \text{ keV}$) can explain the extension found in the ISGRI mosaic image.

6. Discussion

In this paper, we have used the IBIS/ISGRI instrument on board the *INTEGRAL* satellite to investigate the hard X-ray emission from the Coma cluster. We presented a method based on Pixel Illumination Fraction (PIF) to analyse extended sources with a coded mask instrument (Sect. 4.1), and we have shown that the Coma cluster indeed appears like an extended source for ISGRI. Assuming that the emission seen by *INTEGRAL* is extended, we have compared the ISGRI mosaic image with the soft X-ray image from *XMM-Newton*, and shown that there is a displacement between them: the *INTEGRAL* image is displaced towards the south-west, i.e. in the direction of the NGC 4839 group, that is currently merging with the main cluster.

The origin of the extended emission from this region is not clear, but we have investigated two possible explanations for the excess in the image: an additional heavily absorbed point source embedded in the cluster, and an extended region where large-scale shocks occur.

The first model for the hard X-ray excess in the South-West region of the cluster is the presence of a highly absorbed additional point source appearing at higher energies. We have used the imaging capabilities of the instrument to investigate this possibility: we have shown that the shape of the residual image after subtraction of the *XMM-Newton* surface brightness profile from the ISGRI image does not coincide with any known X-ray point source, and that the only possible candidate EXO 1256+281 is located more than 6 arcmin away from the best position found in the *INTEGRAL* image, which makes it an unlikely counterpart. We have also extracted the soft X-ray spectrum of this source and the flux of the south-west region in *INTEGRAL* data, and shown that this spectrum is not compatible with a highly absorbed Seyfert II galaxy. Indeed, the source is not detected in the 30–50 keV band, which is the most sensitive energy band of ISGRI. This implies a spectral index $\Gamma \geq 3.0$, which is too steep for a highly absorbed Seyfert 2 galaxy. As a conclusion, we claim that contribution of a very hard point source embedded in the cluster to the observed spectrum is highly unlikely.

We cannot exclude the possibility that the South-West excess in hard X-rays is due to one or few unknown sources that would emit predominantly in this energy band. If this is the case, these sources must be highly absorbed ($n_{\text{H}} \geq 4 \times 10^{24} \text{ cm}^2$), and have a steep spectral index $\Gamma \geq 3.0$. We note that these characteristics are unlikely, because most of the highly absorbed sources discovered by *INTEGRAL* show a much harder spectrum.

In the scenario of a merging event between the Coma cluster and the NGC 4839 group, we expect a shock front to be created in the region where the gas of the two clusters collides. Our imaging analysis shows that the hard X-ray emission seen

by *INTEGRAL* is extended in the direction of the NGC 4839 group, which is a good indication that the emission we see is indeed coming from a region where large-scale shocks occur. If this explanation is correct, we expect the plasma in this region to be hotter, and hence to have a harder spectrum in X-rays. The temperature map of the cluster (Neumann et al. 2003) shows a region that has low surface brightness in X-rays, but is the hottest region of the cluster ($kT \geq 10 \text{ keV}$). This region coincides with the position of the hard X-ray South-West extension found by *INTEGRAL*, and we can thus associate the hard X-ray excess in this region discussed in Sect. 5 with emission from a very hot region of the cluster ($kT \leq 14 \text{ keV}$). This result is consistent with the temperature found in the merging region of the distant cluster Cl J0152.7-1357 (Maughan et al. 2003), which shows that such a high temperature is possible and might indeed be the signature of a merger. Assuming that the hot region is roughly spherically symmetric and has an angular size of $\sim 6'$ at a distance of 100 Mpc, we deduce that the density of the hot gas is $n_{\text{hot}} \sim 10^{-3} \text{ cm}^{-3}$. Given that the South-West excess in the ISGRI image appears to be extended, *INTEGRAL* data appear to confirm this scenario.

Acknowledgements. We would like to thank M. Chemyakova for help with *XMM-Newton* data analysis and helpful comments. This work is based on observations with *INTEGRAL*, an ESA project with instruments and science data centre funded by ESA member states (especially the PI countries: Denmark, France, Germany, Italy, Switzerland, Spain), Czech Republic and Poland, and with the participation of Russia and the USA.

References

- Briel, U. G., Henry, J. P., Lumb, D. H., et al. 2001, *A&A*, 365, L60
 Courvoisier, T. J.-L., Walter, R., Beckmann, V., et al. 2003, *A&A*, 411, L53
 Feretti, L., & Giovannini, G. 2007, *ArXiv Astrophysics e-prints*
 Fusco-Femiano, R., Orlandini, M., Brunetti, G., et al. 2004, *ApJ*, 602, L73
 Kaastra, J. S., & Mewe, R. 2000, in *Atomic Data Needs for X-ray Astronomy*, ed. M. A. Bautista, T. R. Kallman, & A. K. Pradhan, 161
 Lebrun, F., Leray, J. P., Lavocat, P., et al. 2003, *A&A*, 411, L141
 Maughan, B. J., Jones, L. R., Ebeling, H., et al. 2003, *ApJ*, 587, 589
 Neumann, D. M., Lumb, D. H., Pratt, G. W., & Briel, U. G. 2003, *A&A*, 400, 811
 Read, A. M., & Ponman, T. J. 2003, *A&A*, 409, 395
 Renaud, M., Bélanger, G., Paul, J., Lebrun, F., & Terrier, R. 2006a, *A&A*, 453, L5
 Renaud, M., Gros, A., Lebrun, F., et al. 2006b, *A&A*, 456, 389
 Rephaeli, Y., & Gruber, D. 2002, *ApJ*, 579, 587
 Risaliti, G. 2002, *A&A*, 386, 379
 Rossetti, M., & Molendi, S. 2004, *A&A*, 414, L41
 Sarazin, C. L. 1999, *ArXiv Astrophysics e-prints*
 Schuecker, P., Finoguenov, A., Miniati, F., Böhringer, H., & Briel, U. G. 2004, *A&A*, 426, 387
 Timokhin, A. N., Aharonian, F. A., & Neronov, A. Y. 2004, *A&A*, 417, 391

4.7 Proceeding of the 30th ICRC conference

30TH INTERNATIONAL COSMIC RAY CONFERENCE



A particle acceleration site in the Coma cluster?

D. ECKERT¹, N. PRODUIT¹, A. NERONOV¹ & T. J.-L. COURVOISIER¹

¹ISDC, 16, ch. d'Ecogia, Geneva Observatory, University of Geneva, CH-1290 Versoix, Switzerland
Dominique.Eckert@obs.unige.ch

Abstract: We present the results of a deep (1.1 Ms) observation of the Coma cluster of galaxies in the 18-30 keV band with the ISGRI imager on board the *INTEGRAL* satellite. We show that the source extension in the North-East to South-West (SW) direction ($\sim 17'$) significantly exceeds the size of the point spread function of ISGRI, and that the centroid of the image of the source in the 18-30 keV band is displaced in the SW direction compared to the centroid in the 1-10 keV band. To test the nature of the SW extension we fit the data assuming different models of source morphology. The best fit is achieved with a diffuse source of elliptical shape, although an acceptable fit can be achieved assuming an additional point source SW of the cluster core. In the case of an elliptical source, the direction of extension of the source coincides with the direction toward the subcluster falling onto the Coma cluster. If the SW excess is due to the presence of a point source with a hard spectrum, we show that there is no obvious X-ray counterpart for this additional source, and that the closest X-ray source is the quasar EXO 1256+281, which is located $6.1'$ from the centroid of the excess. Finally, we show that the hard X-ray emission coincides with the 1.4 GHz radio emission, which suggests that the hard X-ray emission comes from the same population of electrons that is responsible for radio haloes through synchrotron emission.

Introduction

In the hierarchical scenario of structure formation, clusters of galaxies are the latest and biggest structures to form. Hence, we expect some of them to be still forming, and experiencing major merging events with smaller clusters. This is the case of the Coma cluster, that is currently merging with the NGC 4839 group.

In such events, the merging of the ICM of the two clusters creates shock fronts, in which theory predicts that an important population of particles would be accelerated to high energies (Sarazin 1999). This phenomenon should then produce a reheating of the gas, and create a higher temperature plasma that would radiate more strongly in hard X-rays. Alternatively, interaction of the population of mildly relativistic electrons that produce the halos of galaxy clusters via synchrotron radiation (Feretti & Giovannini 2007) with the Cosmic Microwave Background would then produce hard X-ray emission through inverse Compton processes, and thus add a power-law tail to the spectrum in the hard X-ray domain. Detection of this hard X-

ray excess would help to learn more about the cosmic ray population detected by radio observations. Furthermore, characterization of the morphology of the hard X-ray emission would bring a possible identification of acceleration sites.

Recent reports of detection of a hard X-ray excess by *Beppo-SAX* (Fusco-Femiano et al. 2004) and *RXTE* (Rephaeli & Gruber 2002) in the Coma cluster seem to confirm the existence of a high energy tail of the spectrum of merging clusters, and thus prove the existence of particle acceleration sites in these clusters. However, these detections are rather weak and controversial (Rossetti & Molendi 2004), and since the hard X-ray instruments on both *Beppo-SAX* and *RXTE* are non-imaging, contamination by very hard point sources inside the cluster could not be excluded (e.g. by the central galaxy NGC 4874, NGC 4889 or the QSO EXO 1256+281). Besides, it was not possible to have any information on the morphology of the hard X-ray emission.

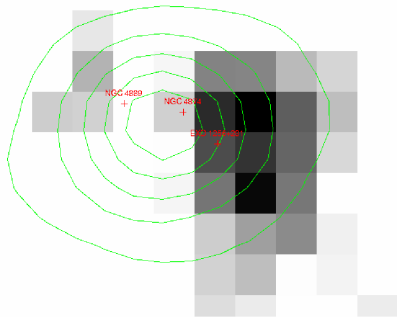


Figure 1: The residuals after the subtraction of the *XMM-Newton* profile from the *INTEGRAL* image (see text). The South-West excess in the residual image is apparent.

INTEGRAL data analysis

After a careful selection of Science Windows (ScWs), we created a mosaic image of the cluster with the standard OSA 6.0 software in the 18-30 keV energy band (see Eckert et al. (2007) for details). From this mosaic, we showed that the source extension in the North-East to South-West (SW) direction ($\sim 17'$) significantly exceeds the size of the point spread function of ISGRI ($12'$ FWHM), and that the centroid of the image of the source in the 18-30 keV band is displaced in the SW direction compared to the centroid in the 1-10 keV band. Figure 1 shows the residuals of the *INTEGRAL* mosaic image after subtraction of the smoothed *XMM-Newton* image, renormalized in a way that the difference between *INTEGRAL* and *XMM-Newton* flux cancels at the maximum of the *XMM-Newton* emission. One can clearly see that significant residuals are left in the South-West (SW) part of the *INTEGRAL* source after the subtraction. This indicates that the hard X-ray source detected by *INTEGRAL* is more extended in the SW direction than the *XMM-Newton* source.

Possible interpretations for this excess

To test the nature of the SW extension, we fitted the data assuming different models of source morphol-

ogy. The best fit is achieved with a diffuse source of elliptical shape, with a semi major axis of $17'$. The direction of the major axis of the ellipse is inclined at the angle $\theta = 61 \pm 4^\circ$, which corresponds to the direction of the NGC 4839 group. Alternatively, an acceptable fit can be achieved assuming an additional point source SW of the cluster core. In this case, the additional point source is found at $RA=194.71 \pm 0.01$ and $DEC=27.87 \pm 0.01$.

There is no obvious X-ray counterpart for this additional source: the closest X-ray source is the quasar EXO 1256+281, which is located $6.1'$ from the centroid of the excess (see Fig. 1) for the position of this quasar). We also extracted the soft X-ray spectrum of this source and the flux of the south-west region in *INTEGRAL* data, in order to check if the spectrum would be compatible with a highly absorbed Seyfert II galaxy. We find that this is very unlikely: indeed, the fit requires a very high absorption ($n_H > 4 \times 10^{24} \text{ cm}^{-2}$) and a steep spectral index $\Gamma \geq 3.0$ for the absorbed component, which would be very unusual for a Seyfert II-type Active Galactic Nucleus. We cannot exclude the possibility that this excess is due to an unknown X-ray point source, but because of the spectral properties required for this object, this hypothesis is very unlikely. As a conclusion, we claim that contribution of a very hard point source embedded in the cluster to the observed flux is highly unlikely.

If we interpret the SW *INTEGRAL* excess as diffuse emission, which gives the best representation of the data, we see that the source is extended towards the sub-cluster around NGC 4839, which gives an indication that the emission might be related to the currently on-going merger between the main cluster and this sub-cluster. We have investigated two possibilities for this additional component: a thermal Bremsstrahlung emission from a hotter region, and a non-thermal Inverse-Compton (IC) component from the $E \sim \text{GeV}$ electrons that produce radio halos.

In the case of a hotter region, we find that this region coincides with a very hot region ($kT \geq 10$ keV, Neumann et al. (2003)). A joint fit of the 1-10 keV spectrum extracted from a circle of a radius of $6'$ centered at the position of the SW excess and the 18-50 keV spectrum extracted from the SW region from the *INTEGRAL* mosaic image give an upper limit to this temperature of $kT \leq 14$

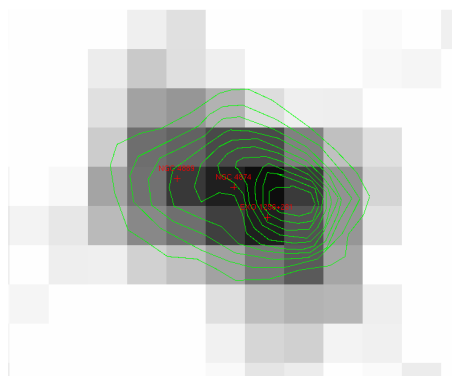


Figure 2: The *INTEGRAL* significance image with 1.4 GHz radio contours overlaid.

keV. This result is comparable with the temperature found in the merging region of the distant cluster Cl J0152.7-1357 (Maughan et al. 2003), which shows that such a high temperature is possible and might indeed be the signature of a merger. We can thus associate the hard X-ray excess in this region with emission from a very hot region of the cluster ($10 \text{ keV} \leq kT \leq 14 \text{ keV}$).

If the emission from the SW region comes from non-thermal IC scattering of mildly relativistic electrons, which is the most popular idea to explain the high-energy tail detected by *Beppo-SAX*, then the morphology of the hard X-ray emission must be correlated to the morphology of the radio halo of the cluster. Figure 2 shows the *INTEGRAL* mosaic image in the 18-30 keV band with 1.4 GHz radio contours overlaid from Deiss et al. (1997). The radio contours are subtracted for the radio galaxies. We can see that the radio emission is also displaced compared to the 1-10 keV thermal emission, and that the maximum of the radio emission coincides with the SW excess. This strongly suggests that the hard X-ray emission from this region is of non-thermal origin, namely of IC scattering from the same population of electrons as the radio emission. This strengthens the controversial result of Fusco-Femiano et al. (2004).

Conclusion

Thanks to the imaging capabilities of ISGRI, we were able for the first time to resolve spatially the Coma cluster in the hard X-ray domain. We showed that the hard X-ray emission is displaced compared to the purely thermal emission in soft X-rays. Investigating this displacement, we found that the contribution of point sources to the observed spectrum is likely negligible. Our analysis shows that a hotter plasma can explain this excess. However, the correlation between the radio and hard X-ray morphology strongly suggests that the SW excess is due to IC scattering of mildly relativistic electrons.

Together with the spectral results obtained by *Beppo-SAX* (Fusco-Femiano et al. 2007), it is now becoming clear that the presence of an additional X-ray spectral component is required by the data. Moreover, the strong correlation between radio and hard X-ray morphology clarifies the nature of this excess, and seems to confirm the existence of a particle acceleration site in the Coma cluster.

References

- Deiss, B. M., Reich, W., Lesch, H., & Wielebinski, R. 1997, *A&A*, 321, 55
- Eckert, D., Neronov, A., Courvoisier, T. J.-L., & Produit, N. 2007, *A&A*, 470, 835
- Feretti, L. & Giovannini, G. 2007, *ArXiv Astrophysics e-prints*
- Fusco-Femiano, R., Landi, R., & Orlandini, M. 2007, *ApJ L*, 654, L9
- Fusco-Femiano, R., Orlandini, M., Brunetti, G., et al. 2004, *ApJ L*, 602, L73
- Maughan, B. J., Jones, L. R., Ebeling, H., et al. 2003, *ApJ*, 587, 589
- Neumann, D. M., Lumb, D. H., Pratt, G. W., & Briel, U. G. 2003, *A&A*, 400, 811
- Rephaeli, Y. & Gruber, D. 2002, *ApJ*, 579, 587
- Rossetti, M. & Molendi, S. 2004, *A&A*, 414, L41
- Sarazin, C. L. 1999, *ArXiv Astrophysics e-prints*

Chapter 5

Hard X-ray observations of the Ophiuchus cluster

5.1 Introduction

Unlike the Coma, Perseus and Virgo clusters, which have been known for a very long time and extensively studied at all wavelengths, the Ophiuchus cluster is rather unknown among the scientific community, although it exhibits a number of very interesting aspects. The reason for this comes from the location of the cluster in the sky, 9 degrees away from the galactic center, where the obscuration by interstellar dust is extremely high. Because of the very strong obscuration, the cluster is unobservable at optical wavelengths, where the large majority of astronomical studies have been performed before 1970. For this reason, the Ophiuchus cluster, first designated as 4U 1708-23, was discovered in the X-ray band in the *Uhuru* all-sky survey, but due to the poor angular resolution of *Uhuru*, the source could not be identified at other wavelengths. Using X-ray observations with the *HEAO-1* mission, Johnston et al. (1981) studied the spectrum of the source, discovered its extended nature, and identified the source as a cluster of galaxies, which they designated as the Ophiuchus cluster. The cluster is, after Perseus, the second brightest X-ray cluster, and it is the most X-ray luminous and most massive cluster in our close neighbourhood. Even though the region is highly obscured in the optical, Wakamatsu & Malkan (1981) detected ~ 150 member galaxies in the optical, confirming the richness of the cluster. In particular, a massive giant elliptical cD galaxy has been detected close to the peak of the X-ray emission.

The X-ray spectrum extracted from *HEAO-1* data reveals a temperature $kT = 8 \pm 2$ keV and a redshifted iron line at 6.7 keV, with a redshift $z = 0.028$ (Johnston et al. 1981). Later *EXOSAT* observations (Arnaud et al. 1987) showed a temperature $kT = 9.4 \pm 1.2$ keV and an iron abundance of 0.26 ± 0.12 relative to the solar value. The data revealed an almost spherical morphology, with a surface brightness profile well represented by a beta-profile. The density profile of the source was found to be peaked around the central galaxy, which the authors interpreted as evidence for a weak cooling flow. However, Watanabe et al. (2001) used the *ASCA*/GIS instrument in the 0.5-10 keV band to create a detailed temperature map of the cluster (see the right panel of Fig. 5.1), and detected a very hot ($kT \gtrsim 15$ keV) region 20 arcmin from the center of the cluster. Their analysis also

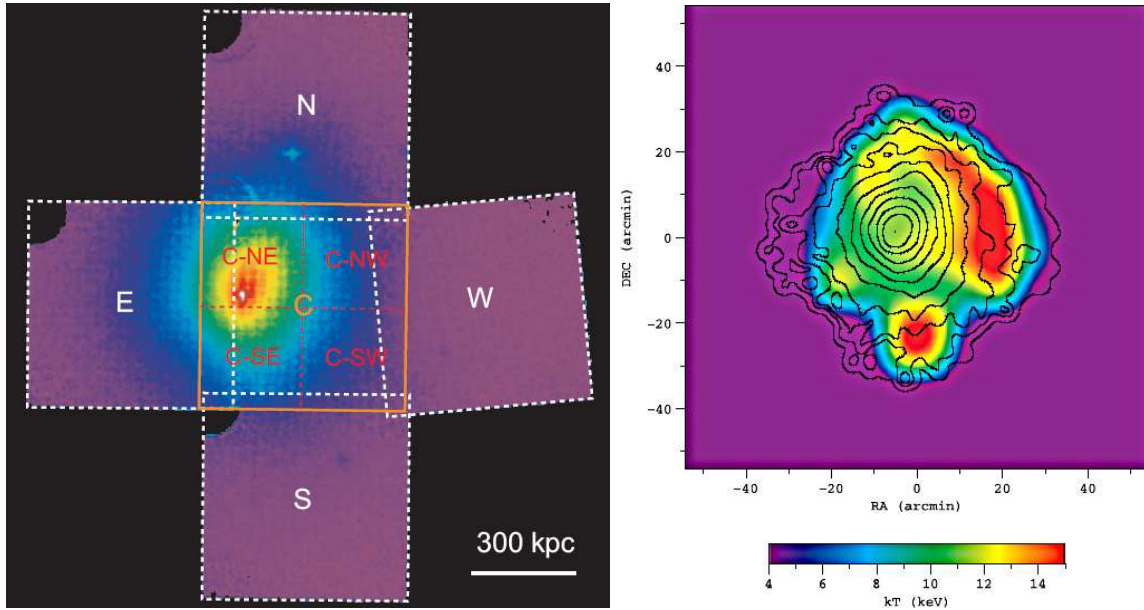


Figure 5.1: Left: *Suzaku*/XIS mosaic image of the Ophiuchus cluster (Fujita et al. 2008). Right: *ASCA*/GIS temperature map of the Ophiuchus cluster (Watanabe et al. 2001). A hot region ($kT \gtrsim 15$ keV) is seen West of the cluster core.

revealed a hotter temperature in the center ($kT = 10.9 \pm 0.4$ keV) compared to previous results. Based on the complicated temperature structure and hot temperature, the authors concluded that the cluster is not dynamically relaxed, and has recently experienced a merging event. However, it must be noted that the calibration of *ASCA* was uncertain above 8 keV. Since the measurements of temperatures higher than 10 keV would be mostly determined by the 8-10 keV band, this result could be affected by calibration issues.

The source was also observed by *BeppoSAX* (Nevalainen et al. 2004). The authors noted that using the temperature value derived by *ASCA* significantly over-estimated the low-energy part of the 15-80 keV hard X-ray spectrum. Data from the PDS instrument revealed a temperature $kT = 9.1^{+0.5}_{-0.6}$, and a possible non-thermal excess at hard X-rays, detected at the 2σ level. Unfortunately, the exposure time (50 ksec) was not sufficient to confirm this result in a statistically significant way.

Recently, the source was also observed by *Suzaku* (Fujita et al. 2008). *Suzaku* performed 5 different 20 ksec pointings covering the source as fully as possible, in particular to observe the hot region detected by *ASCA*, and created a mosaic image of the cluster (see the left panel of Fig. 5.1). Thanks to the large effective area and good sensitivity of the XIS instrument, an accurate temperature map could be obtained. The presence of the hot region detected by Watanabe et al. (2001) was not confirmed by *Suzaku* data. Unlike *ASCA* results, the authors found very little temperature variations within the cluster, and a temperature ranging from ~ 8 keV in the center up to ~ 10 keV in the outer regions. Because of the increasing temperature with radius, the authors deduced that the cluster is in a relaxed state and exhibits a weak cooling flow, which contradicts *ASCA* results.

	kT [keV]	Fe Abundance	Cooling flow	NT excess
<i>HEAO-1/A-2</i> ¹	8 ± 2	?	?	?
<i>EXOSAT/ME</i> ²	$9.4^{+1.5}_{-1.2}$	$0.21^{+0.11}_{-0.10}$	yes	?
<i>Tenma/GSPC</i> ³	11.6 ± 0.6	0.49 ± 0.08	?	yes
<i>ASCA/GIS</i> ⁴	$9.9^{+0.5}_{-0.4}$	0.29 ± 0.04	no	?
<i>ASCA/GIS</i> ⁵	10.9 ± 0.4	0.34 ± 0.05	no	?
<i>BeppoSAX/PDS</i> ⁶	$9.1^{+0.5}_{-0.6}$?	?	yes
<i>INTEGRAL/JEM-X</i> ⁷	8.5 ± 0.4	?	?	yes
<i>Suzaku/XIS</i> ⁸	9.3 ± 0.2	0.33 ± 0.02	yes	?
<i>Suzaku/HXD</i> ⁸	9.0 ± 0.3	?	?	no

Table 5.1: Summary of published X-ray data on the Ophiuchus cluster. The columns represent the central temperature, the iron abundance relative to the solar value, the presence or not of a cooling flow and of a non-thermal excess. References: ¹Johnston et al. (1981) ²Arnaud et al. (1987) ³Okumura et al. (1988) ⁴Matsuzawa et al. (1996) ⁵Watanabe et al. (2001) ⁶Nevalainen et al. (2004) ⁷Eckert et al. (2008) ⁸Fujita et al. (2008)

Apart from X-ray observations, the cluster was also observed in the infra-red and radio domains. In the infra-red band, where the obscuration by dust is much lower than in the optical, Hasegawa et al. (2000) observed the large-scale structure of the region, and detected several clumps of galaxies around the main cluster. They also noted that the density of galaxies around the main cluster was several times larger than in a background field, which they interpreted as the presence of a large-scale structure of supercluster size.

In the radio domain, Johnston et al. (1981) associated the Ophiuchus cluster with the unidentified radio source MSH 17-203. The radio source has a steep spectrum, which is typical of cluster radio halos. This implies the existence of a population of high-energy electrons in the cluster, and therefore, of some sort of particle acceleration mechanism. However, since X-ray observations reveal an almost relaxed state, the origin of the high-energy electrons is puzzling.

To summarize, the Ophiuchus cluster is the most luminous and most massive nearby X-ray cluster. The dynamical state of the gas in the cluster is not yet fully understood, and in particular the temperature structure of the cluster is still under debate (see Table 5.1 for a summary of published X-ray observations). The peaked radial profile, the presence of a weak cooling-flow and the almost symmetric morphology suggest that the gas in the central area is in a relaxed state. However, the very hot temperature of the gas is unusual for a cooling-flow cluster, and the X-ray emission is not centred on the cD galaxy and elongated towards the North-West direction. Moreover, the presence of relativistic electrons, which is demonstrated by the radio emission, indicates that a particle acceleration mechanism is currently at work in the cluster. For all these reasons, I would classify the Ophiuchus cluster as a post-merger cluster, i.e., a cluster which has experienced a merging event in the recent past, and is now switching to a relaxed state.

5.2 *INTEGRAL* observations of the Ophiuchus cluster

The *INTEGRAL* satellite (see Chapt. 3) was designed mainly for the study of galactic hard X-ray sources, and in particular for the detection of transient γ -ray emitting sources. Therefore, a significant part of the exposure time is spent in the Galactic center and Galactic plane regions, where the density of sources is much higher. In particular, the central region of our Galaxy (within 20° from the Galactic center) has been observed for more than 10 Ms (~ 5 months) during the first 5 years of the mission. The Ophiuchus cluster is located 9 degrees away from the Galactic center, which implies that it has been observed for a very long time since the launch of *INTEGRAL*. The detection of the source with the IBIS/ISGRI instrument was first reported by Revnivtsev et al. (2004) in a first 2 Ms survey of the Galactic center region, at a flux level of 4.2 ± 0.2 mCrab in the 18-60 keV band. The detection significance of the source was 20σ . The source was then reported in all *INTEGRAL* source catalogs (e.g. Bird et al. (2007)). We (Eckert et al. (2008), see the full paper in Sect. 5.7) performed a detailed analysis of *INTEGRAL* data on Ophiuchus. In this chapter, I will present the results of our analysis of the cluster in the 3-80 keV band with JEM-X and ISGRI.

5.2.1 ISGRI data analysis

The main problem regarding the analysis of the Ophiuchus cluster with *INTEGRAL* is its location, 9 degrees from the Galactic center and 14 degrees from the very bright low-mass X-ray binary Scorpius X-1. Indeed, uncertainties in the exact shape of the IBIS mask, mainly due to the screws which are used to attach the mask to the supporting structure (NOMEX), as well as the intrinsic periodicity of the mask, introduce important artifacts in standard deconvolved ISGRI sky images (the so-called “ghosts”, see Appendix A.2). Therefore, one must be extremely careful during the analysis to properly take into account the artifacts introduced in the sky images.

For our analysis, we considered only Science Windows (ScWs) for which the Ophiuchus cluster is less than 8 degrees off-axis. Indeed, the intensity of the ghosts increases with the off-axis angle, and the effective area of the instrument decreases, so it is safer to consider only pointings where the source is clearly within the FOV. Therefore, we analyzed 1580 ScWs of ISGRI data where Ophiuchus is at most 8 degrees off-axis, for a total exposure time of slightly more than 3 Ms. To construct mosaic images, we used the mosaicking method described in Appendix A.2, which partially takes the imperfections of the mask into account. The resulting mosaic image in the 20-24 keV band is shown in Fig. 5.2. The source is clearly detected in the mosaic image, with a significance of 16σ . The source is clearly detected in all energy bands between 14 and 40 keV.

For spectral extraction, the standard OSA 7.0 software works in the detector space by fitting shadow patterns (PIFs) to the corrected detector shadowgram, and hence it does not suffer from the systematic effects reported above. However, for a correct spectral extraction, it is necessary to take all sources brighter or similar to the analyzed source in order to avoid contamination from other sources to the spectrum. In the case of the Ophiuchus cluster, selecting the catalog of sources which should be used for spectral extraction

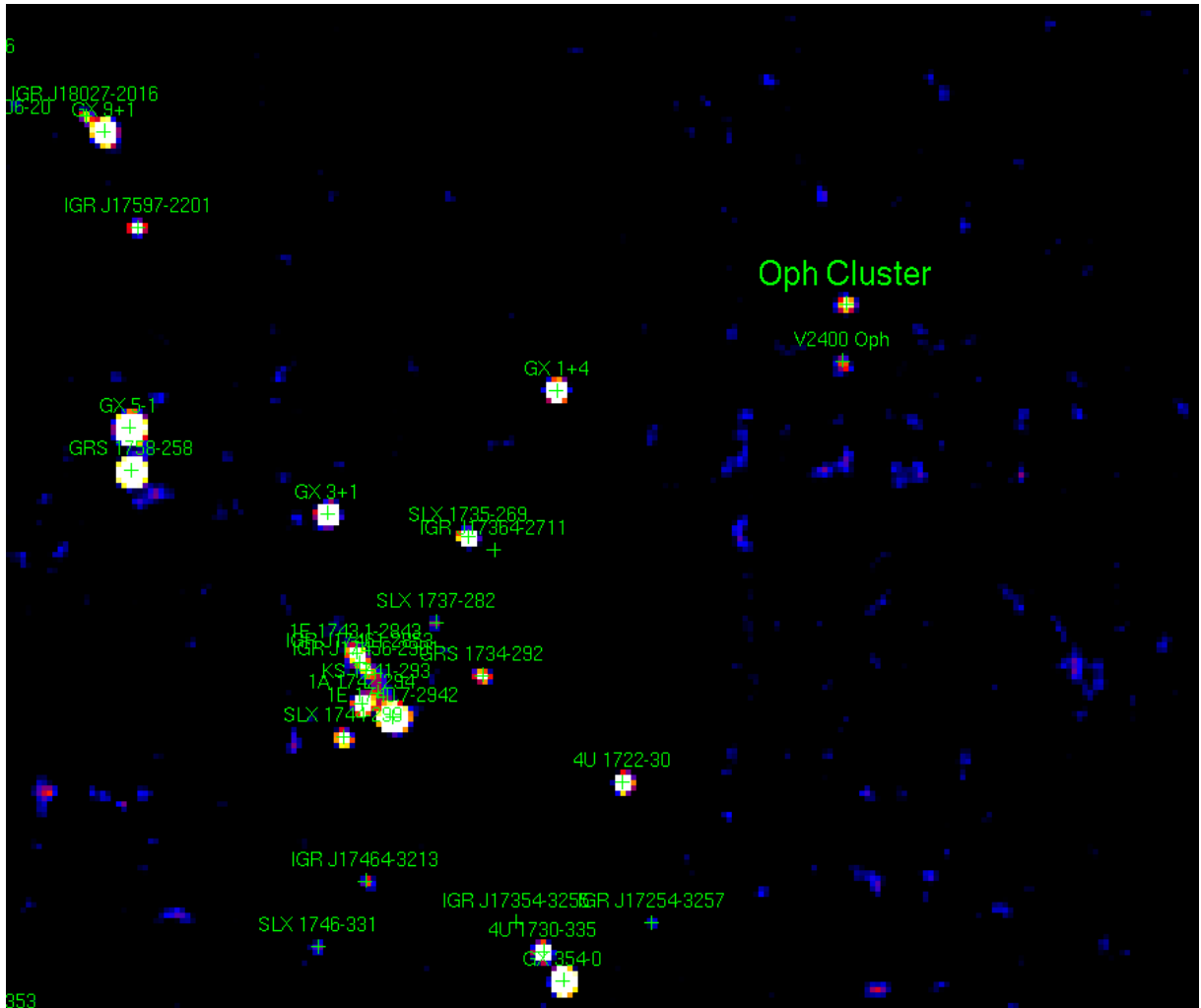


Figure 5.2: *INTEGRAL/ISGRI* mosaic image of the Galactic center region. The Ophiuchus cluster is shown, as well as a number of bright sources in the same field, including the Galactic center “sausage”, which is a blend of many sources in the direction of the Galactic center, in the bottom left corner of the image.

is a bit tricky. Indeed, the field is very crowded (see Fig. 5.2), and many of the sources in the field are transient, so a number of usually faint sources could become very bright during short time periods, and significantly influence the results of the spectral extraction procedure if they are not taken into account by the fitting procedure. On the other hand, for the stability of the results, it is not recommended to have more than 30 sources in the input source catalog used by the standard OSA spectral extraction procedure. Therefore, to select the sources to include in the input catalog, we used the total mosaic created before, and selected all sources which are brighter or similar to the Ophiuchus cluster. We also searched the complete data set for transient sources which appear as faint sources in the mosaic image, but experienced a strong outburst during a short time period. In total, the final source catalog included the Ophiuchus cluster, plus 18 other sources which must be taken into account for the spectral fitting procedure.

5.2.2 JEM-X data analysis

Although the main goal of the analysis was to search for a hard tail in the spectrum of the cluster, for which ISGRI is clearly the required instrument, it is also important to have a good knowledge of the low-energy part of the spectrum to fix the thermal component as well as possible, and to extend the spectrum to an energy band as broad as possible. Therefore, we also analyzed data from the JEM-X monitor (see Sect. 3.1.3), which has the necessary sensitivity down to 3 keV. Since the FOV of the JEM-X instrument (4.5 degrees in diameter full-response) is much smaller than that of IBIS, the exposure time on the cluster is much smaller (~ 250 ksec), but thanks to the brightness of the source at low energy, and given the very important improvements in the JEM-X imaging software brought by OSA 7.0, it should be detectable for JEM-X. Moreover, the angular resolution of JEM-X (3.8 arcmin FWHM) is three times better than that of ISGRI, so it should be possible to resolve the source spatially.

Unlike the IBIS mask, which was designed to have specific geometrical properties, the JEM-X mask has a random pattern. The advantage of the random pattern is that the shadow pattern it casts on the detector is not periodic, and therefore, reconstructed sky images are not affected by ghosts of strong sources. Moreover, it is now possible to combine mosaic images obtained with the two JEM-X instruments for better signal-to-noise. Consequently, we performed a completely standard analysis of the JEM-X data with the OSA software, version 7.0. We extracted mosaic images of the source in the 3-5, 5-7, 7-10 and 10-18 keV bands in order to study the dependence of the morphology with energy. The corresponding mosaics are shown in Fig. 5.3. The source is clearly detected (detection significance $> 10\sigma$) in all energy bands. A comparison with the other source in the FOV (the Cataclysmic Variable V2400 Oph) clearly shows that the source is extended. No obvious energy dependence of the morphology is seen.

For spectral extraction, we used the `mosaic_spec` tool to extract the spectrum from the mosaic images. Indeed, the standard JEM-X spectral extraction tool fits the data with a point-source model, which results in an under-estimation of the source flux. On the other hand, `mosaic_spec` can fit the extent of the source directly from the mosaic, and therefore

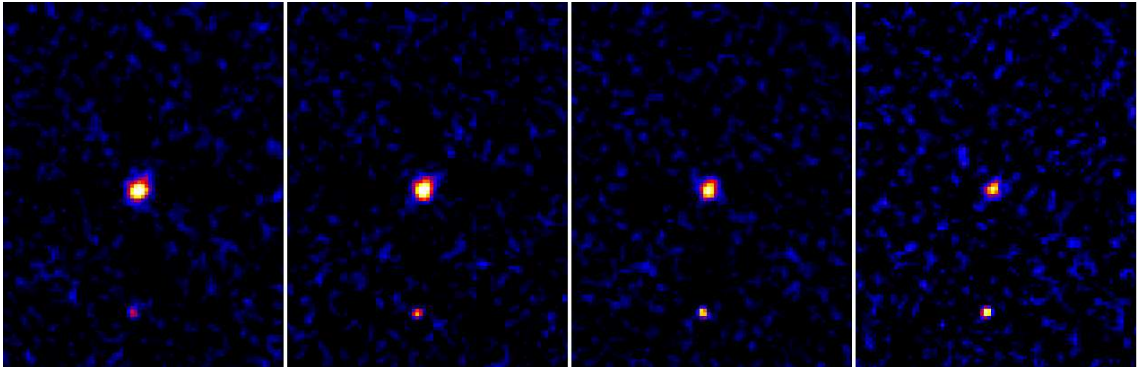


Figure 5.3: *INTEGRAL/JEM-X significance mosaic images of the Ophiuchus cluster region in the 3-5, 5-7, 7-10 and 10-18 keV bands. The source in the bottom of the image is the Cataclysmic Variable V2400 Oph.*

it can fully extract the flux of the source.

5.3 Morphological analysis

We used the mosaics extracted from both ISGRI and JEM-X data to study the morphology of the source and its energy dependence. Figure 5.4 shows the full ISGRI and JEM-X images in the 20-40 keV and 3-18 keV bands. For comparison with the PSF of the instruments, the insets show the image of the point source V2400 Oph, located 50 arcmin from the cluster, re-normalized to the same brightness. In the JEM-X image, we can see that the source is clearly extended. However, the extension of the source is not obvious in the ISGRI image.

Since we detect only the central regions of the cluster, a conventional fit of the JEM-X data with a spherical beta-model is not possible, but fitting the JEM-X image with a Gaussian model,

$$I(r) = A \exp\left(-\ln(2) \frac{r^2}{R^2}\right), \quad (5.1)$$

where R is the half-width at half-maximum (HWHM) of the source, one can get an indication on the size of the detected region. Besides, the model described in Eq. 5.1 is very similar to the spherical beta-model for $r \leq R$, so using this model we can estimate the core radius R_c of the cluster. The best fit to the JEM-X image with the Gaussian model gives $R = 3.6 \pm 0.1$ arcmin. This value is significantly larger than the PSF of JEM-X (1.8 arcmin HWHM), which confirms that the source is extended. The R parameter corresponds to the superposition of the intrinsic radial profile of the source with the PSF of the instrument,

$$R^2 = R_{source}^2 + HWHM_{JEM-X}^2. \quad (5.2)$$

Subtracting the contribution of the JEM-X PSF, we find that the intrinsic radial profile of the source is $R_{source} = 3.1 \pm 0.1$ arcmin. This value is consistent with the core radius

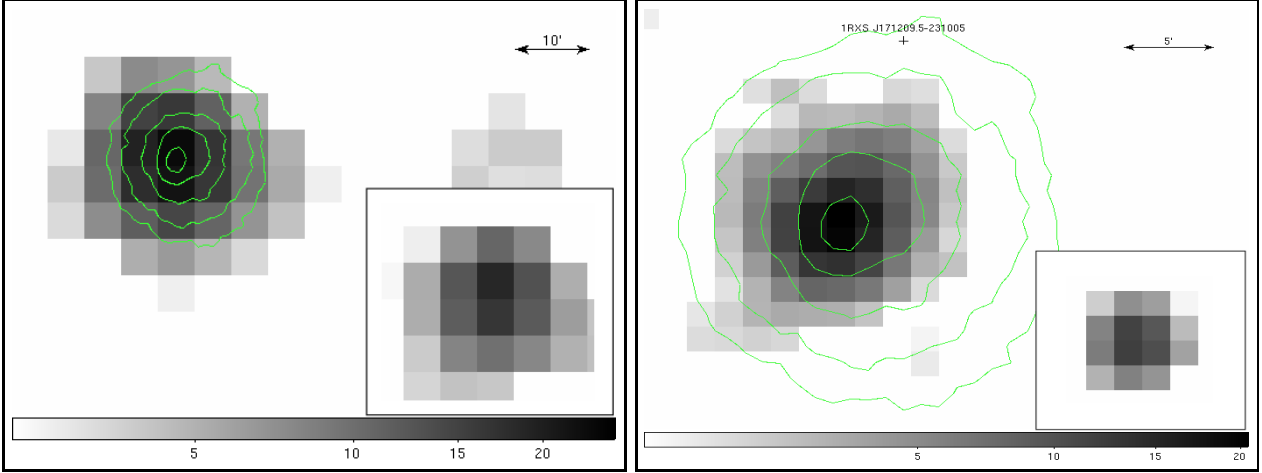


Figure 5.4: *INTEGRAL* images of the Ophiuchus cluster in the 20-40 keV band from ISGRI (left) and in the 3-18 keV band from JEM-X (right). For comparison, the insets show the image of a known point source in the same field, the Cataclysmic Variable V2400 Oph.

obtained from higher-statistics *ASCA* data ($R_c = 3.2$ arcmin, Watanabe et al. (2001)). Figure 5.5 shows the radial profile of the source compared to the PSF of the instrument, as well as the total apparent radial profile from JEM-X data. We can see that the data are very well represented by our model.

Since the source is clearly detected and spatially-resolved in several energy bands, it is possible to investigate the temperature variations within the detected area. Indeed, if we assume that the emission below 20 keV is completely dominated by thermal bremsstrahlung and that the abundance is constant throughout the cluster, the 3-7/7-18 keV hardness ratio depends only on the temperature of the gas in a specific region. In order to convert the JEM-X 3-7/7-18 keV hardness ratio to the gas temperature, we simulated JEM-X spectra for different input temperatures and an abundance fixed to 0.49 (Mohr et al. 1999), and computed the dependence of the 3-7/7-18 keV JEM-X hardness ratio as a function of the gas temperature. In the center of the cluster, we found a hardness ratio $HR = 0.78 \pm 0.09$, which corresponds to a temperature $kT = 9.1_{0.9}^{+1.4}$. Figure 5.6 shows the spatial deviations of the hardness ratio from the central value, in units of σ . No deviations from the central value are found above 0.7σ , which corresponds to temperature variations of ± 2 keV. This result is consistent with the *ASCA* results (see Fig. 5.1). Indeed, even though much hotter temperatures are found in the outer regions of the cluster, the core shows an almost iso-thermal profile, which is consistent with our results. This analysis shows that a single-temperature bremsstrahlung model should describe well the total JEM-X spectrum.

On the other hand, with a core radius $R_c \sim 3.2$ arcmin, the source should be almost point-like for ISGRI. Renaud et al. (2006b) presented the results of ISGRI data simulations assuming a uniform disk. For a disk of an angular size of 5 arcmin, they evaluate that the relative error on the reconstructed flux assuming that the source is point-like is $\sim 5\%$. Since the cluster has a peaked radial profile instead of uniform disk, the relative

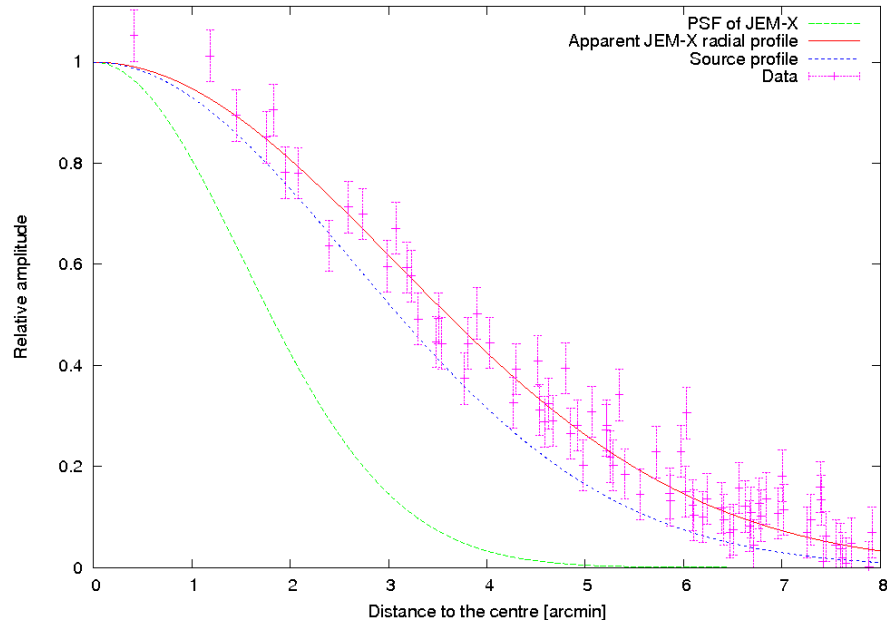


Figure 5.5: Deconvolved radial profile of the *Ophiuchus* cluster extracted from JEM-X data (dashed blue line), compared to the PSF of the instrument (dashed green). The actual data (purple bars) and the apparent profile (red line) are also shown.

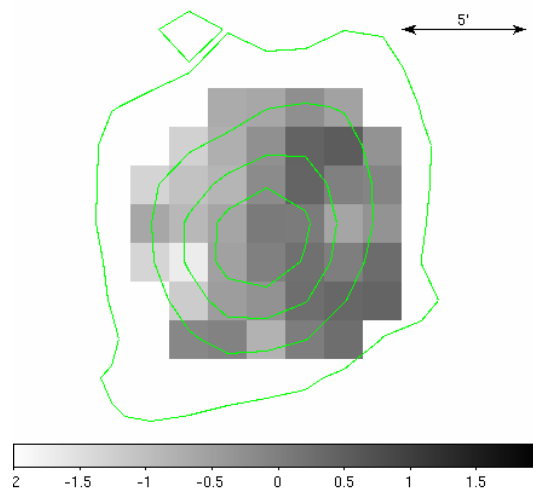


Figure 5.6: Deviations of the JEM-X 3-7/7-18 keV hardness ratio from the central value, in units of σ . No significant temperature variations are found in the detected region.

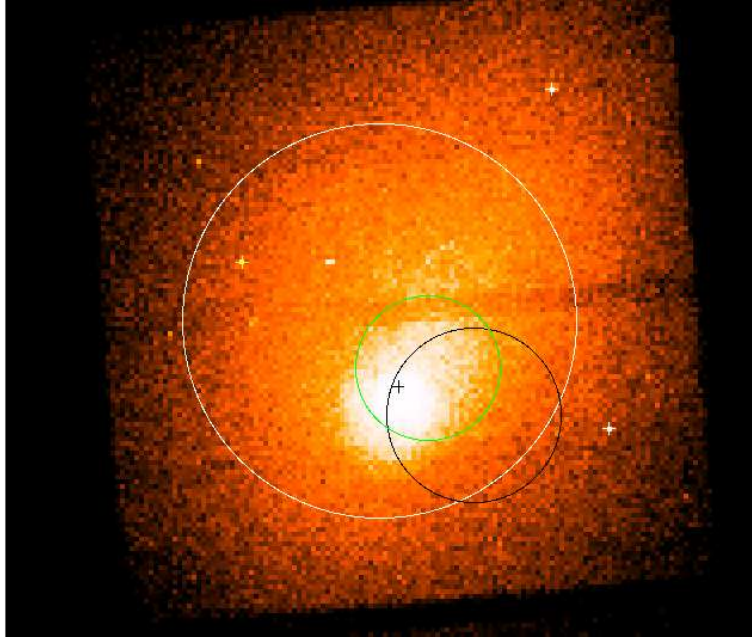


Figure 5.7: *Chandra image of the core of the Ophiuchus cluster. The circles represent the ISGRI best fit position in the 20-24 (green), 24-30 (black) and 30-40 keV (white) bands with 90% error radius. The black cross shows the position of the maximum emission in the cluster on the central cD galaxy, while white crosses show the position of the weak point sources in the cluster.*

error on the flux extracted by the standard OSA spectral extraction tool is $< 5\%$. For this reason, it is safe to treat the source as point-like for ISGRI.

Since the source is not resolved spatially, in principle we cannot exclude the possibility that a hard point source in the cluster (e.g. a very absorbed AGN) has a significant influence on the hard X-ray spectrum. Nevertheless, to study the energy dependence of the source we can compute the best-fit position of the source in several energy bands and compare the results to the low-energy morphology. For comparison, public *Chandra* data on the cluster with very high angular resolution ($< 1''$) are available, which allows us to distinguish the point sources from the diffuse emission. Figure 5.7 shows the 1-10 keV *Chandra* image of the cluster with 90% error circles for the position of the source in the 20-24, 24-30 and 30-40 keV bands. The black cross shows the position of the central cD galaxy, close to the maximum of the low-energy emission. On the other hand, the white crosses indicate the weak point sources detected by *Chandra*. One can clearly see that the best-fit ISGRI positions are well-centered on the central cD galaxy, and is not consistent with any of the weak point sources. This indicates that the emission detected by ISGRI is truly of diffuse origin, and that significant contamination of the high-energy spectrum by point sources is unlikely.

5.4 Broad-band spectrum of the cluster

For spectral analysis, we used the standard ISGRI OSA 7.0 spectral extraction software with a carefully-selected input source catalog (see Sect. 5.2.1), and extracted the JEM-X spectrum from the mosaic in 4 different energy bands in order to take the extension of the source into account (see Sect. 5.2.2). Unlike previous versions of OSA, the calibration of ISGRI is now valid down to 17 keV. Thanks to the very large exposure time, we were able to reach a high signal-to-noise spectrum from both JEM-X (3-18 keV) and ISGRI (17-60 keV). Thanks to the small overlap between the ISGRI and JEM-X energy ranges, we found that no cross-calibration factor between the two instruments was needed, which gives credit to the work of the instrument teams for the release of OSA version 7.0.

To analyze the resulting spectra, we used the XSPEC v11 package (Arnaud 1996) with appropriate instrumental response files. In a first approach, we fitted the total spectrum with a single MEKAL model (Kaastra & Mewe 2000), with the redshift of the cluster fixed to $z = 0.028$ (Johnston et al. 1981) and the abundance fixed to 0.49 relative to the solar value (Mohr et al. 1999). The fit gives a relatively high temperature ($kT = 10.8$ keV) in agreement with *ASCA* results (Watanabe et al. 2001), but the very high reduced chi-squared $\chi_{red}^2 = 2.3$ indicates that the data are not well represented by the model. Using only the 3-20 keV part of the spectrum, we found a good fit with a much lower temperature $kT = 8.5 \pm 0.4$ keV. Fig. 5.8 shows the total ISGRI/JEM-X spectrum and the residuals compared to the MEKAL model at $kT = 8.5$ keV fitted to the 3-20 keV part of the spectrum. Significant positive residuals are found in the high-energy part of the spectrum compared to the extrapolation of the model. This implies the presence of another spectral component in addition to the thermal bremsstrahlung emission. For instance, the bad representation of the data could be due to the presence of non-thermal hard X-ray emission. To test this possibility, we added a second component to the model, under the form of a power-law with photon index fixed to $\Gamma = 2.0$, similar to Nevalainen et al. (2004). The results of the fitting procedure with the addition of the second component can be found in Table 5.2. We can see in the table that the fit is significantly improved by the addition of the non-thermal component. In Method 1, the temperature and normalization of the thermal component are left free while fitting, while in Method 2, these 2 parameters are fixed to the value fitted to the low-energy part of the spectrum. We can see that the temperature values obtained with the two different ways are consistent, which proves that fixing the MEKAL component to the value fitted in the 3-20 keV band is relevant.

To evaluate the improvement to the fit when adding the non-thermal component, we computed the null-hypothesis probability given by the F-test. In more details, let n be the number of data points. We consider a model with p_1 number of parameters and a minimal χ^2 value χ_1^2 . Let model 2 with $p_2 > p_1$ be a more complicated model which gives a better fit to the data, $\chi_2^2 < \chi_1^2$. The F-statistic value is defined as

$$F = \frac{\chi_1^2 - \chi_2^2}{\chi_2^2} \frac{n - p_2}{p_2 - p_1}. \quad (5.3)$$

The probability that the decrease in χ^2 with the addition of new parameters is only due to

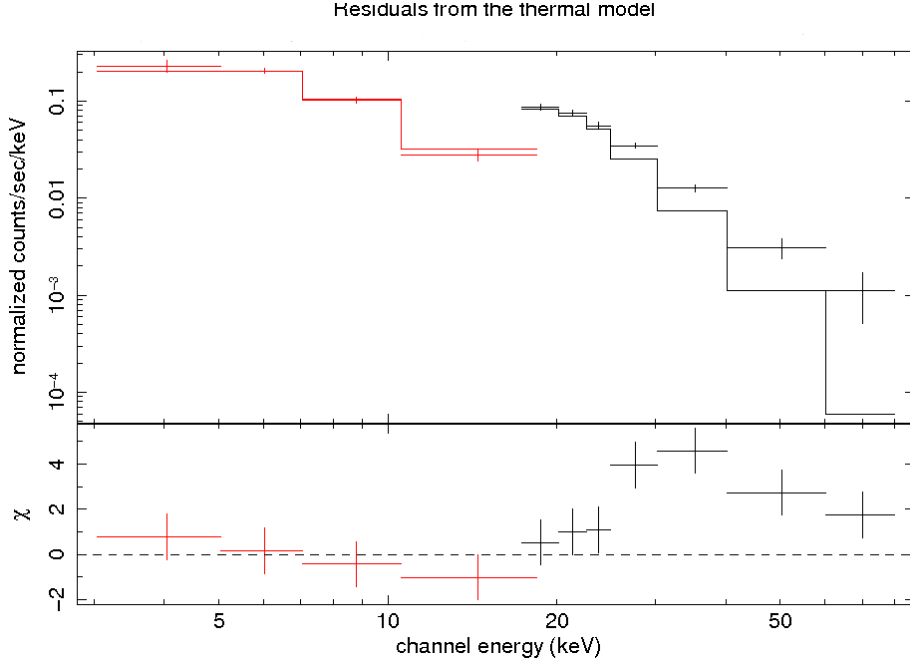


Figure 5.8: Combined *INTEGRAL* JEM-X (red) and ISGRI (black) folded spectrum of the Ophiuchus cluster. The solid line shows the model at $kT = 8.5 \pm 0.4$ keV fitted to the low-energy data (3-20 keV) and extrapolated to higher energies. The bottom panel shows the residuals from the model. A significant excess is found above 25 keV.

	χ_{red}^2	P_{F-test}^a	kT [keV]	Flux _{HXR} ^b	$CL_{HXR\sigma}^c$
Method 1	0.93	$2 \cdot 10^{-4}$	$8.56^{+0.37}_{-0.35}$	10.1 ± 2.5	4.0
Method 2	1.05	$7 \cdot 10^{-5}$	$8.50^{+0.48}_{-0.45}$	8.2 ± 1.3	6.4

Table 5.2: Results of the spectral fitting procedure for a thermal + power-law model, with abundance and redshift values fixed to the literature value and photon index fixed to $\alpha = 2.0$, similar to the work of Nevalainen et al. (2004). In Method 1, the temperature and the normalization of the bremsstrahlung component are left free while fitting. In Method 2, we used the data in the 3-20 keV band to fix the temperature and normalization of the thermal component, and let free only the normalization of the non-thermal component. ^a P_{F-test} is the null hypothesis probability when adding the non-thermal component given by the F-test. ^b 20-60 keV flux of the non-thermal component, in units of 10^{-12} ergs s^{-1} cm^{-2} . The errors are quoted at the 1σ level. ^c Confidence level for the detection of the non-thermal component.

chance is given by the probability associated with the corresponding F value, which can be numerically computed. In our specific case, the addition of a non-thermal component gives a more complicated model with a larger number of parameters. Computing the F-test probability is important to determine if the additional component is required by the data. The second column of Table 5.2 shows the null-hypothesis probabilities when adding the non-thermal component for the two methods. In both cases, the probability is small, which indicates that the fit is significantly improved by the addition of the non-thermal component. For comparison, Nevalainen et al. (2004) analyzed the *BeppoSAX* data by fixing the thermal component to the constraints obtained with the low-energy spectrum similarly to Method 2, and found a 2σ excess at high energies. With this method, we detect the non-thermal component at a much higher confidence level of 6.4σ .

Using Method 2, we were also able to constrain the acceptable range for the photon index of the power-law. Leaving only the photon index and normalization of the power-law free while fitting, we found $\Gamma = 1.62_{-0.35}^{+0.32}$. This is slightly harder than the photon index of 2.0 used to derive the properties of the non-thermal excess, but it is consistent with this value (within 1σ). With such a hard photon index, it is obvious that the excess cannot be due to the presence of a second thermal component. Indeed, if instead of a power-law we fit the excess with a second thermal component, we find an unrealistic lower limit of $kT \geq 50$ keV to the temperature of the second thermal component. This is consistent with the spectro-imaging results obtained from the JEM-X hardness ratio map (see Sect. 5.2.2), which did not reveal the presence of any specifically hot region within the core of the cluster. Therefore, we can conclude with high confidence that the high-energy excess detected by *INTEGRAL* is non-thermal.

5.4.1 Modeling the non-thermal component

We have found with good confidence that the hard X-ray flux detected with *INTEGRAL* is non-thermal. Moreover, comparison with the *Chandra* image (see Fig. 5.7) indicates that significant contamination of the observed spectrum by point sources is unlikely. Therefore, we conclude that there exists diffuse non-thermal emission from relativistic electrons in the cluster (see Chapt. 2). The natural explanation for the excess is inverse-Compton (IC) scattering with the Cosmic Microwave Background (CMB) of the same electrons which produce the radio emission through synchrotron radiation. In this framework, we used the compilation of existing radio data presented by Johnston et al. (1981) to constrain the shape of the Spectral Energy Distribution (SED) of the non-thermal emission from the cluster, and tried to model the resulting SED. To construct our models, we assumed a relativistic electron population with a power-law distribution with spectral index of 2.0, as is typical for shock-accelerated electrons, and a high-energy cut-off E_{cut} . Unfortunately, the existing radio data are old, and were measured by several instruments with very different beam size, so the exact shape of the radio spectrum could not be constrained. Nevertheless, by comparing the strength of the radio and hard X-ray emissions, and using the formula

$$\frac{P_{sync}}{P_{IC}} = \frac{u_B}{u_\gamma} = \frac{B^2/8\pi}{u_{CMB}}, \quad (5.4)$$

where P_{sync} , P_{IC} is the power emitted through synchrotron, respectively IC emission, B is the mean magnetic field strength and u_{CMB} is the well-known energy density of the Cosmic Microwave Background, we can constrain the mean magnetic field value in the cluster. The bottom panel of Fig. 5.9 shows the SED models computed for different values of magnetic field B and electron cut-off energy E_{cut} . Based on these models, we estimate the magnetic field strength to be

$$B \sim 0.1 - 0.2 \mu G. \quad (5.5)$$

This value is consistent with the value obtained with the same method by Fusco-Femiano et al. (1999) in the Coma cluster (see Sect. 2.7.3). However, it is one order of magnitude lower than the typical magnetic field strengths deduced from Faraday rotation measures (see Sect. 2.7.1). Unfortunately, no polarization measurement and high-resolution maps are yet available on the Ophiuchus cluster. With the help of the new generation of low-frequency radio arrays (GMRT, LOFAR), we will be able to probe the population of high-energy electrons and the magnetic field structure in the Ophiuchus cluster. In order to achieve this goal, we proposed a 30 hours Giant Metrewave Radio Telescope (GMRT) observation of the Ophiuchus cluster, which was accepted by the GMRT time allocation committee, and will be performed in August 26-30, 2008. The GMRT array consists of 30 antennae with a diameter of 45 m, with an excellent sensitivity (0.02 mJy at 610 MHz) and angular resolution (5 arcsec at 610 MHz). Thanks to the good sensitivity and angular resolution, we will be able to study the morphology of the radio source. We will also perform the observation at several different frequencies, which will enable us to better constrain the radio spectrum. Finally, we will also measure the polarization of a background source at different frequencies, which will enable us to measure the magnetic field of the cluster through Faraday rotation measure, and compare the result with the value inferred from synchrotron/IC flux ratio. This is extremely important to determine if the origin of the emission detected by *INTEGRAL* indeed comes from the same electron population as the radio emission.

On the other hand, if the mean magnetic field in the cluster is of the order of $1 \mu G$ as it is usually found from Faraday rotation measure, the inverse-Compton model for the HXR emission falls short of the observed value by about 1 order of magnitude. In this case, we have to consider other models for the origin of the HXR emission. In particular, the emission could be due to synchrotron emission from another population of electrons with very high energies ($E \sim 100$ TeV, see Sect. 2.5). The top panel of Fig. 5.9 shows several models for the SED of the non-thermal emission for different values of magnetic field B and cut-off energy E_{cut} . For magnetic field strengths $B = 1 - 10 \mu G$ and cut-off energies $E_{cut} \sim 0.1$ PeV, this model can explain the observed level of hard X-ray emission. Unfortunately, the lack of multi-wavelength information does not allow us to constrain this model any further. In the TeV γ -ray range, the figure also shows the 10 mCrab flux level, which corresponds more or less to the sensitivity level of the HESS Cherenkov telescope array. We can see that the relatively high level of TeV γ -ray emission predicted by this model could be detectable by HESS if the mean magnetic field value is not too high. Therefore, observations of the Ophiuchus cluster with HESS would bring an important input to the understanding of the *INTEGRAL* observations, even in the case of a non-detection. The main problem resides in the fact that the HESS instrument is

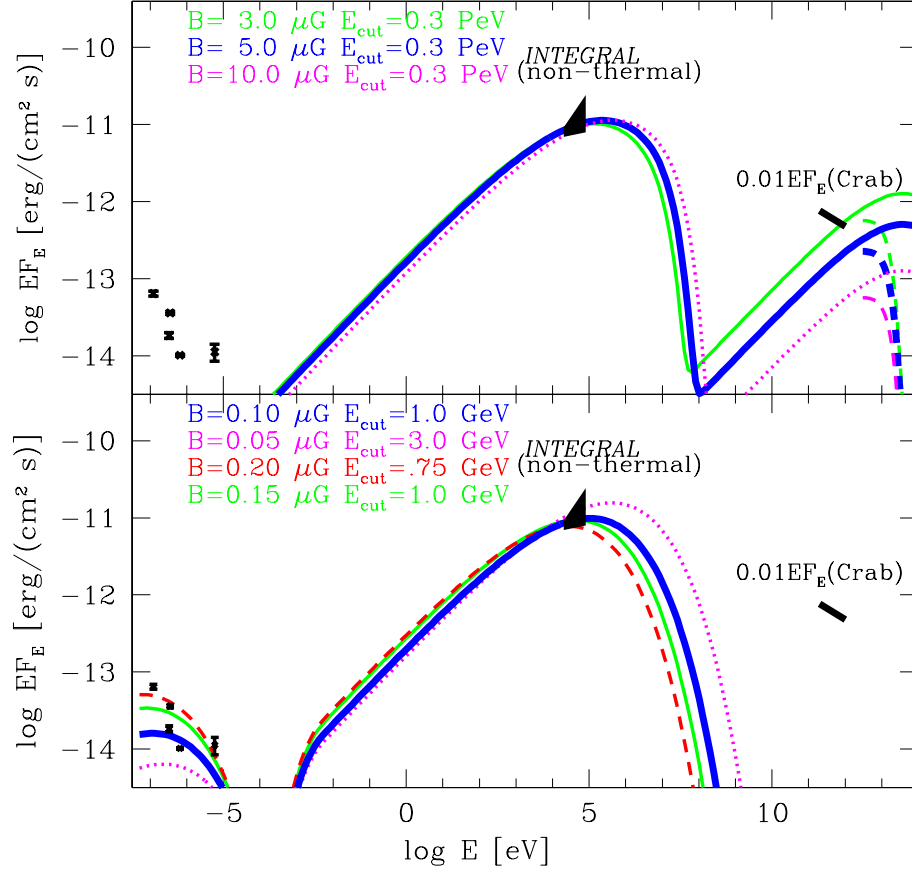


Figure 5.9: Models for the Spectral Energy Distribution (SED) of the non-thermal emission from the Ophiuchus cluster. The radio data are from Johnston et al. (1981). The black triangle represents the INTEGRAL measurement of non-thermal emission (this work). In the top panel, we considered a high-energy electron population of $E \sim \text{PeV}$ electrons radiating in the HXR range through synchrotron emission and in the TeV range through IC scattering, while in the bottom panel, a more conventional modeling with $E \sim \text{GeV}$ electrons was performed. The dashed lines above $\sim 10 \text{ TeV}$ shows attenuation of the spectrum by interaction of the γ -ray photons with the extragalactic infra-red and CMB radiation fields.

operated by a consortium of institutes, and does not work as an observatory. Hence, the observation possibilities for scientists which are not members of the HESS consortium are very small. Nevertheless, we also submitted an observation proposal to the HESS guest observer program, which was unfortunately rejected. We hope that a similar proposal will be accepted in the future for observation in the TeV γ -ray domain by a Cherenkov telescope.

5.5 Discussion

5.5.1 Reliability of the result

Our detection of high-energy emission from the Ophiuchus cluster is the most significant detection of non-thermal emission in a cluster of galaxies up to the present day (6.4σ), especially compared to the *BeppoSAX* claim. Thanks to the angular resolution of the JEM-X and ISGRI instruments, we were able to show that the morphology of the source does not depend on energy. Moreover, the high-resolution *Chandra* image does not show the presence of any bright point source, and therefore, we conclude with good confidence that the emission is truly of diffuse origin, and that any contribution of point sources to the observed spectrum is negligible. We also constructed a JEM-X hardness ratio map, which revealed that the core of the cluster is almost iso-thermal. Recently, this result was confirmed by Fujita et al. (2008) using high signal-to-noise data from the XIS instrument on board *Suzaku*. Together with the unrealistic lower-limit of 50 keV to the temperature of any additional thermal component, we can safely rule out the hypothesis that the excess emission at high energies is due to very hot thermal gas.

In any case, it is clear that the high-energy excess strongly depends on the temperature used to fit the thermal component. The JEM-X temperature measurement ($kT = 8.5$ keV) is one of the lowest published values, especially compared to *Tenma* and *ASCA* ($kT \geq 11.0$ keV, see Table 5.1). If the cluster is so hot, the high-energy excess could disappear. However, all recent measurements of the central temperature (*BeppoSAX*, *INTEGRAL*, *Suzaku*) converge to a similar temperature, $kT \sim 9$ keV. To double-check our result, we re-analyzed the data with a different spectral binning, and fixed the temperature of the gas to the *Suzaku*/XIS result ($kT = 9.3$ keV), because of the much better signal-to-noise compared to JEM-X. Figure 5.10 shows the resulting JEM-X/ISGRI spectrum with a thermal model at $kT = 9.3$ keV and an iron abundance of 0.33 fixed to the XIS value, fitted to the low-energy part of the spectrum (3-20 keV). While the low-energy data ($E < 20$ keV) are well-represented by the model ($\chi_{red}^2 = 1.1$ for 18 d.o.f.), we can see that the high-energy excess is still clearly seen. This proves that the result can still be reproduced with the higher value found by *Suzaku*.

Finally, the ISGRI spectrum could be affected by systematic effects due to the presence of a number of bright sources in the FOV of IBIS. This possibility must be considered seriously, since the ISGRI mosaic image extracted with the standard OSA 7.0 software is strongly affected by systematics. The presence of Scorpius X-1 and other bright hard X-ray sources in the FOV introduces important side lobes (“ghosts”) in the image, especially at low energy. However, we believe that the ISGRI spectrum is reliable. Indeed, while

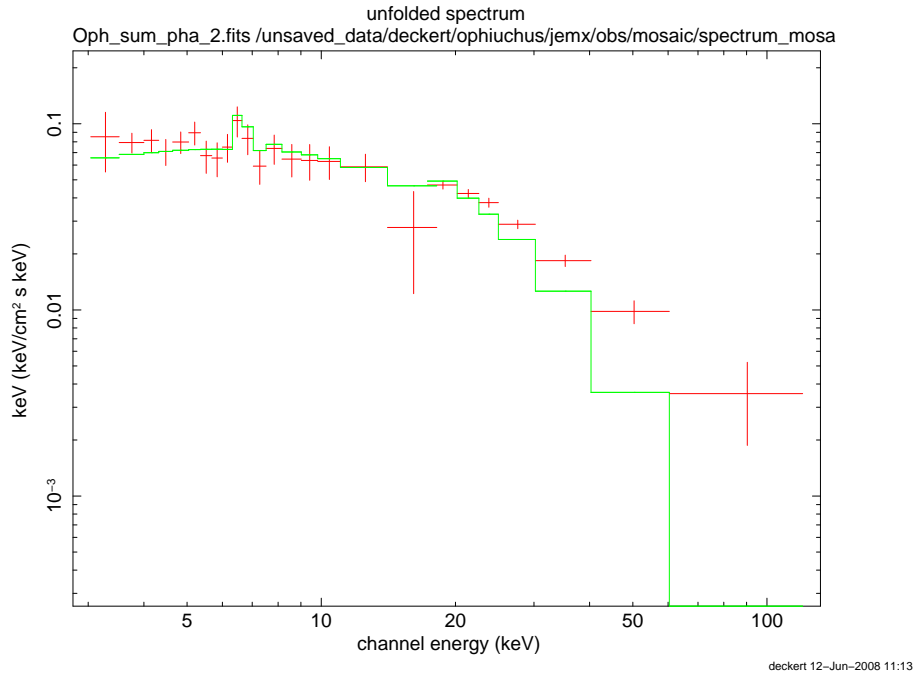


Figure 5.10: *INTEGRAL JEM-X/ISGRI spectrum of the Ophiuchus cluster. The solid line show the thermal model at $kT = 9.3$ keV and abundance 0.33 from Suzaku/XIS, fitted to the low-energy part of the *INTEGRAL* range (3-20 keV) and extrapolated to higher energies.*

the image reconstruction procedure performs cross-correlations to extract the flux of every sky pixel in the FOV, the spectral extraction method extracts the fluxes only at particular sky positions specified by the used and works in the detector space. Thus, it is known to be more robust than the image deconvolution procedure. Deep tests have been performed by the ISGRI and ISDC teams to determine the dependence of the spectral-extraction software on systematic effects, which show that the systematics are well-mastered in the case of spectral extraction. Moreover, in the standard ISGRI mosaic image of the region, no ghosts of strong sources are found around the position of Ophiuchus, so we conclude with good confidence that the ISGRI spectrum of the Ophiuchus cluster is reliable.

5.5.2 Origin of the non-thermal component

In the standard scenario for the origin of the non-thermal excess, the radio and hard X-ray components are produced by the same electrons via synchrotron and inverse-Compton radiation. The main advantage of this model is that it requires only one population of accelerated electrons. However, this model faces one major problem: the level of hard X-ray emission is too high compared to the predictions based on the radio emission and the magnetic field value deduced from Faraday rotation measure (see Sect. 2.7 for a detailed discussion). Even though no magnetic field estimates from Faraday rotation measure are yet available for the Ophiuchus cluster, the typical value measured with this method in a sample of galaxy clusters is in the range $B \sim 1 - 5 \mu G$ (see Sect. 2.7.1). With our forthcoming GMRT observation of the cluster, we will measure the magnetic field value with this method and compare it with the value $B \sim 0.1 - 0.2 \mu G$ which we measured

in this work by computing the ratio between the power emitted through synchrotron and inverse-Compton.

To reconcile the magnetic field values obtained with different methods, Goldshmidt & Rephaeli (1993) suggested a steep radial profile for the magnetic field, such that the radio emission, emitted through synchrotron radiation, would come mostly from the central regions of the cluster with high magnetic field ($B \gtrsim 1 \mu G$), while in the outer regions, the magnetic field would be much lower and IC losses would dominate. In the case of the Coma cluster, this explanation is viable, since the instrument which reported the high-energy excess, *BeppoSAX/PDS*, was non-imaging. However, in the case of the Ophiuchus cluster, the angular resolution of *INTEGRAL* allows us to rule out this hypothesis. Indeed, since we assumed that the source is point-like for the ISGRI spectral analysis, the emission detected by *INTEGRAL* must come from at most 6 arcmin from the center of the cluster, and hence the magnetic field value must be low in the cluster core.

If we find that the magnetic field value from Faraday rotation measure is of the order of $1 \mu G$, only two possibilities remain. Some mechanism (e.g. turbulence, Beck et al. (2003)) could introduce a bias in the magnetic field measurement through Faraday rotation. Indeed, the measurement of magnetic field through Faraday rotation requires some non-trivial assumptions about the topology of the magnetic field, which might not be fulfilled in this case. On the other hand, if this is not the case, then the origin of the non-thermal hard X-ray emission is not inverse-Compton.

In the case where the hard X-ray emission is not due to inverse-Compton of GeV electrons with CMB photons, several alternative models for the origin of the emission have been developed (see Sect. 2.5). If the emission is due to synchrotron radiation from very high energy electrons ($E \sim 100$ TeV, e.g. Timokhin et al. (2004)) in a magnetic field $B \gtrsim 1 \mu G$, our models predict a TeV γ -ray flux which would be detectable by the present generation of Cherenkov telescopes, in particular by the HESS experiment. Figure 5.9 shows that the detection limit of HESS corresponds to a magnetic field $\sim 10 \mu G$ in this model, which is approximately the highest acceptable value for the magnetic field. Therefore, even a non-detection would bring strong constraints to this model. In any case, this model faces a severe energetic problem. Indeed, the life-time of such high energy electrons is very short, so the amount of energy which must be supplied continuously throughout the cluster is enormous. Another alternative model is a non-Maxwellian distribution of the thermal electrons (see Sect. 2.5.1). Unfortunately, this model is rather hard to test, since it does not predict emission at other wavelengths. Like the synchrotron model, this model faces serious energetic problems, because a very large number of electrons should be accelerated to form a non-thermal tail in the Maxwellian distribution.

In conclusion, it is not yet possible to distinguish between the different models which explain the origin of the high-energy X-ray emission. The observation of the cluster in the radio domain with the GMRT will definitely help us to understand the mechanism which produced the hard X-ray emission by constraining the radio spectral shape and the magnetic field. Observations at TeV wavelengths with the present generation of Cherenkov telescopes, if performed, would also bring an important input to our understanding of the

non-thermal emission.

5.5.3 Origin of the high-energy electrons

Although the origin of the hard X-ray emission is not yet known, it is clear that a population of relativistic electrons is present in the cluster. The different mechanisms which could be responsible for the presence of high-energy particles were presented in Chapt. 2. Two main models, the so-called *primary* and *secondary* electron models, have been developed to explain the origin of the high-energy particles.

In the primary electron model, the electrons are directly accelerated (or re-accelerated) through diffusive shock acceleration. Since the life-time of the high-energy electrons is rather short (< 1 Gyr), signs of recent or on-going merging activity must therefore be present. In the case of the Ophiuchus cluster, the state of the gas in the cluster is still under debate. Indeed, while earlier *ASCA* observations indicated a complex temperature structure and an asymmetric surface brightness profile, which are typical for a merging cluster, recent *Suzaku* observations revealed a flat temperature profile, a quasi-symmetric structure and maybe even a weak cooling-core. Unlike previous results, these properties indicate that the cluster is in a relaxed state. This property would be rather unique, since usually a very hot temperature is always associated with signs of a merging event. If this is the case, the electrons cannot be of primary origin. Another possibility is that the collision is seen head-on and is in an early phase of merging. In this case, the rather poor angular resolution of *Suzaku* (2 arcmin) is not sufficient to distinguish the different sub-structures, and observations of the cluster e.g. by *XMM-Newton* would be required.

If the cluster is not in a merging phase, the secondary electron model seems to be more appealing. Indeed, the model suggests that the electrons are continuously produced by proton-proton collisions throughout the cluster. Since the relativistic protons do not radiate, their life-time is very long, and they can be trapped by the potential well of the cluster for timescales similar to the Hubble time. Since the Ophiuchus cluster is very massive (with a mass of $\sim 2 \times 10^{15} M_{\odot}$ within R_{200} (Pfrommer 2007), it is the most massive nearby cluster), it is reasonable to think that a large population of cosmic-ray protons, accelerated some time in the past by several mechanisms (merging events, AGN jets, supernovae), would still be present in the cluster. Another advantage of the model is that it predicts a low magnetic field value. Indeed, it is well-known (e.g. from observation of supernova remnants) that in shock regions the magnetic field can be strongly amplified. Therefore, primary models would have trouble to reproduce the low magnetic-field value $B \sim 0.1 - 0.2 \mu\text{G}$ inferred from synchrotron/IC flux ratio, while in the secondary model, no shock region need to be present at the current time, so the magnetic field value is expected to be smaller.

If the origin of the electrons is secondary, observations of the cluster in the GeV range by the LAT instrument on board *GLAST* will be crucial. Indeed, this model predicts a strong flux at this energy range through π^0 decay. If a large π^0 -decay flux is detected by *GLAST*, it will be a direct proof of the secondary origin of the high-energy electron population.

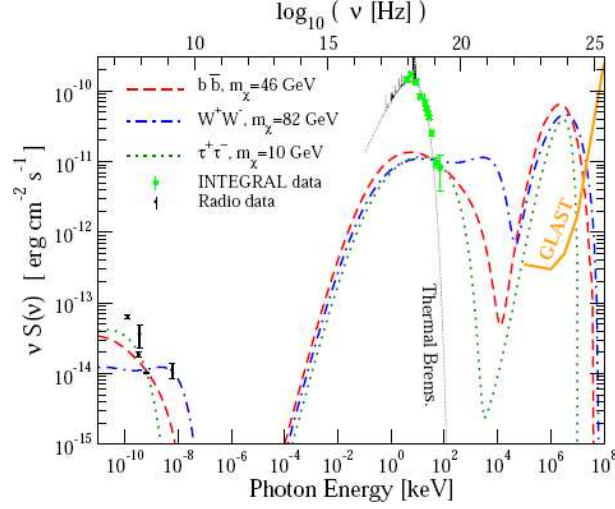


Figure 5.11: Spectral Energy Distribution of the Ophiuchus cluster fitted by a dark-matter annihilation model (Profumo 2008). The radio data are from Johnston et al. (1981) and the X-ray data are from this work. The thermal bremsstrahlung emission was fixed to the MEKAL model at $kT = 8.5$ keV fitted to the JEM-X data.

Recently, an alternative model for the origin of the electrons was proposed by Profumo (2008). Since, as a very massive cluster, the Ophiuchus cluster retains a very large amount of dark matter, the author investigated the production of high-energy electrons in the Ophiuchus cluster through decay of several candidates for the Weakly Interacting Massive Particles (WIMPs), $b\bar{b}$, W^+W^- and $\tau^+\tau^-$. This model also predicts a high flux in the GeV range through direct dark-matter annihilation, which would be firmly detectable by GLAST (see Fig. 5.11). While the existence of a large number of such particles in the cluster is hypothetical, observations of the non-thermal emission from clusters could, if confirmed, give a very important input to the long-standing dark-matter problem.

5.6 Conclusion

The Ophiuchus cluster is a very interesting object, because it is the most massive cluster in our close neighbourhood ($z = 0.028$), and its temperature structure (a cooling-core cluster at $kT = 9$ keV?) is rather unique. Thanks to a very long (3 Ms) observation of Ophiuchus with *INTEGRAL*, we were able to detect unambiguously, at a very robust statistical significance (6.4σ), the sign of non-thermal hard X-ray emission. This result is extremely important, because it settles the long-standing issue of the existence or not of non-thermal hard X-ray emission at a high level in clusters of galaxies.

Of course, it will be important to confirm our results with other instruments. Recently, Fujita et al. (2008) presented an analysis of a first 100 ksec *Suzaku*/HXD data in the hard X-ray domain. No high-energy excess was found in the HXD spectrum. However, we note that their upper limit on the HXR emission (3.5×10^{-11} ergs cm^{-2} s^{-1}) is almost 4 times higher than the emission detected by *INTEGRAL*, and is therefore fully consistent

with our result. A second 100 ksec *Suzaku* observation has recently been performed, and the modeling of the HXD background, which is crucial for a non-imaging instrument, is still improving. Unfortunately, it seems that given the uncertainties on the background estimate, a 200 ksec observation with *Suzaku*/HXD will not be sufficient to confirm our result. In the near future, focusing hard X-ray missions such as *Simbol-X*, *NeXT* and *NuSTAR* will bring a sensitivity improved by at least 2 orders of magnitude compared to *INTEGRAL*, together with excellent angular resolution ($\lesssim 1$ arcmin) up to 80 keV. With these missions, it will be possible to map the hard X-ray emission throughout the cluster and correlate it with the radio emission in order to probe the magnetic field structure and locate the particle acceleration sites.

As explained in Sect. 5.5, the origin of the high-energy emission is still unclear. In the standard inverse-Compton scenario, the low magnetic field value measured through the ratio between the power emitted through synchrotron and inverse-Compton emission is puzzling, because it falls short by 1 order of magnitude of the typical values measured through Faraday rotation. If a more standard magnetic field value is used, then the hard X-ray emission cannot be due to inverse-Compton scattering. In this case, alternative models (synchrotron emission from multi-TeV electrons, non-Maxwellian distribution of the thermal electrons) should be considered. Regarding the origin of the high-energy electrons, recent *Suzaku* results (Fujita et al. 2008) indicate that the cluster is basically in a relaxed state, which discards the standard primary models where electrons are directly accelerated in merging events. In this case, secondary models where the electrons are produced by proton-proton collisions or dark-matter annihilation are favoured. In any case, multi-wavelength information (at radio, GeV and TeV energies) is required to better constrain the spectral energy distribution of the non-thermal emission from the cluster. In particular, the Ophiuchus cluster will be a very appealing target for the *GLAST* mission, which has been launched on June 10, 2008. Indeed, according to Pfrommer (2007), Ophiuchus should be by far the brightest cluster in the GeV range, and should be easily detectable for *GLAST*. *GLAST* observations will therefore bring a crucial input to the understanding of the population of high-energy particles in the cluster.

5.7 Scientific article on the Ophiuchus cluster

A&A 479, 27–34 (2008)
 DOI: 10.1051/0004-6361:20078853
 © ESO 2008

**Astronomy
&
Astrophysics**

INTEGRAL discovery of non-thermal hard X-ray emission from the Ophiuchus cluster

D. Eckert, N. Produit, S. Paltani, A. Neronov, and T. J.-L. Courvoisier

ISDC, Geneva Observatory, University of Geneva, 16, ch. d'Ecogia, 1290 Versoix, Switzerland
 e-mail: Dominique.Eckert@obs.unige.ch

Received 15 October 2007 / Accepted 5 December 2007

ABSTRACT

We present the results of deep observations of the Ophiuchus cluster of galaxies with *INTEGRAL* in the 3–80 keV band. We analyse 3 Ms of *INTEGRAL* data on the Ophiuchus cluster with the IBIS/ISGRI hard X-ray imager and the JEM-X X-ray monitor. In the X-ray band using JEM-X, we show that the source is extended, and that the morphology is compatible with the results found by previous missions. Above 20 keV, we show that the size of the source is slightly larger than the PSF of the instrument, and is consistent with the soft X-ray morphology found with JEM-X and ASCA. Thanks to the constraints on the temperature provided by JEM-X, we show that the spectrum of the cluster is not well fitted by a single-temperature thermal Bremsstrahlung model, and that another spectral component is needed to explain the high energy data. We detect the high energy tail with a higher detection significance (6.4σ) than the *BeppoSAX* claim (2σ). Because of the imaging capabilities of JEM-X and ISGRI, we are able to exclude the possibility that the excess emission comes from very hot regions or absorbed AGN, which proves that the excess emission is indeed of non-thermal origin. Using the available radio data together with the non-thermal hard X-ray flux, we estimate a magnetic field $B \sim 0.1\text{--}0.2 \mu\text{G}$.

Key words. galaxies: clusters: individual: Ophiuchus – X-rays: galaxies: clusters – gamma rays: observations

1. Introduction

Clusters of galaxies are the biggest bound structures of the universe, and, according to the hierarchical scenario of structure formation, the latest ones to form. They are filled by a hot ($10^7\text{--}10^8$ K) plasma, called intra-cluster medium (ICM), and thus radiate in soft X-ray bands through thermal Bremsstrahlung.

The most massive clusters should form by merging of smaller clusters, that would create shock waves when the ICM of the clusters merges (Sarazin 1999). Such events are probably the major source of heating in the ICM. Models predict that a large population of relativistic electrons should be created during the merging event, which are expected to radiate through synchrotron emission in the radio domain, and through inverse-Compton (IC) scattering with the cosmic microwave background (CMB) in the hard X-ray band (Ensslin & Biermann 1998). Another possible model involves a population of multi-TeV electrons that would radiate in hard X-rays through synchrotron emission (Timokhin et al. 2004). While the extended radio emission from several clusters has been known for a long time (see e.g. Ferretti & Giovannini 2007), there is still no firm detection of the hard X-ray emission. *BeppoSAX* observations report on the detection of a hard tail in the X-ray spectrum of at least Coma (Fusco-Femiano et al. 2004) and Abell 2256 (Fusco-Femiano et al. 2005), but these detections are rather weak and controversial (Rossetti & Molendi 2004). Hence, confirmation of these results by other instruments is important.

The Ophiuchus cluster is the second brightest cluster in the 2–10 keV band. It is a nearby ($z = 0.028$, Johnston et al. 1981) rich cluster located in the direction of the Galactic Center ($l = 0.5^\circ$, $b = 9.4^\circ$), with a very high plasma temperature ($kT \sim 10$ keV). Using *ASCA* data, Watanabe et al. (2001) showed that the cluster is not dynamically relaxed and exhibits some regions with very high temperature ($kT > 13$ keV). Because these

characteristics are very similar to the Coma cluster, they concluded that this cluster has also experienced a major merging event in the recent past. In the radio domain, Johnston et al. (1981) claimed that the source is associated with the steep-spectrum radio source MSH 17-203. The identification of this radio source as a radio halo from the Ophiuchus cluster implies the presence of relativistic electrons, and hence predicts the presence of a non-thermal high-energy tail in the X-ray spectrum. Nevalainen et al. (2004) searched for such an excess in a sample of nearby clusters with *BeppoSAX*/PDS. For the Ophiuchus cluster, their analysis reveals a mean temperature of 9.1 ± 0.6 keV, and a 2σ excess at hard X-rays. However, at such a low significance level, the excess might as well be due to statistical fluctuations or instrument systematic effects. Moreover, the PDS instrument on board *BeppoSAX* was non-imaging, so it was impossible to extract any information on the morphology of the hard X-ray emission. Therefore, the spectrum might be contaminated by absorbed point sources.

In this paper, we present the results of deep (3 Ms) observations of the Ophiuchus cluster with the IBIS/ISGRI and JEM-X instruments on board *INTEGRAL*, in the aim of investigating the presence of a high-energy tail. We present the specific method we have used to analyse ISGRI data. Finally, we use radio data to consider possible models for the non-thermal emission of this object.

2. Data analysis

2.1. ISGRI data analysis

The IBIS/ISGRI instrument on board *INTEGRAL* (Lebrun et al. 2003) is a wide-field ($29^\circ \times 29^\circ$) coded-mask instrument sensitive in the 15–400 keV band. Its angular resolution (12 arcmin FWHM nominal) is of the same order of magnitude as the size of the core of the cluster (diameter $\sim 10'$,

Watanabe et al. 2001). Because of the large field-of-view (FOV) and the fact that *INTEGRAL* spends a significant part of its observing time in the Galactic Bulge region, the amount of data accumulated by the instrument on the Ophiuchus cluster is quite large, which allows us to reach a high signal-to-noise ratio for the cluster in the 17–60 keV band. Our analysis covers 1580 pointings (or Science Windows, ScWs), including 1493 ScWs from public data and 87 from the *INTEGRAL* AO-4 Key Programme, for a total observing time of 3 Ms. However, the location of the source (9.3° from the Galactic Center and 14.5° from the very bright X-ray binary Sco X-1) makes difficult the imaging analysis of this region with ISGRI. Furthermore, the periodic shape of the IBIS mask causes the images generated by the standard Offline Scientific Analysis software (OSA, Courvoisier et al. 2003) to present ghosts of bright sources which are not completely removed at some specific positions in the deconvolved sky images. This adds important systematic errors to long exposure mosaics in the vicinity of bright sources.

In a coded-mask instrument, the sky images are produced by the deconvolution of the shadow patterns cast by the sources in the FOV on the plane of the sky. When observing a single source, a large fraction of the detector (>45%) is not illuminated by the source, which allows us to measure the level of the background in each pointing. The detector image, or “shadowgram”, produced when observing a field containing n sources is a superposition of the shadow patterns of all the individual sources,

$$S(x, y) = \sum_{i=1}^n f_i \cdot PIF_i(x, y) + bB(x, y), \quad (1)$$

where f_i and $PIF_i(x, y)$ are respectively the flux of the i th source and the shadow pattern (called “pixel illumination fraction”) it casts, and $B(x, y)$ is a “background map”, i.e. a model of the background, in the pixel with coordinates (x, y) . Therefore, $bB(x, y)$ gives the total background model in the pixel (x, y) . If the background was flat over the whole detector, the deconvolution process would not be sensitive to the background. Therefore, background maps take the deviations from the flat background into account. The properties of the coded mask method allow us to compute a background map by averaging the count rates of a pixel for many pointings, excluding the pixels illuminated by a strong source. To take the variability of the background into account, we computed a specific background map for each revolution of *INTEGRAL*.

To the present day, the exact shape of the IBIS mask is not completely understood, so the PIFs created by the standard OSA software are not perfectly correct. The occurrence of even a handful of wrongly modelled pixels can very strongly affect image reconstruction. The identification of these pixels is made difficult by the fact that bright sources do also affect counts in exposed pixels, which should not be removed. In order to identify badly modelled pixels, we proceed in the following way: we fit the model described in Eq. (1) to the shadowgram and extract the background level and the flux of the sources present in the FOV. Then we remove bright sources and background from the shadowgram:

$$S'(x, y) = S(x, y) - \sum_{i=1}^n f_i \cdot PIF_i(x, y) - bB(x, y), \quad (2)$$

with error map given by error propagation. In the case of a perfect PIF, the pixel distribution of the transformed detector image would be Gaussian, and hence 99.7% of the pixels would have a value within $[\mu - 3\sigma, \mu + 3\sigma]$. Since the ISGRI detector contains

~15 000 pixels, statistically we expect ~45 of them to show a deviation from the mean value larger than 3σ . However, we notice that ~150 pixels deviate from the mean value by more than 3σ , so we conclude that a large fraction of these pixels are incorrectly modelled. Then we perform a standard OSA 7.0 analysis ignoring these pixels. We also neglect the outer parts of the image (with off-axis angle >14°), where the systematic effects are the most important. Finally, we make a mosaic from the modified images in a standard way.

Unlike the image reconstruction process, the standard OSA spectral extraction procedure does not suffer from these problems as long as the input source catalog contains all sources brighter or comparable with the analysed source. Therefore, for spectral extraction we performed a standard OSA 7.0 analysis with a source catalog extracted from the mosaic image.

2.2. JEM-X data analysis

The JEM-X X-ray monitor on board *INTEGRAL* (Lund et al. 2003) consists of two identical X-ray detectors with coded mask, JEM-X 1 and JEM-X 2, sensitive in the 3–35 keV band. It is designed for the spectroscopic and imaging study of the sources detected by IBIS, with a better spatial resolution (3.35 arcmin FWHM nominal) and a field-of-view of 7.5° half-response in diameter. On the Ophiuchus cluster, we reached a 160 ks effective exposure time, for a total observing time of 350 ks.

The analysis of the Ophiuchus field with JEM-X does not present the same difficulties as those affecting the IBIS observations. Indeed, both the Galactic Center and Sco X-1 are outside the field of view of JEM-X. We therefore performed a completely standard image analysis, taking advantage of the improvements in the image reconstruction process introduced in OSA 7.0, in particular regarding the astrometry. In order to reach the deepest sensitivity of JEM-X, we combined all JEM-X 1 and JEM-X 2 ScWs in a single mosaic. Spectral extraction has been performed by extracting the fluxes from this mosaic in four separate energy bands chosen to provide clear detection in each individual band and to complement the ISGRI spectrum without gap. The fact that the Ophiuchus cluster is probably extended with JEM-X is not a problem, since the flux is integrated over the source. Therefore we simply let the width of the fitted Gaussian free.

When extracting fluxes from JEM-X mosaics, there is no standard way in OSA to provide associated responses. The redistribution matrices (RMFs) of both JEM-X instruments are stable with time and quite close for both instruments; we therefore simply use the RMF of JEM-X 1. The area responses (ARFs) are however varying both with time and with the instrument. In particular, the low-energy efficiency changed very strongly (by a factor close to 3 for JEM-X 1) when the event rejection criteria were modified. It is therefore necessary to build an ARF suitable for the analysis of the spectrum extracted from the combined mosaic. To do this, we extract the correct ARF for each ScW and calculate the average of these ARFs weighted by the effective exposure time for each ScW, taking into account the dead time and the vignetting. As most observations use JEM-X 1 with the new rejection criterion, in practice the resulting ARF is quite close to that valid for any of the late JEM-X 1 ScWs. Therefore, the choice of a particular ARF does not affect qualitatively any of the results presented in this paper.

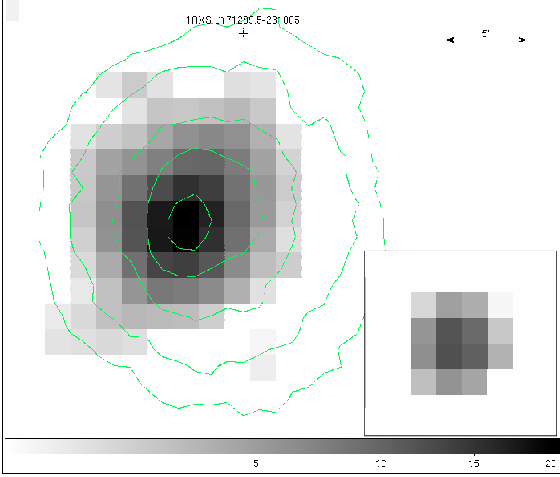


Fig. 1. JEM-X significance image in the 3–18 keV band, with surface brightness contours from ASCA overlaid. The inset shows the image of a known point source in the same field, V 2400 Oph, to show the extended nature of the source. The cross shows the position of 1RXS J171209.5-231005, the nearest X-ray point source.

3. Imaging results

As demonstrated in Eckert et al. (2007) for the Coma cluster, the angular resolution of *INTEGRAL* can be sufficient to get important information on the morphology of the hard X-ray emission from clusters. Since the Ophiuchus cluster is a very bright cluster below 10 keV, one can use the JEM-X monitor to study the change in morphology with energy. Figure 1 shows the JEM-X mosaic image of the cluster in the 3–18 keV band, with contours from ASCA/GIS observations of the cluster. For comparison, the inset shows the JEM-X image of the cataclysmic variable V 2400 Oph, in the same field. The extended nature of the Ophiuchus cluster in the JEM-X images is clear.

Because we detect only the core of the cluster, it is not possible to fit the surface brightness with an isothermal beta profile, but fitting the image with a Gaussian model,

$$I(r) = A \exp\left(-\ln(2)\frac{r^2}{R^2}\right), \quad (3)$$

where R is the half-width at half-maximum (HWHM), one can get an indication of the size of the detected region and of possible deviations from the spherical model. Fitting the JEM-X image shown in Fig. 1 with the model described in Eq. (3), we find $R = 3.6 \pm 0.1$ arcmin. This value is significantly larger than the PSF of JEM-X (1.8 arcmin HWHM), which confirms that the source is seen as extended. This is, after SN 1006 (Kalemci et al. 2006), the second report of an extended source for JEM-X. The R parameter corresponds to the superposition of the radial profile of the source and of the PSF of the instrument, $R^2 = R_{\text{source}}^2 + \text{HWHM}_{\text{JEM-X}}^2$. Therefore, the angular size of the source at half-maximum becomes $R_{\text{source}} = 3.1 \pm 0.1$ arcmin. Figure 2 shows the radial profile of the source compared to the PSF of the instrument, as well as the total apparent radial profile from JEM-X data. We can see that the radial profile is well modelled by a Gaussian. The extension of the source is clear.

From ASCA data, Watanabe et al. (2001) find the same value for the core of the cluster, $R_c = 3.2'$. They also report on an extended region North-West of the center of the cluster that shows

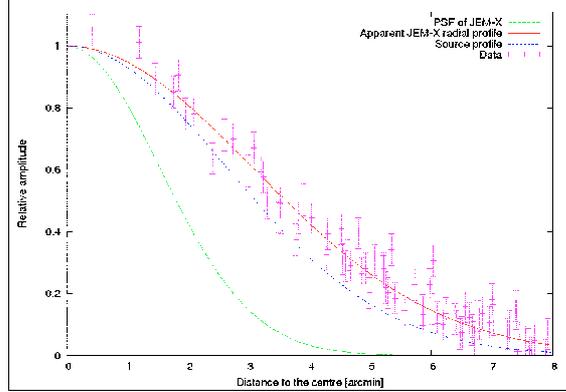


Fig. 2. Radial profile of the source with a core radius of $3.1'$ extracted from JEM-X data (dashed blue line), compared to the PSF of the instrument (dashed green). The solid red line shows the total apparent JEM-X profile. The purple bars show the data points extracted from the JEM-X image.

significant deviations from the spherical model. The authors note that this excess coincides with the closest X-ray point source, 1RXS J171209.5-231005. Figure 3 shows the residuals of the JEM-X image compared to the spherically symmetric model. A clear excess North-West of the center is also visible. However, it is clear that this excess is not due to 1RXS J171209.5-231005, which is located outside the region detected by JEM-X. The deviations from the spherical model are hence more likely due to over-densities or excess temperatures in the ICM, which indicates that the cluster is not dynamically relaxed, probably because of a merger in its recent history.

We used the available JEM-X data to create a hardness ratio map (7–18 keV to 3–7 keV) in order to estimate the temperature variations within the detected region of the cluster. To estimate the dependence of the JEM-X 7–18 to 3–7 keV hardness ratio with temperature, we simulated JEM-X spectra for models with different input temperatures and computed the hardness ratios. The result is shown in the top panel of Fig. 4. Because of the sensitivity up to 18 keV, the temperature dependence is steeper than in the case of ASCA. In the center of the cluster, we find a hardness ratio $HR = 0.78 \pm 0.09$, which corresponds to a temperature $kT = 9.1^{+1.4}_{-0.9}$. The bottom panel of Fig. 4 shows the deviations of the hardness ratio compared to the central value, in units of σ . We find no deviations to the central value at significance level above 0.7σ , which corresponds to variations of ± 2 keV compared to the central value. In ASCA data, although there is evidence for a strong spatial dependence of the temperature, this dependence is found only in the outer parts of the cluster, while the core, which is the only region detected by JEM-X, shows an almost iso-thermal profile, compatible with the JEM-X results. This analysis shows that a single-temperature model should describe well the total JEM-X spectrum.

Figure 5 shows the ISGRI significance image in the 20–40 keV band extracted from the mosaic created with the method described in Sect. 2.1. Because of the lower spatial resolution, the extension of the source is not obvious (see the image of V 2400 Oph in the inset for comparison). However, a more detailed analysis of the source reveals that the source is indeed extended also for ISGRI. Fitting the image with the model described in Eq. (3), one finds $R = 8.9 \pm 0.3$ arcmin, which

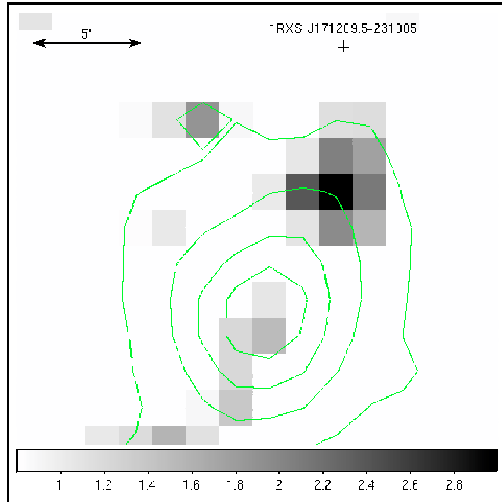


Fig. 3. Residuals from the spherically symmetric model with JEM-X brightness contours overlaid, in units of σ . Similar to previous *ASCA* observations, a significant excess is found North-West of the center of the cluster.

is slightly larger than the PSF of the instrument (7.2 arcmin HWHM). Taking into account the contribution of the radial profile of the source and of the PSF of the instrument similar to the analysis presented above for JEM-X, this corresponds to $R_{\text{source}} = 5.1^{+0.5}_{-0.6}$. Even though the source is seen as extended, the apparent size of the Ophiuchus cluster is smaller than the PSF of the instrument. To estimate the error on the standard flux extraction in the case of extended sources, Renaud et al. (2006) presented the results of simulations assuming a uniform disk. For an angular size of $5'$, they evaluate the relative error to be $\sim 5\%$. Since the cluster has a peaked radial profile instead of a uniform disk, the relative error on the flux extracted by the OSA spectral extraction tool is $< 5\%$. For this reason, from now on we will treat the source as point-like for ISGRI.

Since the apparent size of the source is smaller than the PSF of ISGRI, it is not possible to study in detail the hard X-ray morphology of the source. However, it is possible to measure the best fit position for the center of the source in different energy bands. Figure 6 shows the 90% error circles for the position of the source in the 20–24, 24–30 and 30–40 keV bands overlaid on the JEM-X 3–18 keV mosaic image. The yellow cross shows the position of the center of the cluster from the *Chandra* image. The black crosses represent the position of the 2 brightest point sources close to the center in the *Chandra* image. We can see on this image that the hard X-ray emission is compatible with the soft X-ray morphology of the cluster, and is not displaced towards any of the weak point sources seen in the *Chandra* image, which excludes the possibility that these point sources contribute in a significant way to the high-energy spectrum.

4. Spectral analysis

4.1. *INTEGRAL* broad band spectrum of the cluster

Since, unlike the case of the Coma cluster, the source is only very slightly larger than the PSF of ISGRI, we can use the standard OSA 7.0 spectral extraction tool with our time-dependent background maps to get an accurate flux estimation. Starting from

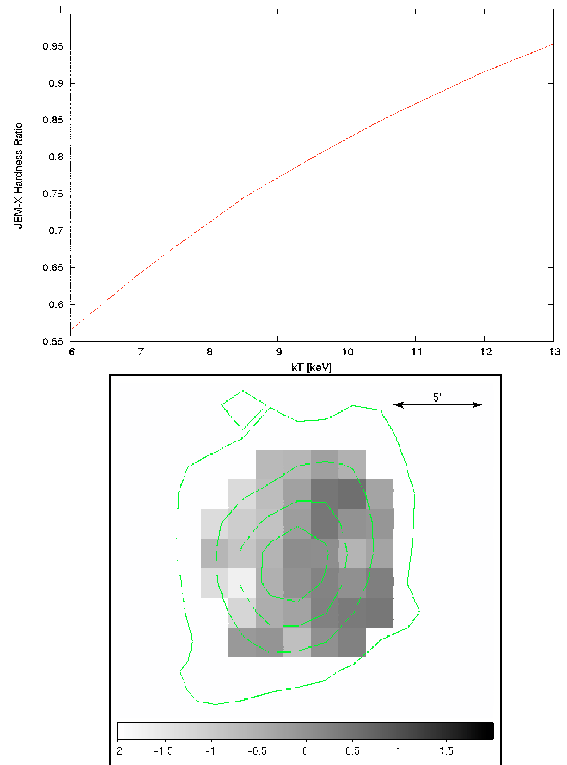


Fig. 4. *Top:* simulated JEM-X 7–18/3–7 keV hardness ratio as a function of temperature. *Bottom:* Deviations of the JEM-X 7–18/3–7 keV hardness ratio compared to the central value in units of σ , with JEM-X brightness contours overlaid. The map does not show any significant spatial dependence of the temperature within the detected region.

OSA version 7.0, the calibration of ISGRI is now valid down to 17 keV. Because of the large exposure time, we were able to reach a high signal-to-noise ratio in both JEM-X (3–18 keV band) and ISGRI (17–60 keV band). In the 40–60 keV band, the detection significance reaches 6σ . In the 60–80 keV band, the source is marginally detected by ISGRI at the 1.5σ level. It is important to note that no cross-calibration factor between ISGRI and JEM-X data was needed for this work. Introducing such a factor in the XSPEC fitting model results in a cross-calibration of 1.0, which shows the excellent calibration work done by the ISGRI and JEM-X teams for the release of OSA 7.0.

Fitting the combined JEM-X/ISGRI data with a single-temperature MEKAL model (Kaastra & Mewe 2000), with the abundance fixed to 0.49 compared to the solar value (Mohr et al. 1999) and redshift fixed to $z = 0.028$ (Johnston et al. 1981), one finds a bad representation of the data, with a reduced χ^2 exceeding 2.3. Another spectral component is hence needed to get a better fit to the data. Figure 7 shows the combined JEM-X/ISGRI spectrum and the residuals from the thermal model with temperature $kT = 8.50$ keV fitted to the spectrum below 20 keV. The model exhibits significant residuals above 20 keV, which could be due to the presence of an additional non-thermal component. Similar to Nevalainen et al. (2004), we assume that the non-thermal component is a power-law with a fixed photon index $\alpha = 2.0$. Figure 8 shows the unfolded spectrum with the

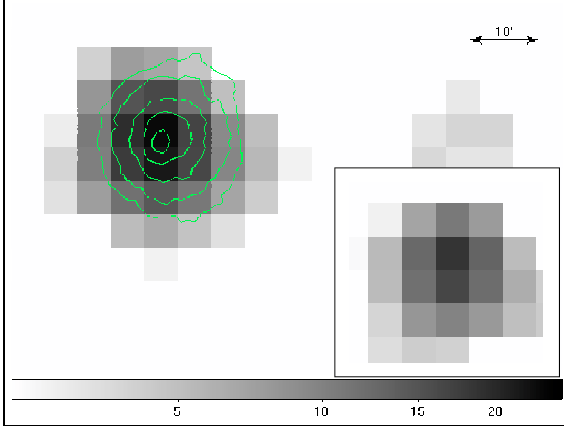


Fig. 5. ISGRI significance map in the 20–40 keV band, with surface brightness contours from ASCA in green. The inset shows the ISGRI image of a point source, the cataclysmic variable V 2400 Oph, for comparison.

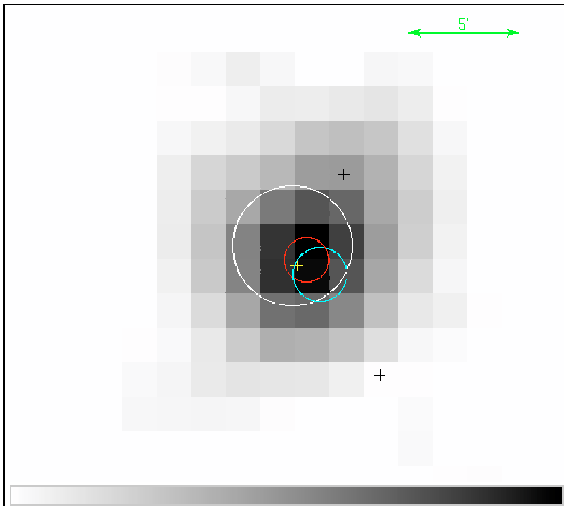


Fig. 6. 90% error circles for the position of the center of the source in the 20–24 (red), 24–30 (blue) and 30–40 keV (white) ISGRI mosaic images, overlaid on the JEM-X 3–18 keV image. The yellow cross shows the position of the centroid of the cluster from the *Chandra* image. The black crosses show the position of the two brightest X-ray point sources detected in the *Chandra* image.

thermal model and an additional power-law component fitted simultaneously (Method 1). Table 1 shows the results of the fitting procedure using such a power-law in addition to the thermal emission, with the plasma temperature left free while fitting (Method 1) and fixed to the value found by fitting independently the 3–20 keV part of the spectrum (Method 2), which is expected to be completely dominated by the thermal component. The *BeppoSAX* claim (2σ excess at high energies) was obtained by fixing the temperature to the value obtained from the low-energy spectrum, which is similar to Method 2. Therefore, we can see that the clear excess (6.4σ) detected with this method

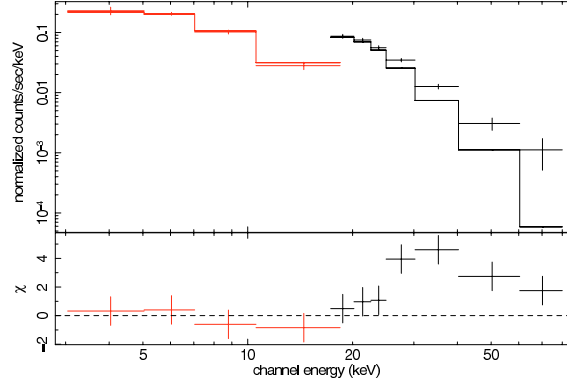


Fig. 7. JEM-X/ISGRI combined spectrum in the 3–80 keV band. The solid line is a fit to the 3–20 keV part of the spectrum with a single-temperature MEKAL model. The bottom panel shows the residuals from the model. The hard X-ray excess is clear.

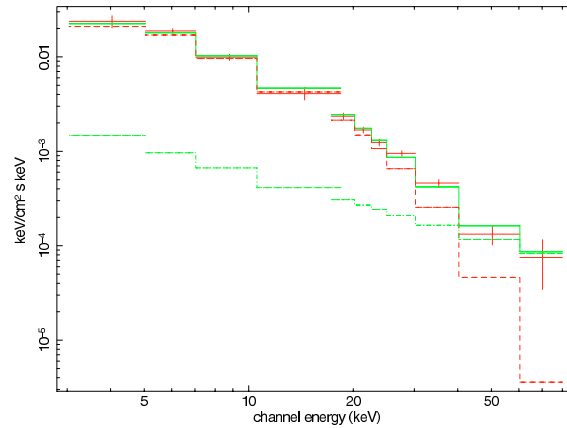


Fig. 8. *INTEGRAL* unfolded spectrum of the Ophiuchus cluster in the 3–80 keV band fitted by a MEKAL+power-law model with fixed photon index $\alpha = 2.0$ (green solid line). The red and green dashed lines represent the contribution of the thermal, respectively non-thermal components as a function of energy.

in *INTEGRAL* data is much more significant than the value obtained by *BeppoSAX*.

The value found for the plasma temperature is consistent with the *BeppoSAX* measurement of $kT = 9.1 \pm 0.6$ keV, but significantly lower than the *ASCA* value of $kT = 10.9 \pm 0.4$ keV. However, the *ASCA*/GIS instrument was sensitive only up to 10 keV, and thus could not detect the cutoff. Because of the sensitivity above 10 keV, the *INTEGRAL* and *BeppoSAX* values certainly provide more accurate measurements.

Fixing the thermal component to the value found in the 3–20 keV band, one can try to constrain the acceptable range for the photon index of the non-thermal component. Leaving only the photon index and the normalisation of the power-law free while fitting, one finds $\alpha = 1.62^{+0.32}_{-0.35}$. The photon index of 2.0 used to derive the values of the HXR emission is compatible (within 1σ) with this value. With such a hard photon index, it is clear that the excess cannot be explained by the presence of hot gas. Indeed, if instead of a power-law we fit the excess with a second thermal component, we can derive a lower

Table 1. Results of the fitting procedure for a thermal + power-law model, with abundance and redshift values fixed to the literature value and photon index fixed to $\alpha = 2.0$, similar to the work of Nevalainen et al. (2004). In Method 1, the temperature and the normalisation of the Bremsstrahlung component are left free while fitting. In Method 2, we used the data in the 3–20 keV band to fix the temperature and normalisation of the thermal component, and let free only the normalization of the non-thermal component.

	χ^2_{red}	$P_{\text{F-test}}^a$	kT [keV]	Flux _{HXR} ^b	$CL_{\text{HXR}}\sigma^c$
Method 1	0.93	2×10^{-4}	$8.56^{+0.37}_{-0.35}$	10.1 ± 2.5	4.0
Method 2	1.05	7×10^{-5}	$8.50^{+0.48}_{-0.45}$	8.2 ± 1.3	6.4

^a $P_{\text{F-test}}$ is the null hypothesis probability when adding the non-thermal component given by the F-test. ^b 20–60 keV flux of the non-thermal component, in units of 10^{-12} ergs s^{-1} cm^{-2} . The errors are quoted at the 1σ level. ^c Confidence level for the detection of the non-thermal component.

limit to the temperature of the second component, which we find to be $kT > 50$ keV. Together with the temperature map from both JEM-X and ASCA, this proves that the excess cannot be explained by the presence of very hot gas.

4.2. Possible origins of the non-thermal component

Since the hard X-ray flux observed by *INTEGRAL* cannot be explained by thermal Bremsstrahlung, there are two possible origins for the non-thermal flux in the hard X-ray band. Indeed, it can be due either to inverse-Compton (IC) scattering of GeV electrons with the CMB (Ensslin & Biermann 1998), or to synchrotron emission from another population of very high energy electrons ($E \sim \text{PeV}$, e.g. Timokhin et al. 2004; Inoue et al. 2005). To construct our models, we assume that the electron distribution is a power-law with spectral index 2.0 and a high-energy cut-off.

Assuming that the non-thermal component comes from IC scattering of the same electrons that produce radio halos, one can try to constrain the physical parameters needed to explain the radio/hard X-ray flux (Thierbach et al. 2003), in particular the value of the magnetic field in the cluster. Unfortunately, the existing radio data are old, and the size of the region used to extract the radio flux differs for all the measurements, so the shape of the radio spectrum cannot be well constrained. Using the radio data presented in Johnston et al. (1981), we tried nevertheless to consider jointly the radio and hard X-ray data of the cluster to constrain models for the spectral energy distribution. The bottom panel of Fig. 9 shows the corresponding spectral energy distribution, with models computed for several values of magnetic field B and cut-off energy E_{cut} .

Because of the low quality of the radio data, we cannot constrain the properties of the electron population. However, the ratio between the synchrotron and IC components is given by

$$\frac{P_{\text{sync}}}{P_{\text{IC}}} = \frac{u_B}{u_\gamma} = \frac{B^2/8\pi}{u_{\text{CMB}}} \quad (4)$$

The only unknown factor in this ratio is the magnetic field, so we can use the mean value of the radio data to estimate the value of B . Figure 9 shows the spectral models computed for different

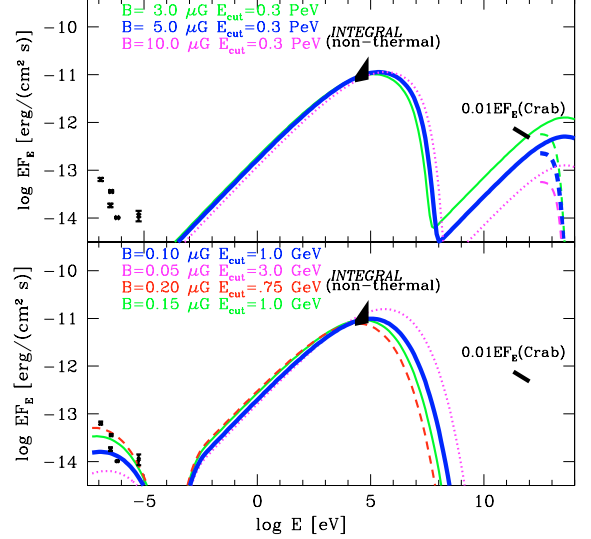


Fig. 9. Models for the spectral energy distribution of the non-thermal emission of the cluster, for a population of $E \sim \text{PeV}$ electrons (*top*) and of $E \sim \text{GeV}$ electrons (*bottom*), for different values of magnetic field and cut-off energy. The solid black line shows the 10 mCrab flux level in the TeV range. The radio data are from Johnston et al. (1981). The dashed lines at energies ~ 10 TeV show the attenuation of the IC spectrum due to absorption by the extragalactic infrared and CMB backgrounds.

values of B . We can see that the best estimate for the magnetic field is

$$B \sim 0.1 - 0.2 \mu\text{G}. \quad (5)$$

This value is similar to the value obtained from the hard X-ray radiation of the Coma cluster ($B \sim 0.15 \mu\text{G}$, Fusco-Femiano et al. 1999), but contradicts the much higher values obtained from Faraday rotation measures in a large sample of radio-emitting clusters (Kim et al. 1991).

If the hard X-ray emission comes from synchrotron radiation from a different population of electrons with highly relativistic velocities, we expect that the peak of the IC emission will be in the TeV domain. The top panel of Fig. 9 shows the corresponding spectral energy distributions for different values of magnetic field and a cut-off energy $E_{\text{cut}} = 0.3$ PeV. The black line shows the 10 mCrab flux level in the TeV domain. We can see that the magnetic-field values deduced from Faraday rotation measures ($\sim 1-5 \mu\text{G}$) predict a TeV flux which is firmly detectable by the present generation of Cherenkov telescopes.

5. Discussion

The combined ISGRI/JEM-X spectrum of the cluster exhibits a clear (6.4σ) excess at high energies. At such significance level, it is now clear that an additional component is needed to explain the relatively high hard X-ray flux observed both by *INTEGRAL* and *BeppoSAX*. Unlike the PDS instrument on board *BeppoSAX*, the ISGRI and JEM-X instruments on board *INTEGRAL* are imaging, which allowed us to study the changes in temperature throughout the detected region, and show that the hard excess cannot be explained by the presence of very hot thermal plasma

in some regions of the cluster. Besides, in the large FOV of the PDS instrument, there was no guarantee that the possible excess was not the result of isolated point sources, for instance absorbed active galactic nuclei. The imaging capabilities of *INTEGRAL* allow us to exclude this possibility. Indeed, we find evidence that the source is extended even above 20 keV, and coincides spatially with the X-ray emission. Moreover, high angular resolution X-ray imaging of the cluster with *Chandra* does not reveal the presence of any bright point source below 10 keV in the region detected by *INTEGRAL*, which shows that contamination of the *INTEGRAL* spectrum by point sources is very unlikely. Therefore, we claim with good confidence that the high-energy tail observed by *INTEGRAL* and *BeppoSAX* is certainly due to non-thermal emission from relativistic particles accelerated during a major merging event in the recent past.

Assuming that the non-thermal component is explained by IC scattering from the same electrons that produce the synchrotron radio halo, we used the existing radio data together with the *INTEGRAL* measurement to make a joint model for the synchrotron/IC components, and estimated the magnetic field value to be $B \sim 0.1\text{--}0.2\ \mu\text{G}$. This value is similar to that estimated with the same method for the Coma cluster (Fusco-Femiano et al. 1999) and with the typical magnetic field values extracted from equipartition assumption (Thierbach et al. 2003), but contradicts the higher values ($B \sim 1\text{--}5\ \mu\text{G}$) derived from Faraday rotation measures (Kim et al. 1991; Clarke et al. 2001). To resolve the discrepancy between the Faraday rotation and Inverse-Compton methods, Goldshmidt & Rephaeli (1993) suggested that the magnetic field might be decreasing with radius, such that in the outer regions the electron cooling through IC emission would dominate, while in the center, the electrons would radiate more strongly in the radio domain. However, the spatial resolution of *INTEGRAL* allows us to measure the magnetic field within a region of radius less than 6 arcmin from the center of the cluster, and therefore to show that the value of B measured from the HXR radiation does not come from the outer regions of the cluster. More recently, Beck et al. (2003) suggested that the presence of turbulence might introduce a bias in the value of B derived from Faraday rotation measures. From X-ray imaging of the Coma cluster, Schuecker et al. (2004) demonstrated that turbulence is indeed playing an important role in unrelaxed clusters. Although it is much less studied, Ophiuchus is similar to Coma in many aspects, so this explanation could apply as well in our case. In any case, the measurement of the magnetic field through Faraday rotation measures relies on several assumptions, whereas the expected radio/hard X-ray flux correlation provides a direct measurement of the magnetic field, so the lower values obtained in both Ophiuchus and Coma ($B \sim 0.1\ \mu\text{G}$) certainly provide a better estimate of the cluster magnetic field. Better constraints on the shape of the radio spectrum are therefore important to measure the magnetic field with better accuracy.

On the other hand, if the magnetic field values derived from Faraday rotation measure are correct, the IC emission from the population of electrons that radiate in the radio domain is not sufficient to explain the hard X-ray flux detected by *INTEGRAL*. This implies the presence of another population of electrons at much higher energies ($E \sim 100\ \text{TeV}$) that would radiate in hard X-rays through synchrotron radiation and would up-scatter the photons of the CMB to produce TeV emission (see the top panel of Fig. 9). In this case, our models predict a flux in the TeV domain that would be firmly detectable by HESS. Indeed, our lowest curve, which corresponds to the highest allowed value for the magnetic field ($10\ \mu\text{G}$), coincides with the sensitivity limit of

HESS. Therefore, observations of the cluster in very high energies are crucial to constrain the models of particle acceleration in Ophiuchus in particular and clusters of galaxies in general.

6. Conclusion

In this work, we presented the results of broad-band *INTEGRAL* observations of the Ophiuchus cluster in the 3–18 keV band with the JEM-X X-ray monitor and in the 17–80 keV with the ISGRI hard X-ray imager. We have shown that the source is extended for both instruments and that the morphology of the source is consistent with previous studies (Sect. 3). We presented a JEM-X hardness-ratio map (7–18 keV to 3–7 keV) and found that the plasma temperature does not vary significantly within the detected region. In Sect. 4, we presented the total *INTEGRAL* spectrum of the cluster in the 3–80 keV band. We explained that the emission cannot be described by a single-temperature MEKAL model, and that an additional spectral component is needed to explain the significant excess found at energies above 20 keV compared to the best fit ($kT = 8.5\ \text{keV}$) for the thermal emission below 20 keV. Consequently, we measure a hard X-ray excess emission from the Ophiuchus cluster, at a much higher confidence level (6.4σ for the fixed temperature model) than the *BeppoSAX* claim.

With spectral and imaging analysis, we have shown that this excess cannot be explained by the presence of very hot thermal gas or by contamination of the spectrum by point sources. Indeed, fitting the excess with a second thermal component, we found an unrealistic lower limit to the temperature, $kT > 50\ \text{keV}$. Comparing the JEM-X and ISGRI images with X-ray images from higher resolution instruments (*Chandra* and *ASCA*), we found that the morphology of the cluster does not depend on energy, and that no bright point sources are detected in the high-resolution images, which excludes the possibility that the hard X-ray emission comes from point sources embedded in the cluster. Therefore, we conclude that the high-energy tail is due to non-thermal emission from relativistic electrons, probably accelerated during a merging event in the recent history of the cluster.

To investigate the origin of this non-thermal component, we presented different models for the spectral energy distribution (Sect. 4.2). If the emission is of inverse-Compton origin from GeV electrons on the CMB, we used the available radio data to construct a joint radio/hard X-ray model for the spectral energy distribution. Comparing the level of the radio and hard X-ray flux, we were able to estimate the magnetic field in the cluster, which we found to be $B \sim 0.1\text{--}0.2\ \mu\text{G}$. On the other hand, if the hard X-ray emission comes from synchrotron radiation of another population of very high energy electrons, our models predict a detectable flux in the TeV domain. Therefore, observations of the Ophiuchus cluster in the TeV domain, as well as better measurements of the radio spectrum of the cluster, will allow us to constrain the models, and determine if clusters of galaxies are able to accelerate particles up to very high energies.

Acknowledgements. We would like to thank P. Lubinski for his help on background maps production, I. Telegzhinsky for his help on ISGRI imaging analysis, and the JEM-X team for their important support. This work is based on observations with *INTEGRAL*, an ESA project with instruments and science data centre funded by ESA member states (especially the PI countries: Denmark, France, Germany, Italy, Switzerland, Spain), Czech Republic and Poland, and with the participation of Russia and the USA.

References

Beck, R., Shukurov, A., Sokoloff, D., & Wielebinski, R. 2003, *A&A*, 411, 99

- Clarke, T. E., Kronberg, P. P., & Böhringer, H. 2001, *ApJ*, 547, L111
- Courvoisier, T. J.-L., Walter, R., Beckmann, V., et al. 2003, *A&A*, 411, L53
- Eckert, D., Neronov, A., Courvoisier, T. J.-L., & Produit, N. 2007, *A&A*, 470, 835
- Ensslin, T. A., & Biemann, P. L. 1998, *A&A*, 330, 90
- Feretti, L., & Giovannini, G. 2007, *ArXiv Astrophysics e-prints*
- Fusco-Femiano, R., Dal Fiume, D., Feretti, L., et al. 1999, *ApJ*, 513, L21
- Fusco-Femiano, R., Orlandini, M., Brunetti, G., et al. 2004, *ApJ*, 602, L73
- Fusco-Femiano, R., Landi, R., & Orlandini, M. 2005, *ApJ*, 624, L69
- Goldshmidt, O., & Rephaeli, Y. 1993, *ApJ*, 411, 518
- Inoue, S., Aharonian, F. A., & Sugiyama, N. 2005, *ApJ*, 628, L9
- Johnston, M. D., Bradt, H. V., Doxsey, R. E., et al. 1981, *ApJ*, 245, 799
- Kaastra, J. S., & Mewe, R. 2000, in *Atomic Data Needs for X-ray Astronomy*, 161, ed. M. A. Bautista, T. R. Kallman, & A. K. Pradhan, 161
- Kalemci, E., Reynolds, S. P., Boggs, S. E., et al. 2006, *ApJ*, 644, 274
- Kim, K.-T., Kronberg, P. P., & Tribble, P. C. 1991, *ApJ*, 379, 80
- Lebrun, F., Leray, J. P., Lavocat, P., et al. 2003, *A&A*, 411, L141
- Lund, N., Budtz-Jørgensen, C., Westergaard, N. J., et al. 2003, *A&A*, 411, L231
- Mohr, J. J., Mathiesen, B., & Evrard, A. E. 1999, *ApJ*, 517, 627
- Nevalainen, J., Oosterbroek, T., Bonamente, M., & Colafrancesco, S. 2004, *ApJ*, 608, 166
- Renaud, M., Gros, A., Lebrun, F., et al. 2006, *A&A*, 456, 389
- Rossetti, M., & Molendi, S. 2004, *A&A*, 414, L41
- Sarazin, C. L. 1999, *ArXiv Astrophysics e-prints*
- Schuecker, P., Finoguenov, A., Miniati, F., Böhringer, H., & Briel, U. G. 2004, *A&A*, 426, 387
- Thierbach, M., Klein, U., & Wielebinski, R. 2003, *A&A*, 397, 53
- Timokhin, A. N., Aharonian, F. A., & Neronov, A. Y. 2004, *A&A*, 417, 391
- Watanabe, M., Yamashita, K., Furuzawa, A., Kunieda, H., & Tawara, Y. 2001, *PASJ*, 53, 605

Chapter 6

Hard X-ray observations of the Perseus cluster

6.1 Introduction

The brightest cluster in the X-ray band, Abell 426, lies at $b = 150.3^\circ$, $l = -13.3^\circ$ and redshift $z = 0.0176$ in the constellation of Perseus. In the optical, more than 500 member galaxies have been identified (Bahcall 1974). An extremely massive cD elliptical galaxy, NGC 1275, dominates the dynamics of the galaxies in the central regions of the cluster. NGC 1275 also hosts a well-known radio-loud Seyfert 2 nucleus, Per A, which interacts with the gas of the cluster through its jets and outflows. The Perseus cluster is also the most massive cluster of a very large scale structure, the “Perseus-Pisces supercluster”.

In the X-ray band, a source, designated as Per XR-1, was detected by a rocket flight carrying X-ray proportional counters (Fritz et al. 1971). The authors report on a 0.5-10 keV flux of 7×10^{-9} ergs s^{-1} cm^{-2} , and associate the source with the nucleus of NGC 1275. Later observations by *Uhuru* revealed that the source was extended (Forman et al. 1972). The authors, who also reported on the detection of the Coma and Virgo clusters, claim the discovery of a new class of X-ray objects, “possibly associated with active galaxies in rich clusters”. Fabian et al. (1974) analyzed the cluster with better spatial resolution (~ 2 arcmin) using the *Copernicus* instrument, and found that the cluster consists in a compact core, consistent with the position of NGC 1275, plus a more extended halo. Finally, Cash et al. (1976) identified the diffuse emission as thermal bremsstrahlung, whereas the central peak was associated with emission from the nucleus of NGC 1275. The discovery with *Ariel 5* of emission lines around 6.5 keV associated with Fe XXV and Fe XXVI (Mitchell et al. 1976) provided strong evidence that the diffuse emission is indeed due to an optically thin hot plasma at a temperature $kT \sim 6$ keV and with an iron abundance of ~ 0.4 compared to the solar value. Using *EXOSAT* and *Ginga* observations, Allen et al. (1992) provided refined values for the parameters of the gas. They derived a mean temperature $kT = 6.3 \pm 0.2$ keV and an iron abundance of 0.41 ± 0.02 solar.

Analyzing the emissivity of the gas in the Perseus cluster, Cowie & Binney (1977) deduced that the cooling time of the gas in the center of the cluster is much smaller than the Hubble time. This implied that the gas should be slowly falling inwards from the outer region

and concentrating in the central region. Therefore, the authors predicted the existence of cooler gas in the central region which would slowly condensate in the central galaxies, and eventually form stars. This is called the “cooling-flow” model (Fabian et al. 1984). Using this model, Allen et al. (1992) calculated that a mass deposition rate of $270 \pm 80 M_{\odot} \text{ yr}^{-1}$ in the central regions. A few years later, Ulmer et al. (1987) from *Ginga* data discovered that the temperature of the central regions is significantly lower than that of the outer regions, which seemed to confirm the presence of a cooling flow in Perseus.

However, the first high-resolution images ($4''$) from the *Einstein* observatory (Fabian et al. 1981) allowed for the detection of a hole in emission $2'$ North-West of the nucleus. Using the highly-improved sensitivity of *ROSAT*, Boehringer et al. (1993) confirmed this result, and showed that the idealized picture of a steady cooling flow did not apply in the case of the Perseus cluster. *ROSAT* data revealed a very complex gas structure, and in particular, the existence of two X-ray brightness minima (“cavities”) close to NGC 1275 coinciding with the lobes of the radio source 3C 84. The authors calculate that in the lobes, the pressure due to cosmic-rays injected by the central AGN exceeds the pressure of the thermal gas, and therefore, they conclude that the cavities could have been deflated by the pressure of the cosmic rays. More recently, the cluster was the target of a very long (900 ksec) *Chandra* observation (Fabian et al. (2003) and further publications). The very high angular resolution ($< 1''$) of *Chandra* revealed a very complex structure of the gas in the central region and confirmed the anti-correlation between the X-ray and radio structures. Figure 6.1 (Fabian et al. 2006) shows the *Chandra* image compared to the radio image. The anti-correlation between the X-ray and radio morphology in the central regions is clearly seen. The temperature structure of the cluster was also found to be very complex, with temperatures ranging from 2.5 keV in the center up to ~ 8 keV in the outer regions.

Overall, it is now believed that the considerable amount of energy ($\sim 10^{60}$ ergs) injected in the ICM by the central nucleus during its active phase plays a crucial role in the center of Perseus and a number of other cooling-core clusters. Shock heating therefore balances radiative cooling and stops the cooling-flow. This process of AGN feedback in the center of cooling-core clusters is now believed to be responsible for the non-observation of cooled gas ($kT < 1$ keV) in the central regions of clusters.

Apart from very deep *Chandra* observations, the cluster was also observed by *XMM-Newton* (Churazov et al. 2003). *XMM-Newton* data confirmed the complex temperature structure of the cluster core, with temperatures ranging from ~ 3 keV in the centre up to ~ 7 keV in the outskirts. Thanks to the larger FOV of *XMM-Newton*, it was also possible to observe the structure of the gas in the outer regions. An asymmetry of the surface brightness profile in the East-West direction was found, possibly corresponding to a small group of galaxies falling onto the main cluster. The contribution of the AGN in the center of NGC 1275 was also estimated. The spectrum of the nucleus could be well fitted by an absorbed power-law with a photon index $\Gamma = 1.65$ typical of radio-loud AGN and a luminosity of 10^{43} ergs s^{-1} in the 0.5-8 keV band.

Apart from X-ray data, the cluster was also intensively observed in the radio domain. The bright radio source 3C 84 is consistent with the position of NGC 1275. While most

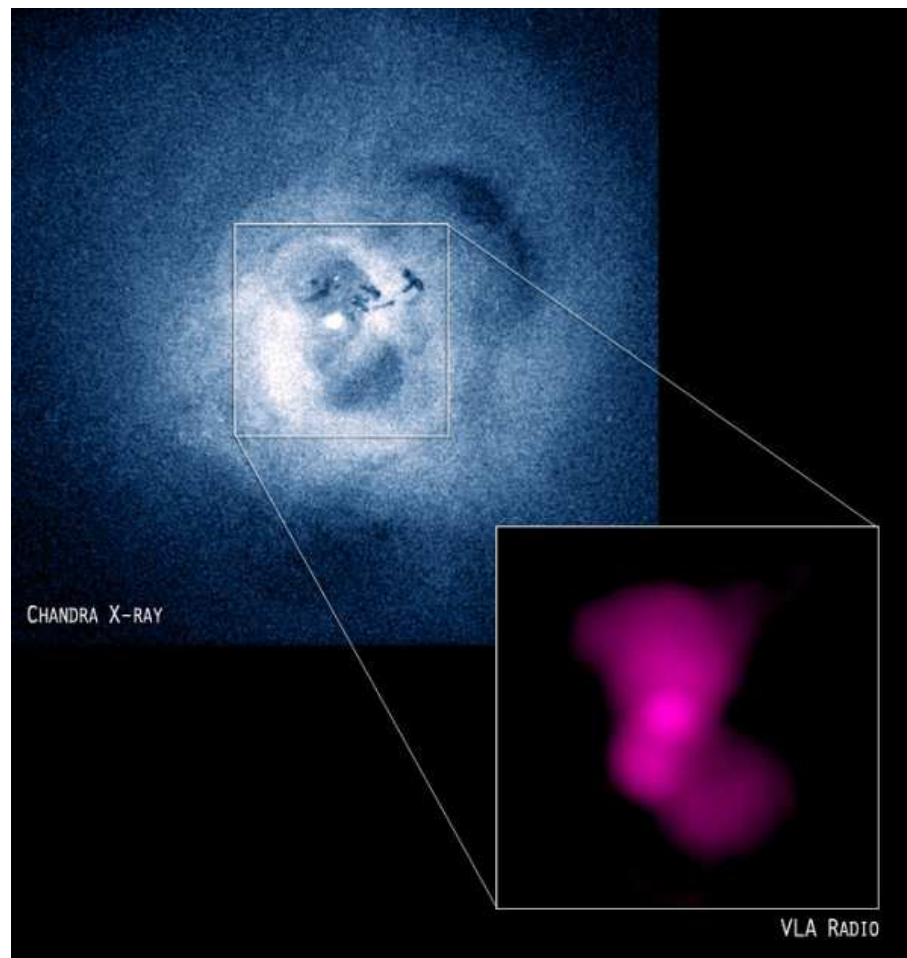


Figure 6.1: Chandra image of the Perseus cluster in the 1-10 keV band, and comparison with the radio image of the same region from the VLA (Credit: NRAO/VLA/G. Taylor). The angular size of the square is 3 arcmin.

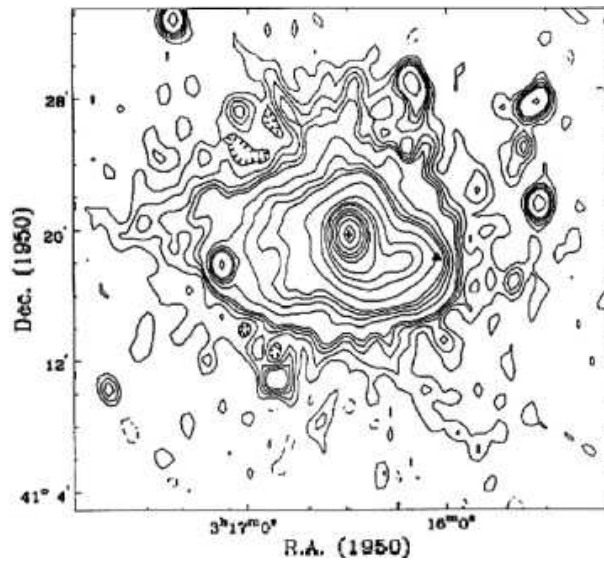


Figure 6.2: Westerbork Synthesis Radio Telescope image of the Perseus mini-halo at 330 MHz (Feretti et al. 2004). The angular resolution of the image is $51'' \times 77''$ (RA \times DEC). The cross shows the position of NGC 1275 in the centre.

of the radio emission certainly comes from the radio galaxy, emission on a larger scale was also detected in the cluster (Burns et al. 1992). The diffuse emission has a radius ~ 10 arcmin. This is significantly smaller than typical radio halos in the center of merging clusters (e.g. Coma). As a consequence, the diffuse radio source in the Perseus cluster is now the prototype of a new class of diffuse radio sources in cooling-core cluster, designated as radio “mini-halos”. Figure 6.2 from Feretti et al. (2004) shows the Perseus mini-halo at 330 MHz taken by the Westerbork Synthesis Radio Telescope. The total diameter of the mini-halo in this image is ~ 25 arcmin.

The presence of large-scale diffuse radio emission from Perseus implies the presence of relativistic electrons. If the AGN jets are hadronic, it is probable that the radio emission comes mostly from secondary electrons produced by proton-proton interactions (Pfrommer & Enßlin 2004). The electrons could also be directly accelerated through turbulence induced by the central nucleus (Gitti et al. 2002), although the shocks produced by the interaction of the AGN jets with the ICM do not seem to be strong enough.

Since the existence of relativistic electrons in the cluster is obvious because of the radio synchrotron emission, we expect that photons of the CMB as well as optical/IR photons coming from the central galaxy/AGN should be up-scattered to higher energies, in particular to the (hard) X-ray domain. Thanks to the very long *Chandra* observation of the cluster, such a component could have been detected in addition to the thermal emission by Sanders et al. (2005). However, the complex temperature structure makes the detection of a power-law below 10 keV difficult, and any uncertainties on the high-energy calibration of *Chandra* could induce such a result, so observations of the cluster above 10 keV are required to confirm this result. In the hard X-ray band, Nevalainen et al. (2004) presented *BeppoSAX*/PDS observations of the cluster, and concluded that the emission was consis-

tent with the extrapolation of the AGN emission. However, since the PDS instrument was non-imaging, it was not possible to put any constraints on the diffuse emission.

In this chapter, I present the results of a 500 ksec observation of the Perseus cluster with *INTEGRAL*. Thanks to its moderate angular resolution above 10 keV, JEM-X is the first instrument which could have the capabilities to disentangle the diffuse emission and the AGN emission above 10 keV. In any case, the extrapolation of the non-thermal flux which was claimed by Sanders et al. (2005) within a radius of 3 arcmin from the center (6.3×10^{-11} ergs cm $^{-2}$ s $^{-1}$ in the 2-10 keV band, and a power-law index in the range 1.4 – 2.2) is clearly above the sensitivity of ISGRI. Therefore, if it is present, *INTEGRAL* has the capabilities to confirm or rule out the *Chandra* result.

6.2 *INTEGRAL* observations of Perseus

The Perseus cluster was observed during *INTEGRAL* revolutions 0052,0096,0168 and 0220 for a total observing time of 500 ksec (ISGRI) and 280 ksec (JEM-X). During revolutions 0052 and 0096, the cluster was observed in staring mode. The advantage of this observing strategy is that the cluster was in the FOV of JEM-X a large fraction of the time. However, staring is very bad for ISGRI, and in particular for imaging, since in this case, the artifacts introduced in the sky images by imperfect knowledge of the IBIS mask (or “ghosts”) become very prominent. Nonetheless, the data in staring mode are fully usable for ISGRI spectral extraction, since the spectral-extraction tool works in the detector space.

6.3 Morphology of the cluster

For imaging, we processed all available ISGRI data with the mosaicking method presented in Appendix A.2 in order to produce the cleanest possible image of the Perseus region. For JEM-X data analysis, we processed the data using the standard OSA 7.0 software. We processed JEM-X1 and JEM-X2 data independently and merged the resulting images in order to create a mosaic with the highest possible signal-to-noise. The source was clearly detected by both instruments at the 16σ (ISGRI, 20-30 keV) and 57σ (JEM-X, 3-7 keV) level. Fig. 6.3 shows the resulting significance images in the 20-30 keV band (ISGRI) and 3-7 keV band (JEM-X). The core radius of the cluster ($R_c \sim 6$ arcmin) is comparable to the size of the IBIS PSF. However, fitting the ISGRI image, we find a half-width of 6.4 arcmin, which is consistent with a point-like source. This could be due to the presence of the Seyfert 2 nucleus in the centre of the cluster, which might be responsible for a significant fraction of the emission above 20 keV.

On the other hand, the extension of the source is clearly seen in the JEM-X image. The total size of the source as seen by JEM-X is ~ 15 arcmin, which is much larger than the PSF of the instrument (3.8 arcmin FWHM). As found by *XMM-Newton* (Churazov et al. 2003), the source is elongated in the East-West direction. Of course, the morphology of the cluster has been extensively studied below 10 keV by telescopes with better angular resolution and sensitivity, so not much information can be extracted from the JEM-X image. In the 7-18 keV band, the source is also clearly detected, at the 21σ level. No

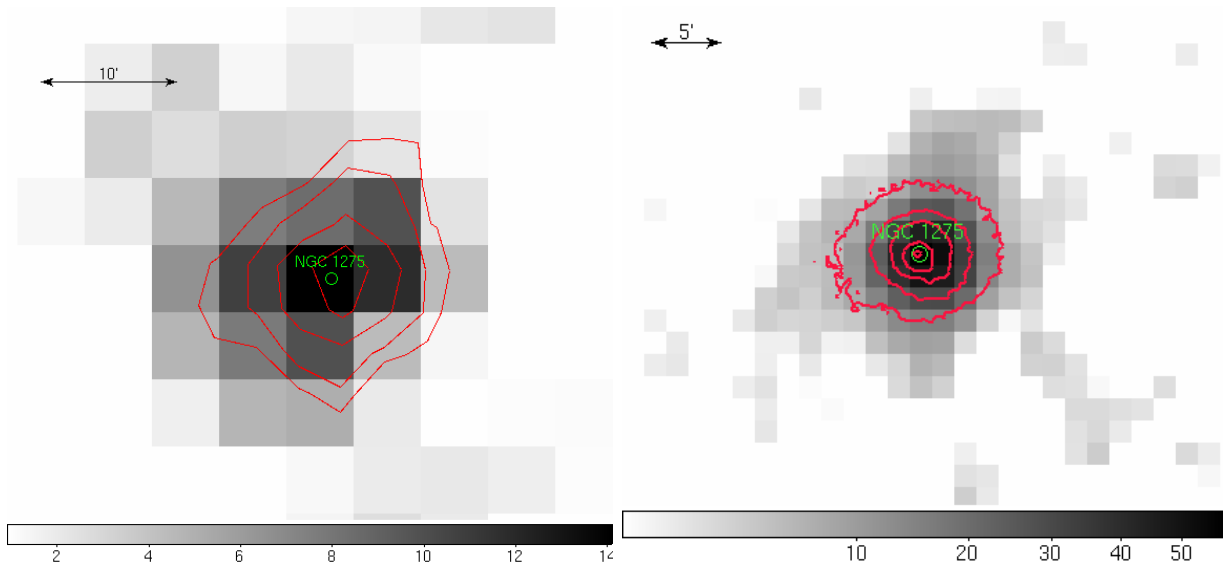


Figure 6.3: Left: ISGRI 20-30 keV significance image of the Perseus cluster region. For comparison, the contours show the JEM-X 3-7 keV emission. The position of the Seyfert 2 nucleus NGC 1275 is also displayed. Right: JEM-X significance image of the cluster in the 3-7 keV band with contours from ROSAT/PSPC. The green circle shows the position of NGC 1275 at the centre of the cluster.

significant morphology change is observed between the 2 bands.

6.4 Broad-band *INTEGRAL* spectrum

In order to study the high-energy emission from the cluster and the central nucleus, we extracted the spectrum of the source in the 17-120 keV band with ISGRI and 3-20 keV band with JEM-X. For ISGRI spectral extraction, we proceeded in the standard way, since no significant extension of the source is observed above 20 keV. For JEM-X spectral extraction, we proceeded in two different ways. First, we extracted the spectrum of the source using the standard OSA 7.0 spectral extraction tool, which back-projects the incoming photons and sorts them into the different spectral channels (256 channels between 0.5 and 60 keV, although only the data between 3 and 35 keV are usable). Since the source is very clearly detected by JEM-X, this allows us to study the spectrum of the source with a very fine spectral binning. In this case, an individual spectrum for each of the two JEM-X instrument was extracted.

On the other hand, we have seen that the source is clearly extended for JEM-X, so only a fraction of the source flux will be extracted with this method. Because of the narrower PSF of JEM-X compared to ISGRI, the regions which will be taken into account by both instruments will not be the same, and the cross-calibration between the two instruments will not be correct. In order to ensure a correct cross-calibration, we created mosaic images in 18 energy bands between 3 and 20 keV, we combined JEM-X1 and JEM-X2 mosaics and then extracted the JEM-X spectrum from the mosaic in a region of radius 6 arcmin

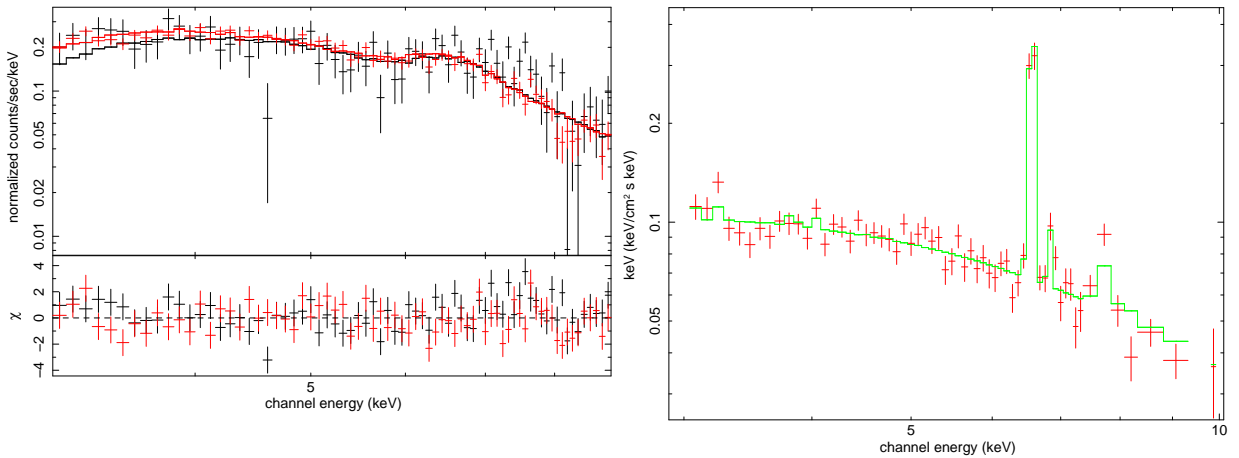


Figure 6.4: Left: *JEM-X1* (black) and *JEM-X2* (red) spectra of *Perseus* in the 3-10 keV band fitted simultaneously by a MEKAL model at $kT = 3.9 \pm 0.1$ keV. The residuals from the model are displayed in the bottom panel. Right: Unfolded *JEM-X2* spectrum in an EF_E representation.

similar to the ISGRI PSF.

6.4.1 Full-resolution JEM-X spectrum

Figure 6.4 shows the full-resolution JEM-X spectra of *Perseus* in the 3-10 keV band. The left panel shows the folded *JEM-X1* (black) and *JEM-X2* (red) spectra fitted simultaneously by a MEKAL model at a temperature $kT = 3.9 \pm 0.1$ keV and an iron abundance of 0.4 ± 0.05 relative to the solar value. The redshift of the cluster was fixed to $z = 0.0176$ (Churazov et al. 2003). The quality of the fit ($\chi_{red}^2 = 1.29$ for 142 d.o.f.) is acceptable. The source was observed longer by *JEM-X2*, so the quality of the *JEM-X2* spectrum is better. The right panel of the figure shows the unfolded *JEM-X2* spectrum in an EF_E representation. Several emission lines are seen, in particular the Fe XXV (He-like) line at 6.5 keV, the Fe XXVI (H-like) line at 6.8 keV and the Fe edge line at 7.8 keV.

From *XMM-Newton* data, Churazov et al. (2003) derived a temperature profile going from 3 keV in the central regions up to ~ 7 keV in the outskirts. The JEM-X spectrum is extracted within a radius ~ 2 arcmin from the center, where *XMM-Newton* derived a temperature between 3 and 4 keV. Therefore, the JEM-X temperature is fully consistent with this result. Churazov et al. (2003) also found an abundance of ~ 0.4 increasing towards the central region up to ~ 0.6 . The abundance determined by JEM-X is slightly lower than this value, but given the larger error on the JEM-X measurement and the larger integration radius, the difference lies within the statistical uncertainties. As a conclusion, we find that the 3-10 keV JEM-X spectrum gives results which are fully consistent with results extracted with more sensitive instruments such as *XMM-Newton*/EPIC. This proves that the calibration status of JEM-X is sufficient for such studies.

6.4.2 Total spectrum

In order to study the high-energy emission of the cluster, we used the JEM-X spectrum extracted from the mosaics as well as the ISGRI spectrum, and fitted them simultaneously in XSPEC. As a first attempt to model the 3-120 keV spectrum, we fitted the spectrum with a single MEKAL model with abundance fixed to 0.4 solar and redshift fixed to $z = 0.0176$. The total spectrum is badly represented by this model ($\chi_{red}^2 = 4.54$ for 24 d.o.f.), which clearly indicates the need for other spectral components. Adding a power-law component to the model, we find a significantly better fit ($\chi_{red}^2 = 1.15$ for 22 d.o.f.), with $kT = 3.7 \pm 0.1$ keV and a photon index $\Gamma = 2.7 \pm 0.2$. The resulting power-law flux in the 2-10 keV band is $(1.6 \pm 0.2) \times 10^{-10}$ ergs cm^{-2} s^{-1} . This is more than an order of magnitude higher than the reported flux of NGC 1275 (e.g. Donato et al. (2004), Churazov et al. (2003)), so this second component cannot be all associated with the central AGN. Fixing the contribution of the nucleus to the value found in *XMM-Newton* data ($F_{2-10 \text{ keV}} \sim 10^{-11}$ ergs cm^{-2} s^{-1} , $\Gamma = 1.65$), we find a significant excess (4.8σ) between 20 and 40 keV, while the high-energy data are consistent with the extrapolation of the AGN flux. This means that a single thermal model plus the contribution from the AGN cannot explain the combined *INTEGRAL* spectrum.

On the other hand, Sanders et al. (2005) reported on a possible diffuse non-thermal component with a 2-10 keV flux of 6.3×10^{-11} ergs cm^{-2} s^{-1} and a photon index ~ 2.0 . The non-thermal component detected in the *INTEGRAL* spectrum is significantly steeper ($\Gamma = 2.7 \pm 0.2$). Adjusting a power-law model with such parameters in the *INTEGRAL* spectrum clearly over-predicts ISGRI data over 30 keV, even when the AGN contribution is completely neglected. Figure 6.5 shows the total *INTEGRAL* spectrum with a model composed of a single thermal component plus a power-law component with the parameters from Sanders et al. (2005). This model obviously over-predicts the high-energy data. The existence of a power-law component without high-energy cut-off at the level claimed by Sanders et al. (2005) is therefore ruled out by ISGRI data.

Because of the complicated thermal properties of the gas in the cluster, modeling the data with a single-temperature thermal component obviously cannot reproduce accurately the overall spectrum. In order to take into account the higher temperature found in the outer regions of the cluster, we added a second thermal component to the spectrum at the temperature $kT = 7$ keV derived from *XMM-Newton* data. Adding such a component to the fit, a significant excess is still found at high-energies. However, this excess is consistent with the extrapolation of the 2-10 keV spectrum of the AGN. Figure 6.6 shows the total *INTEGRAL* spectrum of Perseus modeled with a two-temperature plasma plus the contribution of the AGN. This model gives an excellent fit, $\chi_{red}^2 = 1.08$ for 22 d.o.f. The central temperature $kT = 3.2 \pm 0.2$ keV is in agreement with *XMM-Newton* data. The 2-10 keV relative contribution of the 7 keV component from the outer regions compared to the 3 keV component from the center is $\sim 15\%$. Given that the surface-brightness profile of the source is peaked towards the centre, this result is reasonable. On the other hand, if instead of an additional thermal component we use a cut-off power-law with fixed photon index $\Gamma = 2.0$, we get an equally good fit with a cut-off energy $E_{cut} = 14_{-3}^{+6}$ keV. In this case, the 2-10 keV flux of the cut-off power-law component is 9.1×10^{-11} ergs cm^{-2} s^{-1} . This is slightly higher than the power-law flux reported by Sanders et al. (2005), but given

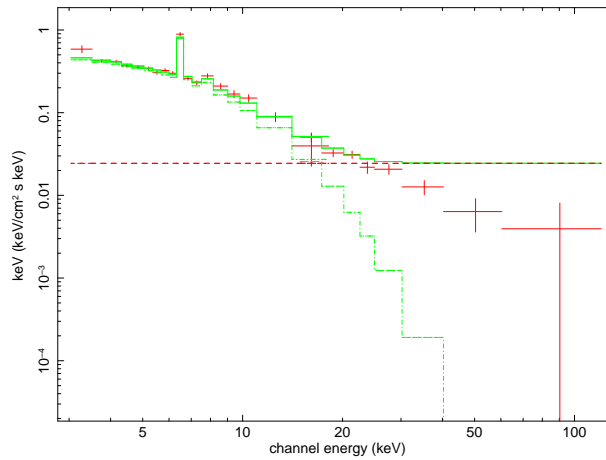


Figure 6.5: Total broad-band *INTEGRAL* spectrum extracted with *JEM-X* (3-20 keV) and *ISGRI* (17-120 keV). The model (green solid line) consists in a thermal component (dashed red) plus a power-law component (dashed green), with the parameters of the power-law as found by Sanders et al. (2005). The presence of a power-law without cut-off at the level claimed by Sanders et al. (2005) is ruled out by *INTEGRAL* data.

that it is integrated in a larger radius (6' versus 3') the flux is consistent.

6.5 Discussion

Analyzing a 500 ksec *INTEGRAL* observation of the Perseus cluster, we have extracted a high signal-to-noise spectrum of the cluster in the 17-120 keV band with *ISGRI* and 3-20 keV band with *JEM-X*. Since the Perseus cluster hosts a variety of known thermal (cool core, complicated temperature structure) and non-thermal phenomena (AGN activity from the central galaxy, diffuse emission from the mini-halo), modeling the total spectrum of the cluster is a complicated task.

Using a very deep *Chandra* observation of the cluster, Sanders et al. (2005) claimed the existence of diffuse non-thermal emission from the ICM, which could be due to inverse-Compton scattering of the relativistic electrons responsible for the radio halo with CMB and infra-red photons. Extrapolating the non-thermal component in the hard X-ray band yields a flux which is clearly detectable by *INTEGRAL*, so a confirmation of this result would be important. We find that the extrapolation of the power-law component largely over-predicts the spectrum above 30 keV, so based on *INTEGRAL* data, we conclude that the existence of a flat power-law component at the level claimed by Sanders et al. (2005) is ruled out.

On the other hand, assuming that the emission could be represented by a single-temperature model plus the contribution of the Seyfert nucleus does not give a good representation of the data. Therefore, an additional component under the form of a second thermal component or of a cut-off power-law is required. We find that both models can reproduce the data accurately, so based on *INTEGRAL* data it is not possible to distinguish be-

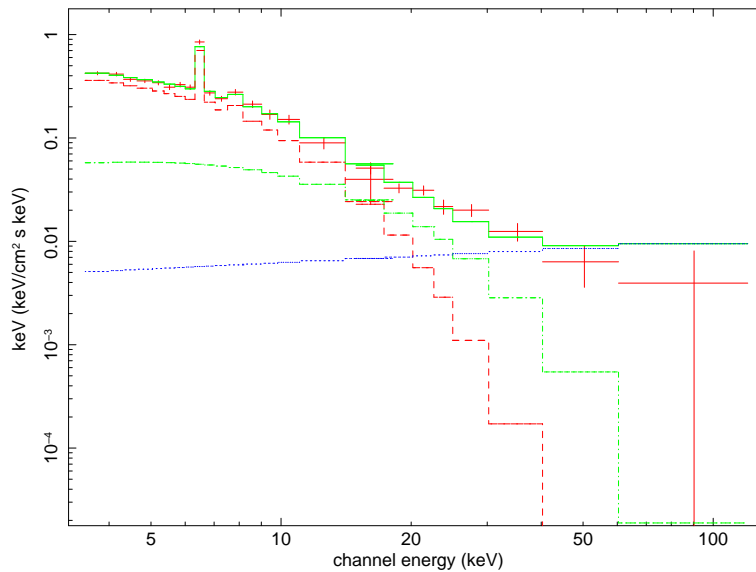


Figure 6.6: Total *INTEGRAL* unfolded spectrum of the Perseus cluster. The green solid line shows the best fit to the data with a 3 keV thermal model (dashed red), plus a 7 keV bremsstrahlung model to describe the emission from the outer regions of the cluster (dashed green), plus the contribution of the central AGN NGC 1275 under the form of a power-law (dashed blue).

tween these two scenarios. However, it is well-known from *Chandra* and *XMM-Newton* observations that the temperature structure of the cluster is complicated. In particular, *XMM-Newton* data (Churazov et al. 2003) reveal a temperature of ~ 3 keV in the inner 3 arcmin and a significantly higher temperature (~ 7 keV) in the outskirts. Since *ISGRI* integrates the flux within a region of 6 arcmin from the cluster centre, it is reasonable to fit the data with an additional thermal component at $kT = 7$ keV.

Even with a two-temperature model, we find that a power-law component is required to fit the high-energy data. However, this component is consistent with the extrapolation of the X-ray emission from the central nucleus. In order to check this, we investigated the variability of the flux at high energies. While the hard X-ray emission from AGN is known to be variable, the diffuse emission should not vary, so any sign of variability would indicate a strong contamination of the high-energy flux by the AGN. Extracting the flux of the source in different time periods in the 30-100 keV band, where the power-law component dominates over the thermal emission, we indeed found that the 30-100 keV flux varies by a factor at least 3 between the different time periods. The maximum flux in the 30-100 keV band was recorded during revolution 0168 at a level of $(3.4 \pm 0.7) \times 10^{-11}$ ergs cm^{-2} s^{-1} , while the source was not detected at all during revolution 0096, with a 2σ upper limit of 9×10^{-12} ergs cm^{-2} s^{-1} . The flux difference is well above the statistical uncertainties, so we conclude that the high-energy flux is variable. On the other hand, the 15-30 keV flux, which should be dominated by diffuse emission, does not show strong variations (between $(3.6 \pm 0.6) \times 10^{-11}$ ergs cm^{-2} s^{-1} (rev. 0220) and $(4.5 \pm 0.5) \times 10^{-11}$ ergs cm^{-2} s^{-1} (rev. 0168)). This is direct evidence that the high-energy flux is dominated by emission from the central AGN, while the 15-30 keV band is still dominated by diffuse emission.

In conclusion, although we cannot completely rule out the possibility that the emission is non-thermal and cuts off at $E \sim 14$ keV, we strongly believe that the power-law component at a high level claimed by Sanders et al. (2005) does not exist. Indeed, the fit with two temperatures of ~ 3 keV and ~ 7 keV is satisfactory, and we know from *XMM-Newton* and *Chandra* that different thermal components exist, and in particular a 3 keV component from the cool core and a 7 keV component from the outer regions. Therefore, we conclude that the total *INTEGRAL* spectrum can be perfectly well described by a thermal model consistent with previous studies, plus a variable power-law component from the central AGN.

Nevertheless, the presence of the radio mini-halo clearly indicates the existence of relativistic electrons not associated with the central AGN. Therefore, a diffuse non-thermal component should exist as well in the X-ray domain. However, in the center of strong cooling-core clusters like Perseus, the density of the gas is very high, and the strong shocks induced by the interaction between the AGN radio lobes and the thermal plasma amplify the magnetic field. Measurements of magnetic fields in cooling-core clusters (see e.g. Carilli & Taylor (2002)) indicate high magnetic field values, $B \sim 10 \mu\text{G}$. If the magnetic field in the centre of Perseus is of the order of $10 \mu\text{G}$, synchrotron losses would dominate over IC losses, and therefore the level of hard X-ray emission should be low. This would explain the non-detection of diffuse non-thermal emission by *INTEGRAL*.

6.6 Conclusion

The Perseus cluster is the prototypical cooling-core cluster. Thanks to its X-ray brightness, it has been extensively studied by focusing X-ray telescopes, and the analysis of the complex structure of its core has brought important progress to our understanding of the phenomena which take place in cooling-core clusters. Because of the presence of a bright Seyfert 2 nucleus in the central galaxy NGC 1275 and the obvious interaction between the AGN radio lobes and the thermal plasma, the study of Perseus is also of prime importance for the understanding of non-thermal phenomena, which play a crucial role to stop the cooling-flow in the central regions. Thanks to its sensitivity and angular resolution in a broad energy band, *INTEGRAL* has the capabilities to study the high-energy properties of the cluster, and in particular the diffuse non-thermal emission which was claimed by Sanders et al. (2005) from *Chandra* data.

In this chapter, I have presented the results of a 500 ksec *INTEGRAL* observation of the Perseus cluster. We have found that the quality of the *INTEGRAL* data is sufficient to study a possible high-energy tail in the spectrum. Although we found clear evidence for a power-law component above 30 keV, the properties of this power-law are consistent with the extrapolation of the X-ray spectrum from the central nucleus. Moreover, we have found that the high-energy (30-100 keV) flux has varied by a factor ~ 3 in the different periods of the observation, covering ~ 1.5 yr. This clearly demonstrates that the high-energy data are dominated by the AGN.

On the other hand, when we extrapolate the power-law claimed by Sanders et al. (2005)

from *Chandra* data (6.3×10^{-11} ergs cm $^{-2}$ s $^{-1}$ in the 2-10 keV band with a photon index $\Gamma \sim 2.0$) to the ISGRI band, we find that such a model clearly over-predicts the high-energy data by a factor 3 in the 40-60 keV band. Therefore, the presence of a flat power-law at such a high level is ruled out by ISGRI data. Moreover, the result of Sanders et al. (2005) was not confirmed by a longer *XMM-Newton* observation (F. Gastaldello, private communication). This could be due to uncertainties in the ancillary response (ARF) normalization of *Chandra* in the highest band, which would strongly affect the results in such cases. Indeed, since the band-pass of *Chandra* stops at 8 keV, it is very difficult to distinguish between a high-temperature bremsstrahlung and a power-law emission. For a $\Gamma = 2.0$ power-law model and a $kT = 7.0$ keV bremsstrahlung model with the same 2-10 keV flux, the difference between the two models in the 7-8 keV band is 2.5%. In order to distinguish between the two models, the ARF normalization of *Chandra* should therefore be known to an accuracy better than 2.5% in the 7-8 keV band, which is difficult to reach.

In conclusion, using *INTEGRAL* data, we found no evidence for a diffuse power-law emission which would dominate the emission over 30 keV. Unfortunately, the angular resolution of IBIS/ISGRI is not sufficient to disentangle the point-like emission from the diffuse component, so it is difficult to put any upper limit on the diffuse non-thermal emission. Observations of the cluster in the hard X-ray band with better angular resolution and sensitivity would be very important to detect the diffuse non-thermal component and map the magnetic field strength over the cluster, which could bring a very important input to the understanding of the interactions between the AGN radio lobes and the thermal plasma.

In this framework, the *Simbol-X* project, which should be launched around 2014, will have a crucial role to play. Thanks to the formation-flight technology, the project should extend the grazing-incidence focusing technique up to 80 keV, and therefore reach a sensitivity 2-3 orders of magnitude better than ISGRI and an angular resolution of 10 arcsec. Other hard X-ray focusing missions like *NuSTAR* and *NeXT* should also be able to detect the diffuse non-thermal component. However, the angular resolution of these two missions will be ~ 1 arcmin, which is probably not enough to make a detailed mapping of the central regions of the cluster. Therefore, it seems that *Simbol-X* will have the best chances to study the high-energy emission in the core of the Perseus cluster.

Chapter 7

Other scientific activities

During the past 4 years, I also spent a significant amount of time working on other *INTEGRAL*-related activities. In particular, I was a member of the ISDC shift team as a scientist on duty. In this chapter, I will summarize some of the findings related to my activities as an *INTEGRAL* scientist on duty and the work following these findings. I will mainly focus on the discovery and the analysis of the milli-second pulsar IGR J00291+5934, which is to the present day the fastest accreting milli-second pulsar.

7.1 The ISDC shift team

The ISDC (Courvoisier et al. 2003), as the ground segment for the *INTEGRAL* satellite (see Chapt. 3), is responsible for receiving, processing and archiving the data from the satellite. On the scientific side, the center also has the responsibility to analyze the data in near-real-time (NRT), and, if necessary, to react as fast as possible and inform the astronomical community.

In more details, the ISDC shift team is split into two main activities: the data flow and processing activities, and the scientific activities. For the latter ones, all ISDC scientists spend in average one week every three months as scientists on duty. The operations are organized by the Operations Coordinators, Drs. Volker Beckmann and Simon Shaw.

The main activities of the scientists on duty are split into two main tasks: monitoring gamma-ray bursts (GRBs), and searching for new or transient sources with the Quick-Look Analysis (QLA) software. Gamma-ray bursts are the most energetic explosions in the Universe, probably triggered by beamed supernova explosions of massive stars along the line of sight. Their origin is extra-galactic, and they can be observed up to very high redshift ($z \sim 6$). As a consequence, the sky distribution of GRBs is uniform. Given that GRBs occur approximately once per day and the FOV of IBIS is $\sim 2\%$ of the total sky area, the imager on *INTEGRAL* detects in average one GRB per month in the IBIS FOV. In this case, the *INTEGRAL* Burst Alert System (IBAS) automatically triggers an alert. Low-level alerts (i.e., level 1 and 2) must be checked by the scientist on duty in order to determine if the alert was indeed due to a GRB. On the other hand, high-significance alerts (i.e. level 3) automatically send a GRB report to the community, in order for optical robotic telescopes to point towards the position of the burst, and possibly detect the

prompt optical emission associated with the GRB.

In the case of GRBs outside the FOV of the instruments, the events can also be triggered by the shield of the SPI spectrometer, SPI/ACS. Indeed, the SPI/ACS can measure with excellent timing resolution (50 msec) the total number of counts (due to γ -rays and cosmic rays) which hit the shield in a given time interval. In the case of a fast increase of the total number SPI/ACS count rate, an alert is automatically triggered, which must be checked by the scientist on duty to determine the origin of the alert. Unfortunately, the SPI/ACS cannot provide any information on the position of a GRB, but in the case of GRBs also detected by other means it can provide very accurate light-curves.

The other main activity of a scientist on duty concerns the monitoring of new and transient hard X-ray sources. A large fraction of the sources detected by *INTEGRAL* are binary systems composed of a compact object (black hole, neutron star or white dwarf) and a main-sequence companion. The compact object accretes matter from its companion, either by Roche-lobe overflow (in the case of a low-mass companion) or by stellar wind (for a high-mass companion). The accreted matter falls in the deep potential well of the compact object and is therefore heated to very high temperatures, which produces X- and γ -ray emission. The level of X-ray emission strongly depends on the accretion rate from the companion, which can significantly vary. Therefore, binary systems are normally variable in X-rays. In some systems, the X-ray emission is normally rather weak ($L_X \simeq 10^{33}$ ergs/s), and the system exhibits strong outbursts, where the luminosity of the object increases by several orders of magnitude ($L_X \simeq 10^{37} - 10^{38}$ ergs/s). These systems are called “transients”. Thanks to the large field of view of the instruments on *INTEGRAL*, a significant number of transient X-ray binary systems have been discovered. The task of the scientist on duty is to check the sky images produced by the QLA software, which provides sky images in Near-Real Time (NRT), approximately 2 hours after the data were received by the system. At the end of an observation, the scientist on duty creates a mosaic from the individual pointings in order to increase the signal-to-noise and search for fainter sources.

7.2 IGR J00291+5934

7.2.1 Introduction on pulsars

The existence of neutron stars was first predicted by Baade & Zwicky (1934), only 2 years after the discovery of the neutron. The authors predicted that the core of massive stars after supernova explosions could consist of a very compact object ($R \sim 10$ km) in which the gravitational pressure is balanced by the degeneracy pressure of neutrons. These objects were then almost completely forgotten until 1967, when Bell & Hewish (1967) discovered a pulsating radio source in the Crab nebula, which led to the discovery of a large number of pulsating galactic radio sources. These sources, designated as “pulsars”, show pulse periods ranging from 10^{-3} (“milli-second pulsars”) up to several seconds. Pulsars were then associated with strongly-magnetized objects emitting beamed radiation along their magnetic axis. In the general case where the magnetic axis is not aligned with the spin axis of the object, the beam of light points towards the observer once per period, which

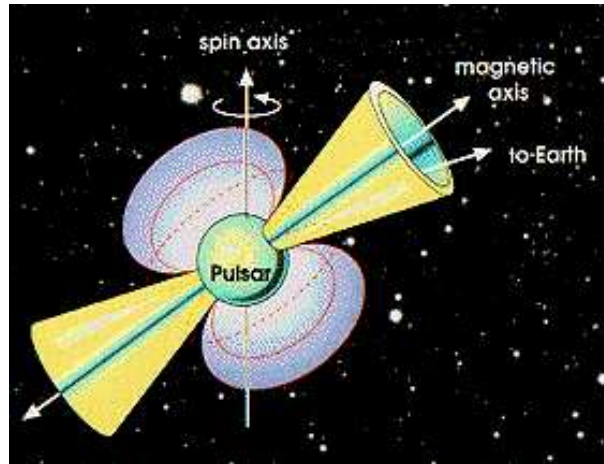


Figure 7.1: Schematic view of a pulsar.

is then observed as pulsed emission. This interpretation implies that the spin period of the object is very fast, and hence that the object is compact. Among the class of compact objects, only neutron stars have the required properties to be at the origin of pulsars. Indeed, while black holes do not have a surface and therefore cannot emit such radiation, white dwarfs have a radius of several thousand kms, which implies that the rotation velocity necessary to reach such high spin periods would disrupt the system.

As a consequence, pulsars have been associated with fast-spinning neutron stars which emit radiation along their magnetic axis, which is not co-aligned with the spin axis of the system (see Fig. 7.1 for a schematic view of a pulsar). Because of the radiative energy losses, the spin period of the neutron star slows down. In the case of the Crab pulsar, which results from the 1054 supernova explosion, the rotation period is 33 ms, with a spin-down $\dot{P} = 4 \times 10^{-13}$. In this regard, the existence of several pulsars with rotation periods $P \sim 1$ msec is curious. Indeed, if young pulsars like the Crab are created with periods more than an order of magnitude higher and constantly spin down, there should not exist pulsars with such short spin periods.

Apart from normal isolated pulsars, the improvements of X-ray astronomy in the 1970s allowed for the detection of a new class of pulsars, called “X-ray pulsars”. These are actually close binary systems where a neutron star is accreting matter from a stellar companion. The accreted material is heated to high temperatures and emits X-ray radiation. If the accreted material carries a significant angular momentum, the neutron star gains angular momentum and spins up. In this section, I present the discovery and the analysis of such a system, the milli-second X-ray pulsar IGR J00291+5934, which was discovered by *INTEGRAL* during my duty cycle at the ISDC.

7.2.2 The discovery of IGR J00291+5934

IGR J00291+5934 was discovered on December 2, 2004 during a routine scan of the Galactic plane (Galactic Plane Scan, GPS) by the IBIS/ISGRI telescope on board *INTEGRAL*

(Eckert et al. (2004), see Sect. 7.3). The source was clearly detected by ISGRI (21σ) and JEM-X (11σ) in individual pointings. *INTEGRAL* had observed the same area only 2 weeks before and did not detect the source, which indicated the transient nature of this source. The location of the source is found less than one degree away from two other known X-ray sources (the Cataclysmic Variable V709 Cas, and 4U 0027+59). This demonstrates the importance of the imaging capabilities of the instruments on board *INTEGRAL*. Indeed, we were able to clearly distinguish (with an error on the position of 1 arcmin) that IGR J00291+5934 is not the counterpart of any of these sources.

One day after the discovery of the source, a follow-up observation of the source was made by the PCA instrument on board *RXTE* (Markwardt et al. 2004b). Thanks to the large effective area and good timing resolution of the PCA, the authors discovered a 1.67 msec period which they associated with the spin period of a neutron star. During the observation, the frequency was drifting by approximately 36 mHz, in a manner consistent with Doppler orbital modulation. This suggests that the frequency shift is due to the motion of a neutron star in a 2.4 hr orbit. In the optical, the source was detected by the Robotic Palomar telescope on Dec. 4 at a magnitude $R \sim 17.4$ (Fox & Kulkarni 2004). No source was previously known at this position, and therefore the authors concluded that the optical emission was coming from an accretion disk rather than from the companion star. During the following month, the decay of the source was further monitored by several instruments at all wavelengths. After 3 weeks, the source was not detectable any more by ISGRI.

To summarize, although the companion star has not been firmly detected, the short orbit of the system ($P = 147.412 \pm 0.006$ min, Markwardt et al. (2004a)) indicates that the companion is a low-mass star. The very fast pulsation period clearly shows that the compact object in the system is a neutron star. Finally, the detection of optical emission associated with an accretion disc indicates that the compact object is accreting matter from its companion through Roche-lobe overflow. Therefore, it is likely that IGR J00291+5934 is a low-mass X-ray binary (LMXRB) system containing a neutron star which has been spun up by accretion of matter from a companion star. This makes IGR J00291+5934 the 6th member of the class of accreting milli-second pulsars. Moreover, the very fast spin frequency of 599 Hz makes it the fastest accretion-powered pulsar discovered to the present day.

7.2.3 Analysis of IGR J00291+5934

The discovery by *INTEGRAL* as well as the follow-up observations at other wavelengths were presented in Shaw et al. (2005) (see the full paper in Sect. 7.4). Unfortunately, most of the available *INTEGRAL* observations of the source were private observations of the Cassiopeia region, so only the data from the Galactic Plane Scan (20 ksec) could be used. The broad-band *INTEGRAL* spectrum could be well-represented by a CompST model (Sunyaev & Titarchuk 1980), where soft photons coming from a region close to the compact object are comptonized by an optically-thick hot corona surrounding the neutron star, for which we found a temperature $kT = 25_{-7}^{+21}$ keV. The total luminosity of the object was found to be $L \sim 10^{36}$ ergs s^{-1} in the 20-60 keV band. Identifying the object as

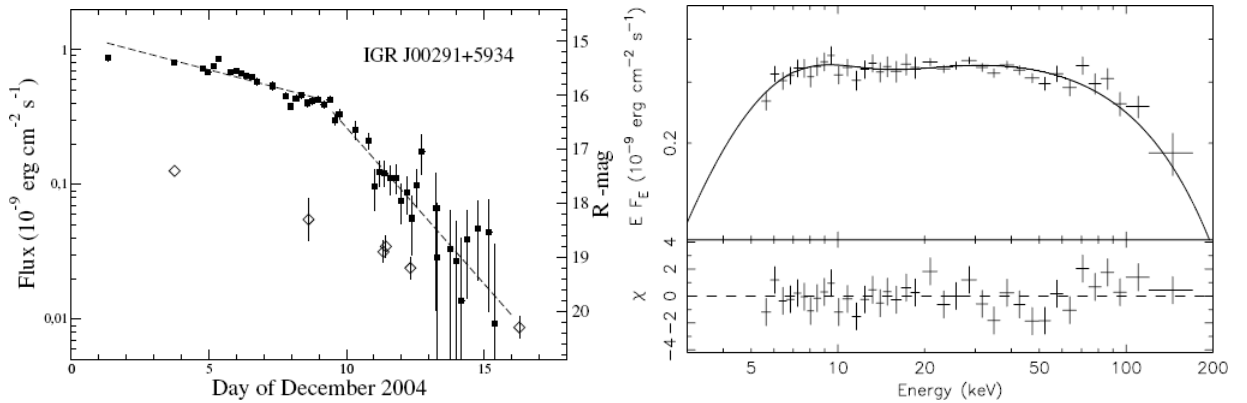


Figure 7.2: Left: IBIS/ISGRI light-curve of the 2004 outburst of IGR J00291+5934. Right: JEM-X/ISGRI total spectrum of IGR J00291+5934. The solid line shows the best fit to the data using a CompPS model with a disc temperature $kT = 1.5 \pm 0.2$ keV and an optically-thick corona at $kT = 49^{+2}_{-6}$ keV. Both figures are from Falanga et al. (2005).

the 6th member of the class of milli-second pulsar, following Chakrabarty et al. (2003) we concluded that the system is composed of a weakly-magnetized ($B \sim 10^8$ G) old neutron star.

Following the *INTEGRAL* results, the timing results from *RXTE* data have been summarized by Galloway et al. (2005). The authors confirmed the spin frequency of 599 Hz and measured a pulsed fraction of 8% in the 3-13 keV band. They also analyzed the decay of the intensity of the source using the All-Sky Monitor (ASM) data from December 2004. Finally, they analyzed historical light curves of the ASM at the position of IGR J00291+5934, and discovered two previous outbursts of the source in 1998 and 2001, which possibly indicated a 3-year period for the outbursts from this source.

Using all the available *INTEGRAL* and *RXTE* data, Falanga et al. (2005) made a detailed analysis of the object. They analyzed the long-term ISGRI light-curve (see the left panel of Fig. 7.2) and found a decay similar to observations of other milli-second pulsars. They also extracted a broad-band (3-200 keV) *INTEGRAL* spectrum using all ISGRI (440 ksec) and JEM-X (170 ksec) data (see the right panel of Fig. 7.2). They found that the spectrum is well-fitted by a CompPS model (Poutanen & Svensson 1996), which describes the comptonization of soft photons by a hot corona surrounding the system. The parameters of the fit give a temperature of $kT = 1.5 \pm 0.2$ keV for the soft photons and a coronal temperature $kT = 49^{+2}_{-6}$ keV. The model also allowed to constrain the inclination angle of the accretion disc compared to the line-of-sight. Overall, the quality of the fit with this model was good ($\chi^2/\text{d.o.f.}=44/37$).

Using all *RXTE* data, Falanga et al. (2005) could also show that the pulsar has been spun-up during the current outburst. The best timing model for the PCA data gives $\nu = 598.89213060(1)$ Hz and $\dot{\nu} = (+8.4 \pm 0.6) \times 10^{-13}$ Hz s^{-1} . This gives a nice confirmation of the hypothesis that milli-second pulsars are normal pulsars which were spun-up to very high frequencies by the accretion of matter from a companion star through Roche-lobe

overflow. The angular momentum of the matter which falls onto the compact object is then used to increase the spin period of the neutron star. In extreme objects such as IGR J00291+5934, the spin velocity of the neutron star becomes as high as $0.1c$. It is expected that neutron stars cannot be accelerated much further, since such a spin velocity is close to the velocity where tidal forces become sufficient to disrupt the neutron star. Therefore, it is expected that accreting milli-second pulsars, and in particular IGR J00291+5934, are the missing link between isolated milli-second pulsars and normal pulsars.

7.2.4 New analysis of the *INTEGRAL* data with OSA 7.0

In the framework of a “Travaux Pratiques 3” work at the University of Geneva with an under-graduate student (C. Tchernin), we performed a new analysis of the existing *INTEGRAL* data with the latest Offline Scientific Analysis (OSA) software, version 7.0. Indeed, Falanga et al. (2005) used OSA v4.2 to analyze the *INTEGRAL* data, and several very important improvements in the calibration of the instruments have been implemented in further OSA versions, so a new analysis could lead to refined results. For our analysis, we used all available ScWs from revolutions 0261-0268 (Dec. 02-25, 2004), for a total observation time of 760 ksec (ISGRI) and 165 ksec (JEM-X1).

Figure 7.3 shows the significance images of the region obtained by ISGRI (left) in the 20-40 keV band and by JEM-X1 (right) in the 3-6 keV band, extracted with the standard OSA 7.0 software. The source was clearly detected by both instruments at the level of 84σ (ISGRI) and 35σ (JEM-X1). The images clearly demonstrate the need for instruments with sufficient angular resolution in the hard X-ray domain. Indeed, the position of the source is found only 17 arcmin away from the Cataclysmic Variable V709 Cas and ~ 1 degree away from the blazar 1ES 0033+59.5, which are clearly detected by both instruments. The discovery of IGR J00291+5934 therefore demonstrates the ability of *INTEGRAL* to detect new hard X-ray sources and locate them with sufficient accuracy.

Analyzing the ISGRI and JEM-X mosaics, we extracted the list of sources which must be taken into account by the spectral extraction tool, and extracted the spectrum of IGR J00291+5934. The quality of the total *INTEGRAL* spectrum is excellent, and leads to a broad-band coverage (3-200 keV) of the source. To model the high-energy emission of the source, we used the XSPEC spectral fitting package version 11.3.2. We started from the simplest possible model, a single power law, and then tried more complex models in order to improve the quality of the fit. Fitting the data with a single power law, we find an unacceptable fit ($\chi_{red}^2 = 3.05$ for 65 d.o.f). Positive residuals are found below 10 keV and around 50 keV. In the standard model which describes the emission from such objects, a soft emission (thermal emission from the surface of the neutron star or from an accretion disc) is comptonized by a hot corona surrounding the system. Therefore, the excess at low energies could be explained by black-body-like emission from the surface of the star or from the accretion disc. Adding a second component to the fit under the form of a soft black-body, we find a significantly better fit ($\chi_{red}^2 = 1.87$ for 63 d.o.f.) with a black-body temperature $kT_{bb} \sim 2$ keV. However, the quality of the fit is still not optimal, and significant negative residuals are found above 80 keV. This could indicate the presence of a high-energy cut-off in the power-law component. Including a high-energy cut-off in our

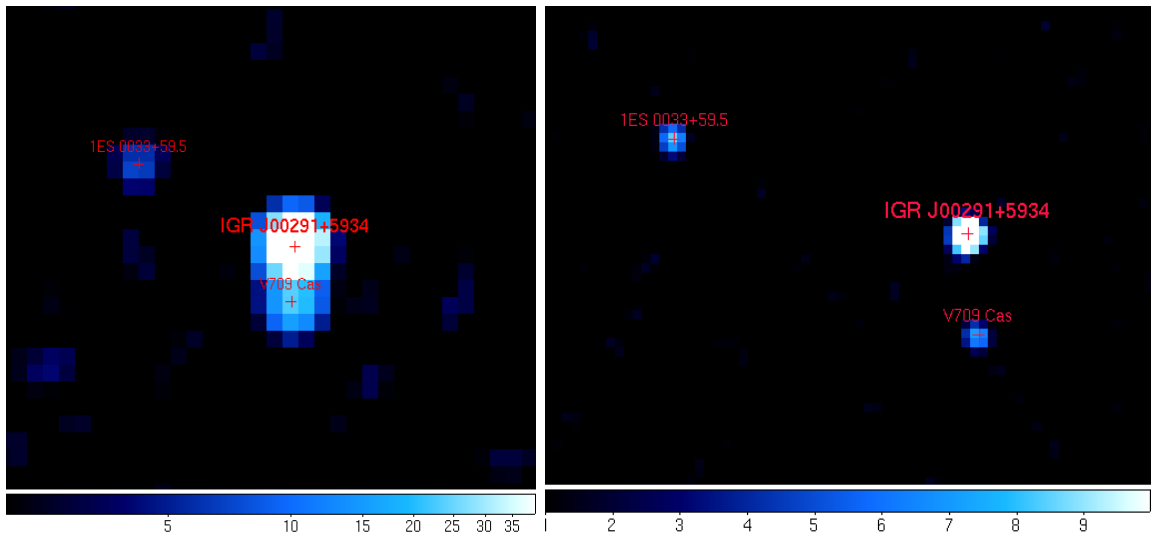


Figure 7.3: ISGRI (left) and JEM-X1 (right) significance images of IGR J00291+5934 during the 2004 outburst. Two other known sources (the Cataclysmic Variable V709 Cas and the blazar 1ES 0033+59.5) are found less than one degree away from the source.

kT_{bb} [keV]	2.08 ± 0.06
kT_{cor} [keV]	31 ± 3
τ	3.3 ± 0.2

Table 7.1: Results of spectral fitting when modeling the spectrum of IGR J00291+5934 as soft black-body emission comptonized by a hot corona. The parameters of the fit are the black-body temperature kT_{bb} , the coronal temperature kT_{cor} and the optical depth of the corona τ .

modeling further improves the fit ($\chi_{red}^2 = 1.61$ for 62 d.o.f.), although the cut-off energy cannot be well constrained. This indicates that the radiation could indeed be described as comptonized emission from a hot corona at a temperature $kT \sim 50$ keV (the cut-off energy).

In order to model the emission as black-body emission from the surface of the neutron star comptonized in a hot corona, we used the CompST model (Sunyaev & Titarchuk 1980), which models the comptonized emission from the corona using approximate solutions of the radiative transfer equation. The parameters of the model are the coronal temperature kT_{cor} and the optical depth τ of the medium. This model provides the best fit to the data ($\chi_{red}^2 = 1.42$ for 62 d.o.f.). The spectrum of IGR J00291+5934 with the best-fit model is displayed in Fig. 7.4. The left panel shows the folded spectrum and the residuals compared to the model, while the right panel shows the unfolded spectrum in an EF_E representation. Table 7.1 gives the best-fit parameters for this model.

Fitting the data using more complex models for the comptonized emission (CompTT, CompPS) did not provide significant improvements to the fit, so we decided to keep the

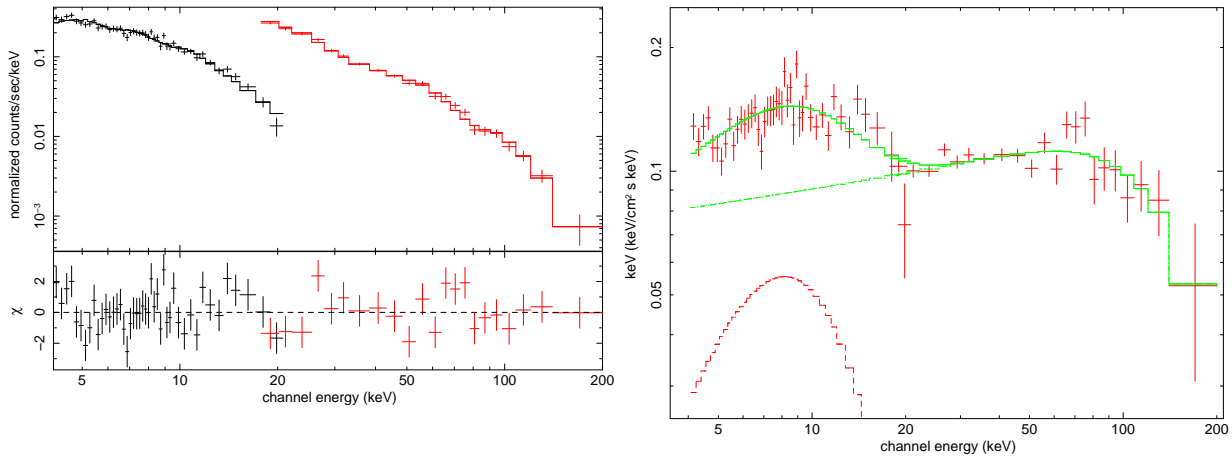


Figure 7.4: Left: Folded spectrum of IGR J00291+5931 extracted with JEM-X (black) and ISGRI (red). The bottom panel shows the deviations of the data compared to the best fit with a black-body+CompST model (solid line). Right: Unfolded spectrum of IGR J00291+5931 in $E E_E$ representation. The solid green line shows the total model made of black-body emission from the neutron star (dashed red) plus comptonized emission from the corona, approximated by a CompST model (dashed green).

simplest acceptable model to describe the source. Instead of a black-body emission, it is also possible to model the soft emission as an optically-thick accretion disc using the DiskBB model (Shakura & Sunyaev 1973). The quality of the fit is similar to our best fit, so based only on *INTEGRAL* data it is not possible to determine if the soft emission comes from the surface of the neutron star (black-body) or from the accretion disc (DiskBB). Using a *Chandra* observation of the source, Paizis et al. (2005) detected an additional very soft component which they model as an accretion disc at $kT \sim 0.3$ keV. Since the bandpass of JEM-X starts only at 3 keV, it is not possible for us to detect this component. Therefore, the 2 keV soft component is probably due to black-body emission from the surface of the neutron star, while the cooler disc component cannot be detected by *INTEGRAL*.

Overall, the results are consistent with the results of Falanga et al. (2005) extracted with OSA 4.2. The calibration improvements introduced in OSA 7.0 allowed us to refine some physical parameters such as the black-body temperature of the soft emission and the temperature of the corona.

7.2.5 Conclusion

The transient X-ray system IGR J00291+5934, discovered by *INTEGRAL* in Dec. 2004 by *INTEGRAL* during a bright outburst, is the fastest known accreting milli-second pulsar to the present day (598 Hz). It is a close binary system consisting of a fast-spinning neutron star and a low-mass star which fills its Roche lobe and transfers material onto the compact object. The angular momentum of the accreted material is used to spin up the neutron star, which explains the extreme rotation velocity ($> 0.1c$) of the pulsar. Spectral analysis of the source reveals that the emission can be well-described by soft black-body

emission from the surface of the neutron star at a temperature $kT = 2$ keV plus comptonized emission from a hot corona at $kT \sim 30$ keV surrounding the system. Optical and soft X-ray emission also reveal the presence of an accretion disc around the compact object.

While the existence of milli-second pulsars has been known for a long time, it was not understood how these objects can reach such high rotation velocities. The discovery of IGR J00291+5934 and the detection of a spin-up by Falanga et al. (2005) provides a natural explanation to this mystery: milli-second pulsars are normal pulsars in close binary systems which have been spun up by accretion of material from the companion star.

7.3 Astronomer's Telegram (ATel) on the discovery of IGR J00291+5934

ATel # 352: IGR J00291+5934, a new X-ray transient discovered with INTEGRAL

D. Eckert, R. Walter (ISDC, Versoix, Switzerland), P. Kretschmar (MPE, Garching, Germany), M. Mas-Hesse (LAEFF, Madrid, Spain), G.G.C Palumbo (University di Bologna, Italy), J.-P. Roques (CESR, Toulouse, France), P. Ubertini (IASF, Roma, Italy), C. Winkler (ESTEC, Noordwijk, The Netherlands)

A new transient X-ray source was discovered with the IBIS/ISGRI and JEM-X detectors on board INTEGRAL on Dec. 2, 2004, during 3 successive pointings dedicated to the Galactic Plane Scan. The source was located with both ISGRI and JEM-X at R.A.= 00h 29.1', Dec.= +59d 34m, (equinox 2000.0) with an error radius of 1.5'. This position is about 20 arcmin off the cataclysmic variable V* V709 Cas and 0.5 degrees off 4U 0027+59. The S/N ratio was 21 in the ISGRI 20-60 keV band. The corresponding average flux is 55+/-5 mCrab. The source flux measured in each of the successive pointings remained constant within 20%. JEM-X detected the source in the 3-10 keV band during the only pointing in which the source was in its field of view, with a flux of 23+/-5 mCrab. The source will be in the field of view of INTEGRAL again on Dec. 5, 2004 for about 2 days for an open program observation. We encourage follow-up observations of this source at all wavelengths.

7.4 Scientific article on IGR J00291+5934

A&A 432, L13–L16 (2005)
 DOI: 10.1051/0004-6361:200500011
 © ESO 2005

**Astronomy
&
Astrophysics**

Discovery of the *INTEGRAL* X/γ-ray transient IGR J00291+5934: A Comptonised accreting ms pulsar?

S. E. Shaw^{1,2}, N. Mowlavi^{2,4}, J. Rodriguez^{3,2}, P. Ubertini⁵, F. Capitanio⁵, K. Ebisawa^{6,2}, D. Eckert^{2,4},
 T. J.-L. Courvoisier^{2,4}, N. Produit^{2,4}, R. Walter^{2,4}, and M. Falanga³

¹ School of Physics and Astronomy, University of Southampton, SO17 1BJ, UK

² *INTEGRAL* Science Data Centre, 1290 Versoix, Switzerland
 e-mail: simon.shaw@obs.unige.ch

³ CEA Saclay, DSM/DAPNIA/SAP (CNRS FRE 2591), 91191 Gif-sur-Yvette Cedex, France

⁴ Observatoire de Genève, 51 Chemin des Maillettes, 1290 Sauverny, Switzerland

⁵ Istituto di Astrofisica Spaziale, CNR/INAF, via Fosso del Cavaliere 100, 00133 Rome, Italy

⁶ NASA Goddard Space Flight Center, Code 661, Building 2, Greenbelt, MD 20771, USA

Received 16 December 2004 / Accepted 23 January 2005

Abstract. We report the discovery of a high-energy transient with the IBIS/ISGRI detector on board the *INTEGRAL* observatory. The source, namely IGR J00291+5934, was first detected on 2nd December 2004 in the routine monitoring of the IBIS/ISGRI 20–60 keV images. The observations were conducted during Galactic Plane Scans, which are a key part of the *INTEGRAL* Core Programme observations. After verifying the basic source behaviour, the discovery was announced on 3rd December. The transient shows a hard Comptonised spectrum, with peak energy release at about 20 keV and a total luminosity of $\sim 0.9 \times 10^{36}$ erg s⁻¹ in the 5–100 keV range, assuming a distance of 3 kpc. Following the *INTEGRAL* announcement of the discovery of IGR J00291+5934, a number of observations were made by other instruments. We summarise the results of those observations and, together with the *INTEGRAL* data, identify IGR J00291+5934 as the 6th member of a class of accreting X-ray millisecond pulsars.

Key words. gamma-rays: observations – pulsars: individual IGR J00291+5934

1. Introduction

IGR J00291+5934 was discovered on 2nd December 2004 (Eckert et al. 2004), during the routine monitoring of IBIS/ISGRI 20–60 keV images of Galactic Plane Scan (GPS) observations at the *INTEGRAL* Science Data Centre (ISDC). In following GPS observations, on 8th December, the source flux remained basically stable at $\sim 8 \times 10^{-10}$ erg cm⁻² s⁻¹ with a marginal monotonic decrease. However, by 11th December, the source flux had reduced by around 50% (see Sect. 2).

The day after the discovery the same sky region was observed by the *Rossi X-ray Timing Explorer (RXTE)*, which detected a 35 mCrab excess with a coherent pulsation at ~ 598.88 Hz (1.67 ms) and pulsed fraction $\sim 6\%$, making IGR J00291+5934 the fastest known accreting X-ray pulsar (Markwardt et al. 2004b). Further analysis of *RXTE*/Proportional Counter Array data, showed that the source has an orbital period of 147.412 ± 0.006 min (Markwardt et al. 2004a). The *RXTE* spectrum was consistent with an absorbed power law with an equivalent absorption column density $N_{\text{H}} \sim 7 \times 10^{21}$ cm⁻², and a photon index of ~ 1.7 (Markwardt et al. 2004b). Archival *RXTE*/All Sky Monitor data suggested that the source had also entered in outburst in 1998 and 2001,

which may indicate that IGR J00291+5934 has a ~ 3 year recurrence time (Remillard 2004). No such activity was seen in archival *BeppoSAX* and *INTEGRAL* data (e.g. in 't Zand & Heise 2004), although these instruments did not make contemporaneous observations with *RXTE*. Later observations by the *Chandra* X-ray telescope made a more accurate determination of $N_{\text{H}} = (2.8 \pm 0.4) \times 10^{21}$ cm⁻² (Nowak et al. 2004).

Observations at radio and optical wavelengths revealed the presence of a transient counterpart at a position consistent with that of the high-energy source, with possible optical emission features (Markwardt et al. 2004b; Pooley 2004; Roelofs et al. 2004; Fender et al. 2004). The most accurate optical position has been reported by Fox & Kulkarni (2004), $(\alpha, \delta) = (00^{\text{h}}29^{\text{m}}03^{\text{s}}.06, +59^{\circ}34'19''.0) \pm 0''.5$; the source is located in the galactic plane, away from the galactic centre at $(l, b) = (120^{\circ}09'64, -3^{\circ}17'65)$.

In view of the high-energy behaviour, the presence of pulsations, the short orbital period and other similarities with the object SAX J1808.4–3658 (in 't Zand et al. 1998; Wijnands & van der Klis 1998; in 't Zand et al. 2001) we consider IGR J00291+5934 to be the 6th member of a class of accreting X-ray binaries with weakly magnetised pulsars.

L14

S. E. Shaw et al.: Discovery of IGR J00291+5934

1.1. INTEGRAL

The *INTEGRAL* satellite was launched on 17 October 2002 and contains several instruments dedicated to observing the high-energy sky in the 3 keV–10 MeV band (Winkler et al. 2003). The prime instruments for this work are the following: the coded mask imager IBIS/ISGRI, which is sensitive in the 15 keV–1 MeV band and has a large $29^\circ \times 29^\circ$ field of view (Lebrun et al. 2003; Ubertini et al. 2003); the X-ray monitor JEM-X, which is sensitive from 3–30 keV and has a $13^\circ 2$ diameter field of view (although noise towards the rim of the detector limits the usable area for weak sources to the central $10^\circ 5$; Lund et al. 2003). The JEM-X instrument consists of two identical telescopes, but for this work, only the JEM-X1 unit was operational.

Data from the satellite are analysed very quickly after an observation; the ISDC Quick Look Analysis (QLA) pipeline runs continuously on the incoming telemetry (Courvoisier et al. 2003). Images are produced by QLA in the following energy bands: 3–10 keV and 10–30 keV (JEM-X); 20–60 keV and 60–200 keV (ISGRI). The images are automatically monitored for new or highly variable sources, which can lead to an automatic alert being issued with a delay of < 2 h from the end of the observation. All images are also inspected manually by the ISDC Scientist on Duty (Shaw et al. 2004).

In this *INTEGRAL* observing period, $\sim 30\%$ of the total amount of observing time is split between the Galactic Centre Deep Exposure (GCDE) and the GPS. The GPS are regular pointings in a saw-tooth pattern along the Galactic Plane, between galactic latitude $b = \pm 10^\circ$, conducted every ~ 12 days (one *INTEGRAL* revolution is 3 days long). Each GPS pointing, or Science Window (ScW), lasts 2200 s and is separated from the next one by 6° (Winkler et al. 2003).

2. Discovery of IGR J00291+5934

The ISDC QLA pipeline first suggested that a new X/ γ -ray source had been discovered in ISGRI images of GPS observations, by an automatic alert issued on 2nd December 2004 at 09:00:19 UTC (Eckert et al. 2004). The alert was triggered because a previously unknown source was detected, at a significance $> 10\sigma$, in a 20–60 keV ISGRI image of GPS pointing 0261-2 (ScW 2 of *INTEGRAL* revolution 0261). This was confirmed at 09:42:03 UTC after the following pointing, 0261-3, by another alert issued at the same sky position. In both cases the alerts were issued approximately 1 h and 40 min after the end of the pointing (see Table 1 for a summary).

Further QLA images showed that the source persisted in the ISGRI QLA images in 0261-3, and had also been detected in the JEM-X1 instrument in 0261-2 (albeit at a level below that required to trigger an automatic alert). Due to the progression of the GPS, the source was not in the instrument field of view for the following pointings. The pointing 0261-2 was also the first pointing of the revolution that could be analysed, since the previous pointing was affected by the passage of the satellite through the Earth's radiation belts. The next GPS observations, during revolution 0263 on 8th December 2004, also yielded four detections of the source by ISGRI. However, in the

Table 1. Detections of IGR J00291+5934 by the ISDC QLA pipeline, based on ISGRI data from single GPS pointings during *INTEGRAL* revolutions 0261 (2nd December 2004), 0263 (8th December 2004) and 0264 (11th December 2004). The detected position, angular distance of the source from the spacecraft pointing axis (θ) and 20–60 keV count-rate (F) are shown. The last line shows the detection by JEM-X1 and the 3–10 keV flux. Pointings marked with * are those where the source was not automatically detected and localised manually.

Pointing (Rev-ScW)	UTC Start (hh:mm)	(α, δ) ($^\circ$)	θ ($^\circ$)	F_{20-60} (cps)
0261-2	06:43	(7.26, 59.57)	3.3	7.5 ± 0.5
0261-3	07:23	(7.24, 59.58)	6.7	6.1 ± 0.5
0261-4*	08:03	(7.3, 59.57)	12.2	7.9 ± 1.2
0263-1*	06:31	(7.3, 59.57)	10.2	5.5 ± 0.8
0263-2	07:10	(7.28, 59.58)	6.7	4.3 ± 0.5
0263-3	07:50	(7.27, 59.58)	7.6	4.6 ± 0.6
0263-4*	08:30	(7.3, 59.57)	11.8	5.3 ± 1.0
0264-2*	06:18	(7.28, 59.59)	10.4	1.9 ± 0.8
0264-3*	06:58	(7.4, 59.5)	4.6	2.2 ± 0.5
0264-4*	07:38	(7.29, 59.55)	2.3	2.6 ± 0.5
0264-5*	08:18	(7.2, 59.5)	7.9	2.4 ± 0.7
0261-2	06:43	(7.279, 59.568)	3.3	1.6 ± 0.2

following GPS pointing, conducted on 11th December (revolution 0264), the source was observed to have faded in ISGRI, and not detected at all in JEM-X.

After the detection, the source was also observed in an already scheduled observation of the CasA/Tycho region and was the subject of an *INTEGRAL* ToO observation, which began on 6th December. The analysis of these data is the responsibility of the respective PIs, and will not be discussed here (Falanga et al. 2005, in preparation).

2.1. Analysis of *INTEGRAL* GPS observations

The ISGRI GPS pointings, listed in Table 1, have been analysed using the standard OSA 4.2 software¹. Figure 1 shows the location of the source in an ISGRI mosaic image, made from all 7 pointings of revolutions 0261 and 0263, and the single JEM-X detection. In both instruments the source is very clearly identified with the optical position of Fox & Kulkarni (2004). Within the ISGRI mosaic image the HMXB 3A 0114+650 is also detected; this gives confidence that some problem with the spacecraft pointing is not responsible for falsely identifying a new source and that IGR J00291+5934 is not a misidentification of another nearby object.

The most significant detection of IGR J00291+5934 was during the first pointing, 0261-2, and it was possible to construct a composite JEM-X1 and ISGRI spectrum. However, the sensitivity of ISGRI is such that it is hard to constrain a physical fit to this source on the strength of just one pointing. A simple absorbed power-law, with the value of $N_H = 0.2 \times 10^{22} \text{ cm}^{-2}$

¹ The OSA software can be obtained from www.isdc.unige.ch

S. E. Shaw et al.: Discovery of IGR J00291+5934

L15

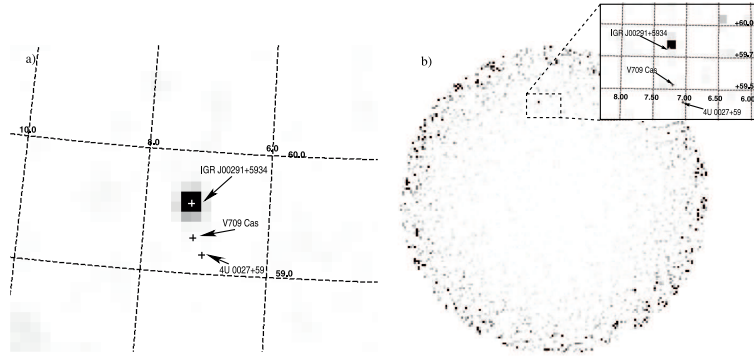


Fig. 1. a) Zoomed 15–40 keV ISGRI significance image made from a mosaic of 7 exposures from revolutions 0261 and 0263 (see Table 1). **b)** 3–10 keV JEM-X1 intensity image, with zoomed inset corresponding to the dashed area (diameter of main image is 10:5). In both images a squared grey-scale, ranging from 0 to the peak pixel value (23 σ for ISGRI, 4.4 cps for JEM-X1) has been used. It is clear that the *INTEGRAL* detections are co-located with the optical position of IGR J00291+5934 reported by Fox & Kulkarni (2004) (white cross) and not with the positions of other nearby sources.

fixed, gives a reduced $\chi^2_{\nu} = 1.1$. The photon index is 1.81 ± 0.13 corresponding to a 5–50 keV flux of $8.3^{+3.7}_{-2.6} \times 10^{-10}$ erg cm $^{-2}$ s $^{-1}$ in agreement with Markwardt et al. (2004b).

The broad band count-rates of IGR J00291+5934 are also noted in Table 1. These show that the flux faded slightly during the course of ~ 10 days, as reported by Swank & Markwardt (2004). Note that the uncertainties on flux measurements with ISGRI increases with the off-axis angle, θ , as the source flux is not fully coded by the mask.

If IGR J00291+5934 is an accreting ms pulsar, then a power-law does not necessarily describe the physics of the source and it is interesting to investigate the possibility of a Comptonised spectrum. To increase the high-energy statistics, an average ISGRI spectrum was made, using the method described in Rodriguez et al. (2005), from those pointings in Table 1 with $\theta < 10^\circ$; this was added to the JEM-X1 spectrum from 0261-2. A reasonable fit was obtained with the CompST model (Sunyaev & Titarchuk 1980): $\chi^2_{\nu} = 0.7$, electron temperature $kT = 25^{+21}_{-7}$ keV and optical depth $\tau = 3.6^{+1.0}_{-1.3}$; the 5–100 keV flux is $8.5^{+0.5}_{-0.2} \times 10^{-10}$ erg cm $^{-2}$ s $^{-1}$. However, it should be noted that a simple power-law also gives a valid fit, $\chi^2_{\nu} = 1.0$, albeit with a softer photon index of 2.05 ± 0.10 . The drop in the flux above 100 keV confirms the presence of a cut-off in the spectrum at high energies (Fig. 2).

Unfortunately, the source was not bright enough to extend the high-energy spectral information with the *INTEGRAL* spectrometer (SPI; Vedrenne et al. 2003). The source was, however, detected at a corresponding position to the other instruments, $(\alpha, \delta) = (6^{\text{h}}3, +59^{\circ}8) \pm 1'$, and the measured 20–60 keV flux of $(5.3 \pm 1.6) \times 10^{-10}$ erg cm $^{-2}$ s $^{-1}$ (assuming a photon index of 1.8) is in good agreement with ISGRI.

The ISGRI data have also been searched for pulsations at the 1.67 ms period of Markwardt et al. (2004b). To maximize the signal to noise ratio, the 20–60 keV band was used, noisy pixels were removed and only those pixels that were fully illuminated by IGR J00291+5934 were selected. The event arrival time was corrected to the solar barycentre

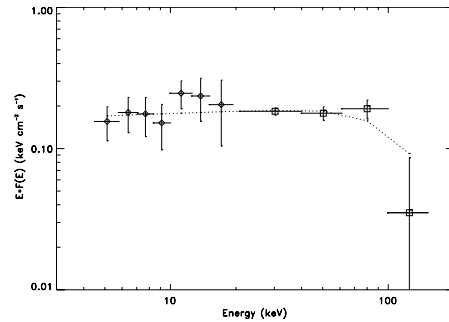


Fig. 2. X/gamma-ray spectrum of IGR J00291+5934 made with JEM-X1 from observation 0261-2 (circles), and an average of ISGRI observations (squares, see text for data selection). The line shows a simultaneous fit to the two sets of data with the CompST model.

and a folded analysis was conducted around the known pulse-frequency of 598.88 Hz. An upper limit for the pulsed amplitude at 598.88 Hz was found to be $\sim 20\%$, which is consistent with the value of 6% by Markwardt et al. (2004b).

3. Discussion

We report the discovery of the fastest known accreting X-ray pulsar, IGR J00291+5934, with *INTEGRAL*. It is likely that IGR J00291+5934 is a low mass X-ray binary (LMXB) system containing a NS pulsar that has been spun up by accretion of material, from a companion star, via an accretion disc. IGR J00291+5934 is one of the fastest X-ray pulsars discovered to date and is second only to PSR B1937+21 (an isolated pulsar showing radio and X-ray pulsations at $P \sim 1.57$ ms; Backer et al. 1982; Takahashi et al. 2001). The absorbing column measured by Nowak et al. (2004) with *Chandra* is approximately a factor of two lower than the estimate of the galactic total on the same line of sight ($N_{\text{H}} \sim 4.5 \times 10^{21}$ cm $^{-2}$; Dickey & Lockman 1990). Given that the source is 120° from

L16

S. E. Shaw et al.: Discovery of IGR J00291+5934

the Galactic Centre and assuming that the galactic disk has a radius of 13 kpc, with the Earth 8.5 kpc from the centre then the average density of absorbing material in the source direction is $\sim 0.2 \text{ cm}^{-3}$. Assuming no local absorption puts an upper limit on the source distance of ~ 3.3 kpc. Although this is a highly simplistic argument, it seems likely that the source is reasonably local. It should also be noted that the Perseus arm of the Milky Way, at $l = 120^\circ$, is located approximately 2.5 kpc away (Taylor & Cordes 1993). Using 3 kpc as an estimate of the source distance, and the 5–100 keV flux quoted in Sect. 2.1, gives a luminosity for the source of $\sim 0.9 \times 10^{36} \text{ erg s}^{-1}$.

The other five known ms X-ray pulsars (SAX J1808.4-3658, XTE J1751-305, XTE J0929-314, XTE J1807-294, XTE J1814-338), are believed to be old NS (age $\sim 10^9$ years), with moderately weak magnetic field, $B \sim 10^8$ G (see e.g. Chakrabarty et al. 2003; Wijnands et al. 2003). In fact all of them are transient systems with short orbital periods, accreting at very low rates. This implies that the magnetic field of the NS is very weak, which is also suggested by the perceived age of the systems (Heindl & Smith 1998; Titarchuk et al. 2002). The *INTEGRAL* high-energy spectral information is limited with this very small data set, but is consistent with properties of other ms X-ray pulsars, with $\tau \sim 3$ and $k_B T \sim 20$ keV. The upper limit on the high-energy pulsations, coupled with the peak energy release at ~ 24 keV, could be consistent with a Comptonised flux being emitted from a hot plasma near the inner part of the disc. Some of this plasma may be channeled towards the NS by the magnetic field, resulting in the pulsed part of the spectrum. In this model, the seed photons would be supplied by the cold intermediate part of the disc rather than the higher temperature NS black-body emission.

It is remarkable that in all of these objects the pulse fraction is of the same order ($\sim 6\%$). IGR J00291+5934, shares many common characteristics with the other objects, particularly SAX J1808.4-3658. The latter has a relatively similar orbital period of ~ 2 h (Chakrabarty & Morgan 1998), a ~ 2 year recurrence time of the outburst and is also the only other known ms pulsar for which a radio counterpart was detected during outburst (Gaensler et al. 1999). It is reasonable to assume that IGR J00291+5934 is an old NS that has been spun up by the accretion of material, with a magnetic field of the same order as the other ms pulsars. The spectral analysis of IGR J00291+5934 reveals that this source is more similar to XTE J1814-338 than the 3 others for which evidence of black body radiation have been seen. However, this may simply be due to the high lower boundary of the JEM-X detector. This is reinforced by the fact that black body emission has been detected in SAX J1808.4-3658 with detectors allowing a broader coverage towards the low energies (e.g. Wijnands et al. 2003).

The spectral analysis of these objects reveal that they are not so different to other NS/pulsar LMXBs, in the sense that the emission processes are thought to originate through thermal + Comptonised processes. It is therefore quite puzzling that only some of these systems show persistent coherent pulsations at the NS spin period. The fact that all ms X-ray pulsars have very short orbital periods may be a clue to why these systems

do or do not show persistent pulsations (see recent review by Wijnands 2005). Despite being the fastest accreting ms pulsar to date, it is interesting to note that the period remains significantly higher than 1 ms.

Acknowledgements. This paper is based on observations made with the ESA *INTEGRAL* project. The authors thank A. Paizis for useful comments in the preparation of this paper. S.E.S. thanks PPARC for financial support. The useful comments and timely response of the anonymous referee were greatly appreciated.

References

- Backer, D. C., Kulkarni, S. R., Heiles, C., Davis, M. M., & Goss, W. M. 1982, *Nature*, 300, 615
- Chakrabarty, D., & Morgan, E. H. 1998, *Nature*, 394, 346
- Chakrabarty, D., Morgan, E. H., Munro, M. P., et al. 2003, *Nature*, 424, 42
- Courvoisier, T. J.-L., Walter, R., Beckmann, V., et al. 2003, *A&A*, 411, L53
- Dickey, J. M., & Lockman, F. J. 1990, *ARA&A*, 28, 215
- Eckert, D., Walter, R., Kretschmar, P., et al. 2004, *ATel*, 352
- Fender, R., de Bruyn, G., Pooley, G., & Stappers, B. 2004, *ATel*, 361
- Fox, D. B., & Kulkarni, S. R. 2004, *ATel*, 354
- Gaensler, B. M., Stappers, B. W., & Getts, T. J. 1999, *ApJ*, 522, L117
- Heindl, W. A., & Smith, D. M. 1998, *ApJ*, 506, L35
- in 't Zand, J. J. M., & Heise, J. 2004, *ATel*, 362
- in 't Zand, J. J. M., Heise, J., Muller, J. M., et al. 1998, *A&A*, 331, L25
- in 't Zand, J. J. M., Comelisse, R., Kuulkers, E., et al. 2001, *A&A*, 372, 916
- Lebrun, F., Leray, J. P., Lavocat, P., et al. 2003, *A&A*, 411, L141
- Lund, N., Budtz-Jørgensen, C., Westergaard, N. J., et al. 2003, *A&A*, 411, L231
- Markwardt, C. B., Galloway, D. K., Chakrabarty, D., & Strohmayer, T. E. 2004a, *ATel*, 360
- Markwardt, C. B., Swank, J. H., & Strohmayer, T. E. 2004b, *ATel*, 353
- Nowak, M. A., Paizis, A., Wilms, J., Ebisawa, K., et al. 2004, *ATel*, 369
- Pooley, G. 2004, *ATel*, 355
- Remillard, R. 2004, *ATel*, 357
- Rodriguez, J., Cabanac, C., Hannikainen, D., et al. 2005, *A&A*, in press [arXiv:astro-ph/0412555]
- Roelofs, G., Jonker, P. G., Steeghs, D., Torres, M., & Nelemans, G. 2004, *ATel*, 356
- Shaw, S., Mowlavi, N., Ebisawa, K., et al. 2004, in 5th *INTEGRAL* Workshop – The *INTEGRAL* Universe: ESA SP-552, 897
- Sunyaev, R. A., & Titarchuk, L. G. 1980, *A&A*, 86, 121
- Swank, J. H., & Markwardt, C. B. 2004, *ATel*, 365
- Takahashi, M., Shibata, S., Torii, K., et al. 2001, *ApJ*, 554, 316
- Taylor, J. H., & Cordes, J. M. 1993, *ApJ*, 411, 674
- Titarchuk, L., Cui, W., & Wood, K. 2002, *ApJ*, 576, L49
- Ubertini, P., Lebrun, F., Di Cocco, G., et al. 2003, *A&A*, 411, L131
- Vedrenne, G., Roques, J.-P., Schönfelder, V., et al. 2003, *A&A*, 411, L63
- Wijnands, R. 2005, in *Pulsars New Research* (NY: Nova Science Publishers), in press [arXiv:astro-ph/0501264]
- Wijnands, R., & van der Klis, M. 1998, *Nature*, 394, 344
- Wijnands, R., van der Klis, M., Homan, J., et al. 2003, *Nature*, 424, 44
- Winkler, C., Courvoisier, T. J.-L., Di Cocco, G., et al. 2003, *A&A*, 411, L1

Chapter 8

Conclusion and future prospects

The study of galaxy clusters in the hard X-ray band is essential to measure intra-cluster magnetic fields and to constrain the particle acceleration models which explain the presence of a large population of relativistic electrons in clusters. Thanks to the good sensitivity up to 100 keV, the moderate angular resolution and the broad-band coverage, observations of the Coma, Ophiuchus and Perseus clusters with *INTEGRAL* lead to several interesting new results, from the significant detection of a non-thermal component in Ophiuchus to the discovery of a region $\sim 10'$ from the center of the Coma cluster which emits more strongly in the hard X-ray band compared to the 1-10 keV surface brightness profile. *INTEGRAL* is therefore an important step forward for the study of galaxy clusters above 10 keV.

On the other hand, a very long integration time is necessary to extract spectra of sufficient quality, and only the brightest nearby objects can be detected with *INTEGRAL*. Moreover, the satellite spends most of its time observing the galactic bulge and galactic plane regions, while the extragalactic sky has been very inhomogeneously covered by *INTEGRAL*. Therefore, it is probable that a number of objects which could be detected with a sufficient integration time are still not detected. In this framework, the Burst Alert Telescope (BAT) instrument on the NASA *Swift* satellite may have a role to play. BAT is an instrument similar to ISGRI dedicated to the detection of gamma-ray bursts. It has a very wide field-of-view, and therefore its coverage of the sky is very homogeneous. On the other hand, due to a very high background BAT is less sensitive than ISGRI by a factor ~ 2 , and because of the very large field-of-view bright sources might cause important systematic effects in the reconstructed sky images. Therefore, BAT will detect a significantly larger number of clusters compared to ISGRI, but it will be difficult to extract spectra of sufficient quality on these clusters. In the BAT 22-month all-sky survey, 10 clusters have been detected so far (T. Okajima, private communication). Rather tight upper limits on the non-thermal emission could be obtained. Only Ophiuchus shows a possible excess at high energies, consistent with the *INTEGRAL* result. During the next few years, *INTEGRAL* and *Swift* will continue to monitor the sky in the hard X-ray band, and possibly detect new clusters above 20 keV.

Using a very long focal length, it is now technologically possible to extend the grazing-incidence technique used by modern X-ray telescopes up to higher energies (> 50 keV).

Future missions such as *NuSTAR*, *NeXT* and *Simbol-X*, which should be launched in 2012-2015, will have a better sensitivity by 2-3 orders of magnitude in the hard X-ray band. In particular, *Simbol-X*¹ will be the most ambitious of these missions. Thanks to the formation-flight technology, it will be sensitive up to 80 keV. It will also have a significantly better angular resolution compared to *NuSTAR* and *NeXT* (10'' compared to $\sim 1'$). Observations of galaxy clusters with *Simbol-X* will allow for the detection of non-thermal emission in a large number of clusters, and for a detailed mapping of the magnetic field throughout clusters. Finally, the most exciting prospects for the study of non-thermal emission in particular and clusters of galaxies in general are the X-ray Evolving Universe Spectrometer² (*XEUS*) project, which has been proposed for the ESA Cosmic Vision call for missions. *XEUS* is a formation-flight project consisting of an X-ray telescope operating in the 0.1-50 keV band with an extremely large effective area of 5 m² at 1 keV and an angular resolution of 2''. This will allow for the detection of non-thermal emission with high signal-to-noise and for high-resolution mapping of the non-thermal component. *XEUS* has been selected by ESA's Space Science Advisory Committee as a candidate large Cosmic Vision mission for further study and a possible launch in 2018.

Apart for the hard X-ray band, the recent launch of *GLAST* also opens prospects for the detection of high-energy γ -ray emission from a number of nearby clusters of galaxies. Indeed, several particle acceleration models predict the existence of significant GeV emission from π^0 decay or non-thermal electron bremsstrahlung (see Sect. 2.6.3). Observations of clusters of galaxies with *GLAST* will put strong constraints on the particle acceleration models, in particular on secondary models. Together with the development of low-frequency radio telescopes with better sensitivity, the next decade will provide a broad-band coverage of the non-thermal emission from galaxy clusters covering more than 13 decades of the electromagnetic spectrum. This will open an exciting new window on the particle acceleration processes in the Universe.

¹<http://www.cnes.fr/web/5848-simbol-x.php>

²<http://sci.esa.int/xeus>

Chapter 9

Acknowledgements/Remerciements

Obviously, the work presented in this thesis could not have been performed without the help of many people, in the professional as well as personal life. I would like to say a few words to thank the people who have helped all along these 4 years as a PhD student.

D’abord, il m’est impossible d’exprimer combien je dois à Christel. Dans les bons comme dans les mauvais moments, que j’aie été grognon ou de bonne humeur, tu as toujours été là pour me soutenir, et je te dois pour une grande partie le bon déroulement de ma thèse. Pour pouvoir se concentrer pleinement sur sa vie professionnelle, il est indispensable d’avoir une vie personnelle épanouie, et grâce à toi, je suis fier de dire que c’est mon cas. J’espère que notre futur sera aussi heureux que notre présent.

Bien sûr, je tiens à remercier particulièrement mes parents pour leur soutien indéfectible et leur confiance en moi inébranlable. Vous avez été le roc qui m’a toujours remis dans le droit chemin lorsque je doutais, et rien de tout ceci n’aurait été possible sans vous. Merci pour tout, P’pa et Mimi.

Un grand merci aussi à Rapha et Vangheli, mes grand-parents, et tout le reste de ma famille que je n’oublie pas, et sans qui la stabilité familiale n’aurait pas été possible. Un grand merci à Manu, pour son amitié fidèle, les longues parties de Mario Kart et le “Dabo Contest”. Merci à Walid pour toutes ces années d’amitié et plus de parties de tennis que je ne peux compter. Merci à Ariel pour le UHC Céligny. Merci à Cambyse, Nicola, Nicolas, Anna-Sabina, Fabrice et les autres pour ces années d’université qui n’auraient pas été pareilles sans vous. Merci enfin à tous mes autres proches et amis que j’ai omis ici, mais à qui je pense aussi³.

Je voudrais adresser des remerciements particuliers au Prof. Courvoisier pour m’avoir donné la chance de travailler sous sa direction à l’ISDC. Grâce à votre gestion humaine de l’institut, l’ISDC est un endroit où il fait bon travailler, et où les idées fourmillent. Un grand merci aussi pour avoir su m’encourager dans la bonne direction lorsque c’était nécessaire, lorsque moi-même je n’y croyais plus trop. Enfin, je vous suis infiniment recon-

³Merci à Maude et à Jo pour avoir demandé d’être dans les remerciements.

naissant de me permettre de continuer encore une année à l'ISDC, ce qui me permettra d'envisager mon futur sereinement. Merci pour tout.

De l'ISDC, je voudrais remercier en particulier Stéphane Paltani et Nicolas Produit. Pour moi, il est évident que ma production scientifique a décuplé dès le moment où j'ai commencé à travailler avec Stéphane. Merci infiniment de m'avoir ouvert ta porte à chaque fois que j'en avais besoin. Tes conseils avisés et ton intelligence m'ont été extrêmement précieux. Merci aussi à Nicolas, pour m'avoir toujours aidé avec le sourire lorsque je me battais avec les instruments et la programmation. Les connaissances techniques que j'ai acquises à ton contact me seront importantes durant toute ma carrière, j'en suis convaincu.

I would like to thank especially Andrii Neronov, who started the work which became the basis of this PhD thesis. Thank you for all the help and all the ideas. Big thanks to Arash for sharing so many things with me (office, work, music, etc.). From the ISDC, I thank: Volker for all the parties and the "Planeten" CD, Simona for going through the same things at the same time (even the defence...), Carla for always being in a good mood, Claudio for Mario, Piotr for his rabbits, Juan and JC for helping me to get out of the football pitch, Wako for hearing me complain about everything without saying a word, Igor and Volodya for believing in my coding skills, Pierre, Marc A. and the secretary team for the coffee breaks, the operators for the shift, and of course all the others that I didn't mention here, but contribute to the good atmosphere of the ISDC. Finally, I also would like to thank Jukka Nevalainen from Helsinki University for a fruitful collaboration and a good time in Granada.

Appendix A

Calibration work related to extended source analysis

As it is the case for every space mission, the knowledge of the instruments is not perfect at the moment of the launch. Therefore, in-flight calibration is required to understand the behaviour of the hardware as well as possible. In some cases, the analysis of extended sources with *INTEGRAL* required the use of some aspects of the instruments which were not yet properly known. In this section, I will present some of the calibration work that I have done in order to improve some pieces of the IBIS analysis software. In particular, I will present my work on the imperfections of the IBIS mask, which introduce important artifacts in the image reconstruction software and in the PIF models.

A.1 IBIS PIFs and misalignment

The method presented in Sect. 3.3 requires an excellent knowledge of the shadow pattern cast by a point source on the detector. Namely, if several imperfections affect the exact pattern of the IBIS mask, they will introduce systematic errors on the Pixel Illumination Fraction (PIF), which is computed geometrically from the ideal MURA pattern (see Fig. 3.2). Since our method to construct the shadow pattern of an extended source is based on the standard point-source PIF, these systematic errors will also affect our extended-source analysis method. On the other hand, it has been known since the calibration phase after launch that the axis of the spacecraft is slightly misaligned compared to the axis of the star-trackers (Favre 2004), which introduces systematic errors in source location. While this effect has been known for a long-time and is now relatively well understood, any mistakes in the computation of the correction matrix could affect the method presented in Sect. 3.3. In this section, I will briefly present the tests that I have performed in order to find the misalignment correction matrix in two independent ways, and the tests regarding the accuracy of the PIF build software.

To find the alignment, we analysed a selection of more than 1,000 pointings (Science Windows, ScWs) with the calibration source, the Crab nebula, in the FOV. We used the `ii_pif_build` software to build the PIF, that we fitted thereafter to the real shadowgram. Then we compared the position of the Crab found by this method with the known position of the Crab in the ScWs we were using, and we calculated the offset between these

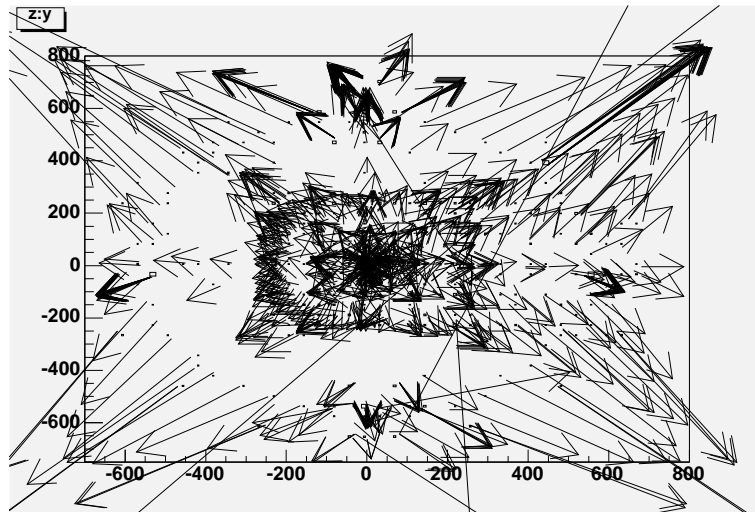


Figure A.1: Difference between the fitted position of the Crab nebula and the known position (arrows), as a function of the position of the source on the detector (dots), for a selection of pointings. The X and Y axes represent the position of the source with respect to the axis of the spacecraft in detector pixel coordinates. The size of the arrows is multiplied by a factor 100 for better readability.

two positions for all the ScWs. The result of this analysis is shown in Fig. A.1. Each dot shows the known detector position of the Crab nebula in a single pointing, while the arrows point towards the position which was fitted by our software.

We can see on the figure that for low off-axis angles (i.e., when the source is close to the direction of the spacecraft), the software finds the position of the source very close to the correct position. However, for large off-axis angles, a clear off-set between the fitted position and the catalog position is found. In the most extreme cases, the off-set can reach a value of 2 sky pixels, i.e. 9 arcmin. However, such a large off-set is not consistent with the measurements from Favre (2004), who found that the accuracy of the alignment is ~ 10 arcsec. Indeed, we found that this discrepancy comes from inaccurate PIFs for large off-axis angles. A number of effects which introduce shadows on the detector in addition to the mask shadow are not taken into account into the `ii_pif_build` software, and therefore, systematic errors are introduced in the fitting procedure because of uncertainties in the shadow pattern. In addition to `ii_pif_build`, there exists an alternative software for PIF creation, `ii_pif`. We performed the same analysis with the `ii_pif` code, and did not find the same effect. Hence, we conclude that `ii_pif` provides a more accurate shadow pattern model, and from now on, we will use the `ii_pif` code for PIF creation.

Although `ii_pif` provides a better description of the instrument compared to `ii_pif_build`, there are still a number of imperfections in the shadow pattern which are not modeled in the code. These imperfections introduce artifacts in the deconvolved sky images which are not properly understood. In order to look for the problems in PIF creation, we decided to produce an empirical mask model and compare it with the existing models. Using a large number of archival ScWs on the Crab nebula, we computed the detector position of

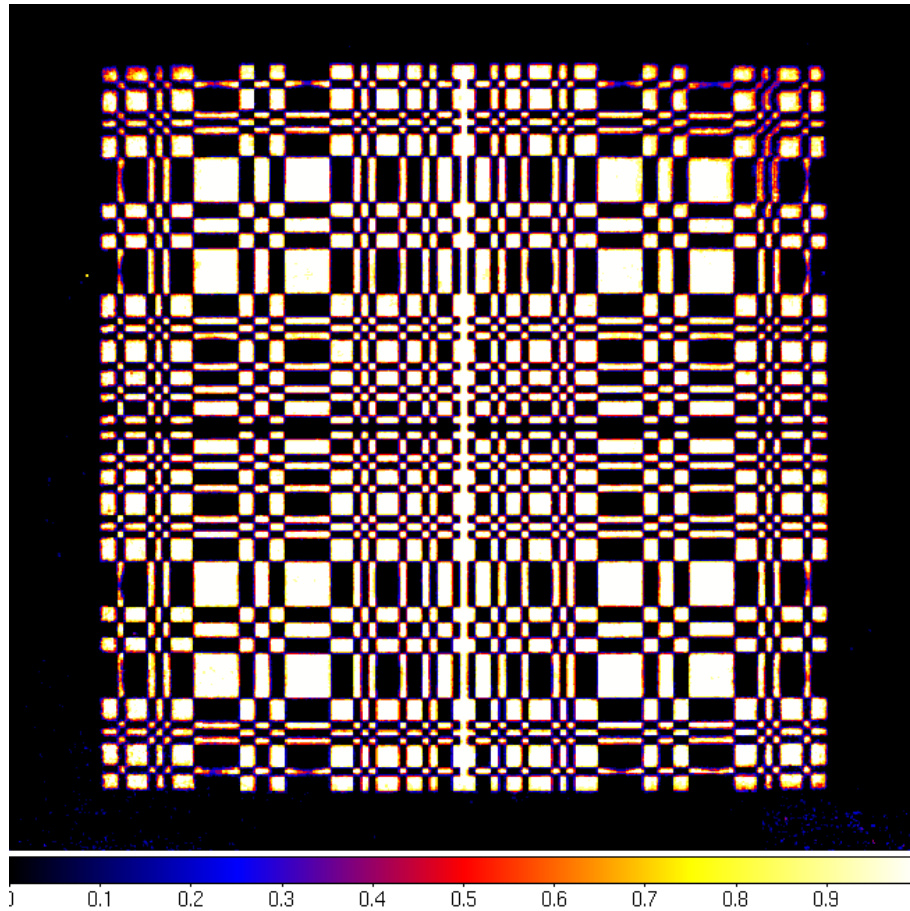


Figure A.2: Empirical mask model (“SuperPIF”) renormalized such that the mean background level is 0 and the mean Crab count rate is set to 1.

the Crab relative to the direction of the spacecraft for each pointing, placed the corrected shadowgrams in a larger array (the “SuperPIF”) at the correct detector position and then stacked all the shadowgrams in order to increase the signal-to-noise at each position. The resulting image shows the mask as it is empirically seen. Figure A.2 shows our empirical mask model, renormalized such that the mean background level is set to 0 and the mean Crab count rate is set to 1.

Analyzing the SuperPIF and comparing it to the existing mask models, we found several differences which had not been identified before. They are mostly due to the screws which were used to attach the mask to the supporting structure (NOMEX). For large off-axis angles, the screws block some of the holes in the mask, and therefore introduce unexpected differences between the mask model and the data. In order to take the effect of the screws into account, we made a simple model for the obscuration by the screws and modified the standard PIFs produced by the `ii_pif` executable. For the modeling of the screws, we assumed a constant transparency of the screws with energy. This is certainly not accurate enough, since it is expected that the fraction of photons absorbed by the screws strongly depends on energy, and a more precise model is required to treat the effect of the screws

accurately. In any case, we expect that our simple modeling of the screws already brings significant improvements in the PIF model, in particular at low-energy. But more work is required in order to model the screws correctly.

A.2 ISGRI mosaicking method

Because of the periodic properties of the IBIS mask, the IBIS/ISGRI imaging software is affected by the presence of “ghosts”, i.e. artifacts in the sky images introduced by the presence of bright sources in the Field Of View (FOV). Since the method for the analysis of extended sources with IBIS presented in Sect. 3.3 requires the knowledge of the morphology of the source, it is crucial to reconstruct sky images in the best possible way. In the ideal case of a “perfect” MURA mask, the periodicity of the mask produces known side-lobes of point sources which can be accurately modeled. In the standard OSA image deconvolution software, the program searches for sources in the deconvolved image, and then applies a side-lobe model in order to produce an artifact-free sky image. However, we have shown in the previous section that several instrumental problems (in particular the screws which are used to attach the mask to the NOMEX structure) imply that the side-lobes produced by the image deconvolution process are not well modeled by the standard imaging process, which introduces artifacts in the deconvolved sky images.

In order to implement our modeling of the screws in the imaging process, we developed a different approach to the image deconvolution process. In order to use our modeling of the screws which was already implemented in the PIF computation, we decided to look for sources in the detector image and model them using our modified PIF instead of modeling them in the deconvolved sky images.

In more details, the method can be described in several major steps. For this work, we assumed that for weak sources ($F_{20-40 \text{ keV}} \lesssim 20 \text{ mCrab}$) the error induced by the incorrect mask model is negligible. First, we extracted a catalog of 83 sources whose persistent flux is larger than 20 mCrab or which exhibited a strong outburst with a flux greater or equal to 20 mCrab. For each single pointing, we produce corrected shadowgrams and compute a modified PIF for all the sources in our catalog which are present in the Field of View (FoV). Then we make a multi-parameter fit similarly to the method described in Sect. 3.3.2 in order to get the fluxes f_i and errors Δf_i for all the catalog sources and the background b . Thereafter, we remove bright sources and background from the shadowgram S to produce a corrected shadowgram S' :

$$S'(x, y) = S(x, y) - \sum_{i=1}^n f_i \cdot PIF_i(x, y) - bB(x, y), \quad (\text{A.1})$$

where $B(x, y)$ is a background map, and a corrected variance map V' given by error propagation,

$$V'(x, y) = V(x, y) + \sum_{i=1}^n \Delta f_i \cdot PIF_i(x, y) + \Delta b \cdot B(x, y). \quad (\text{A.2})$$

The resulting shadowgram is therefore free of strong sources, and can be deconvolved in the normal way in order to look for fainter sources without contamination from the bright

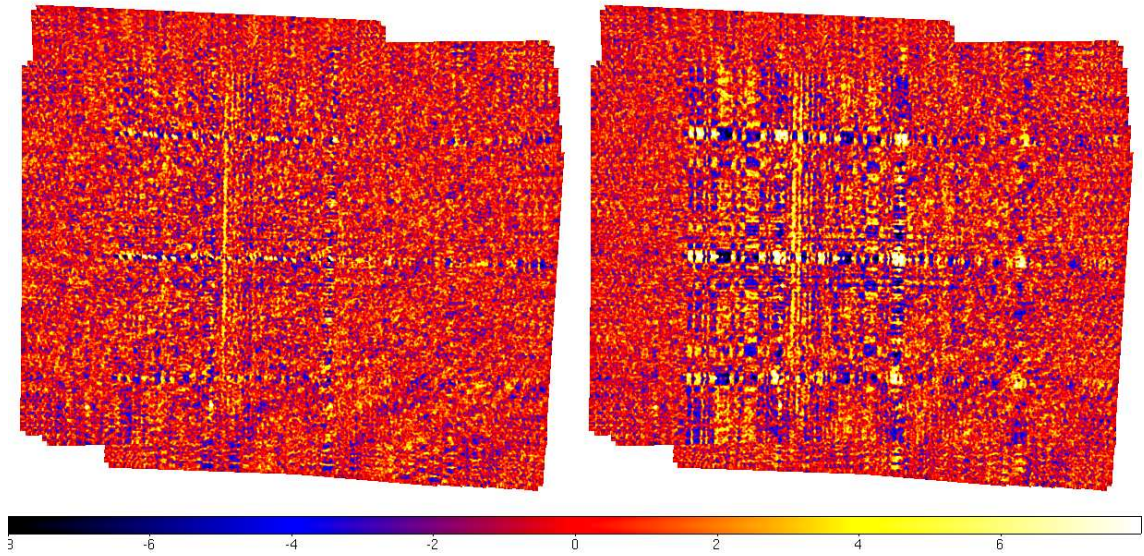


Figure A.3: ISGRI 20-40 keV mosaic images produced from a sample of 130 ScWs with the Crab nebula in the FOV, processed with our method (left) and with the standard OSA 7.0 software (right).

sources in the FOV.

To test our method, we selected a sample of 130 ScWs from different observations of the Crab nebula, and produced a mosaic using the standard OSA imaging software and with our method for direct comparison. Figure A.3 shows the resulting significance images in the 20-40 keV band, at the same scale. We can see that the artifacts induced by the presence of the Crab in the FoV are dramatically reduced thanks to the modeling of the screws. However, a number of artifacts are still present in the resulting sky image. In particular, it seems that the remaining artifacts are split into a negative and a positive part. This could be due to the misalignment of the star trackers with respect to the spacecraft, which is still not completely understood.

In conclusion, important improvements to the imaging software could be implemented thanks to the modeling of the screws which are used to attach the mask to the supporting structure. However, more work is required in order to get artifact-free sky images with ISGRI, for example by making a more accurate modeling of the screws (in particular to take the dependence of the screw transparency with energy into account) and by re-computing the misalignment between the star trackers and the spacecraft using the newly-implemented mask models.

Appendix B

List of publications

2004

- Eckert, D., Walter, R., Kretschmar, P., Mas-Hesse, M., Palumbo, G. G. C., Roques, J.-P., Ubertini, P., Winkler, C. 2004, *IGR J00291+5934, a new X-ray transient discovered with INTEGRAL*, ATel # 352

2005

- Mereghetti, S., Gotz, D., Mowlavi, N., Eckert, D., Beck, M., Borkowski, J. 2005, *GRB 051211B: a long GRB detected by INTEGRAL*, GCN # 4327,1
- Shaw, S. E., Mowlavi, N., Rodriguez, J., Ubertini, P., Capitanio, F., Ebisawa, K., Eckert, D., Courvoisier, T. J.-L., Produit, N., Walter, R., Falanga, M. 2005, *Discovery of the INTEGRAL X/γ-ray transient IGR J00291+5934: A Comptonised accreting ms pulsar?*, A&A432, L13
- Foschini, L., Di Cocco, G., Malaguti, G., Pian, E., Tagliaferri, G., Ghisellini, G., Maraschi, L., Giommi, P., Gehrels, N., Walter, R., Eckert, D. 2005, *INTEGRAL observation of the blazar 3C454.3 in outburst*, ATel # 497
- Steiner, C., Eckert, D., Mowlavi, N., Decourchelle, A., Vink, J. 2005, *IGR J01583+6713, a new hard X-ray transient discovered by INTEGRAL*, ATel # 672

2006

- Soldi, S., Walter, R., Eckert, D., Balman, S., Bazzano, A., Beckmann, V., Belloni, T., Boggs, S., Capitanio, F., Chenevez, J., Del Santo, M., Diehl, R., Donnarumma, I., Goldoni, P., Gotz, D., Leyder, J.-C., Mereghetti, S., Paizis, A., Pottschmidt, K., Sidoli, L., Tarana, A., Tueller, J., Watanabe, K., Weidenspointner, G. 2006, *IGR J17497-2821: a new hard X-ray transient detected by INTEGRAL*, ATel # 885
- Walter, R., Eckert, D., Kreykenbohm, I., Lubinski, P., Paltani, S., Produit, N., Zurita, J. 2006, *IGR J17497-2821: further observations with Swift and INTEGRAL*, ATel # 889

2007

- Turler, M., Balman, S., Bazzano, A., Beckmann, V., Belloni, T., Boggs, S., Capitanio, F., Chenevez, J., Del Santo, M., Diehl, R., Donnarumma, I., Eckert, D., Goldoni, P., Gotz, D., Leyder, J.-C., Mereghetti, S., Paizis, A., Pottschmidt, K., Sidoli, L., Tarana, A., Tueller, J., Walter, R., Watanabe, K., Weidenspointner, G. 2007, *INTEGRAL observation of a bright X-ray outburst of XTE J1739-302 / IGR J17391-3021*, ATel # 1019
- Turler, M., Balman, S., Bazzano, A., Beckmann, V., Belloni, T., Boggs, S., Capitanio, F., Chenevez, J., Del Santo, M., Diehl, R., Donnarumma, I., Eckert, D., Ferrigno, C., Goldoni, P., Gotz, D., Leyder, J.-C., Mereghetti, S., Paizis, A., Pottschmidt, K., Sanchez-Fernandez, C., Sidoli, L., Tarana, A., Tueller, J., Walter, R., Watanabe, K., Weidenspointner, G. 2007, *IGR J17191-2821: a new hard X-ray transient detected by INTEGRAL*, ATel # 1021
- Eckert, D., Neronov, A., Courvoisier, T. J.-L., Produit, N. 2007, *South-West extension of the hard X-ray emission from the Coma cluster*, A&A470, 835
- Haymoz, P., Eckert, D., Shaw, S., Kuulkers, E. 2007, *INTEGRAL detects hard X-rays from SAX J1810.8-2609 during its current outburst*, ATel # 1185
- Eckert, D., Produit, N., Neronov, A., Courvoisier, T. J. -L. 2007, *A particle acceleration site in the Coma cluster?*, ICRC proceeding

2008

- Eckert, D., Produit, N., Paltani, S., Neronov, A., Courvoisier, T. J.-L. 2008, *INTEGRAL discovery of non-thermal hard X-ray emission from the Ophiuchus cluster*, A&A479, 27
- Eckert, D. 2008, *INTEGRAL Observations Of Galaxy Clusters: The Search For Non-thermal Emission*, HEAD meeting #10, #9.11

Figures

- 2.1 *Left:* *Chandra* temperature map of the Perseus cluster (Sanders et al. 2005). The uncertainties range from 0.1 keV in the coolest regions to 0.5 keV in the hottest regions. The white spots are subtracted point sources. *Right:* *Chandra* X-ray image of the “Bullet cluster” 1ES 0657-55.8 super-imposed on an optical image of the region (Markevitch et al. 2004). 4
- 2.2 *Left:* Loss function $b(\gamma)$ for the different electron cooling processes: Coulomb losses, non-thermal bremsstrahlung emission, synchrotron and inverse-Compton radiation. The curves assume $n_e = 10^{-3} \text{ cm}^{-3}$, $B = 1 \mu\text{G}$ and $z = 0$. *Right:* Cooling timescale t_{loss} as a function of γ in a cluster with $n_e = 10^{-3} \text{ cm}^{-3}$ and $B = 1 \mu\text{G}$ (solid curve). The dashed curve assumes a magnetic field of $5 \mu\text{G}$, and the dot-dashed curve uses a density $n_e = 10^{-4} \text{ cm}^{-3}$. The figures are from Sarazin (1999). 6
- 2.3 Interaction geometry for the diffusive shock acceleration process. Particle distributions are isotropised upstream and downstream of the shock in zones 1 and 2 (Credit: T. Courvoisier). 7
- 2.4 Electron spectra predicted by a primary re-acceleration model where $\gamma \sim 100$ electrons are re-accelerated to higher energies through diffusive shock acceleration (Brunetti et al. 2001), for different magnetic field values. The models assume a re-acceleration time-scale $\tau = 0.8 \text{ Gyr}$ and a re-acceleration efficiency $\chi = 2 \times 10^{-16} \text{ s}^{-1}$ 9
- 2.5 Spectrum of cosmic-ray protons entering the Earth’s atmosphere (data compiled by J. Swordy). The spectrum is well-represented by a broken power-law with a break energy $E_b \sim 10^{15} \text{ eV}$ (“the knee”). A possible hardening at the highest energies, the so-called “ankle”, can be seen. 10
- 2.6 Spectra of thermal electrons accelerated because of turbulence in the ICM at different time periods (from Blasi (2000)). At $t = 0$ (thin solid line), the distribution is assumed to be Maxwellian with $kT = 8.21 \text{ keV}$, typical of the Coma cluster. The dashed line and the thick solid line show the evolution of the spectrum after an acceleration time $t = 5 \times 10^8$, respectively 10^9 yr 13
- 2.7 *Left:* 1.4 GHz image of the Coma C radio halo from the 100-m Effelsberg telescope (Deiss et al. 1997). Compared to the thermal X-ray emission from the ICM, the centroid of the source is displaced by ~ 5 arcmin. *Right:* Radio spectrum of Coma C compiled by Thierbach et al. (2003). The spectrum shows a break at high frequencies. 15
- 2.8 0.2-2 keV X-ray image of the Abell 3376 cluster from the *ROSAT* PSPC instrument with 1.4 GHz radio contours from the Very Large Array overlaid (Bagchi et al. 2006). The relics unveil one of the most powerful merging events detected so far. 16

2.9	Hard X-ray spectrum of the Coma cluster obtained with the PDS (15-80 keV) and HPGSPC (4.5-20 keV) instruments on board <i>BeppoSAX</i> (Fusco-Femiano et al. 1999). The dashed line represents the thermal component ($kT = 8.5 \pm 0.5$ keV), while the dashed straight line is the non-thermal component with a photon index $\Gamma = 1.6$	17
2.10	Predictions for the γ -ray flux from π^0 decay from a model considering both primary and secondary electron populations (Pfrommer 2007).	18
2.11	Energy spectrum of electrons required in a Coma-like cluster to explain the thermal X-ray emission (Maxwellian at $T \approx 10^8$ K), the radio synchrotron and HXR inverse-Compton emission (non-thermal power-law). A possible non-thermal tail in the Maxwellian distribution, discussed in Sect. 2.5.1, is also displayed. The figure is from Petrosian et al. (2008).	21
3.1	An exploded view of the <i>INTEGRAL</i> spacecraft (Credits: ESA 2002). The 4 scientific instruments are loaded on the “payload module”, on top of the “service module”, which contains the operational systems.	23
3.2	The IBIS mask pattern. The geometrical properties of the mask have been chosen such that the decoding array $G = 2M - 1$	25
3.3	Sensitivity of the ISGRI detector as a function of energy (Lebrun et al. 2003). The solid curve shows the minimum flux level for which a 3σ detection can be achieved in a 1 Msec observation, compared to the mCrab flux level (dashed line).	26
3.4	The shadow pattern (or PIF) of the mask of the IBIS telescope cast by a point source (left) and a circular source with a radius of 30 arcmin (right) located along the axis the instrument.	28
3.5	Relative reconstructed peak flux as a function of the source radius for a uniform disk observed on-axis (triangles) and 9° off-axis (squares) (Renaud et al. 2006b). Below $\sim 8'$, the flux loss is limited, whereas above this value, the peak flux decreases as R^{-2}	29
3.6	Left: Relative flux extracted by the standard OSA spectral extraction tool for an extended source with a surface brightness profile described by a beta profile with $\beta = 0.75$ and different values of R_c . Right: Effective radius R_{eff} as a function of the core radius R_c (see text).	32
3.7	<i>XMM-Newton</i> /MOS1 and <i>INTEGRAL</i> /ISGRI spectrum of the Coma cluster centre. For correct cross-calibration, the MOS spectrum has been extracted in a radius of 7.2 arcmin from the centre (see text).	33
4.1	Combined optical (blue, Sloan Digital Sky Survey) and IR (red, Spitzer) image of the core of the Coma cluster (Jenkins et al. 2007). The core is dominated by the two giant ellipticals NGC 4874 (right) and NGC 4889 (left). The faint green dots are mostly dwarf galaxies inside the cluster.	36
4.2	<i>XMM-Newton</i> image of the cluster in the 0.3-2.0 keV band (Briel et al. 2001). The falling sub-cluster around NGC 4839 SW of the cluster core is clearly seen. Several point sources detected in X-rays are highlighted as well.	37

4.3	Standard OSA 6.0 significance image of the Coma cluster with ~ 1.1 Ms of data, in the 18-30 keV energy band. Significance contours from 3 to 10σ in steps of 1σ are overlaid in red. The position of the 3 brightest X-ray point sources is also displayed. For comparison, the inset in the bottom right corner shows a mosaic image of a known point source in the same field, NGC 4388.	39
4.4	Left: <i>XMM-Newton</i> /PN mosaic image of the center of the Coma cluster extracted from the Coma mosaic observation. The lines are artifacts due to the gaps between the modules of the detector. The positions of the two central cD galaxies, NGC 4874 and NGC 4889, as well as the quasar EXO 1256+281 are displayed. Right: Same as previous, but convolved with a two-dimensional Gaussian to match the angular resolution of ISGRI. The green contours represent the ISGRI 18-30 keV brightness contours extracted with OSA version 6.0.	39
4.5	ISGRI significance image after the subtraction of the properly renormalized PN image (see text). Significant excess ($\sim 6\sigma$) are found SW of the cluster core. The green contours show the 1-10 keV surface brightness profile extracted from the smoothed PN mosaic.	40
4.6	Left: <i>XMM-Newton</i> /PN spectrum of the Coma cluster. The solid line shows a MEKAL model at $kT = 7.9$ keV fitted to the 2-10 keV part of the spectrum. Significant residuals are found below 2 keV. Right: <i>XMM-Newton</i> /PN and <i>INTEGRAL</i> /ISGRI spectrum of the Coma cluster extracted in the region which gives the best fit to the hard X-ray morphology in order to ensure the best signal-to-noise at high energy. No obvious excess is found in the ISGRI spectrum.	42
4.7	<i>XMM-Newton</i> /MOS temperature map of the Coma cluster (from Neumann et al. (2003)). Red regions correspond to temperatures below 8 keV, yellow regions to $8 \text{ keV} < kT < 10 \text{ keV}$ and white regions to $kT > 10 \text{ keV}$	44
4.8	<i>INTEGRAL</i> South-West excess image compared to 1.4 GHz radio contours from Deiss et al. (1997). The position of the radio peak is remarkably well correlated with the <i>INTEGRAL</i> excess.	44
4.9	Spectral Energy Distribution of the non-thermal emission assuming that the <i>INTEGRAL</i> SW excess comes from inverse-Compton scattering of relativistic electrons with the CMB. The radio data are from Thierbach et al. (2003). The color curves show numerical models for the SED with different values of magnetic field B and electron cut-off energy E_{cut}	45
4.10	IBIS/ISGRI OSA 7.0 significance images of the Coma cluster in the 15-20, 20-30, 30-60 and 60-200 keV bands (from left to right). The green contours show the 1.4 GHz radio emission.	46
4.11	<i>INTEGRAL</i> /JEM-X significance images of the Coma cluster in the 3-10 (left) and 10-18 keV bands. The green contours represent the surface brightness profile of the source extracted from <i>XMM-Newton</i> /PN. In the lower energy range, the full extent of the source is about 25 arcmin. In the higher energy band, the source is still not detected, but a 3σ excess is found close to the centre of the <i>XMM-Newton</i> emission.	46

4.12	<i>INTEGRAL</i> /ISGRI 15-60 keV significance OSA 7.0 image subtracted for the 1-10 keV <i>XMM-Newton</i> /PN profile. The contours show the radio emission at 1.4 GHz from Deiss et al. (1997).	47
4.13	Calibration of the FeXXV/FeXXVI line ratio method (figure from Nevalainen et al. (2003)). Left: Dependence of the relative intensity of both lines on the gas temperature. Right: FeXXV/FeXXVI line ratio as a function of temperature.	47
4.14	Temperature map of the Coma cluster based on FeXXV/FeXXVI line ratio (figure courtesy of Jukka Nevalainen).	47
4.15	ISGRI OSA 7.0 spectrum of the SW region, fitted by a thermal bremsstrahlung (dashed red line) plus a power-law with a fixed photon-index $\Gamma = 2.0$ (dashed green line). The temperature of the thermal component was fixed to the value $kT = 9.0$ keV measured through the <i>XMM-Newton</i> /PN FeXXV/FeXXVI line ratio.	48
5.1	Left: Suzaku/XIS mosaic image of the Ophiuchus cluster (Fujita et al. 2008). Right: <i>ASCA</i> /GIS temperature map of the Ophiuchus cluster (Watanabe et al. 2001). A hot region ($kT \gtrsim 15$ keV) is seen West of the cluster core. . .	64
5.2	<i>INTEGRAL</i> /ISGRI mosaic image of the Galactic center region. The Ophiuchus cluster is shown, as well as a number of bright sources in the same field, including the Galactic center “sausage”, which is a blend of many sources in the direction of the Galactic center, in the bottom left corner of the image. . .	66
5.3	<i>INTEGRAL</i> /JEM-X significance mosaic images of the Ophiuchus cluster region in the 3-5, 5-7, 7-10 and 10-18 keV bands. The source in the bottom of the image is the Cataclysmic Variable V2400 Oph.	67
5.4	<i>INTEGRAL</i> images of the Ophiuchus cluster in the 20-40 keV band from ISGRI (left) and in the 3-18 keV band from JEM-X (right). For comparison, the insets show the image of a known point source in the same field, the Cataclysmic Variable V2400 Oph.	68
5.5	Deconvolved radial profile of the Ophiuchus cluster extracted from JEM-X data (dashed blue line), compared to the PSF of the instrument (dashed green). The actual data (purple bars) and the apparent profile (red line) are also shown.	68
5.6	Deviations of the JEM-X 3-7/7-18 keV hardness ratio from the central value, in units of σ . No significant temperature variations are found in the detected region.	69
5.7	<i>Chandra</i> image of the core of the Ophiuchus cluster. The circles represent the ISGRI best fit position in the 20-24 (green), 24-30 (black) and 30-40 keV (white) bands with 90% error radius. The black cross shows the position of the maximum emission in the cluster on the central cD galaxy, while white crosses show the position of the weak point sources in the cluster.	70

5.8	Combined <i>INTEGRAL</i> JEM-X (red) and ISGRI (black) folded spectrum of the Ophiuchus cluster. The solid line shows the model at $kT = 8.5 \pm 0.4$ keV fitted to the low-energy data (3-20 keV) and extrapolated to higher energies. The bottom panel shows the residuals from the model. A significant excess is found above 25 keV.	71
5.9	Models for the Spectral Energy Distribution (SED) of the non-thermal emission from the Ophiuchus cluster. The radio data are from Johnston et al. (1981). The black triangle represents the <i>INTEGRAL</i> measurement of non-thermal emission (this work). In the top panel, we considered a high-energy electron population of $E \sim$ PeV electrons radiating in the HXR range through synchrotron emission and in the TeV range through IC scattering, while in the bottom panel, a more conventional modeling with $E \sim$ GeV electrons was performed. The dashed lines above ~ 10 TeV shows attenuation of the spectrum by interaction of the γ -ray photons with the extragalactic infra-red and CMB radiation fields.	74
5.10	<i>INTEGRAL</i> JEM-X/ISGRI spectrum of the Ophiuchus cluster. The solid line show the thermal model at $kT = 9.3$ keV and abundance 0.33 from <i>Suzaku</i> /XIS, fitted to the low-energy part of the <i>INTEGRAL</i> range (3-20 keV) and extrapolated to higher energies.	75
5.11	Spectral Energy Distribution of the Ophiuchus cluster fitted by a dark-matter annihilation model (Profumo 2008). The radio data are from Johnston et al. (1981) and the X-ray data are from this work. The thermal bremsstrahlung emission was fixed to the MEKAL model at $kT = 8.5$ keV fitted to the JEM-X data.	78
6.1	<i>Chandra</i> image of the Perseus cluster in the 1-10 keV band, and comparison with the radio image of the same region from the <i>VLA</i> (Credit: NRAO/VLA/G. Taylor). The angular size of the square is 3 arcmin.	90
6.2	Westerbork Synthesis Radio Telescope image of the Perseus mini-halo at 330 MHz (Feretti et al. 2004). The angular resolution of the image is $51'' \times 77''$ (RA \times DEC). The cross shows the position of NGC 1275 in the centre.	91
6.3	Left: ISGRI 20-30 keV significance image of the Perseus cluster region. For comparison, the contours show the JEM-X 3-7 keV emission. The position of the Seyfert 2 nucleus NGC 1275 is also displayed. Right: JEM-X significance image of the cluster in the 3-7 keV band with contours from <i>ROSAT</i> /PSPC. The green circle shows the position of NGC 1275 at the centre of the cluster.	92
6.4	Left: JEM-X1 (black) and JEM-X2 (red) spectra of Perseus in the 3-10 keV band fitted simultaneously by a MEKAL model at $kT = 3.9 \pm 0.1$ keV. The residuals from the model are displayed in the bottom panel. Right: Unfolded JEM-X2 spectrum in an EF_E representation.	93

6.5	Total broad-band <i>INTEGRAL</i> spectrum extracted with JEM-X (3-20 keV) and ISGRI (17-120 keV). The model (green solid line) consists in a thermal component (dashed red) plus a power-law component (dashed green), with the parameters of the power-law as found by Sanders et al. (2005). The presence of a power-law without cut-off at the level claimed by Sanders et al. (2005) is ruled out by <i>INTEGRAL</i> data.	94
6.6	Total <i>INTEGRAL</i> unfolded spectrum of the Perseus cluster. The green solid line shows the best fit to the data with a 3 keV thermal model (dashed red), plus a 7 keV bremsstrahlung model to describe the emission from the outer regions of the cluster (dashed green), plus the contribution of the central AGN NGC 1275 under the form of a power-law (dashed blue).	95
7.1	Schematic view of a pulsar.	101
7.2	Left: IBIS/ISGRI light-curve of the 2004 outburst of IGR J00291+5934. Right: JEM-X/ISGRI total spectrum of IGR J00291+5934. The solid line shows the best fit to the data using a CompPS model with a disc temperature $kT = 1.5 \pm 0.2$ keV and an optically-thick corona at $kT = 49_{-6}^{+2}$ keV. Both figures are from Falanga et al. (2005).	103
7.3	ISGRI (left) and JEM-X1 (right) significance images of IGR J00291+5934 during the 2004 outburst. Two other known sources (the Cataclysmic Variable V709 Cas and the blazar 1ES 0033+59.5) are found less than one degree away from the source.	104
7.4	Left: Folded spectrum of IGR J00291+5931 extracted with JEM-X (black) and ISGRI (red). The bottom panel shows the deviations of the data compared to the best fit with a black-body+CompST model (solid line). Right: Unfolded spectrum of IGR J00291+5931 in EF_E representation. The solid green line shows the total model made of black-body emission from the neutron star (dashed red) plus comptonized emission from the corona, approximated by a CompST model (dashed green).	105
A.1	Difference between the fitted position of the Crab nebula and the known position (arrows), as a function of the position of the source on the detector (dots), for a selectron of pointings. The X and Y axes represent the position of the source with respect to the axis of the spacecraft in detector pixel coordinates. The size of the arrows is multiplied by a factor 100 for better readability.	118
A.2	Empirical mask model (“SuperPIF”) renormalized such that the mean background level is 0 and the mean Crab count rate is set to 1.	118
A.3	ISGRI 20-40 keV mosaic images produced from a sample of 130 ScWs with the Crab nebula in the FOV, processed with our method (left) and with the standard OSA 7.0 software (right).	120

Tables

4.1	INTEGRAL observation log on the Coma cluster	38
5.1	Summary of published X-ray data on the Ophiuchus cluster. The columns represent the central temperature, the iron abundance relative to the solar value, the presence or not of a cooling flow and of a non-thermal excess. References: ¹ Johnston et al. (1981) ² Arnaud et al. (1987) ³ Okumura et al. (1988) ⁴ Matsuzawa et al. (1996) ⁵ Watanabe et al. (2001) ⁶ Nevalainen et al. (2004) ⁷ Eckert et al. (2008) ⁸ Fujita et al. (2008)	65
5.2	Results of the spectral fitting procedure for a thermal + power-law model, with abundance and redshift values fixed to the literature value and photon index fixed to $\alpha = 2.0$, similar to the work of Nevalainen et al. (2004). In Method 1, the temperature and the normalization of the bremsstrahlung component are left free while fitting. In Method 2, we used the data in the 3-20 keV band to fix the temperature and normalization of the thermal component, and let free only the normalization of the non-thermal component. ^a P_{F-test} is the null hypothesis probability when adding the non-thermal component given by the F-test. ^b 20-60 keV flux of the non-thermal component, in units of 10^{-12} ergs s^{-1} cm^{-2} . The errors are quoted at the 1σ level. ^c Confidence level for the detection of the non-thermal component.	71
7.1	Results of spectral fitting when modeling the spectrum of IGR J00291+5934 as soft black-body emission comptonized by a hot corona. The parameters of the fit are the black-body temperature kT_{bb} , the coronal temperature kT_{cor} and the optical depth of the corona τ	105

Bibliography

- Allen, S. W., Fabian, A. C., Johnstone, R. M., Edge, A. C., & Nulsen, P. E. J. 1992, MNRAS, 254, 51
- Arnaud, K. A. 1996, in *Astronomical Society of the Pacific Conference Series*, Vol. 101, *Astronomical Data Analysis Software and Systems V*, ed. G. H. Jacoby & J. Barnes, 17–+
- Arnaud, K. A., Johnstone, R. M., Fabian, A. C., et al. 1987, MNRAS, 227, 241
- Arnaud, M. 2005, in *Background Microwave Radiation and Intracluster Cosmology*, ed. F. Melchiorri & Y. Rephaeli, 77–+
- Arnaud, M., Aghanim, N., Gastaud, R., et al. 2001, A&A, 365, L67
- Baade, C. & Zwicky, F. 1934, Phys. Review, 45, 138
- Bagchi, J., Durret, F., Neto, G. B. L., & Paul, S. 2006, Science, 314, 791
- Bahcall, N. A. 1974, ApJ, 187, 439
- Beck, R., Shukurov, A., Sokoloff, D., & Wielebinski, R. 2003, A&A, 411, 99
- Bell, S. J. & Hewish, A. 1967, Nature, 213, 1214
- Berrington, R. C. & Dermer, C. D. 2003, ApJ, 594, 709
- Bird, A. J., Malizia, A., Bazzano, A., et al. 2007, ApJS, 170, 175
- Biviano, A. 1998, in *Untangling Coma Berenices: A New Vision of an Old Cluster*, ed. A. Mazure, F. Casoli, F. Durret, & D. Gerbal, 1–+
- Blandford, R. D. & Ostriker, J. P. 1978, ApJ L, 221, L29
- Blasi, P. 2000, ApJ L, 532, L9
- Blasi, P., Gabici, S., & Brunetti, G. 2007, ArXiv Astrophysics e-prints
- Blumenthal, G. R. & Gould, R. J. 1970, Reviews of Modern Physics, 42, 237
- Bodaghee, A., Courvoisier, T. J.-L., Rodriguez, J., et al. 2007, A&A, 467, 585
- Boehringer, H., Voges, W., Fabian, A. C., Edge, A. C., & Neumann, D. M. 1993, MNRAS, 264, L25
- Bowyer, S., Korpela, E. J., Lampton, M., & Jones, T. W. 2004, ApJ, 605, 168
- Briel, U. G., Henry, J. P., & Boehringer, H. 1992, A&A, 259, L31

- Briel, U. G., Henry, J. P., Lumb, D. H., et al. 2001, *A&A*, 365, L60
- Brunetti, G., Setti, G., Feretti, L., & Giovannini, G. 2001, *MNRAS*, 320, 365
- Burns, J. O., Sulkanen, M. E., Gisler, G. R., & Perley, R. A. 1992, *ApJ L*, 388, L49
- Carilli, C. L. & Taylor, G. B. 2002, *ARA&A*, 40, 319
- Cash, W., Malina, R. F., & Wolff, R. S. 1976, *ApJ L*, 209, L111
- Chakrabarty, D., Morgan, E. H., Munro, M. P., et al. 2003, *Nature*, 424, 42
- Churazov, E., Forman, W., Jones, C., & Böhringer, H. 2003, *ApJ*, 590, 225
- Clarke, T. E., Kronberg, P. P., & Böhringer, H. 2001, *ApJ L*, 547, L111
- Colless, M. & Dunn, A. M. 1996, *ApJ*, 458, 435
- Courvoisier, T. J.-L. 2007, *Lectures On High-Energy Astrophysics (Doctoral Formation in Astrophysics, Geneva Observatory, University of Geneva)*
- Courvoisier, T. J.-L., Walter, R., Beckmann, V., et al. 2003, *A&A*, 411, L53
- Cowie, L. L. & Binney, J. 1977, *ApJ*, 215, 723
- Deiss, B. M., Reich, W., Lesch, H., & Wielebinski, R. 1997, *A&A*, 321, 55
- Di Cocco, G., Caroli, E., Celesi, E., et al. 2003, *A&A*, 411, L189
- Dogiel, V. A., Colafrancesco, S., Ko, C. M., et al. 2007, *A&A*, 461, 433
- Donato, D., Sambruna, R. M., & Gliozzi, M. 2004, *ApJ*, 617, 915
- Eckert, D., Neronov, A., Courvoisier, T. J.-L., & Produit, N. 2007a, *A&A*, 470, 835
- Eckert, D., Produit, N., Neronov, A., & Courvoisier, T. J. . 2007b, *ArXiv e-prints*, 710
- Eckert, D., Produit, N., Paltani, S., Neronov, A., & Courvoisier, T. J.-L. 2008, *A&A*, 479, 27
- Eckert, D., Walter, R., Kretschmar, P., et al. 2004, *The Astronomer's Telegram*, 352, 1
- Fabian, A. C. 1994, *ARA&A*, 32, 277
- Fabian, A. C., Hu, E. M., Cowie, L. L., & Grindlay, J. 1981, *ApJ*, 248, 47
- Fabian, A. C., Nulsen, P. E. J., & Canizares, C. R. 1984, *Nature*, 310, 733
- Fabian, A. C., Sanders, J. S., Allen, S. W., et al. 2003, *MNRAS*, 344, L43
- Fabian, A. C., Sanders, J. S., Taylor, G. B., et al. 2006, *MNRAS*, 366, 417
- Fabian, A. C., Zarneck, J. C., Culhane, J. L., et al. 1974, *ApJ L*, 189, L59+
- Falanga, M., Kuiper, L., Poutanen, J., et al. 2005, *A&A*, 444, 15
- Favre, P. 2004, *PhD thesis, University of Geneva*

- Feretti, L., Burigana, C., & Enßlin, T. A. 2004, *New Astronomy Review*, 48, 1137
- Feretti, L., Dallacasa, D., Giovannini, G., & Tagliani, A. 1995, *A&A*, 302, 680
- Feretti, L. & Giovannini, G. 2007, *ArXiv Astrophysics e-prints*
- Forman, W., Kellogg, E., Gursky, H., Tananbaum, H., & Giacconi, R. 1972, *ApJ*, 178, 309
- Fox, D. B. & Kulkarni, S. R. 2004, *The Astronomer's Telegram*, 354, 1
- Fritz, G., Davidsen, A., Meekins, J. F., & Friedman, H. 1971, *ApJ L*, 164, L81+
- Fujita, Y., Nagai, M., Hayashida, K., et al. 2008, *Submitted to PASJ*
- Fusco-Femiano, R., dal Fiume, D., Feretti, L., et al. 1999, *ApJ L*, 513, L21
- Fusco-Femiano, R., Landi, R., & Orlandini, M. 2005, *ApJ L*, 624, L69
- Fusco-Femiano, R., Orlandini, M., Brunetti, G., et al. 2004, *ApJ L*, 602, L73
- Gabici, S. & Blasi, P. 2003, *ApJ*, 583, 695
- Galloway, D. K., Markwardt, C. B., Morgan, E. H., Chakrabarty, D., & Strohmayer, T. E. 2005, *ApJ L*, 622, L45
- Giovannini, G., Feretti, L., Venturi, T., Kim, K.-T., & Kronberg, P. P. 1993, *ApJ*, 406, 399
- Giovannini, G., Tordi, M., & Feretti, L. 1999, *New Astronomy*, 4, 141
- Gitti, M., Brunetti, G., & Setti, G. 2002, *A&A*, 386, 456
- Goldshmidt, O. & Rephaeli, Y. 1993, *ApJ*, 411, 518
- Goldwurm, A., Goldoni, P., Gros, A., et al. 2001, in *ESA Special Publication, Vol. 459, Exploring the Gamma-Ray Universe*, ed. A. Gimenez, V. Reglero, & C. Winkler, 497–500
- Gottesman, S. R. & Fenimore, E. E. 1989, *Applied Optics*, 28, 4344
- Hasegawa, T., Wakamatsu, K.-i., Malkan, M., et al. 2000, *MNRAS*, 316, 326
- Inoue, S., Aharonian, F. A., & Sugiyama, N. 2005, *ApJ L*, 628, L9
- Jansen, F., Lumb, D., Altieri, B., et al. 2001, *A&A*, 365, L1
- Jenkins, L. P., Hornschemeier, A. E., Mobasher, B., Alexander, D. M., & Bauer, F. E. 2007, *ApJ*, 666, 846
- Johnston, M. D., Bradt, H. V., Doxsey, R. E., et al. 1981, *ApJ*, 245, 799
- Kaastra, J. S., Lieu, R., Tamura, T., Paerels, F. B. S., & den Herder, J. W. 2003, *A&A*, 397, 445

- Kaastra, J. S. & Mewe, R. 2000, in *Atomic Data Needs for X-ray Astronomy*, p. 161, ed. M. A. Bautista, T. R. Kallman, & A. K. Pradhan, 161–+
- Kim, K.-T., Kronberg, P. P., & Tribble, P. C. 1991, *ApJ*, 379, 80
- Lebrun, F., Leray, J. P., Lavocat, P., et al. 2003, *A&A*, 411, L141
- Lund, N., Budtz-Jørgensen, C., Westergaard, N. J., et al. 2003, *A&A*, 411, L231
- Lutovinov, A. A., Vikhlinin, A., Churazov, E. M., Revnivtsev, M. G., & Sunyaev, R. A. 2008, *ArXiv e-prints*, 802
- Markevitch, M., Gonzalez, A. H., Clowe, D., et al. 2004, *ApJ*, 606, 819
- Markwardt, C. B., Galloway, D. K., Chakrabarty, D., Morgan, E. H., & Strohmayer, T. E. 2004a, *The Astronomer's Telegram*, 360, 1
- Markwardt, C. B., Swank, J. H., & Strohmayer, T. E. 2004b, *The Astronomer's Telegram*, 353, 1
- Mas-Hesse, J. M., Giménez, A., Culhane, J. L., et al. 2003, *A&A*, 411, L261
- Matsuzawa, H., Matsuoka, M., Ikebe, Y., Mihara, T., & Yamashita, K. 1996, *PASJ*, 48, 565
- Meekins, J. F., Gilbert, F., Chubb, T. A., Friedman, H., & Henry, R. C. 1971, *Nature*, 231, 107
- Mellier, Y., Mathez, G., Mazure, A., Chauvineau, B., & Proust, D. 1988, *A&A*, 199, 67
- Mitchell, R. J., Culhane, J. L., Davison, P. J. N., & Ives, J. C. 1976, *MNRAS*, 175, 29P
- Mohr, J. J., Mathiesen, B., & Evrard, A. E. 1999, *ApJ*, 517, 627
- Neumann, D. M., Lumb, D. H., Pratt, G. W., & Briel, U. G. 2003, *A&A*, 400, 811
- Nevalainen, J., Lieu, R., Bonamente, M., & Lumb, D. 2003, *ApJ*, 584, 716
- Nevalainen, J., Oosterbroek, T., Bonamente, M., & Colafrancesco, S. 2004, *ApJ*, 608, 166
- Okumura, Y., Tsunemi, H., Yamashita, K., et al. 1988, *PASJ*, 40, 639
- Paizis, A., Nowak, M. A., Wilms, J., et al. 2005, *A&A*, 444, 357
- Petrosian, V. 2001, *ApJ*, 557, 560
- Petrosian, V., Rephaeli, Y., & Bykov, A. 2008, *ArXiv e-prints*, 801
- Pfrommer, C. 2007, *ArXiv e-prints*, 707
- Pfrommer, C. & Enßlin, T. A. 2004, *A&A*, 413, 17
- Pfrommer, C., Ensslin, T. A., & Springel, V. 2007, *ArXiv e-prints*, 707
- Poutanen, J. & Svensson, R. 1996, *ApJ*, 470, 249

BIBLIOGRAPHY

155

- Profumo, S. 2008, ArXiv e-prints, 801
- Read, A. M. & Ponman, T. J. 2003, *A&A*, 409, 395
- Reimer, O., Pohl, M., Sreekumar, P., & Mattox, J. R. 2003, *ApJ*, 588, 155
- Renaud, M., Bélanger, G., Paul, J., Lebrun, F., & Terrier, R. 2006a, *A&A*, 453, L5
- Renaud, M., Gros, A., Lebrun, F., et al. 2006b, *A&A*, 456, 389
- Rephaeli, Y. 1979, *ApJ*, 227, 364
- Rephaeli, Y. & Gruber, D. 2002, *ApJ*, 579, 587
- Rephaeli, Y., Ulmer, M., & Gruber, D. 1994, *ApJ*, 429, 554
- Revnivtsev, M. G., Sunyaev, R. A., Varshalovich, D. A., et al. 2004, *Astronomy Letters*, 30, 382
- Rossetti, M. & Molendi, S. 2004, *A&A*, 414, L41
- Rottgering, H. J. A., Wieringa, M. H., Hunstead, R. W., & Ekers, R. D. 1997, *MNRAS*, 290, 577
- Rybicki, G. B. & Lightman, A. P. 1985, *Radiative Processes in Astrophysics* (Wiley)
- Ryu, D., Kang, H., Hallman, E., & Jones, T. W. 2003, *ApJ*, 593, 599
- Sanders, J. S., Fabian, A. C., & Dunn, R. J. H. 2005, *MNRAS*, 360, 133
- Sarazin, C. L. 1999, *ApJ*, 520, 529
- Shakura, N. I. & Sunyaev, R. A. 1973, *A&A*, 24, 337
- Shaw, S. E., Mowlavi, N., Rodriguez, J., et al. 2005, *A&A*, 432, L13
- Strüder, L., Briel, U., Dennerl, K., et al. 2001, *A&A*, 365, L18
- Sunyaev, R. A. & Titarchuk, L. G. 1980, *A&A*, 86, 121
- Thierbach, M., Klein, U., & Wielebinski, R. 2003, *A&A*, 397, 53
- Timokhin, A. N., Aharonian, F. A., & Neronov, A. Y. 2004, *A&A*, 417, 391
- Tucker, W., Blanco, P., Rappoport, S., et al. 1998, *ApJ L*, 496, L5+
- Ubertini, P., Lebrun, F., Di Cocco, G., et al. 2003, *A&A*, 411, L131
- Ulmer, M. P., Cruddace, R. G., Fritz, G. G., Snyder, W. A., & Fenimore, E. E. 1987, *ApJ*, 319, 118
- Vedrenne, G., Roques, J.-P., Schönfelder, V., et al. 2003, *A&A*, 411, L63
- Voit, G. M. 2005, *Reviews of Modern Physics*, 77, 207
- Wakamatsu, K. & Malkan, M. A. 1981, *PASJ*, 33, 57

- Watanabe, M., Yamashita, K., Furuzawa, A., Kunieda, H., & Tawara, Y. 2001, PASJ, 53, 605
- Weidenspointner, G., Skinner, G., Jean, P., et al. 2008, Nature, 451, 159
- White, D. A., Fabian, A. C., Johnstone, R. M., Mushotzky, R. F., & Arnaud, K. A. 1991, MNRAS, 252, 72
- Willson, M. A. G. 1970, MNRAS, 151, 1
- Winkler, C., Courvoisier, T. J.-L., Di Cocco, G., et al. 2003, A&A, 411, L1
- Wolf, M. 1901, Astronomische Nachrichten, 155, 127
- Zwicky, F. 1937, ApJ, 86, 217